T2R2 東京科学大学 リサーチリポジトリ
Science Tokyo Research Repository

論文 / 著書情報
Article / Book Information

題目(和文)	
Title(English)	CVD Growth of Single-Walled Carbon Nanotubes and their Anisotropic Optical Properties
著者(和文)	村上陽一
Author(English)	Yoichi Murakami
出典(和文)	学位:博士(工学), 学位授与機関:東京大学大学院工学系研究科, 報告番号:, 授与年月日:2005年3月24日, 学位の種別:課程博士, 審査員:
Citation(English)	Degree:Doctor (Engineering), Conferring organization: The University of Tokyo, Report number:, Conferred date:2005/3/24, Degree Type:Course doctor, Examiner:
学位種別(和文)	博士論文
Type(English)	Doctoral Thesis

Powered by T2R2 (Science Tokyo Research Repository)

CVD Growth of Single-Walled Carbon Nanotubes and their Anisotropic Optical Properties

by

Yoichi Murakami

A THESIS SUBMITTED IN PARTIAL FULFILLMENT OF THE
REQUIREMENTS FOR THE DEGREE OF
DOCTOR OF ENGINEERING

Department of Mechanical Engineering
The University of Tokyo

December 2004

CVD Growth of Single-Walled Carbon Nanotubes and their Anisotropic Optical Properties

by Yoichi Murakami

Approved, Thesis Committee:

Shigeo Maruyama, Thesis advisor and Chairman
Professor of Mechanical Engineering,
The University of Tokyo

Yoichiro Matsumoto
Professor of Mechanical Engineering,
The University of Tokyo

Yuichi Ikuhara
Professor of Materials Engineering,
The University of Tokyo

Atsumu Tezaki
Associate Professor of Mechanical Engineering, The University of Tokyo

Tatsuya Okubo
Associate Professor of Chemical System Engineering, The University of Tokyo

Shinji Yamashita
Associate Professor of Electronics Engineering,
The University of Tokyo

Table of Contents

Chapter 1: Introduction **1**
1.1 Introduction and overview of the thesis 2
1.2 Structural representation of SWNTs 5
References for Chapter 1

Chapter 2: CVD growth of SWNTs and their analyses **15**
2.1 Characteristics of SWNT growth from zeolite-supported catalysts 16
2.1.1 Research background
2.1.2 Catalyst preparation and experimental procedure
2.1.3 Definition of SWNT yield
2.1.4 Effect of CVD time and reduction of catalyst on SWNT yield
2.1.5 Microscopic analyses of obtained SWNTs on zeolite support
2.1.6 Effect of catalyst metal selection on growth of SWNTs
2.1.7 Summary
2.2 Catalyzed growth of SWNTs from mesoporous silica thin films 30
2.2.1 Research background and motivation
2.2.2 Preparations and experiments
2.2.3 Results and discussions
2.2.4 Summary of SWNT growth from MPS thin films
2.3 Development of techniques for direct synthesis of SWNTs on solid flat substrates 38
2.3.1 Research background and motivation
2.3.2 Development of dip-coat catalyst supporting method
2.3.3 Direct synthesis of SWNTs on Si and quartz substrates
2.3.3.1 Experimental procedure
2.3.3.2 Resonant Raman scattering analysis
2.3.3.3 Microscopic analysis
2.3.3.4 Discussions
2.3.4 Summary of direct growth of SWNTs on flat substrates

2.4 Morphology and chemical state analysis of Co-Mo catalysts supported on substrates by TEM and XPS analyses 60
2.4.1 Questions to be resolved for dip-coat supported Co-Mo catalysts
2.4.2 Methods for catalyst characterization
2.4.2.1 TEM observation and its sample preparation
2.4.2.2 Procedure for XPS measurement
2.4.3 Results of TEM and XPS analyses
2.4.3.1 Morphology of calcined and reduced Co-Mo catalyst
2.4.3.2 Chemical state of calcined and reduced Co-Mo catalysts analyzed by XPS
2.4.3.3 Mechanism and formation process of Co-Mo catalyst
2.4.4 Summary of formation process and role of Co-Mo catalyst
2.5 Summary of Chapter 2 70
Acknowledgements for Chapter 2
References for Chapter 2

Chapter 3: Growth of vertically aligned SWNT films on substrates and their formation process 79
3.1 Research background and motivation 80
3.2 Experimental and analysis procedures 81
3.3 Effect of CVD chamber vacuum on SWNT growth 82
3.4 Microscopic and optical analyses 84
3.4.1 Morphological investigations by FE-SEM and HR-TEM
3.4.2 Resonant Raman scattering analysis
3.5 Discussion of vertical alignment formation in SWNTs 90
3.6 Transient investigations and modeling of growth process of vertically aligned SWNT films 92
3.6.1 Growth and formation process of vertically aligned SWNT film
3.6.2 *In situ* measurement of growth process of vertically aligned SWNT film
3.6.3 Formulation for growth process of vertically aligned SWNT film
3.7 Summary of Chapter 3 107
Acknowledgements for Chapter 3
References for Chapter 3

Chapter 4: Anisotropic optical properties of SWNTs and their optical applications 111

4.1 Determination of optical anisotropy of the vertically aligned SWNT film and optical absorption cross-section of SWNTs 112

4.1.1 Research background for polarized optical properties of SWNTs

4.1.2 Experimental and optical measurement setup

4.1.3 Dependence of optical absorption spectrum on SWNT morphology

4.1.4 Polarized optical absorption of vertically aligned SWNT film

4.1.5 Anisotropic optical properties of graphite

4.1.6 Modeling and formulation of multi-dipole optical absorption of SWNTs

4.1.6.1 Transition probability

4.1.6.2 Optical absorption by dipole transition moment

4.1.6.3 Formulation for multiple dipole absorption by vertically aligned SWNTs

4.1.7 Determination of optical anisotropy and bare optical absorption cross-section of SWNTs

4.1.8 Summary of anisotropy optical properties of SWNTs

4.2 Polarization dependence of Raman scattering characteristics from vertically aligned SWNT film 131

4.2.1 Introduction - Role of Raman scattering in SWNT analysis

4.2.2 Raman scattering measurement

4.2.3 Experimental results and analyses

4.2.3.1 Raman spectrum dependence on laser polarization

4.2.3.2 RBM peak behavior by molecular adsorption

4.2.3.3 RBM peak dependence on laser intensity

4.2.4 Discussion and interpretation of obtained data

4.2.4.1 Interpretation of data based on $\Delta\mu = \pm 1$ transition by cross-polarized light

4.2.4.2 Another possibility of interpreting the data

4.2.5 Summary of polarization dependence of Raman scattering

4.3 Optical applications of SWNT film directly synthesized on solid surfaces 154

4.3.1 Motivation and research background

4.3.2 Experimental setup
4.3.3 Principles of mode-locked ring fiber laser
4.3.4 Results and summary
4.4 Summary of Chapter 4 160
Acknowledgements for Chapter 4
References for Chapter 4

Chapter 5: Summary 167

Appendix: Perturbated Hamiltonian for one-photon process

Acknowledgements

List of publications

Chapter 1:
Introduction

1.1 Introduction and overview of the thesis

Single-walled carbon nanotubes (SWNTs) are a new group of carbon materials possessing one-dimensional cylindrical geometry that is formed by rolling a sp^2-bonded graphene sheet. Immediately after its landmark discovery and structure determination in 1993 by Iijima and Ichihashi [1], theoretical studies on SWNTs commenced; these revealed several distinctive physical properties of SWNTs, such as their unique electronic density of states (eDOS) and metal-semiconducting distinction that is solely dependent on their chirality [2].

Experimental studies on SWNTs became possible after the establishment of production methods in the late 1990s, such as laser-furnace (1996) [3], arc-discharge (1997) [4], and catalytic CVD methods with supported catalysts (1996) [5] and floated catalysts (1998) [6,7]. These methods are intended for use in the mass synthesis of SWNTs in which the SWNTs are obtained as soot adhered on the wall of the production chambers. Since the as-obtained soot contains amorphous carbons, multi-shelled graphites, fullerenes, and/or catalyst metal particles as impurities, a purification process [8–11] is generally required prior to its use. Although the SWNTs produced by these methods usually necessitates such a purification process, these production methods are firmly established at present. In particular, the HiPco method (1999) [12] that utilizes the disproportionation reaction of CO gas is now regarded as a commercially feasible method for the mass production of SWNTs. At the same time, the CVD method with a supported catalyst is currently being intensively studied as a promising technique. The alcohol CCVD method (2002) [13], which is used in this thesis, is one of such technique and can produce high-quality SWNTs that are almost free from the aforementioned impurities even in the as-synthesized state.

With the establishment of production methods of SWNTs, experimental studies for specific applications have become active and many innovative applications have been studied and proposed [14], such as one-dimensional (1D) quantum wire [15], field effect transistor (FET) [16–19], cold cathodes for electron emitters [20,21], chemical sensors [22,23], probe tips for atomic force microscopes (AFM) [24–26], saturable optical absorbers for ultrafast all-optic switches [27–29], and nano-sized infrared detectors/emitters [30,31]. In any application, the 1D geometry, nanoscale size, and the physical/chemical properties of SWNTs are of great importance.

However, in order to completely achieve such innovative applications, the following problems should be resolved:

1) Direct growth of SWNTs on Si or other flat substrates.
2) Elucidation of the function of the catalyst that is optimal for the growth of SWNTs and construction of guidelines for the selection of a catalyst.
3) Morphologically aligned growth of SWNTs on Si or other flat substrates.
4) Elucidation of anisotropic optical properties of SWNTs toward light polarization.
5) Separation of bulk-synthesized SWNTs based on metallic/semiconducting distinction, or ideally, their chirality.
6) Selective growth of SWNTs as either metallic or semiconducting SWNTs, or ideally, chirality-specific growth.

A brief overview of these topics follows. Regarding problem 1, a SWNT-based FET has often been fabricated from bulk-produced SWNTs dispersed and spun coated on Si/SiO_2 substrates [15–19]. However, the yield of electrical devices fabricated by this method is considerably low because favorably isolated SWNTs on Si have to be found by atomic force microscopy (AFM) prior to the device fabrication. Kong et al. [32] demonstrated for the first time that SWNTs could be grown on Si substrates by CVD. However, the SWNTs in that study were *indirectly* grown on the surface of the Si substrate, that is, the SWNTs were grown from Fe-Mo catalyst mixed with patterned alumina islands [32]. These supporting islands ($3 \times 3\ \mu m^2$) are not essential for the functioning of the device; therefore, it is desireble to eliminate them in order to enable high-density fabrication of the devices. A method of growing SWNTs directly on the surface of the Si/SiO_2 substrate is developed in Section 2.3, in which the catalyst metal is directly supported on the Si/SiO_2 surface without using an intermediate supporting layer.

Regarding problem 2, several types of catalysts, either monometallic or bimetallic, have been proposed for the growth of SWNTs. Empirically, it is known that a bimetallic catalyst such as Fe-Mo [32–36], Fe-Co [13,37], or Co-Mo [38–40] is more effective than a monometallic catalyst in enhancing the growth of SWNTs. Section 2.1 discusses the effect of the Fe-Co catalyst in terms of a thermo-gravimetric analysis (TGA) and thermodynamic properties of catalytic metals. In section 2.4, the role of the Co-Mo catalyst on Si/SiO_2 surface is elucidated, and a new model for catalyst dispersion is proposed, which is different from the previously proposed model for the Co-Mo system [39,40].

Regarding problem 3, significant effort was devoted to the morphologically controlled growth of SWNTs on solid surfaces. The vertical growth of multi-walled carbon nanotubes

(MWNTs) on a flat substrate has been successfully achieved [41–43]; however, when SWNTs are concerned, they have only been aligned parallel to the substrate surface [44-46]. Since it is well known that the transport properties of SWNTs are superior to those of MWNTs [14], the achievement of vertically aligned growth of SWNTs on flat substrates would accelerate their application as a cold cathode for electron emission electrodes. In Chapter 3, a new method, which is easy and reproducible, is developed for the vertical growth of SWNTs uniformly over the quartz substrate, and the growth process and mechanism are investigated in detail.

Regarding problem 4, SWNTs are also considered as a promising material for optical devices [27–29]. Since a SWNT has a 1D shape, its optical properties are expected to exhibit anisotropy toward light polarization with respect to the axis of SWNTs. However, it should be noted that the fundamental anisotropic optical properties of SWNTs have not yet been elucidated to a great extent. This is partly because it is difficult to prepare a well-aligned SWNT film that exhibits sufficient light absorption. Using the vertically aligned SWNT film developed in Chapter 3, the anisotropic optical absorption properties and Raman scattering characteristics are elucidated in Chapter 4.

Problem 5 is presently being resolved for metallic/semiconducting separation [47,48]. Regarding problem 6, the preferential growth of semiconducting SWNTs was recently reported [49] although chirality-specific growth, an important target for the future, has not yet been achieved.

The scope and originality of this thesis are related to the resolutions of problems 1–4. Although all of these have originally been investigated and resolved in this thesis, the most important originalities of this thesis lie in the resolutions of problems 3 and 4. In Chapter 2, a new method for the direct growth of SWNTs on Si and quartz substrates is presented, extensively analyzed, and discussed with respect to problems 1 and 2. In Chapter 3, high density, vertically aligned growth of SWNTs on the substrates—with respect to problem 3—is achieved, and a mechanism for vertical growth is investigated and modeled. In Chapter 4, using a vertically aligned SWNT film grown on quartz substrates, the polarization-dependent optical absorption property of SWNTs—with respect to problem 4—is elucidated. Finally, the contents of the thesis are summarized in Chapter 5.

A detailed introduction and background for each topic accompanies the beginning of the respective section or chapter.

1.2 Structural representation of SWNTs

The structure of the sp^2 carbon network of a two-dimentional (2D) graphene sheet is schematically presented as a hexagonal lattice in Fig. 1-1a. The shadowed rhombus indicates a unit cell of the graphene, which contains two non-equivalent C atoms. The distance between neighboring atoms $a_{c\text{-}c}$ is 1.42 Å, and vectors $\boldsymbol{a}_1$ and $\boldsymbol{a}_2$ represent the unit vectors of the cell. The Brillouin zone of the graphene is denoted in Fig. 1-1b as a shadowed hexagon, and vectors $\boldsymbol{b}_1$ and $\boldsymbol{b}_2$ are the reciprocal vectors. These are expressed as

$$\boldsymbol{a}_1 = \left(\frac{\sqrt{3}}{2}a, \frac{a}{2}\right), \quad \boldsymbol{a}_2 = \left(\frac{\sqrt{3}}{2}a, -\frac{a}{2}\right) \tag{1}$$

and

$$\boldsymbol{b}_1 = \left(\frac{2\pi}{\sqrt{3}a}, \frac{2\pi}{a}\right), \quad \boldsymbol{b}_2 = \left(\frac{2\pi}{\sqrt{3}a}, -\frac{2\pi}{a}\right) \tag{2}$$

based on the x-y and k_x-k_y coordinates, respectively, as shown in Fig. 1-1. In these equations, the lattice constant of the 2D graphene is defined as $a \equiv |\boldsymbol{a}_1| = |\boldsymbol{a}_2| = 1.42\ \text{Å} \times 3^{1/2} = 2.46\ \text{Å}$. By convention, high symmetry points at the center, corner, and the midpoint of the neighboring corners of the Brillouin zone are denoted as Γ, M, and K points, respectively.

The unit cell of SWNTs is enlarged when compared to that of the graphene due to the lower symmetry of SWNTs. Figure 1-2 shows an unrolled hexagonal lattice of a SWNT, in which the unit cell of a certain type of SWNT is indicated as a shadowed area. The vectors $\boldsymbol{C}_h$ and $\boldsymbol{T}$ that connect two crystallographically equivalent sites in the circumferential and axial directions of SWNTs, respectively, are also shown. These vectors are termed the chiral vector and the translational vector, respectively, as further explained below.

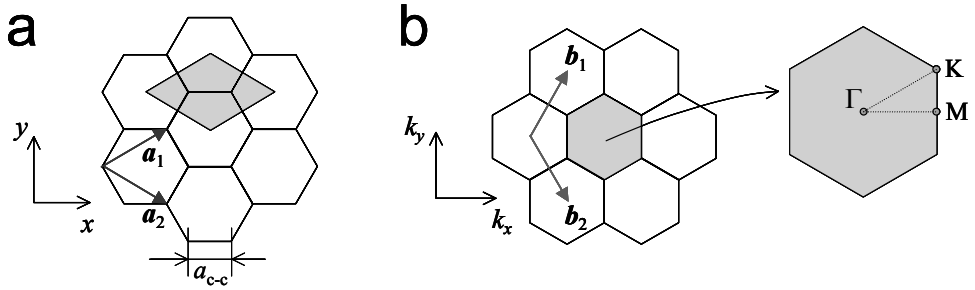


Fig. 1-1. (a) Unit cell and (b) Brillouin zone of 2D graphite represented as the shadowed rhombus and hexagon, respectively. $\boldsymbol{a}_i$ and $\boldsymbol{b}_i$ (i = 1, 2) are unit vectors and reciprocal lattice vectors, respectively. The high-symmetric points in the 2D Brillouin zone conventionally called Γ, K, and M point, are also shown.

The chiral vector $\boldsymbol{C}_h$ is expressed in terms of real-space unit vectors $\boldsymbol{a}_1$ and $\boldsymbol{a}_2$ and two integers n and m ($0 \le m \le n$) as

$$\boldsymbol{C}_h = n\boldsymbol{a}_1 + m\boldsymbol{a}_2 \equiv (n,m) \tag{3}$$

The type of SWNT is completely specified by the two integers (n, m) through the definition given in Eq. 3. Since the length of $\boldsymbol{C}_h$ indicates the circumferential length of the SWNT, the diameter of the SWNT, d_t, is expressed as

$$d_t = \frac{|\boldsymbol{C}_h|}{\pi} = \frac{\sqrt{\boldsymbol{C}_h \cdot \boldsymbol{C}_h}}{\pi} = \frac{a\sqrt{n^2 + m^2 + nm}}{\pi} \tag{4}$$

Here, $a \equiv |\boldsymbol{a}_1| = |\boldsymbol{a}_2| = 1.44$ Å $\times\, 3^{1/2} = 2.49$ Å is the lattice constant of the honeycomb lattice of the SWNT. A slightly greater C–C bond length in SWNTs compared to that in the graphene (1.42 Å) should be noted.

The angle formed by $\boldsymbol{C}_h$ and $\boldsymbol{a}_1$ is termed chiral vector θ, and its value is $0 \le \theta \le 30°$ due to the hexagonal symmetry of the honeycomb lattice; specifically, it is expressed as

$$\cos\theta = \frac{\boldsymbol{C}_h \cdot \boldsymbol{a}_1}{|\boldsymbol{C}_h||\boldsymbol{a}_1|} = \frac{2n + m}{2\sqrt{n^2 + m^2 + nm}} \tag{5}$$

The translational vector $\boldsymbol{T}$ is defined as the unit vector of a 1D SWNT, which is parallel to the SWNT axis. From the relationship $\boldsymbol{C}_h \cdot \boldsymbol{T} = 0$,

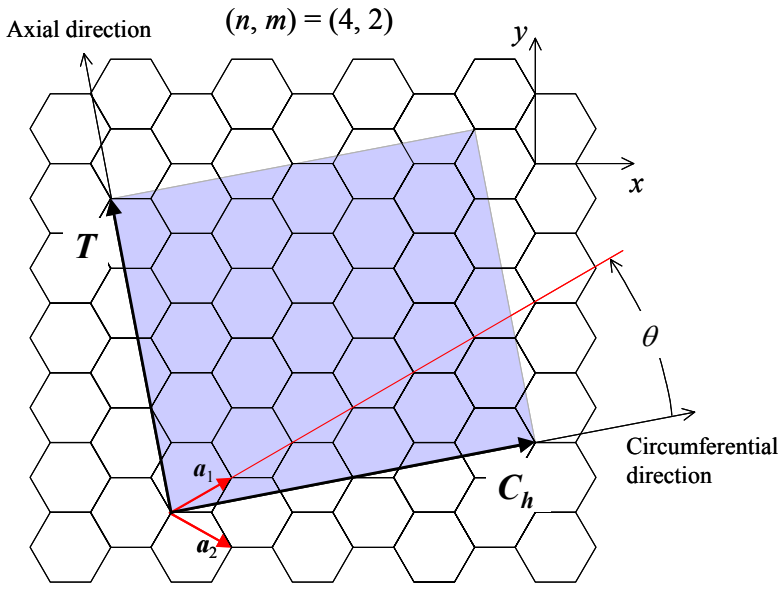


Fig. 1-2. Unrolled hexagonal lattice of a SWNT. The chiral vector $\boldsymbol{C}_h$ and translational vector $\boldsymbol{T}$ are presented for the case of $\boldsymbol{C}_h = 4\boldsymbol{a}_1 + 2\boldsymbol{a}_2$ SWNT. Its unit cell is denoted as shadowed area in which $N = 28$ hexagons are contained. The angle between $\boldsymbol{a}_1$ and $\boldsymbol{C}_h$ gives the chiral angle θ ($0 \le \theta \le 30°$).

$$\boldsymbol{T} = t_1\boldsymbol{a}_1 + t_2\boldsymbol{a}_2 \equiv (t_1, t_2), \quad t_1 = \frac{2m+n}{d_R}, \quad t_2 = -\frac{2n+m}{d_R} \tag{6}$$

where d_R is the greatest common divisor (gcd) of $(2m + n)$ and $(2n + m)$. Using the above defined d_R, the number of hexagons in the unit cell of a SWNT N is expressed as

$$N = \frac{\left|\boldsymbol{C}_h \times \boldsymbol{T}\right|}{\left|\boldsymbol{a}_1 \times \boldsymbol{a}_2\right|} = \frac{2\left(n^2 + m^2 + nm\right)}{d_R} \tag{7}$$

Therefore, there are $2N$ carbon atoms in the unit cell of a SWNT. For example, $(n, m) = (4, 2)$ SWNT shown in Fig. 1-2 has 28 hexagons in the unit cell.

Since the unit cell of a SWNT is 2D and specified by the orthogonal lattice vectors $\boldsymbol{C}_h$ and $\boldsymbol{T}$, as shown in Fig. 1-2, the reciprocal lattice vectors corresponding to the circumferential direction $\boldsymbol{K}_1$ and the axial direction $\boldsymbol{K}_2$ are defined such that the following relationships are satisfied:

$$\boldsymbol{C}_h \cdot \boldsymbol{K}_1 = \boldsymbol{T} \cdot \boldsymbol{K}_2 = 2\pi, \quad \boldsymbol{C}_h \cdot \boldsymbol{K}_2 = \boldsymbol{T} \cdot \boldsymbol{K}_1 = 0 \tag{8}$$

Solving these relations using Eqs. 6 and 7, $\boldsymbol{K}_1$ and $\boldsymbol{K}_2$ are expressed as

$$\boldsymbol{K}_1 = \frac{1}{N}\left(-t_2\boldsymbol{b}_1 + t_1\boldsymbol{b}_2\right) \tag{9}$$

$$\boldsymbol{K}_2 = \frac{1}{N}\left(m\boldsymbol{b}_1 - n\boldsymbol{b}_2\right) \tag{10}$$

Figure 1-3 shows the reciprocal lattice vectors $\boldsymbol{K}_1$ and $\boldsymbol{K}_2$ for $(n, m) = (4, 2)$ SWNT. The first Brillouin zone of the SWNT is expressed as a line segment W-W' as shown in Fig. 1-3a. Therefore, N line segments $\mu\boldsymbol{K}_1$ ($\mu = 1, \cdots, N - 1$) give rise to N discrete wave vectors, which originate from the quantized wave vector in the direction of $\boldsymbol{C}_h$ due to the periodic boundary condition imposed in this direction.

The electronic structure of a SWNT can be obtained from that of 2D graphite. When the energy dispersion relation of 2D graphite is denoted as $E_{g,\,2\mathrm{D}}$, N pairs of 1D energy dispersion relation $E_\mu(k)$ are expressed as

$$E_\mu(k) = E_{g,2\mathrm{D}}\left(k\frac{\boldsymbol{K}_2}{\left|\boldsymbol{K}_2\right|} + \mu\boldsymbol{K}_1\right), \quad (\mu = 0, \cdots, N-1, \text{ and } -\frac{\pi}{\left|\boldsymbol{T}\right|} < k < \frac{\pi}{\left|\boldsymbol{T}\right|}) \tag{11}$$

Here, k denotes the wave number along the SWNT axis. If these energy dispersion curves are collected (or folded) into the first Brillouin zone of the 2D graphite by translating them using multiples of $\boldsymbol{K}_1$ and $\boldsymbol{K}_2$, Fig. 1-3a is equivalently expressed as Fig. 1-3b in the reduced zone scheme. This expression shows that the wave vectors possible in the case of SWNTs

are limited from the case of 2D graphite. The line indicating the possible wave vector shown in Fig. 1-3b will hereafter be referred to as "cutting line".

Such a quantized wave vector of SWNTs causes a sharp divergence in their eDOS, termed "van Hove singularities," that is characteristic of 1D materials. Figure 1-4 shows the eDOS of $(n, m) = (4, 2)$ SWNT calculated by the tight-binding method with parameters $\gamma_0 = 2.9$ eV, $s = 0$, and $a_{c\text{–}c} = 0.144$ nm. Since it is obvious that the cutting line of this SWNT—described by Eq. 11—does not pass the K-point, in which the valence and conduction bands meet in the case of 2D graphite, the $(n, m) = (4, 2)$ SWNT is *semiconducting* in which eDOS is absent at the Fermi level. On the other hand, when the

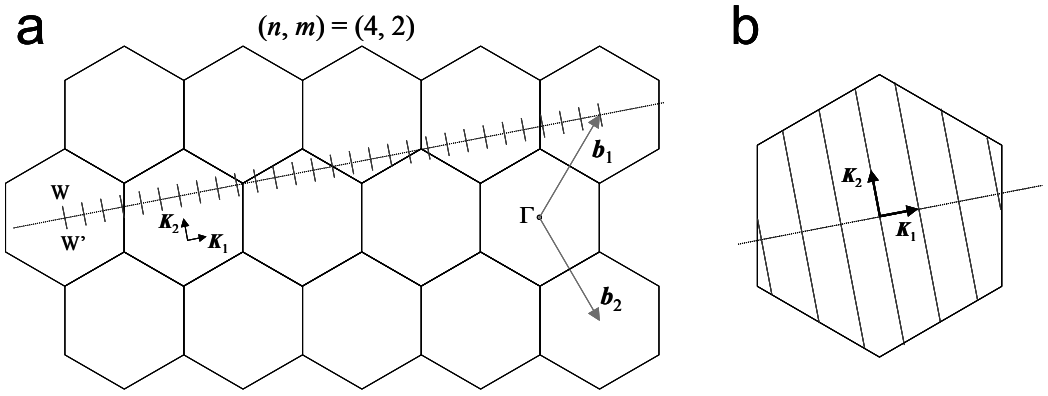


Fig. 1-3. (a) Brillouin zone of a SWNT represented by the line segment W-W' for the case of $(n, m) = (4, 2)$ SWNT, and (b) its equivalent representation displayed by the reduced-zone scheme. The vectors $\boldsymbol{K}_1$ and $\boldsymbol{K}_2$ are reciprocal lattice vectors correspond to $\boldsymbol{C}_h$ and $\boldsymbol{T}$, respectively.

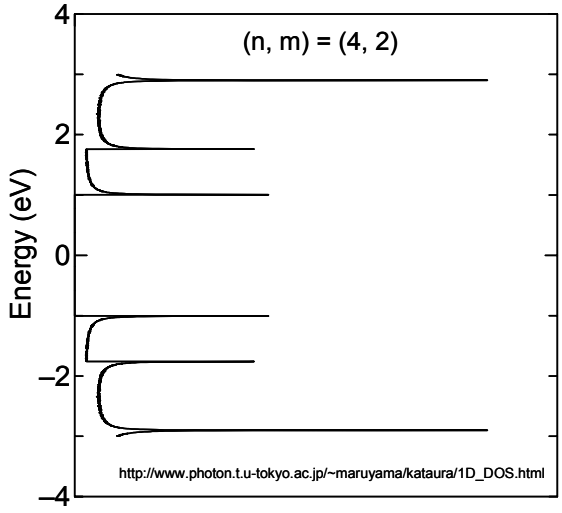


Fig. 1-4. (a) 3D Brillouin zone of graphite and cutting lines for $(n, m) = (4, 2)$ SWNT. (b) eDOS of $(n, m) = (4, 2)$ SWNT calculated by tight-binding method with $\gamma_0 = 2.9$ eV, $s = 0$, and $a_{c\text{-}c} = 0.144$ Å.

cutting line passes the K-point in the case of e.g. (n, m) = (5, 2) SWNT, the SWNT is metallic in which eDOS is at the Fermi level. In general, mod($n - m$) = 0 SWNTs are metallic and mod(n – m, 3) ≠ 0 SWNTs are semiconducting. One of the most important characteristics of SWNTs is that the difference of metallic/semiconducting transport properties is determined solely by the chirality.

Figure 1-5 shows the chiral mapping of (n, m) SWNTs that are either metallic (open circles) or semiconducting (solid circles). Any chirality is specified either by two integers (n, m) or equivalently, a combination of diameter d and chiral angle θ, as schematized in this figure. Among these, the SWNTs with m = 0 (i.e., θ = 0°) and $n = m$ (i.e., θ = 30°) chirality are termed "*zig-zag*" and "*armchair*" types, respectively. This is because the edges of their tubes look like a zigzag and an armchair, as shown in Fig. 1-6a and 1-6b, respectively. The SWNTs that do not belong to either of these types are the "*chiral*" type, as shown in Fig. 1-6c.

The fundamental characteristics, structure, and notational system presented in this section will be used in subsequent chapters, in which specific topics are studied in detail.

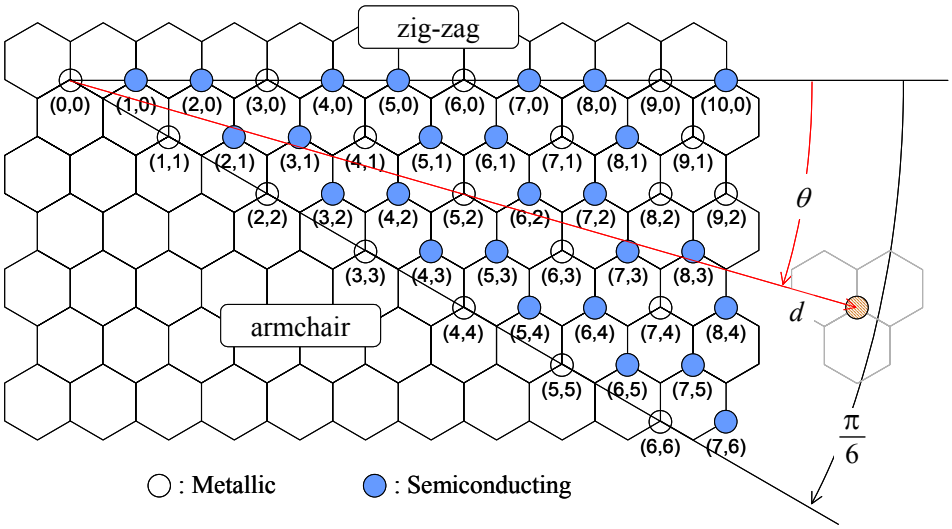


Fig. 1-5. The (n, m) of SWNTs that are metallic (open circles) and semiconducting (solid circles), respectively, denoted on the map of chiral vectors (n, m). Any chirality is specified either by two integers (n, m) or, equivalently, a combination of diameter d and chiral angle θ.

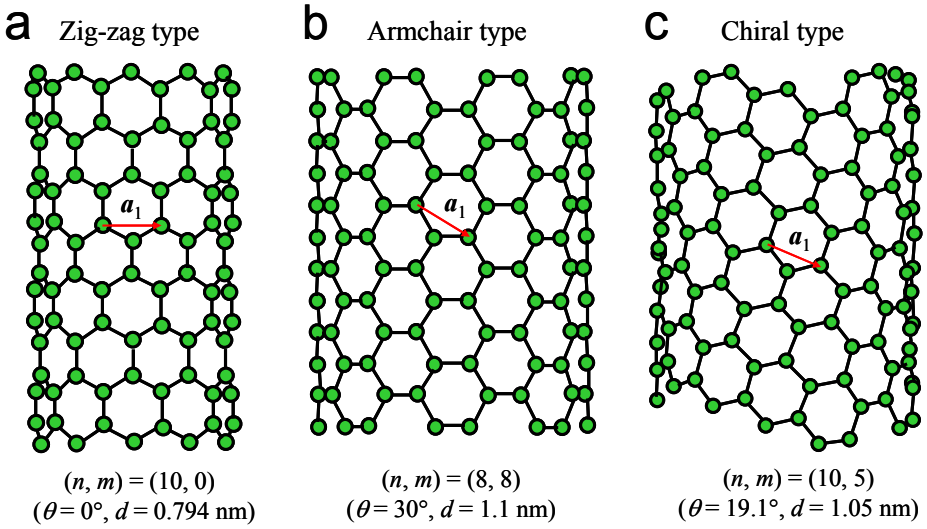


Fig. 1-6. Structure of (a) zig-zag type, (b) armchair type, and (c) chiral type SWNTs represented by (n, m) =(10, 0), (8, 8), and (10, 5) tubes.

References for Chapter 1

1. S. Iijima, T. Ichihashi, Nature **363** (1993) 603.
2. R. Saito, G. Dresselhaus, M.S. Dresselhaus, *Physical Properties of Carbon Nanotubes*, Imperial College Press, London, 1998.
3. A. Thess, R. Lee, P. Nikolaev, H. Dai, P. Petit, J. Robert, C. Xu, Y.H. Lee, S.G. Kim, A.G. Rinzler, D.T. Colbert, G.E. Scuseria, D. Tománek, J.E. Fischer, R.E. Smalley, Science **273** (1996) 483.
4. C. Journet, W. K. Maser, P. Bernier, A. Loiseau, M. L. de la Chapelle, S. Lefrant, P. Deniard, R. Lee, J. E. Fisher, Nature **388** (1997) 756.
5. H. Dai, A. G. Rinzler, P. Nikolaev, A. Thess, D. T. Colbert, R. E. Smalley, Chem. Phys. Lett. **260** (1996) 471.
6. B.C. Satishkumar, A. Govindaraj, R. Sen, C.N.R. Rao, Chem. Phys. Lett. **293** (1998) 47.
7. H.M. Cheng, F. Li, G. Su, H.Y. Pan, L.L. He, X. Sun, M.S. Dresselhaus, Appl. Phys. Lett. **72** (1998) 3282.
8. K.B. Shelimov, R.O. Esenaliev, A.G. Rinzler, C.B. Huffman, R.E. Smalley, Chem. Phys. Lett. **282** (1998) 429.
9. A.G. Rinzler, J. Liu, H. Dai, P. Nikolaev, C.B. Huffman, F.J. Rodriguez-Macias, P.J. Boul, A.H. Lu, D. Heymann, D.T. Colbert, R.S. Lee, J.E. Fischer, A.M. Rao, P.C. Eklund, R.E. Smalley, Appl. Phys. A **67** (1998) 29.
10. P. Hou, C. Liu, Y. Tong, S. Xu, M. Liu, H. Cheng, J. Mater. Res. **16** (2001) 2526.
11. I.W. Chiang, B.E. Brinson, R.E. Smalley, J.L. Margrave, R.H. Hauge, J. Phys. Chem. B **105** (2001) 1157.
12. P. Nikolaev, M.J. Bronikowski, R.K. Bradley, F. Rohmund, D.T. Colbert, K.A. Smith, R.E. Smalley, Chem. Phys. Lett. **313** (1999) 91.
13. S. Maruyama, R. Kojima, Y. Miyauchi, S. Chiashi, M. Kohno, Chem. Phys. Lett. **360** (2002) 229.
14. *Carbon Nanotubes: Synthesis, Structure, Properties and Applications*, edited by M.S. Dresselhaus, G. Dresselhaus, and Ph. Avouris, Springer-Verlag, Berlin, 2001.

15. S.J. Tans, M.H. Devoret, H. Dai, A. Thess, R.E. Smalley, L.J. Geerligs, C. Dekker, Nature **386** (1997) 474.

16. R. Martel, T. Schmidt, H. R. Shea, T. Hertel, P. Avouris, Appl. Phys. Lett. **73** (1998) 2447.

17. S. J. Tans, A. R. M. Verschueren, C. Dekker, Nature **393** (1998) 49.

18. A. Bachtold, P. Hadley, T. Nakanishi, C. Dekker, Science **294** (2001) 1317.

19. P. Avouris, Chem. Phys. **281** (2002) 429.

20. W.B. Choi, D.S. Chung, J.H. Kang, H.Y. Kim, Y.W. Jin, I.T. Han, Y.H. Lee, J.E.Jung, N.S. Lee, G.S. Park, J.M. Kim, Appl. Phys. Lett. **75** (1999) 3129.

21. W. Zhu, C. Bower, O. Zhou, G. Kochanski, S. Jin, Appl. Phys. Lett. **75** (1999) 873.

22. T. Someya, J. Small, P. Kim, C. Nuckolls, J.T. Yardley, Nano Lett. **3** (2003) 877.

23. J. Li, Y. Lu, Q. Ye, M. Cinke, J. Han, M. Meyyappan, Nano Lett. **3** (2003) 929.

24. S.S. Wong, E. Joselevich, A.T. Woolley, C.-L. Cheung, C.M. Liber, Nature **394** (1998) 52.

25. J.H. Hafner, C.-L. Cheung, C.M. Lieber, Nature **398** (1999) 761.

26. J.H. Hafner, C.-L. Cheung, A.T. Woolley, C.M. Lieber, Progress in Biophys. Molecular Biology **77** (2001) 73.

27. Y.C. Chen, N.R. Raravikar, L.S. Schadler, P.M. Ajayan, Y.P. Zhao, T.M. Lu, G.C. Wang, X.C. Zhang, Appl. Phys. Lett. **81** (2002) 975.

28. Y. Sakakibara, S. Tatsuura, H. Kataura, M. Tokumoto, Y. Achiba, Jpn. J. Appl. Phys. **42** (2003) L494.

29. S. Yamashita, Y. Inoue, S. Maruyama, Y. Murakami, H. Yamaguchi, M. Jablonski, S.Y. Set, Opt Lett. **29** (2004) 1581.

30. J.A. Misewich, R. Martel, P. Avouris, J.C. Tsang, S. Heinze, J. Tersoff, Science **300** (2003) 783.

31. M. Freitag, Y. Martin, J.A. Misewich, R. Martel, P. Avouris, Nano Lett. **3** (2003) 1067.

32. J. Kong, H.T. Soh, A.M. Cassell, C.F. Quate, H. Dai, Nature **395** (1998) 878.

33. J.H. Hafner, M.J. Bronikowski, B.R. Azamian, P. Nikolaev, A.G. Rinzler, D.T. Colbert, K.A. Smith, R.E. Smalley, Chem. Phys. Lett. **296** (1998) 195.

34. A.M. Cassell, J.A. Raymakers, J. Kong, H. Dai, J. Phys. Chem. B. **103** (1999) 6484.

35. M. Su, B. Zheng, J.A. Liu, Chem. Phys. Lett. **322** (2000) 321.

36. A.R. Harutyunyan, B.K. Pradhan, U.J. Kim, G.G. Chen, P.C. Eklund, Nano Lett. **2** (2002) 525.

37. K. Mukhopadhyay, A. Koshio, T. Sugai, N. Tanaka, H. Shinohara, Z. Konya, J. B. Nagy, Chem. Phys. Lett. **303** (1999) 117.

38. B. Kitiyanan, W.E. Alvarez, J.H. Harwell, D.E. Resasco, Chem. Phys. Lett. **317** (2000) 497.

39. W.E. Alvarez, B. Kitiyanan, A. Borgna, D.E. Resasco, Carbon **39** (2001) 547.

40. J.E. Herrera, L. Balzano, A. Borgna, W.E. Alvarez, D.E. Resasco, J. Catalysis **204** (2001) 129.

41. Z.F. Ren, Z.P. Huang, J.W. Xu, J.H. Wang, P. Bush, M.P. Siegal, P.N. Provencio, Science **282** (1998) 1105.

42. S. Fan, M.G. Chapline, N.R. Franklin, T.W. Tombler, A.M. Cassell, H. Dai, Science **283** (1999) 512.

43. B.Q. Wei, R. Vajtai, Y. Jung, J. Ward, R. Zhang, G. Ramanath, P.M. Ajayan, Nature **416** (2002) 495.

44. Y. Zhang, A. Chang, J. Cao, Q. Wang, W. Kim, Y. Li, N. Morris, E. Yenilmez, J. Kong, H. Dai, Appl. Phys. Lett. **79** (2001) 3155.

45. E. Joselevich, C.M. Lieber, Nano Lett. **2** (2002) 1137.

46. J.E. Fischer, W. Zhou, J. Vavro, M.C. Llaguno, C. Guthy, R. Haggenmueller, M.J. Casavant, D.E. Walters, R.E. Smalley, J. Appl. Phys. **93** (2003) 2157.

47. R. Krupke, F. Hennrich, H.v. Lohneysen, M.M. Kappes, Science **301** (2003) 344.

48. D. Chattopadhyay, I. Galeska, F. Papadimitrakopoulos, J. Am. Chem. Soc. **125** (2003) 3370.

49. Y. Li, D. Mann, M. Rolandi, W. Kim, A. Urai, S. Hung, A. Javey, J. Cao, D. Wang, E. Yenilmez, Q. Wang, J.F. Gibbons, Y. Nishii, H. Dai, Nano Lett. **4** (2004) 317.

Chapter 2:
CVD growth of SWNTs and their analyses

2.1 Characteristics of SWNT growth from zeolite-supported catalysts

2.1.1 Research background

To date, the unique physical properties of SWNTs have suggested several novel applications [1] that would not be possible to achieve with conventional materials; further, there is much scope to realize such inventions using SWNTs. Therefore, a low-cost synthesis technique of high-quality SWNTs is currently a pressing necessity.

In addition to the initial laser-furnace [2] and arc-discharge [3] techniques, a variety of studies have been reported [4–13] using the chemical vapor deposition (CVD) technique that is suitable for mass production. Several types of carbon sources, support materials, and synthesis conditions have so far been tested, but the best approach has not yet been attained. Toward this goal, our group reported [14] that SWNTs with remarkable purity were synthesized at a temperature as low as 600°C using alcohol (ethanol and methanol). Further merits of using alcohol lie in its harmlessness, low cost, and easy-handling properties.

There have been no reports that support the validity of the SWNT yield using a simultaneous combination of Raman, TGA, and transmission electron microscopy (TEM), other than a report by Alvarez et al. [11], in which MWNTs coexisted as a byproduct. Furthermore, in a majority of the reports, the characteristics of the reported highest yield were not presented. It is the author's belief that a comprehensive discussion should be made regarding the definition of SWNTs yield, with an clear notation of the upper yield limit for practical quality. In this section, the effects of CVD reaction time and pre-reduction of catalytic metal on the quality and yield of synthesized SWNTs are investigated in order to discuss the feasibility of using our alcohol CCVD method for mass production.

2.1.2 Catalyst preparation and experimental procedure

The catalyst powder mentioned in this section is prepared as follows: Cobalt acetate $(CH_3CO_2)_2Co\text{-}4H_2O$ and iron acetate $(CH_3CO_2)_2Fe$ were dissolved in ethanol along with Y-type zeolite powder (TOSOH Corp. HSZ-390HUA, over 99% SiO_2) so that the weight concentration of each metal species over the total catalyst powder (i.e., zeolite + metal) is 2.5 wt%. Their typical amounts are 108.4 mg (Co acetate), 81.1 mg (Fe acetate), 20 ml (ethanol), and 1 g (zeolite powder). The mixture was sonicated for 1 h in a beaker submerged in a bath-type sonicator; subsequently, it was placed in a furnace maintained at 80°C for 1 h for evaporation of the ethanol. Sonication and evaporation were alternatively repeated until the contents of the beaker dried uniformly. The resultant white-yellow

powder was ground into fine powder by a mortar and stored for future use in a furnace at a temperature of 80°C. This procedure was developed based on the procedure originally presented in Refs. 15 and 16.

Figure 2-1 shows a schematic of the CVD apparatus used in Sections 2.1 and 2.2. For the CVD procedure, 30–50 mg of the catalytic powder was sparsely mounted on a quartz boat, and the boat was then is placed at the center of a quartz tube (26 mm inner diameter, 1 m length). As shown in Fig. 2-1, a 30-cm central portion of the quartz tube was heated in an electric furnace with an Ar flow of approximately 300 sccm, so that the pressure inside the tube could be maintained at 300 Torr by operating only the "needle valve." After the reaction temperature was achieved typically within 30 min, the supply of Ar was stopped and the quartz tube was evacuated by opening the "valve," as shown in Fig. 2-1. Subsequently, ethanol vapor was introduced keeping the pressure at just before entrance of the quartz tube constant as measured by the "pressure manometer." Finally, the ethanol supply was stopped and the furnace was turned off before returning the system to room temperature with an Ar flow of 100 sccm. In some experiments, instead of pure Ar, Ar containing 3% of hydrogen (referred to as "Ar/H_2") was used for the reduction purpose.

As-prepared blackened powder was characterized by TGA, Raman spectroscopy, and TEM. TGA was performed using Seiko Instruments Inc. Exter 6000 and TG/DTA 6300 under a heating rate of 5 °C/min with an Ar flow of 100 sccm. In every TGA measurement, a sample weighing 10 ± 1 mg was used in order to reduce the TG error to below 1%, and the temperature was maintained at 100°C for 2 h prior to the start of the measurement in order to ensure reproducibility. Raman measurement was conducted using Chromex 501is

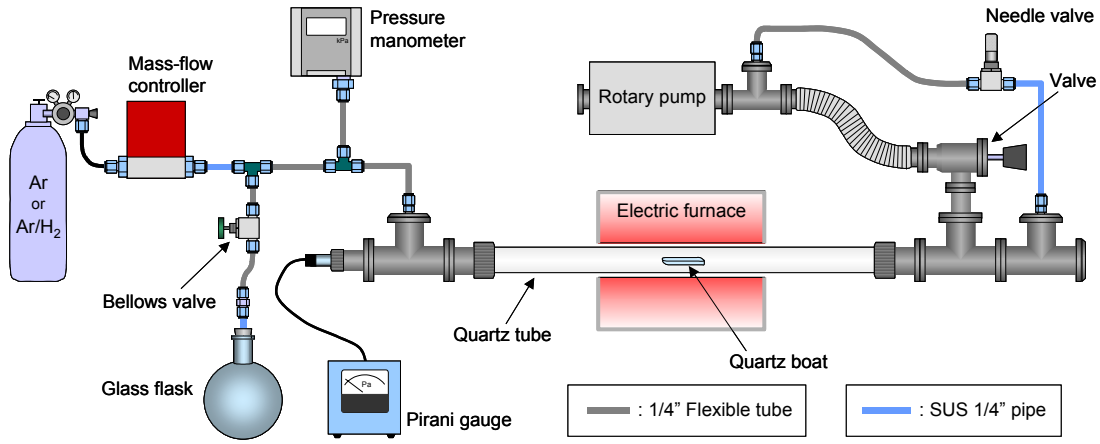


Fig. 2-1. Schematic description of CVD apparatus used in Section 2.1 and 2.2.

and Andor Technology DV401-FI as the spectrometer and CCD system, respectively, along with an optical system, Seki Technotron Corp. STR250. A laser wavelength of 488 nm was used in all the measurements.

2.1.3 Definition of SWNT yield

Recent findings by TG or temperature-programmed oxidation (TPO) analyses [9,11,17–21] are utilized to estimate the SWNT yield. The burning temperature of SWNTs is greatly influenced by the condition of the SWNTs specimen; therefore, caution must be exercised in comparing these results. It is remarkable that when catalytic metal particles are mixed with SWNTs, the decomposition temperature is somewhat lower than that of purified SWNTs [17–20]. At least, the burning temperatures of purified and annealed SWNTs produced by the laser furnace method [2,18] or the HiPco method [7,19,20] are in the same temperature range of 500–700°C.

Since amorphous carbon decomposes at approximately 300–500°C [9,11,17], which is lower than the decomposition temperature of SWNTs, its existence is readily recognized from the TG or TPO curves. However, when graphitized carbon products such as MWNTs coexist with SWNTs, it becomes considerably difficult to specify the amount of SWNTs using only the TGA or TPO curves. As pointed out by Alvarez et al. [11], this is because a certain type of well-graphitized product burns at slightly higher temperature range that overlaps the range of SWNTs. As a method for estimating the amount of each constituent, Alvarez et al. [11] decomposed their TPO curves into several Gaussian-Lorentzian components and attempted to estimate the amount of each carbon species, including amorphous carbons and MWNTs. However, this method has large scope for freedom in the choice of fitting parameters; hence, although physically effective, it may not be the most effective method for accurate yield estimation.

Therefore, the most appropriate method is to perform the estimation on a specimen that contains negligible amounts of amorphous carbon and MWNTs, for which Gaussian-Lorentzian decomposition is not required. The absence of amorphous carbon and MWNTs can be confirmed by TGA and TEM, respectively. The yield of SWNTs in this study is defined as the ratio of the weight loss between 500 and 700°C to the weight that remained at 1000°C; both are measured by TGA. In other words, the yield is a representative ratio of the weight of SWNTs to that of the catalytic powder.

2.1.4 Effect of CVD time and reduction of catalyst on SWNT yield

Figure 2-2a shows the TG and DTG curves of the *as-prepared* powders for several CVD reaction times when Ar was used during the heating of the electric furnace. The reaction temperature and pressure were 800°C and 10 Torr, respectively. For these conditions, this temperature was confirmed to be optimal (i.e., achieving minimum impurities) by Raman and TEM analyses. In our previous report [14], SWNTs with sufficiently high quality/purity were synthesized even at 650°C; however, this was possible because the pressure was much lower (2–5 Torr) than that in the present study in which the conditions for the highest yield are discussed. A slight weight gain at approximately 250°C is due to the oxidation of catalytic metals [19,20], and the following weight loss up to 500°C is due to the burning of amorphous carbons. The weight loss between 500 and 700°C was attributed to the burning of SWNTs, which strongly depends on the CVD reaction time. It should be noted that the burning temperature of the current SWNTs is equal to that of purified and annealed SWNTs that are synthesized by the laser-furnace [18] and HiPco [19,20] methods, indicating that the sidewalls of the SWNTs in this study are of good quality and are devoid of metal particles. The gradual shift of the DTG peaks toward a higher temperature is attributed to the increase in the diameter of SWNTs or thickening of the bundles. In the 300-min case, this shift is partially due to the formation of MWNTs. TEM observations displayed no multi-layered carbons such as MWNTs in the 120-min case, while a small amount of MWNTs was observed in the 300-min case (data not shown).

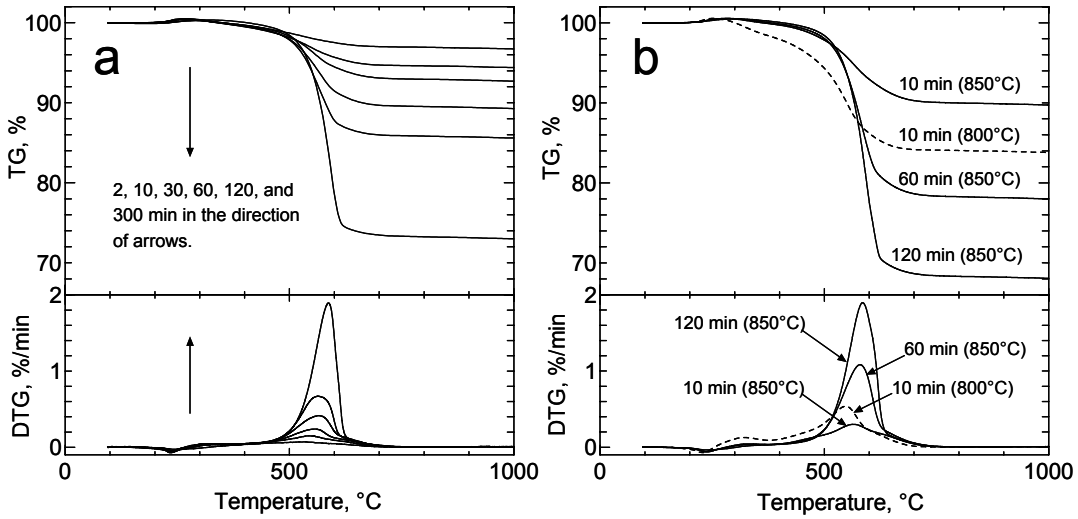


Fig. 2-2. TG/DTG curves when (a) Ar and (b) Ar/H_2 were used during the heat-up of the electric furnace. The ethanol pressure during CVD reaction was 10 Torr in all cases. The reaction temperature in panel (a) was 800°C for all cases.

A series of experiments were carried out using Ar/H_2, and their TG and DTG results are presented in Fig. 2-2b. The ethanol pressure during the reaction was 10 Torr. For a comparison with the curves in Fig. 2-2a, the first experiment was conducted under the conditions of 800°C and 10 min. The TG curve in the case of Ar/H_2 (dashed line) exhibits a greater total carbon yield than in the case of Ar (Fig. 2-2a). This increase is thought to arise from the additional reduction of catalytic metals that would otherwise be reduced by carbon atoms at a lower speed. A side effect, i.e., a simultaneous increase of amorphous carbon, can be suppressed by employing a higher reaction temperature. The solid lines in Fig. 2-2b represent the TG/DTG curves of SWNTs synthesized at 850°C, showing that the amount of amorphous carbon was suppressed to the same extent as that in Fig. 2-2a. It is noted that this comparison implies not only that Ar/H_2 enhances the yield of SWNTs but also that Ar lowers the reaction temperature, which can be an important controllable parameter in the production of SWNTs.

Figure 2-3 shows the Raman spectra corresponding to Fig. 2-2b. Detailed interpretations of the Raman spectra are presented in elsewhere [22]. The decrease in the D-band magnitude from "10 min at 800°C" to "10 min at 850°C" coincides with the observation in Fig. 2-2b. Although the magnitudes of the D band gradually increased with the reaction time, they retained sufficiently good quality, according to the TEM observations. Since the TGA results indicate a negligible amount of amorphous carbon compared with SWNTs

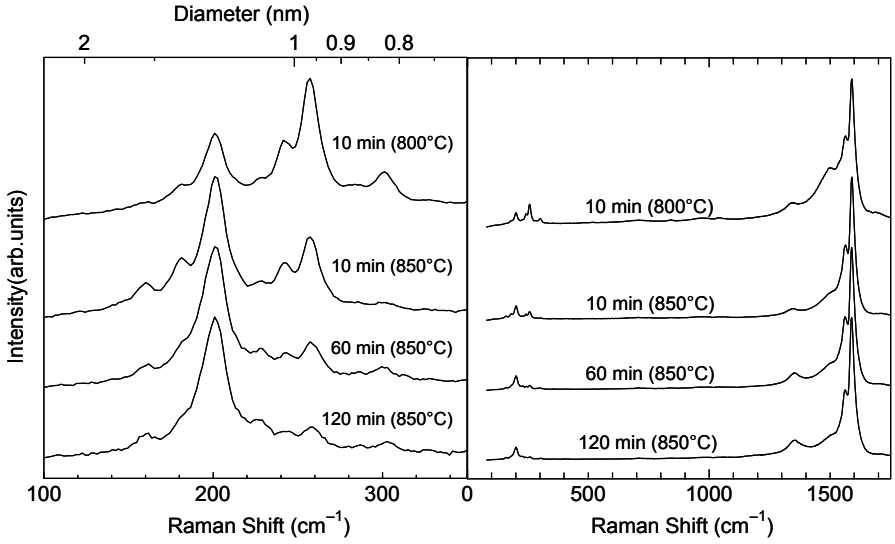


Fig. 2-3. Raman spectra corresponding to Fig. 2-2b taken with 488 nm laser light. The left panel is a magnification of the low-frequency area of the right. The gas used in the heating-up of the electric furnace and the ethanol pressure during CVD reaction were Ar/H_2 and 10 Torr, respectively.

even for longer-CVD-time cases, the D band increase in this case may partly be ascribed to the double resonance effect by SWNTs with defects. The left panel displays the radial breathing mode (RBM) of SWNTs, from which the diameter distribution of SWNTs can be estimated using the relationship "d (nm) = 248/ν (cm^{-1})" [23,24], where d is the diameter of a SWNT and ν is the Raman shift. The observed increases in the diameter with CVD reaction time are partly because larger catalytic particles, which would produce SWNTs with larger diameter, require a longer time until they are activated and saturated with C atoms. As the reaction time increases, SWNTs begin to grow from larger catalyst particles, and at 300 min (shown in Fig. 2-2a), catalytic particles that are large enough to produce MWNTs are finally activated. Since it is more difficult to properly anneal SWNTs grown from larger catalyst particles at the moment of separation from the catalyst [5], these SWNTs are considered to possess a greater amount of defects. The above reasons serve to explain the increase in the D-band magnitude with CVD time that is observed in Fig. 2-3.

Figure 2-4 shows the time sequence plots of the SWNT yields. The error arising from TG was ± 0.5%. The definition of the SWNT yield is not strictly applicable for the 300-min case in which MWNTs were observed. This figure also displays the enhanced yield in the case of "850°C, 10 Torr, Ar/H_2" compared with that of "800°C, 10 Torr, Ar".

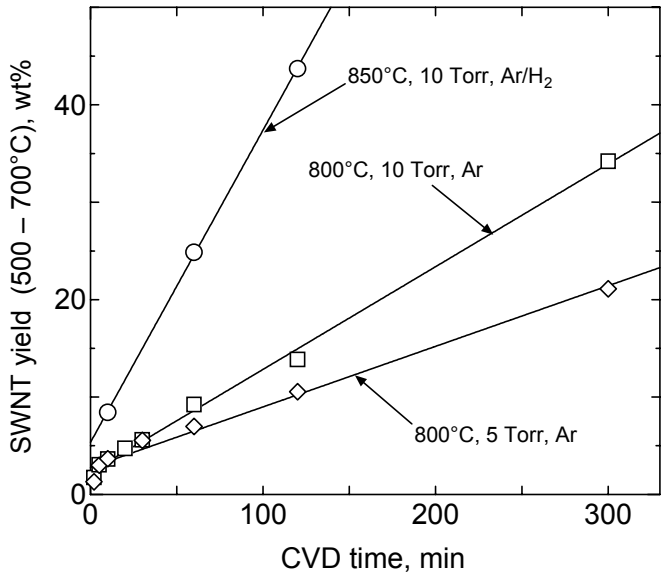


Fig. 2-4. Time progresses of SWNT yields for the conditions of '850°C, 10 Torr, Ar/H_2' (circle), '800°C, 10 Torr, Ar' (square), and '800°C, 5 Torr, Ar' (diamond), for the temperature, pressure, and gas used in the heating-up of the electric furnace, respectively. A straight line for each condition denotes a least-squares fit. Note that a small amount of multi-layered carbon products were observed in cases of 300 minutes.

2.1.5 Microscopic analyses of obtained SWNTs on zeolite support

The quality of the above-described SWNTs was investigated by TEM. The as-grown sample was sonicated in methanol for 5 min and the solution was dropped onto a TEM grid. Figure 2-5 presents a few representative TEM images. In the context of the simultaneous achievement of *yield and quality*, "850°C, 10 Torr, 60 min, Ar/H_2" (Fig. 2-5a) was the best among the tested cases. The quality of the "850°C, 10 Torr, 120 min, Ar/H_2" case was almost the same (Fig. 2-5b) but these SWNTs had thicker bundles, and that of the "10 Torr, 60 min, Ar" case followed them. In this study, therefore, the practical limit of the reaction time in order to assure sufficient quality/purity of the product is 120 min, in which a SWNT yield 40% relative to the weight of the zeolite support powder with Fe-Co catalyst was achieved. This corresponds to a yield of more than 800% over the weight of the catalytic metal since the total metallic weight in the catalytic powder was 5%. The "as-grown" high quality of our SWNTs is evident when the TEM images (Fig. 2-5) are compared with those presented in previous reports, for example [7–11,13,19]. The choice of ethanol for the carbon feedstock appears to be a crucial factor.

Figure 2-6 shows FE-SEM micrographs for the as-grown stage of the "850°C, 10 Torr, 60 min, Ar/H_2" SWNTs obtained at different magnifications. The low-magnification image reveals that zeolite powder particles of several hundreds of nanometers were bound to each other by web-like SWNT bundles. The surface of the zeolite powder was densely covered with SWNT bundles whose typical thickness is 10–20 nm. Thinner bundles of ~10 nm were observed at the highest magnification particularly near the surface of the zeolite particle, and the thickness of the bundles appears to increase toward the zeolite surface. At the outermost surface, where the bending stiffness of the thickened bundles exceeded the van der Waals attraction force from the surface of zeolite, the bundles finally depart into space. It should be noted that the surfaces of the SWNT bundles are smooth and no contamination is observed on them; this also verifies the high quality of the pure SWNTs grown by the proposed method.

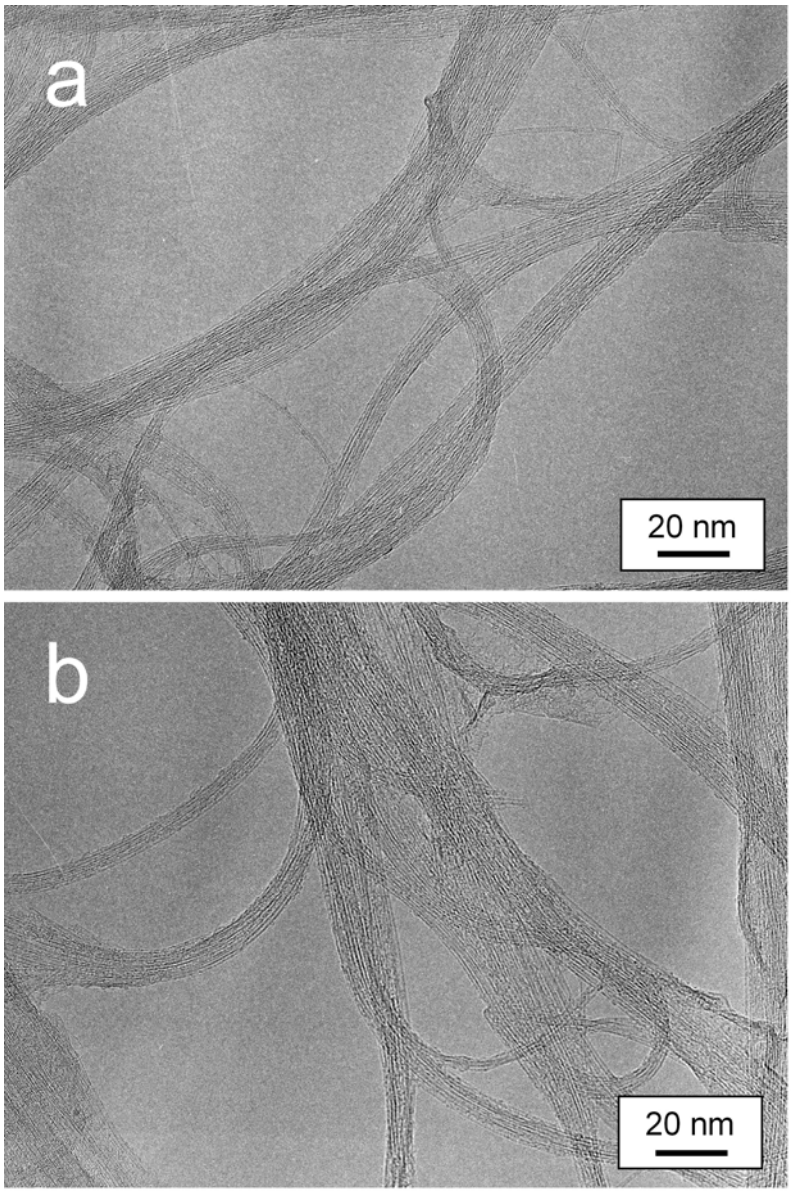


Fig. 2-5. TEM images for 'as-grown' SWNTs synthesized at the conditions of (a) '850°C, 10 Torr, 60 min, Ar/H_2', and (b) '850°C, 10 Torr, 120 min, Ar/H_2', for the temperature, pressure, time, and gas used during the heat-up of the electric furnace, respectively. Note the high purity of SWNTs without contaminants such as metallic particles, amorphous carbons, or MWNTs.

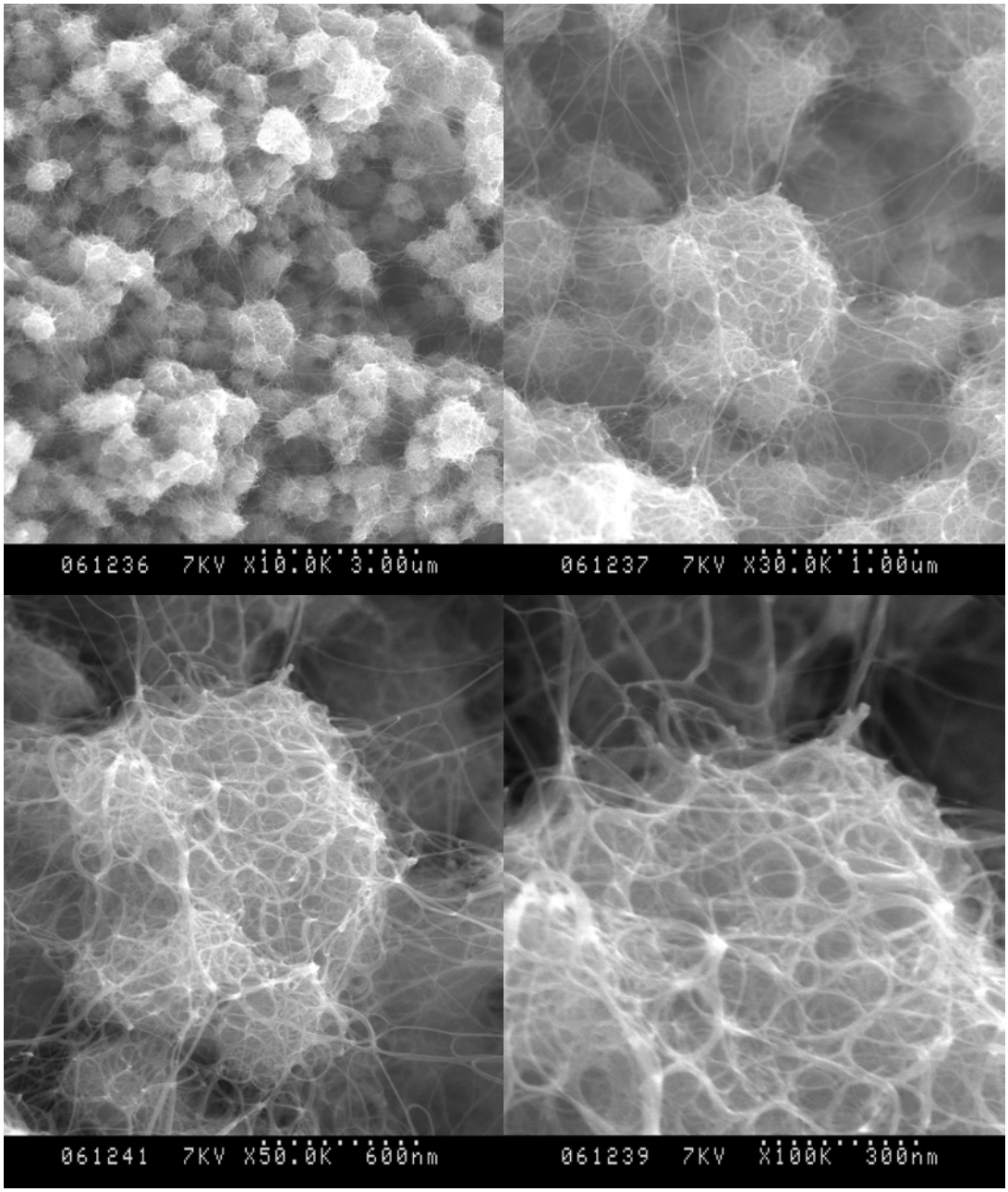


Fig. 2-6. FE-SEM micrographs for the '850°C, 10 Torr, 60 min, Ar/H_2' SWNTs in 'as-grown' state on zeolite support powder, taken at several different magnifications. The same sample has been investigated and presented in Figs. 2-2 - 2-5.

2.1.6 Effect of catalyst metal selection on growth of SWNTs

Previous experiments have used a catalyst prepared by an impregnation of Fe and Co acetates into Y-type zeolite powder, as described in Section 2.1.2. The use of Fe-Co catalyst leads to a high yield of the SWNTs, as seen in Fig. 2-4. This subsection investigates the effect of different catalyst metals on the growth of SWNTs on SiO_2 supports. Mo, Fe, Co, and Ni, in particular, are examined because they are often used and are thought to be suitable as catalysts for SWNT growth. They are *d*-orbital transition metals known to have strong catalyst activity in general [25].

Figure 2-7 shows the Raman spectra, measured with 488-nm laser light, of SWNTs grown using different catalyst metals supported by the impregnation of their metallic acetates into Y-type zeolite powder. In all the cases, the weight% of metal over the support was set as 5 wt%. The CVD experiments were performed under the same conditions: 800°C, 5 Torr, and 10 min for reaction temperature, ethanol pressure, and reaction time, respectively, with the use of Ar while heating up the electric furnace. The output powders appeared to be colored almost white (Mo), gray (Fe, Ni), and black (Co), and they are investigated later in greater quantitative detail. With the exception of Mo (Fig. 2-7a), the Raman spectra obtained with a high G/D ratio at ~1593 cm^{-1} and a clear indication of RBM

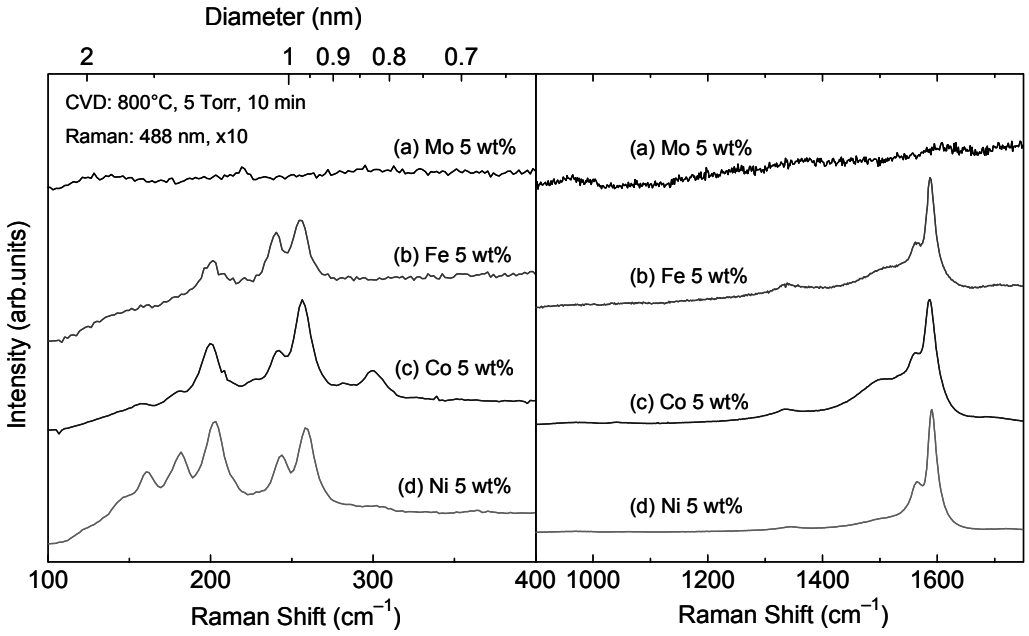


Fig. 2-7. Raman scattering spectra measured with 488 nm laser light from SWNTs grown from (a) Mo, (b) Fe, (c) Co, or (d) Ni catalyst supported on USY-zeolite powder through impregnation of their acetates as described in Section 2.1.2. The metallic concentration over the support powder is 5 wt% for all cases..

in lower frequency region are identified as those of SWNTs. It is evident that the diameter of the produced SWNT increases in the order of Fe < Co < Ni, indicating that the diameter of the metal particles formed on the SiO_2 support also varied in the same order.

This experimental observation can be explained in terms of the thermodynamic properties of metals, according to the methodology originally proposed by Hu et al. [26] used for explaining the morphologies of sputtered metals on TiO_2 substrates. Table 2-1 lists several thermodynamic properties of the metals employed in Fig. 2-7. $\Delta H_f°_{oxide}$ and $\Delta H_f°_{sublimation}$ denote the heat of formation of metal oxide per mole of the metal and the heat of sublimation of the metal, respectively, both at standard state, cited from Ref. 27. The former assumes the oxidized state shown in the table and the latter is the so-called cohesive energy that well correlates with the melting point of the metal. An alternative property of $\Delta H_f°_{sublimation}$, experimentally measured surface energy γ cited from Ref. 28, is also shown in Table 2-1.

These thermodynamic properties are reflected in the behavior of the metals supported on the oxidized surface provided there are no significant changes in the chemical states at the elevated temperature (~800°C) at which CVD is performed. Since $\Delta H_f°_{sublimation}$ (or γ) represents the affinity of metals with themselves and $\Delta H_f°_{oxide}$ represents that of metals with oxygen, these ratios should provide a measure of the degree of wetting of the metal on the SiO_2 support. The last two rows of Table 2-1 show these ratios, and the agreement of their tendency with the experimental observation in Fig. 2-7 is excellent. Other studies have also reported these tendencies in the catalyst for SWNT growth. For example, the SEM

Table 2-1. Thermodynamic properties of Fe, Co, Ni, and Mo.

Element	Mo	Fe	Co	Ni
Atomic number [-]	42	26	27	28
Melting point [K]	2895	1811	1770	1728
Oxidized state	MoO_3	Fe_2O_3	Co_3O_4	Ni_2O_3
$\Delta H_f°_{oxide}$ [kJ/mol] (oxide per mol of metal)	-745.58	-412.40	-297.26	-244.92
$\Delta H_f°_{sublimation}$ [kJ/mol] (cohesive energy of metal)	658.58	416.59	424.96	427.95
$\gamma \times 10^3$ [kJ/m^2] (surface energy of metal)	3.00	2.48	2.55	2.45
$-\Delta H_f°_{sublimation} / \Delta H_f°_{oxide}$ [-]	0.883	1.01	1.43	1.75
$-\gamma / \Delta H_f°_{oxide} \times 10^6$ [mol/m^2]	4.02	6.00	8.58	10.0
	← highly wet on SiO_2		highly agglomerated on SiO_2 →	

micrograph of the Si substrate after C_2H_2 molecular beam epitaxy (MBE) growth of carbon nanotubes at 750°C from vacuum-deposited Ni catalyst layer (thickness 5 nm) reveals significant agglomeration of Ni metal, as large as ~50 nm in diameter [29]. Even at a reduced amount (~1 nm) of deposited Ni, the catalyst agglomerates into ~10 nm particles, resulting in the growth of only MWNTs. Since Ni has often been used for growing vertically aligned MWNTs on a flat substrate [30,31], such an empirical choice of catalyst could be quantitatively explained using the method shown in Table 2-1.

Figure 2-8 shows the TGA curves of SWNT-grown zeolite powders that were examined in Fig. 2-7 along with that of our standard Fe-Co (2.5 wt% each) catalyst used in Figs. 2-2 to 2-6. Once again, all the CVD experiments were performed at 800°C, 5 Torr, and 10 min. For *monometallic* catalyst, it is recognized that Co yields the largest amount of SWNTs, while Ni and Fe yield a lower amount. TGA was not performed on the sample with Mo catalyst examined in Fig. 2-7 because virtually no production of SWNT was confirmed by the result of Raman scattering analysis. This result indicates the existence of an optimum point in the choice of catalyst. Based on the current discussion, it is reasoned that Fe and Ni produce a lower amount of SWNTs because they exhibit excess wetting and agglomerating

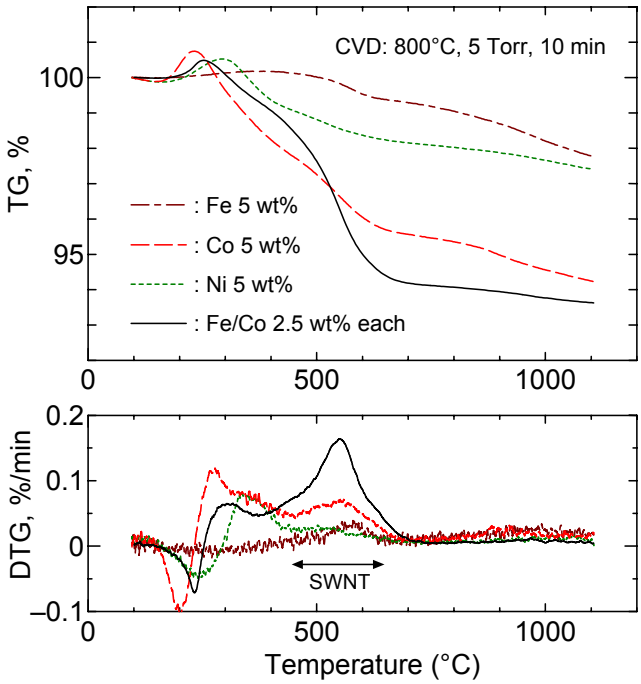


Fig. 2-8. TG and DTG curves measured from as-prepared SWNTs grown from Fe, Co, Ni, and Fe/Co catalyst supported on Y-type zeolite powder. The metallic concentration over the support powder is 5 wt% for all cases. The elevating speed of temperature and flow rate of air during TG measurements were 5 °C/min and 100 sccm, respectively.

on the SiO_2 support, respectively. On the other hand, Co exhibits the best performance among these because the wettability is moderate; hence, particle formation is appropriate for the efficient growth of SWNTs.

As shown in Fig. 2-8 with a solid curve, the yield of SWNTs can be further enhanced by the use of a *bimetallic* Fe-Co catalyst. Several studies have demonstrated the effectiveness of the use of bimetallic catalysts; this will be investigated and discussed in depth in Section 2.3 and 2.4. The effect of bimetals on the surface of the SiO_2 support is considered to be as follows: The metal with higher wettability to SiO_2 (such as Fe or Mo) comes closer to the SiO_2 surface and stabilizes the other metal species (such as Co or Ni) that works as the main catalyst for the SWNT growth. Thus, the main catalyst (i.e., Co or Ni) is dispersed and even protected from deactivation due to a chemical reaction with SiO_2 (e.g., oxidation or silicidation) by the underlying wetting metal (i.e., Fe or Mo) that serves as a sacrificing layer. It should be noted that this discussion (i.e., the effectiveness of bimetal) is limited to the case of the *supported* catalyst used for the growth of SWNTs. In the case of a *floated* catalyst, in which the wettability of the metal to the support is irrelevant, many studies have demonstrated that monometallic Fe serves as an excellent catalyst for SWNTs such as in the HiPco process [4,7].

Finally, for subsection 2.1.6, Fig. 2-9 shows a phase diagram for the Fe-Co alloy system, cited from Ref. 29. Since both metals do not form a eutectic compound, they can work respectively, as described above.

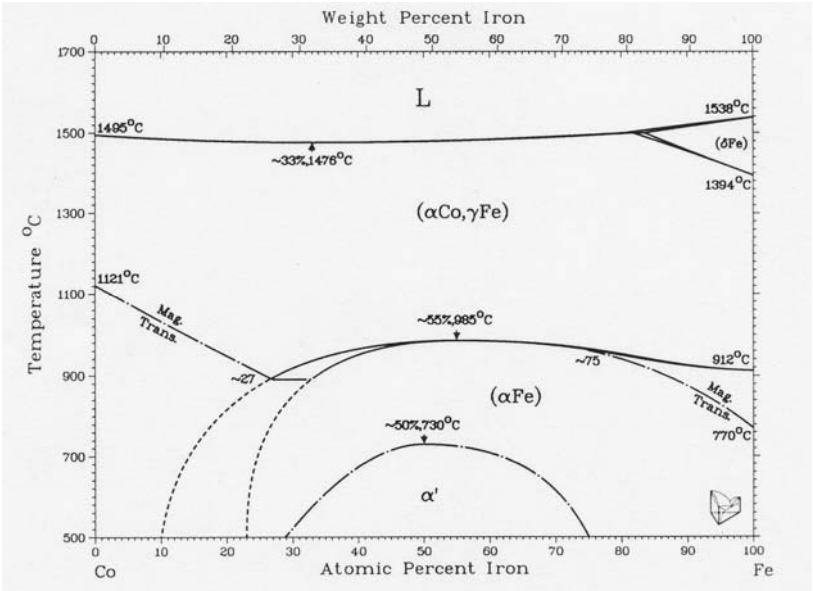


Fig. 2-9. Phase diagram for Fe-Co alloy system cited from Ref. 29.

2.1.7 Summary

In Section 2.1, the growth of SWNTs by the alcohol CCVD method was investigated and characterized by means of Raman scattering and TG analyses. The bimetallic Fe-Co catalyst supported through the impregnation of its acetate solution into Y-type zeolite powder is effective and feasible for the bulk production of SWNTs. The effect of reduction on the yield and diameter of the resultant SWNTs was elucidated through the comparative experiments. The reduction of the catalyst prior to the CVD reaction was shown to be effective in enhancing the growth of SWNTs.

The definition of SWNT yield has been clearly described in this study based on the appropriate interpretation of TGA results with a support by TEM observations. It has been demonstrated that a yield of SWNTs greater than 40% with sufficiently high quality can be achieved from ethanol within a CVD time of 120 min; thus, the feasibility of the proposed method toward mass production was confirmed. The reduction of the catalytic metal, which leads to an effective enhancement of the yield, plays an important role in the synthesis of SWNTs. Finally, the effect of the choice of catalyst metal on the growth of SWNTs was investigated in terms of the thermodynamic properties of the metal catalysts Fe, Co, Ni, and Mo. It was clarified that the ratio $\Delta H_f^\circ{}_{sublimation}/\Delta H_f^\circ{}_{oxide}$ (or $\gamma/\Delta H_f^\circ{}_{oxide}$) explains the observed difference in the growth of SWNTs from different monometallic catalysts; further, it provides a theory-based index for the choice of catalyst for SWNT growth. The effect of the bimetallic catalyst was also explained in this discussion. Further detailed investigations and discussions will be presented later in Section 2.3 and 2.4.

2.2 Catalyzed growth of SWNTs from mesoporous silica thin films

2.2.1 Research background and motivation

So far, several studies [30-33] have been reported to synthesize carbon nanotubes directly on silicon wafer as a preliminary step for incorporating them into electronic circuits. However, this approach has resulted in the occasional production of multi-walled nanotubes (MWNTs) [31-33] due to a sintering of deposited/sputtered catalytic metals, which can be caused by their higher CVD temperature (typically 900°C) and almost perfect flatness of Si surface. From this concern, mesoporous silica (MPS) could be an ideal material for achieving well-regularized synthesis of carbon nanotubes with an expected effect of preventing sintering of catalytic metals.

To date, several attempts have been made to synthesize carbon nanotubes using MPS as a catalytic support [34-41]. Powders of various types of MPS were employed for mass production [34,37,38], but they all have resulted in MWNTs. Among them, Okamoto et al. [38] have reported growth of some amount of SWNTs in addition to MWNTs. Films of MPS were sometimes formed on solid substrates [35, 36, 39-41], but their major products were MWNTs and no successful synthesis of SWNTs has yet been reported. Although the growth of SWNTs was insisted by Huang et al. [41], no experimental evidence has been given by the authors concerning whether the grown nanotubes were SWNTs or MWNTs.

In this section, a new methodology of synthesizing high-quality SWNTs is proposed employing a 3-dimensional (3D) MPS thin film with accessible pores on the surface, which has near-"SBA-16" cubic structure. The method of metal loading differs from any of the past reports [35,36,39-41], where the catalytic metal was pre-mixed in the stage of silica formation. By this, the ability of MPS thin film to support of catalyst for the growth of SWNTs are demonstrated and the role of MPS layer are discussed in order to solve aforementioned problems in the selective growth of SWNTs on flat substrates.

2.2.2 Preparations and experiments

A thin film of 3D MPS was coated on a Si substrate based on the procedure developed by Yamakita [42], which had been established from the original recipe shown by Zhao et al. [43] for the fabrication of SBA-16 type MPS. First, TEOS (tetra-ethyl-ortho-silicate), ethanol, H_2O, and HCl were mixed and stirred for 1 h at 65 °C to form a sol-gel solution. This solution was mixed with an ethanol solution of amphiphilic triblock copolymer $[(C_2H_2O)_{106} - (C_3H_4O)_{70} - (C_2H_2O)_{106}]$ (BASF, F127) and stirred for another 2 h at room

temperature. The self-assembled polymers served as a structure-directing agent (SDA) in the formation of mesopores. The overall composition of prepared mixture was fixed to {TEOS : H_2O : HCl : Ethanol : polymer = 1 : 9.2 : 0.021 : 40 : 7.2×10^{-3}} in molar ratio [42]. The solution thus prepared was mounted on a piece of Si substrate (2 cm × 2 cm) by the dip-coating method at a constant pull-up rate of 6 cm/min. After the coating, the piece was dried in air at 80°C overnight and calcinated in air at 500°C for 4 h to remove the polymers, by which an MPS thin film with a typical thickness of 50 nm was formed [42].

Subsequently, catalytic metal was loaded on the MPS-coated Si substrate (referred to as "MPS/Si substrate"). Iron acetate $(CH_3CO_2)_2Fe$ and cobalt acetate $(CH_3CO_2)_2Co\text{-}4H_2O$ were dissolved in ethanol (typically 20 ml) to form a metal acetate solution so that the weight concentration of both metals were made equal, either 0.01 wt % or 0.001 wt % in this report. The MPS/Si piece was placed on the bottom of a beaker containing the metal acetate solution and was then transferred into a desiccator for evacuation by a rotary pump for 1 h. It is crucial to set the initial solution level below 10 mm to avoid sudden boiling during the evacuation. With this process, air remaining inside the mesoporous film was replaced with the solution. The piece's surface was washed immediately after drawn-out from the solution with ethanol by two different procedures, as described in a later section. The metal-loaded MPS/Si piece was heated up to about 400 °C in the flow of He/O_2 (5 % O_2) to remove organic residues and to form oxidized bimetallic particles inside (or partly on the surface) of the thin film. As reference experiments, silica-coated Si substrates (referred to as "Silica/Si substrate") without mesoporous structure were employed to examine the role of the mesopores. This silica/Si piece was fabricated by identical procedures for the metal loading process but without addition of the polymers.

The subsequent CVD procedure and employed CVD apparatus are the same as those presented in subsection 2.1.2. The reaction temperature, time, and ethanol vapor pressure employed in this study are 750°C, 10 min, and 10 Torr, respectively. The gas used while heating up and cooling down of the electric furnace is Ar/H_2 (3 % H_2). Thereby synthesized SWNTs are characterized with FE-SEM observation (HITACHI, S-900) and Raman spectroscopic analysis (CHROMEX 501is and ANDOR DV401-FI for the spectrometer and CCD system, respectively). Laser wavelength of 488 nm is used for all Raman measurements.

2.2.3 Results and discussions

Figure 2-10 presents a FE-SEM image of the MPS/Si surface before catalytic metal was loaded. Platinum film with a thickness of less than 0.5 nm (measured by a quartz crystal microbalance) was sputtered on the surface to enhance the visibility, and the observation was performed at 6 kV, where no charge-up occurred. The dark circular apertures correspond to the mesopores formed in the silica framework. The inset reveals that the mesopores were periodically located with an approximate interval of 15 nm.

Figure 2-11 shows the pore size distribution of this MPS film determined by the

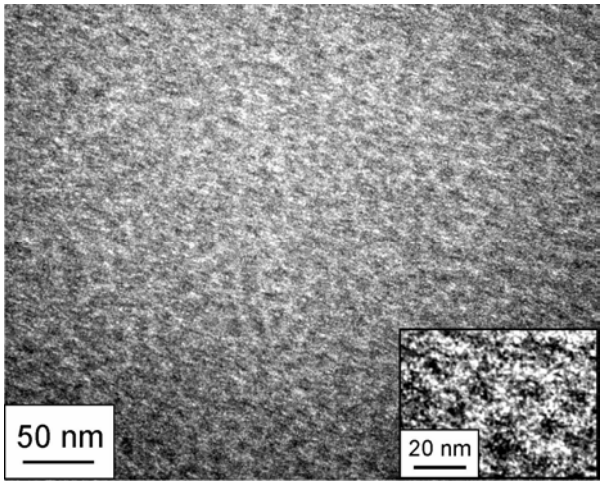


Fig. 2-10. FE-SEM image of platinum-sputtered MPS/Si surface before loading of catalytic metal. taken by Hitachi S-900 at 6 kV. The dark apertures are the mesopores formed in silica framework.

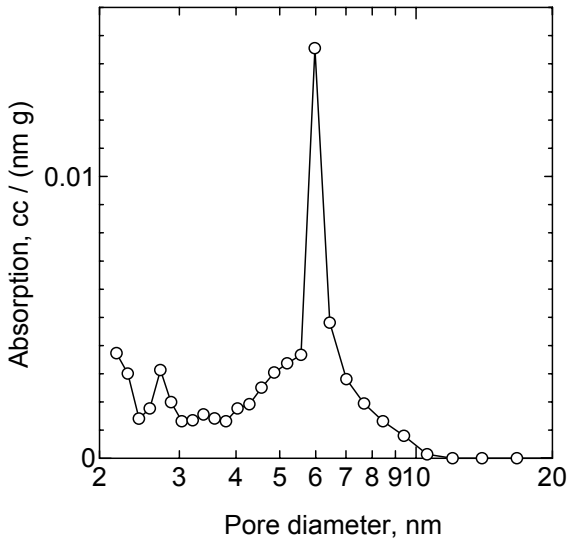


Fig. 2-11. Pore size distribution of current MPS thin film calculated using the BJH analysis.

Barrett-Joyner-Halenda analysis using the MPS films coated on glass substrates in the N_2 absorption/desorption measurement. A sharp peak at 6 nm corresponds to the mesopores, and a less remarkable peak around 2.6 nm is ascribed to the diameter of connecting holes between the pores (refer to Ref. 44 for 3D schematic of SBA-16 type MPS).

Figure 2-12 shows FE-SEM images of the MPS/Si surfaces after the CVD reaction with several magnifications. The metallic concentrations of the acetate solution used in Figs. 2-12a and 2-12b were 0.01wt% and 0.001 wt%, respectively. In both cases, the substrate surface was rinsed with ethanol immediately after the metal loading for about 3 s. The bright lines represent the bundles of SWNTs, which look somewhat blurred and thicker than actual: This is due to a change in the local emission property of secondary electrons, often observed for the SWNTs grown on Silica/Si surface [45]. The SWNTs in Fig. 2-12a look sparser and less uniform than those in Fig. 2-12b. Notably, metal particles larger than 10 nm (bright dots) are densely inhabited on the MPS surface, where some of them seem to have sintered. These particles are seen to 'clog' the mesopores beneath them, which might be a partial reason for such sparser population of SWNTs.

In contrast, SWNTs shown in Fig. 2-12b look more densely and uniformly populated and

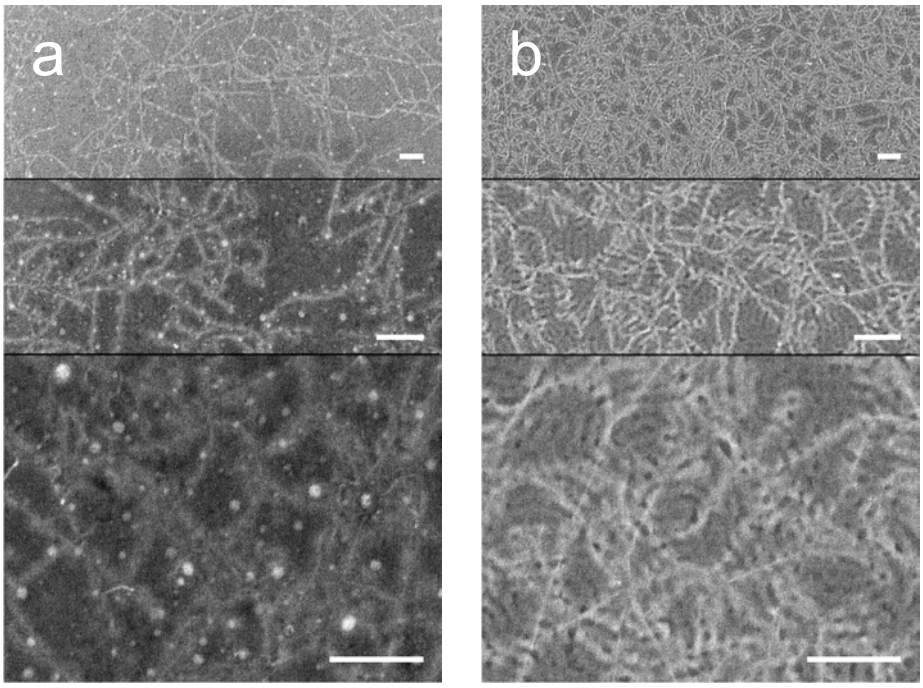


Fig. 2-12. FE-SEM micrographs of MPS/Si surface after the CVD reaction when the metallic concentration in the solution used in the metal loading process was (a) 0.01 wt% and (b) 0.001 wt%, measured by Hitachi S-900 at 10 kV. The employed washing treatment was a light rinsing in ethanol. Horizontal lines denote 100 nm.

very few metal particles are found on the surface. Then it is reasonably speculated that a certain amount of SWNTs were grown from inside of the MPS thin film. Another noticeable difference lies in the visibility of the surface: The surface structure is hardly recognizable in Fig. 2-12a, while in Fig. 2-12b the fine structure of the MPS surface is clearly observed. Note that these two substrates were treated in the same batch in the processes of preparation, metal loading, CVD, and SEM observation. Usually, the surface of MPS cannot be observed without sputtering of metal particles, as exemplified in Fig. 2-10. This improved visibility was caused by a uniform coverage of its surface with SWNTs, which can act as an excellent conductor.

In order to examine the function of the MPS layer, SWNTs synthesized on the MPS/Si were compared with those on the Silica/Si substrate at a fixed metallic concentration of 0.001 wt%. Figure 2-13 presents Raman spectra of the SWNTs synthesized on the MPS/Si and Silica/Si substrates measured with 488 nm laser light, and for each substrate two types of washing treatment were employed: The first method is that employed in Fig. 2-12, or a rinse of the surface with ethanol for about 3 s (denoted as 'lightly rinsed'). The other method is a soak of the substrate into ethanol (typically 20 ml) for 10 minutes before it was drawn out from the ethanol and dried in air (denoted as '10 min soaked'). In each case, spectra were measured at five different locations chosen randomly, and they were

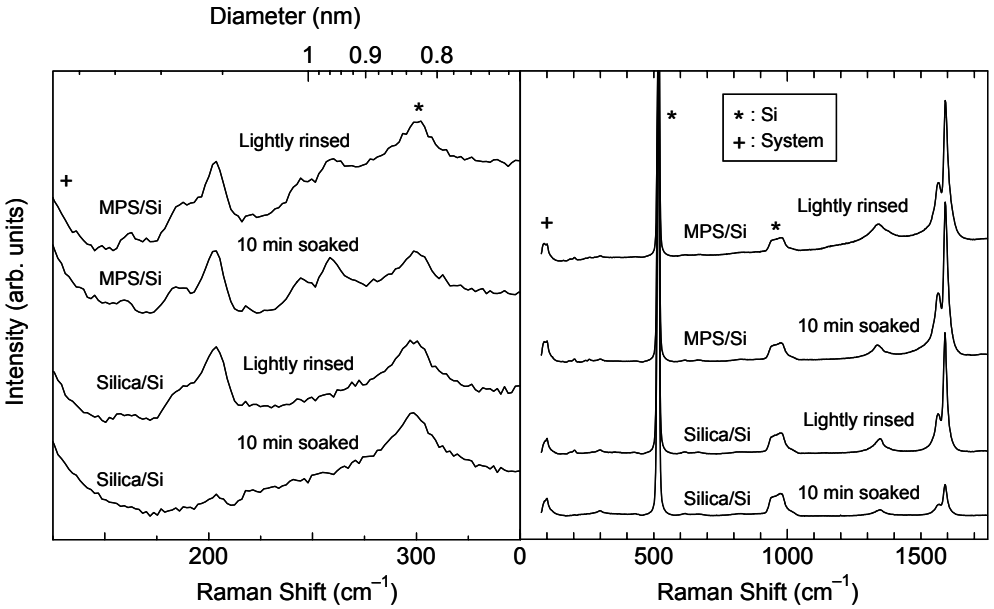


Fig. 2-13. Raman spectra of MPS/Si and Silica/Si substrates after the synthesis of SWNTs measured with 488 nm laser light. The metallic concentration during the metal loading process was 0.001 wt% for all cases. For each substrate, two types of washing treatment noted in text were employed.

arithmetically averaged. All spectra were normalized by the height of the silicon-derived peak around 960 cm^{-1}. The interpretation of the Raman spectra of SWNTs is presented in elsewhere [22].

The right panel of Fig. 2-13 shows a high-frequency area, where the magnitude of the G-band around 1590 cm^{-1} relative to the Si peak at 960 cm^{-1} approximates the amount of synthesized SWNTs. When the 'lightly rinsed' washing treatment was employed, no significant difference in the G-band magnitude was observed between MPS/Si and Silica/Si cases. However, the difference became much clearer when they were treated with '10 min soaked' washing: No significant change in the G-band magnitude was observed in MPS/Si, while the magnitude in Silica/Si drastically decreased as expected. This indicates that the MPS layer serves as an efficient capacitor for catalytic metals, supporting our idea that many of SWNTs were grown from the metals inside of the mesopores.

A peak around 1350 cm^{-1} called the D-band represents the extent of disorder in the sp^2 arrangement of carbon atoms, from which the quality of SWNTs were estimated. Interestingly, in the case of MPS/Si the '10 min soaking' treatment has enhanced the quality of SWNTs. Furthermore, the standard deviation of the G-band intensities among the five measurements in the 'lightly rinsed' case was over 50 %, whereas that in the '10 min soaked' case was only 8 %, indicating that the soaking process has improved the uniformity of the catalytic distribution. As we speculate, the metals on the surface are also reduced through the '10 min soaked' process, but a more detailed analysis is essential for further discussion. The lower Raman spectra are magnified in the left panel of Fig. 2-13, presenting the radial breathing mode (RBM) peaks that identify SWNTs. The diameter distribution of SWNTs is estimated using "d (nm) = 248 / ν cm^{-1}" [23,24] where d is the SWNT diameter and ν is Raman shift. The SWNTs synthesized on MPS/Si have diameters around 0.9 - 1.5 nm.

Figure 2-14 shows FE-SEM images of the above discussed MPS/Si substrate with ’10 min soaked’ treatment, taken from tilted angles so that their broken cross-sections can be included. The cross-section exhibits a three-layered structure of this MPS/Si substrate: The MPS top layer has an approximate thickness of 50 nm, and the SiO_2 layer with a thickness of 100 nm is seen below it. In the base is the Si substrate that looks darkened. The upper picture reveals that most of the SWNT bundles are adhered to the MPS surface to form a uniform, web-like network of SWNTs. The lower picture with larger magnification shows the fine structure of MPS beneath the SWNTs. No remarkable difference in the form of synthesized SWNTs from the case of ‘Lightly rinsed’ is observed in the FE-SEM observation. Some of the SWNT bundles are observed to detach from the surface, but they eventually collide with the surface again due to the flexibility of SWNTs and are captured by the van der Waals attraction of silica frameworks.

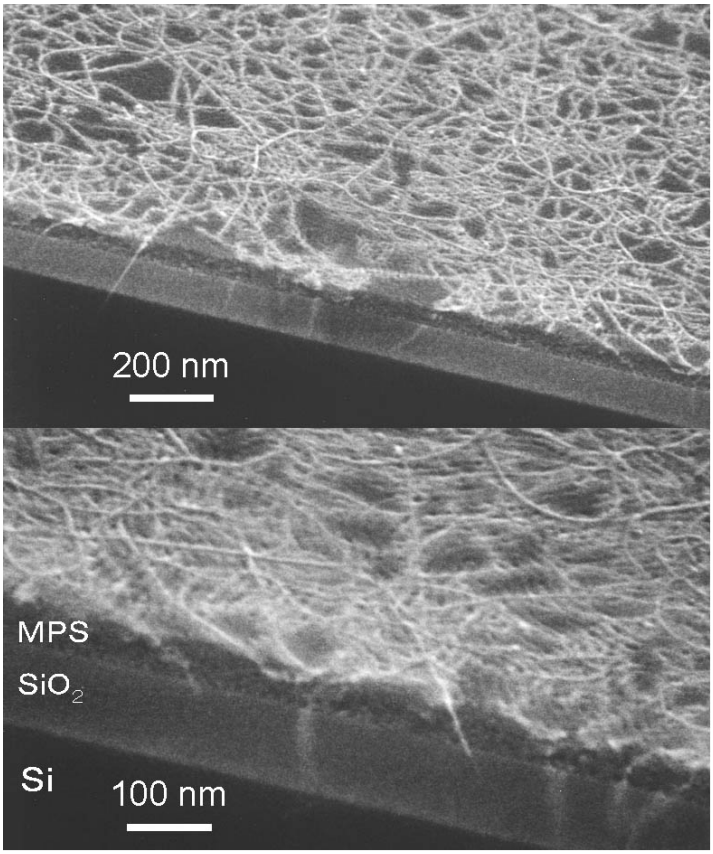


Fig. 2-14. FE-SEM micrographs of MPS/Si substrate after the synthesis of SWNTs taken from a tilted angle taken by Hitachi S-900 at 8 kV. The metallic concentration during the metal loading process was 0.001 wt%, and the substrate was subsequently soaked in ethanol for 10 min.

With further FE-SEM observation of the broken cross-section with higher magnification, we have occasionally observed metal particles embedded in the MPS layer from which SWNTs were extended. These images support our idea regarding the role of the MPS layer; however, they are not sufficiently convincing for a clearer discussion on the morphology of SWNTs and the metallic particles located inside or on the surface of the MPS layer. A further detailed study is needed for their characterization by the use of e.g. a cross-sectional HR-TEM analysis [46].

2.2.4 Summary of the SWNT growth from MPS thin films

High-quality SWNTs have been synthesized on 3D MPS thin film and its function has been elucidated through a reference experiment with Silica/Si substrate. The MPS layer provides an additional volumetric capacity for holding catalytic metals inside it, and a physical potential for prevention of sintering. The present CVD process at relatively low temperature contributes to the prevention of metallic sintering at the same time to the preservation of the MPS structure. This study has suggested a possibility of growing SWNTs regularly in well-defined intervals by utilizing the periodic structure of MPS.

2.3 Development of techniques for direct synthesis of SWNTs on solid flat substrates

2.3.1 Research background and motivation

When the fabrication of SWNT-based devices is attempted, an appropriate incorporation of SWNTs into silicon or other material-based systems is essential. Thus far, several studies have been reported in which carbon nanotubes were synthesized on the substrates by various methods. Kong et al. [47] and Franklin et al. [30] spun coated their Fe-Mo catalyst with alumina support particles to form patterned catalytic islands on Si surfaces and synthesized small amounts of SWNTs. Cassell et al. mounted mesoporous alumina/silica on Si substrates to support their Fe-Mo catalyst and produced SWNTs [48].

In other studies, mesoporous silica was coated as a supporter on a Si substrate in the form of a thin film, leading to the production of MWNTs [35,36,40] or SWNTs [49]. However, such supporting material is often undesirable because it is an additional material not essential for the functioning of the devices. A way to circumvent the use of the support material was proposed by Li et al. [50], in which ferritin protein was utilized for sparsely located iron nanoparticles on a flat SiO_2 substrate to synthesize SWNTs. Homma et al. [51] dispersed commercially available Fe or Fe_2O_3 nanoparticles in ethanol and loaded them onto an Si substrate. They produced thin carbon nanotubes including SWNTs at 950°C using Fe_2O_3 as the catalyst; however, the selectivity to SWNTs is unknown.

The above-mentioned studies [30,35,36,40,47–51] made use of liquid-based approaches for catalyst preparation; however, in some cases, catalytic metals were mounted on substrates using dry processes such as sputtering or vacuum vapor deposition [32,33,52–55]. Although the selective synthesis of SWNTs on a flat Si surface was recently reported [55], this method usually accompanies agglomerated catalyst metals with larger diameters (i.e., greater than 5 nm) that can result in an undesirable production of MWNTs. For example, the dominant products in the studies by Nerushev et al. [32] and Yoon et al. [33] were MWNTs although SWNTs were also reportedly produced; in both reports, agglomerations of metals were clearly observed in the SEM micrographs. Delzeit et al. [52] synthesized SWNTs with relatively high quality and selectivity by pre-depositing 20 nm of an Al underlayer on a Si surface before depositing 1 nm of Fe-Mo catalyst; however, due to an agglomeration of Al, such an underlayer resulted in significant surface roughness. A similar procedure was performed by Zhang et al. [53], in which SWNTs were grown from Ni

Catalyst dispersed by the Al layer; however, this method also accompanies serious agglomeration of Al in the order of several tens of nanometers. Further, although SWNTs were not produced in the case of a Si substrate, Hongo et al. [54] sputtered Fe on the A-face of a sapphire crystal and synthesized a relatively abundant amount of SWNTs at a CVD temperature of 800°C.

In other reports, SWNTs were incorporated on a catalyst-patterned substrate as a field-emission transistor (FET) [56,57], in a manner different from the conventional method of post-dispersion of bulk-produced SWNTs [58]. In their prototypes, a very small quantity (one or a few) of SWNTs were grown from catalytic islands having much larger dimensions (3 μm [56] and 100 μm [57]), indicating that there were very few active sites and most catalyst areas did not participate. However, it is desirable to increase the area efficiency of the catalyst in order to improve the concentration of FET-device density.

In the beginning of this section, a new catalyst supporting method was presented that achieves the direct growth of high-quality SWNTs on the surface of flat substrates. This method does not necessitate any intermediate supporting material such as the aforementioned oxide porous materials or Al deposition layers, which often result in undesirable roughness of the substrate surface after CVD. It was elucidated that the proposed liquid-based technique, employing Co-Mo bimetallic catalyst, excels in controlling the amount of supported metals, resulting in a fine monodispersion of Co particles with diameters ranging from 1–2 nm. The advantages and details of the proposed catalyst supporting technique will be discussed.

2.3.2 Development of dip-coat catalyst supporting method

In the first step, molybdenum acetate $(CH_3COOH)_2$ Mo and cobalt acetate $(CH_3COOH)_2$ Co-$4H_2O$ are dissolved in ethanol by sonication for 2 h in order that the concentration of each metallic species over the weight of the solution is 0.01 wt%. Their typical amounts are as follows: ethanol: 40 g, Co-acetate: 16.9 mg, and Mo acetate: 8.92 mg. An n-type Si wafer with (001)-surface (Nilaco Corp., SI-500452) and a fused quartz with both sides optically polished (Fujitok Corp., #19983) were employed as the substrates. Both substrates had a thickness of 0.5 mm. The silicon substrate was cut into a strip of approximately 7 mm × 20 mm, while a strip of size 25 mm × 25 mm was used for the quartz substrate. A larger dimension was chosen in the case of quartz for the optical measurement described as follows. These substrates are held by a small clip with a stabilizing weight and a nylon fishing line. The substrate piece is then submerged into the prepared metallic acetate solution for 10 min, with its top 5 mm remaining above the solution level to prevent the clip from coming into contact with the solution. The piece is then withdrawn from the solution at a constant speed of 4 cm/min. The surface of the substrate is rapidly dried at several millimeters above the liquid-contact level immediately after withdrawal from the solution. As soon as this process is complete, the piece is placed in a furnace in air maintained at

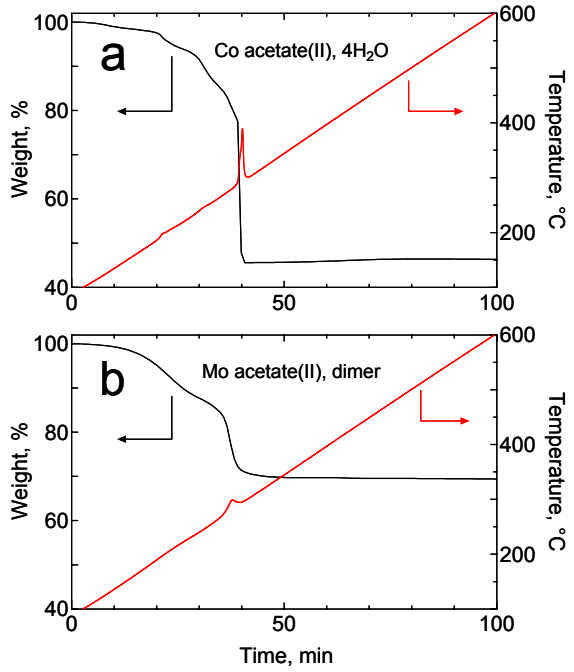


Fig. 2-15. TG (left ordinate) and temperature (right ordinate) curves measured for (a) $(CH_3COOH)_2$ Co-$4H_2O$ and (b) $(CH_3COOH)_2$ Mo measured. Measurement was performed with Seiko Instruments Inc. Exter 6000 and TG/DTA 6300, at a heating rate of 5 °C/min with 100 sccm flow of air.

400°C for 5 min to decompose acetic or any organic residue in order to form an oxide of bimetallic Co-Mo catalyst. As shown in Fig. 2-15, the decomposition of these metallic acetates below 400°C was confirmed by TGA.

2.3.3 Direct synthesis of SWNTs on Si and quartz substrates

2.3.3.1 Experimental procedure

Figure 2-16 shows the CVD apparatus used in this section and later in Chapter 3. A piece of substrate on which the catalyst was supported is placed at the center of a quartz tube with a length of 1 m and an inner diameter of 26 mm. When the substrate piece is small, a quartz boat is used to mount it. The quartz tube was set inside an annular electric furnace (60 cm in length) and heated with 300 sccm of Ar/H_2 (3% H_2) typically at 300 Torr, adjusted by operating only the "bellows needle valve" shown in Fig. 2-16. When the desired temperature is attained, the supply of Ar/H_2 is stopped and inside the quartz tube is brought to vacuum by opening the "valve" shown in Fig. 2-16. Subsequently, ethanol vapor is supplied so that the pressure just before the entrance of the quartz tube, monitored by the "pressure manometer" shown in Fig. 2-16, is maintained at 10 Torr. After the CVD reaction, the electric furnace is turned off and cooled to room temperature with an Ar/H_2 flow of 100 sccm. Hydrogen is used for reducing the catalyst in order to retrieve its catalytic function; its effects were confirmed in Section 2.1 and will be discussed below.

The synthesized SWNTs are characterized with FE-SEM (Hitachi, S-900) and micro-Raman scattering measurement using an optical system (Seki Technotron STR250) comprising a spectrometer (Chromex 501is) and a CCD system (Andor DV401-FI). All

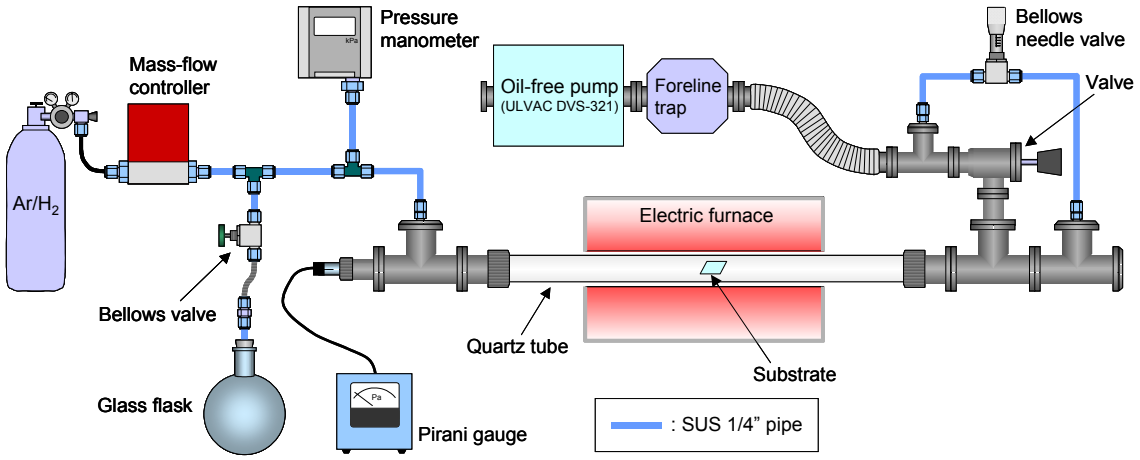


Fig. 2-16. Schematic of CVD apparatus used in Section 2.3 and Chapter 3 for the direct synthesis of SWNTs on flat substrates.

Raman spectra presented in this section are an arithmetic average of the measurements at 10 randomly chosen locations on the substrate. The VIS-NIR absorption spectra are measured using Hitachi U-4000.

2.3.3.2 Resonant Raman scattering analysis

Figure 2-17 shows the Raman spectra of SWNTs directly grown on Si and quartz substrates measured with 488-nm laser light. The CVD reaction time was 10 and 60 min for Si and quartz, respectively. As for the Si substrates, the spectra for several CVD temperatures are presented. The amount of synthesized SWNTs was quantitatively compared using a height ratio of the G-band to Si-derived peak at 518 cm^{-1}, which was determined to be 0.07, 0.23, 5.2, and 1.5 for the temperatures of 650, 750, 800, and 850°C, respectively. No SWNTs were synthesized at 900°C (data not shown). Therefore, the optimum temperature for maximizing the amount of SWNTs in this study is 800°C. The decrease in the amount beyond 850°C is considered to arise from the formation of silicide, as demonstrated by Arcos et al. [59] with their Fe catalyst. It should be noted that the optimum synthesis temperature may be affected by the thickness of a natural oxidation

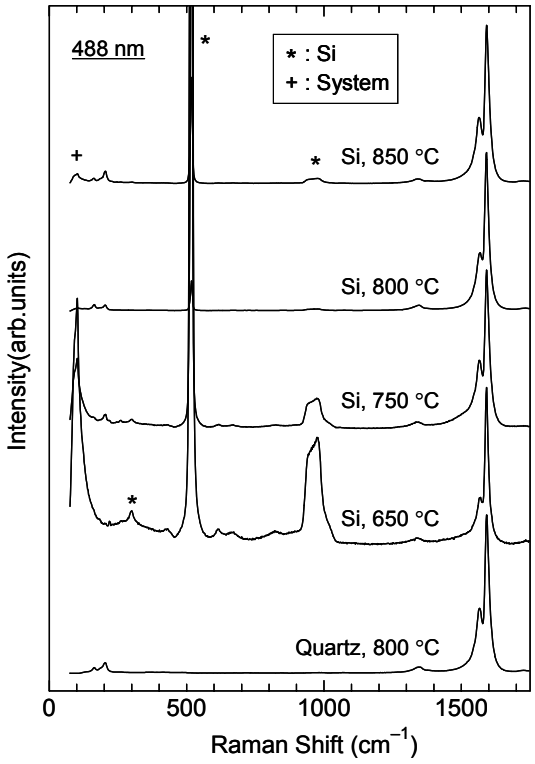


Fig. 2-17. Raman spectra of SWNTs synthesized on silicon and quartz substrates at various CVD temperatures measured by 488 nm laser light.

layer on the surface of the employed Si wafer, which, as described later, is typically in the range of 0.5 to 3 nm. Several Si wafers purchased from different manufacturers were tested and the optimum temperature of certain Si wafers was found to be 750°C. At any temperature, sufficiently high-quality SWNTs were confirmed from their high G/D ratio (e.g., 30 at 800°C). The RBM peaks were observed at all the temperatures. It should be noted that the synthesis of SWNTs on the Si substrate at a temperature of 650°C is by far the lower than the previous reports [30,32,33,47,48,50–52], in which a temperature of 900–1000°C was required for the growth of SWNTs. The spectrum of SWNTs synthesized on a quartz substrate at 800°C indicates high quality (G/D ratio > 25) despite a relatively long CVD exposure of 60 min.

Figure 2-18 shows the RBM spectra of SWNTs directly grown on Si and quartz substrates at 800°C at three different excitation wavelengths—488, 514.5, and 633 nm. For the purpose of comparison, the RBM spectrum of HiPco SWNTs [7,60] (batch #: HPR113.4) supplied by Rice University is also included in Fig. 2-18. The CVD reaction time was 10 and 60 min for Si and quartz, respectively. At the top of the figure, the Kataura plot [61] calculated with the parameters γ_0 = 2.9 eV and a_{c-c} = 0.144 nm [23,24] is exhibited along with the horizontal lines corresponding to the energies of the employed laser lights. The diameter of the SWNTs d was estimated from the RBM Raman shift ν using the relationship "d (nm) = 248/ν (cm^{-1})" [23,24]. The locations of the measured Raman peaks closely match the prediction by the Kataura plot, and a diameter distribution in the range of 1.1–1.7 nm was observed.

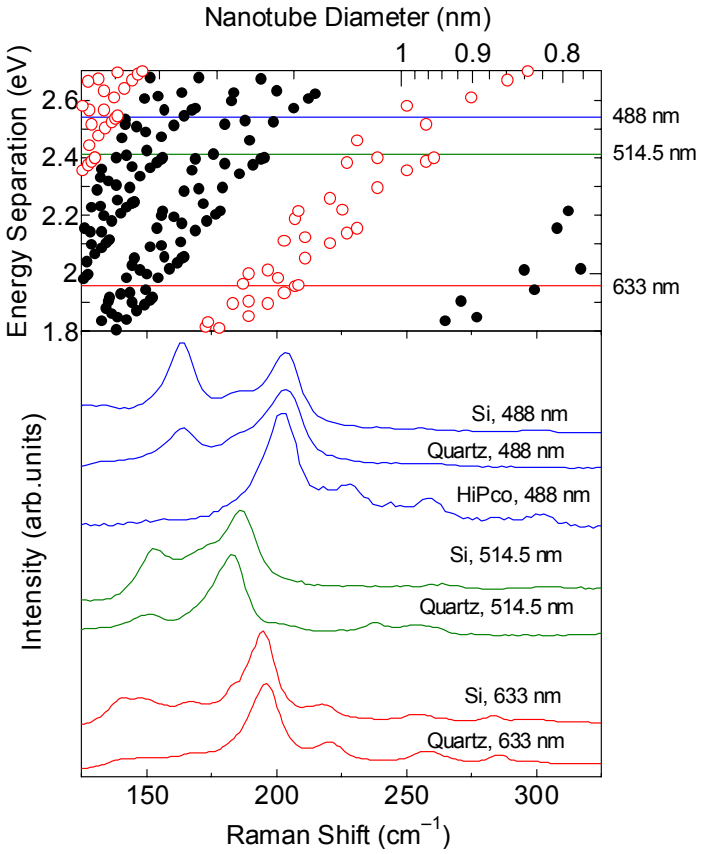


Fig. 2-18. RBM spectra of SWNTs grown at 800°C on the surface of Si and quartz substrates corresponding to Fig. 2-17, measured by 488, 514.5, and 633 nm excitations. 'HiPco' is the reference spectrum of a pristine HiPco sample measured by 488 nm excitation. The Kataura plot for the corresponding range is attached on the top, where solid and open circles denote semiconducting and metallic SWNTs, respectively.

2.3.3.3 Microscopic analysis

Figures 2-19a and 2-19b show the FE-SEM micrographs of SWNTs directly grown on the Si and quartz substrates, respectively, at 800°C, which correspond to the Raman spectra shown in Figs. 2-17 and 2-18. The dark background area of Fig. 2-19a represents the surface of the Si substrate on which a uniform layer of web-like SWNT bundles is observed. Figure 2-19b shows an image acquired at a tilted angle including a broken cross section of the quartz substrate. A film of SWNTs with a thickness of a few hundred nanometers is observed to be formed on the surface. In both micrographs, the observed strings are SWNT bundles.

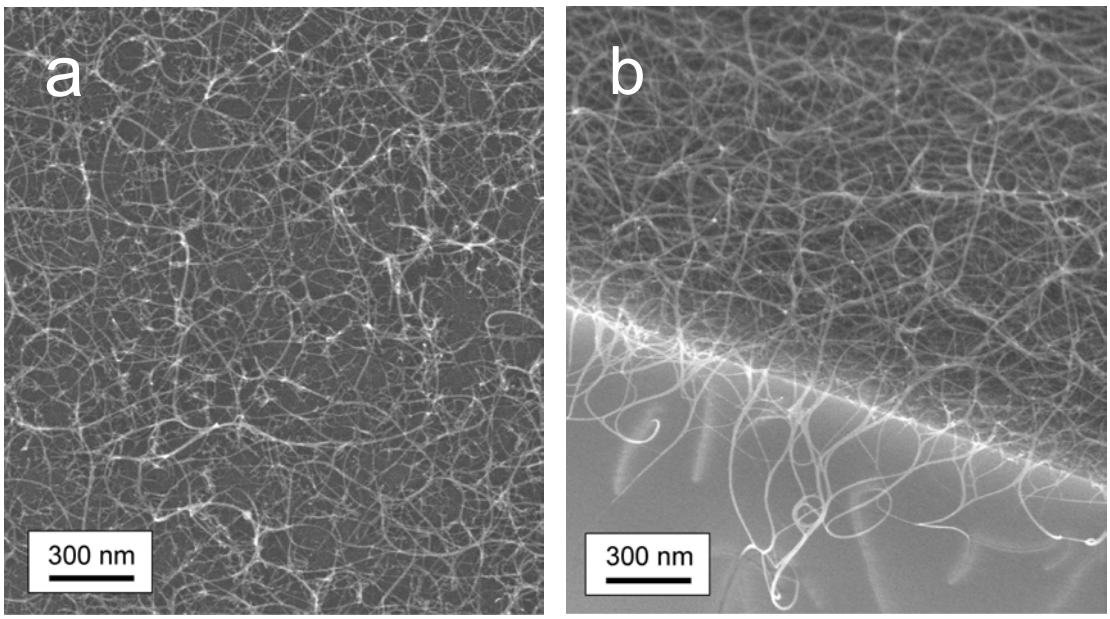


Fig. 2-19. FE-SEM micrographs of SWNTs synthesized on (a) silicon substrate taken from top and (b) quartz substrate taken from slanted angle, taken by Hitachi S-900 at 7 kV. Both samples correspond to those presented in Fig. 2-18.

Figure 2-20 shows images of an identical SWNT-grown quartz substrate acquired at different magnifications. Figure 2-20a is a picture showing the change in appearance of the substrate from before CVD (left) to after CVD (right). After CVD, a film of SWNTs has grown uniformly over the region in which the catalyst was dip coated. Figure 2-20b shows an optical microscope image observed at a scratched region of the film from which the uniformity of the film is recognized. Figures 2-20c and 2-20d show magnified images, ×20K and ×50K, respectively, of the scratched area acquired by a Hitachi FE-SEM S-900 at 7 kV. These images confirm that SWNTs are randomly oriented on the surface of substrate. The film observed in Figs. 2-20c and 2-20d was locally scratched and peeled off for the

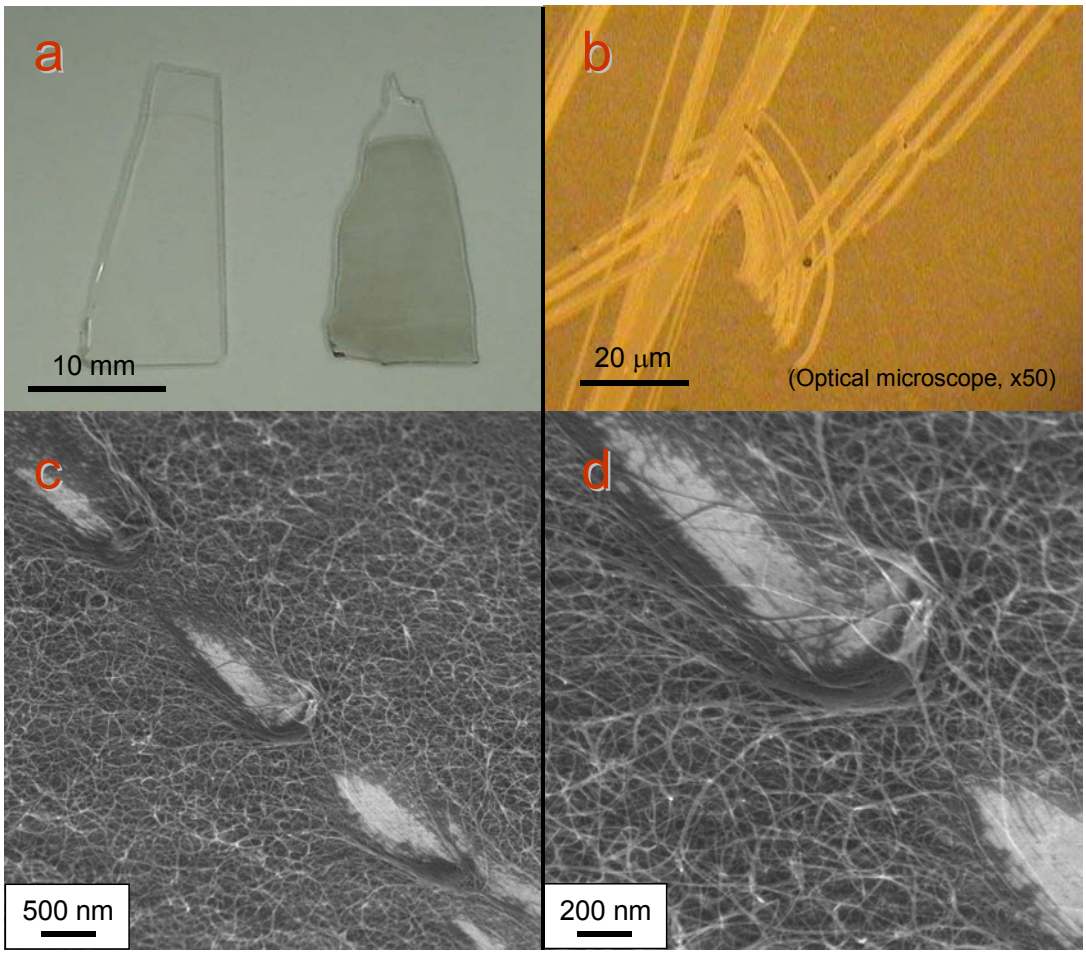


Fig. 2-20. Observations on the same SWNT-grown quartz substrate at various magnifications. (a) A picture of the substrate before (left) and after CVD (right). (b) An optical microscope image of scratched site of the film. (c, d) Magnified images on the scratched area observed by Hitachi FE-SEM S-900 at 7 kV in different magnifications. The film is scratched and partially peeled off for the purpose of investigating morphology of the film as well as the substrate surface after CVD.

purpose of investigating the morphology of the film and the surface of the substrate. No particular agglomerated metals were observed on the exposed surface of the substrate.

For a further detailed investigation of the morphological state of the substrate surface after CVD, FE-SEM observations by Hitachi S-5200 at 2 kV were performed on a quartz substrate on which SWNTs were sparsely grown. Figure 2-21a shows the micrograph obtained from the top of the substrate, in which the surface of the substrate is observed beneath the randomly oriented SWNT bundles. Although agglomerated metallic particles

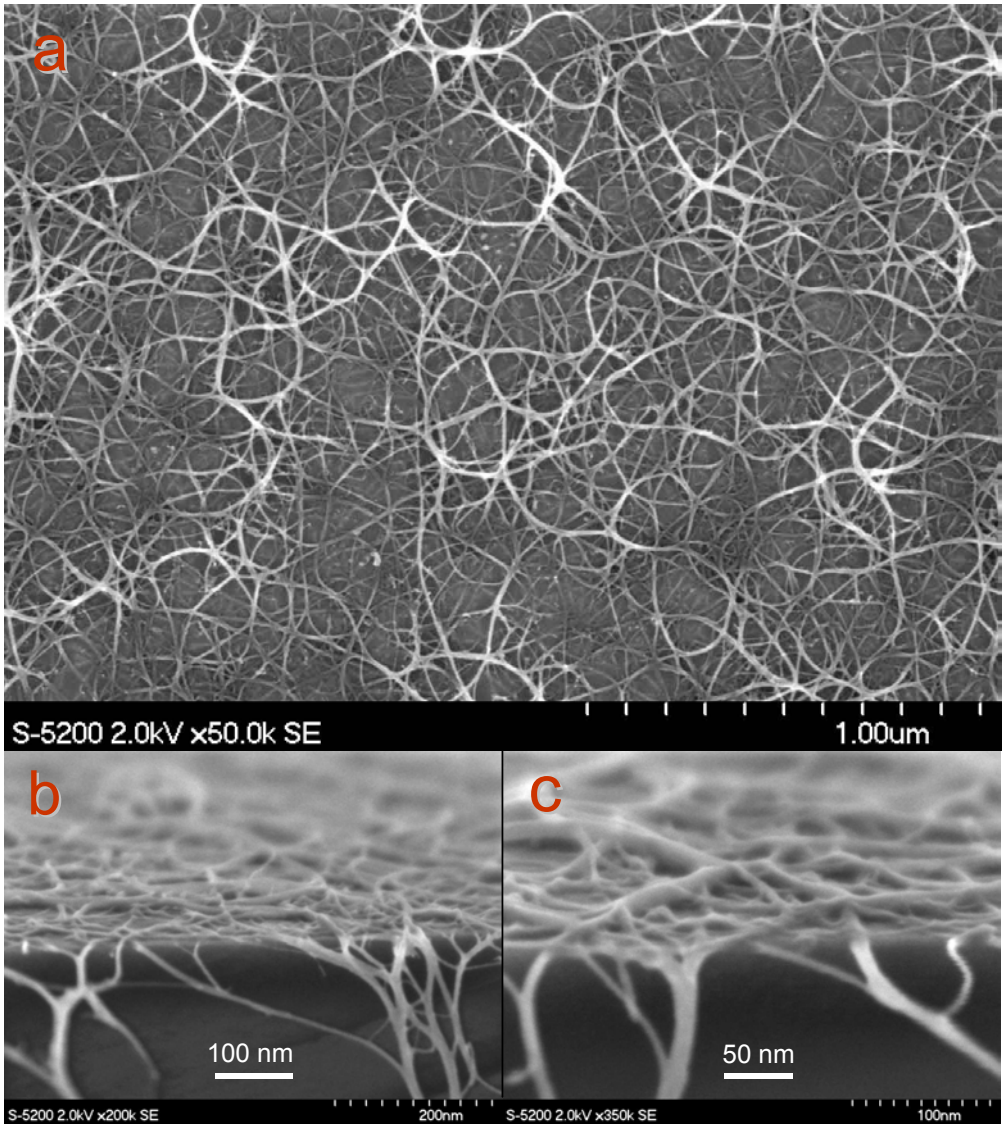


Fig. 2-21. Observations on a quartz substrate on which SWNTs were sparsely grown by Hitachi FE-SEM S-5200 at 2 kV from (a) top of the substrate in ×50k and (b, c) side of the substrate at fractured edge of the substrate in ×200k and in ×350k, respectively.

are locally observed as bright dots in a few locations, no metal agglomerates were recognized in major part of the surface. The occasional presence of agglomerated metals could be due to an imperfection in the surface cleanness that arose during the dip-coat process. Figures 2-21b and 2-21c are micrographs obtained at the fractured edge of the substrate at higher magnifications, ×200 K and ×350 K, respectively. These figures provide strong evidence that the proposed catalyst supporting method is virtually devoid of metal agglomerates, in contrast to the previously reported methods [32,33,52–57]. This smooth surface (i.e., devoid of agglomerated metals on the surface) is considered to be advantageous for various device applications because, in general, agglomerated metals do not contribute to the functioning of devices.

Figure 2-22 shows a TEM image of the SWNTs investigated in Fig. 2-20. A TEM micro-grid was directly rubbed against the blackened quartz surface in order to observe the as-grown state of the SWNTs. An edge of a SWNT drapery was observed to assure the transmittance of the electron beam. Figure 2-22 reveals that the synthesized SWNTs possess a fine quality that is free from any type of metal particles, amorphous carbon, and multi-walled nanotubes.

In order to clarify the morphologies of SWNTs and the catalyst, cross-sectional TEM (X-TEM) analysis was performed. The sample for the X-TEM observation was prepared by placing the two pieces of Si(001) substrate—on which SWNT were randomly grown—facing each other, so that the structure is "Si/SWNT/glue/SWNT/Si"; the

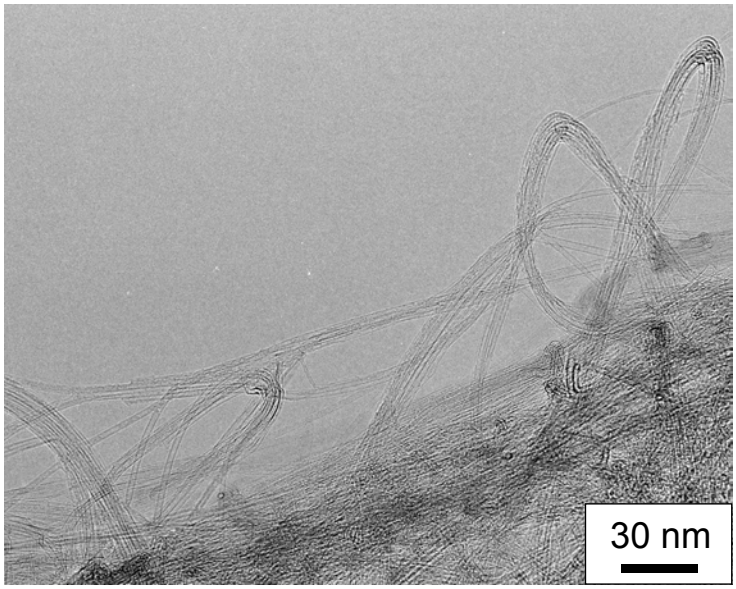


Fig. 2-22. TEM image of an edge of a SWNT drapery by JEOL 2000EX at 120 kV. A TEM grid was directly rubbed onto the substrate in order to observe as-grown state of the SWNTs.

sandwiched structure was subsequently sliced and thinned from its side.

Figure 2-23 presents the X-TEM images observed at the surface of the Si substrate. Despite the lower contrast due to the SWNTs embedded in glue, several SWNTs were clearly observed on the Si(001) substrate. At the top of the surface, an approximately 2-nm

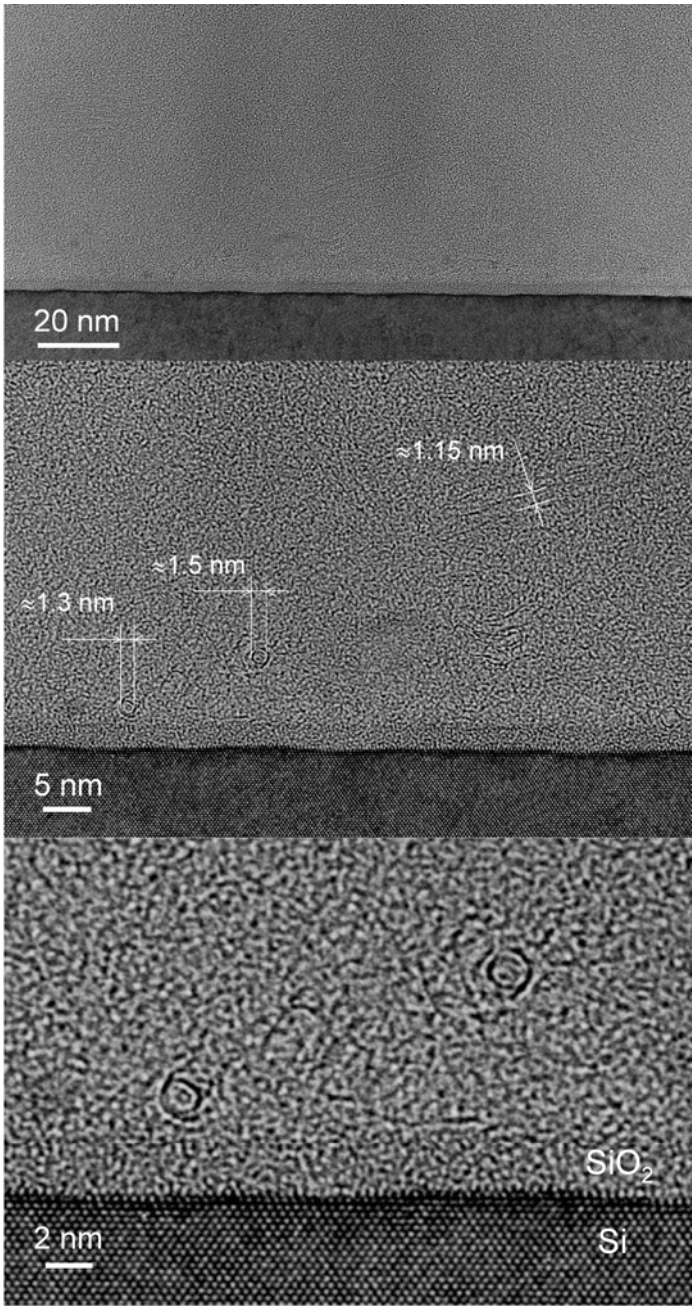


Fig. 2-23. X-TEM images of SWNTs directly grown on Si(001) surface viewed from [110] direction of Si. A native SiO_2 layer with a thickness of approximately 2 nm is seen on the top surface of the substrate.

thick native SiO_2 layer is observed. In the middle panel, some of the observed SWNTs are indicated with their estimated diameters whose range agrees with the diameters measured in Fig. 2-22. Several dark circles with diameters similar to those of SWNTs are sparsely observed, and these are believed to be metallic catalysts. Their lattice planes were not recognized from the image. The lowermost panel shows a magnified image in which the cross sections of two SWNTs that extend perpendicular to the page are observed. The ordering of Si atoms in the substrate is also observed, and the hexagonal alignment of atoms indicates that the direction of electron transmission is the [110] direction. Figure 2-24 presents a schematic description of Si atomic ordering in this X-TEM observation.

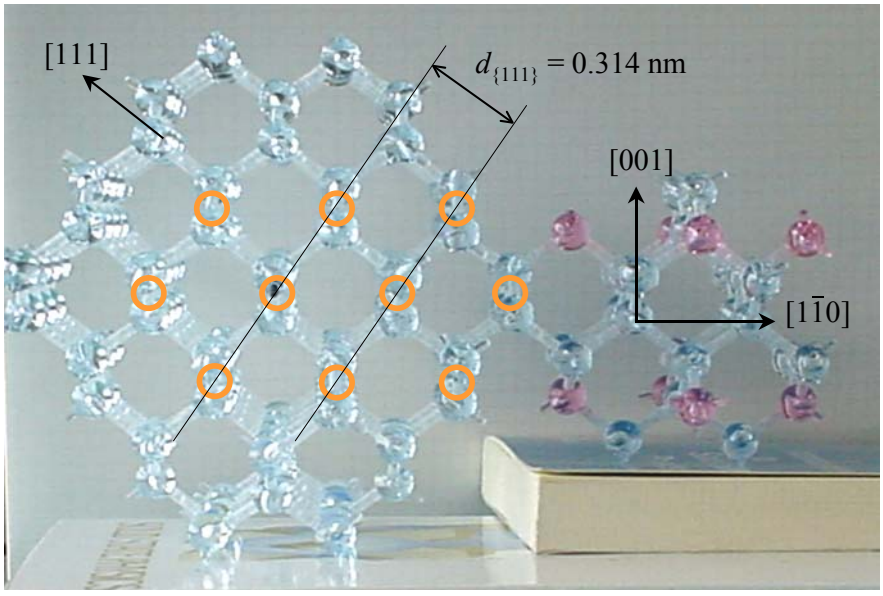


Fig. 2-24. Schematic representation of the cross-sectional view of Si(001) substrate exhibited in Fig. 2-23. Spheres and orange circles denote Si atoms and Bravais lattice points of the crystal, respectively, viewed from $[\bar{1}\,\bar{1}\,0]$ direction. Pink spheres correspond to Si atoms at eight corners of FCC Bravais lattice. Inter-plane distance for [111] direction is presented as $d_{\{111\}}$.

2.3.3.4 Discussions

a. Effect of catalyst reduction

Prior to the CVD reaction, H_2 gas is supplied during the heating of the electric furnace for the purpose of catalyst reduction. Since the catalyst is oxidized before the CVD and therefore has less activity, it should be reduced prior to the reaction. It was confirmed in Section 2.1 that the amount of SWNTs is low when the catalyst is not reduced prior to the CVD reaction. This situation also occurs in the case of a flat substrate. Figure 2-25 shows the Raman spectra measured with a 488-nm laser light from the surface of the Si substrate after CVD at 750°C. Figure 2-25a shows the spectrum when Ar/H_2 (3% H_2) is supplied during the heating of the electric furnace, and Fig. 2-25b shows the spectrum when Ar is supplied instead of Ar/H_2. The intensity of the G-band shown in Fig. 2-25a is approximately 40 times larger than that shown in Fig. 2-25b. This demonstrates that the amount of SWNTs on the Si surface can be significantly enhanced by using H_2 to reduce the catalyst prior to the CVD reaction.

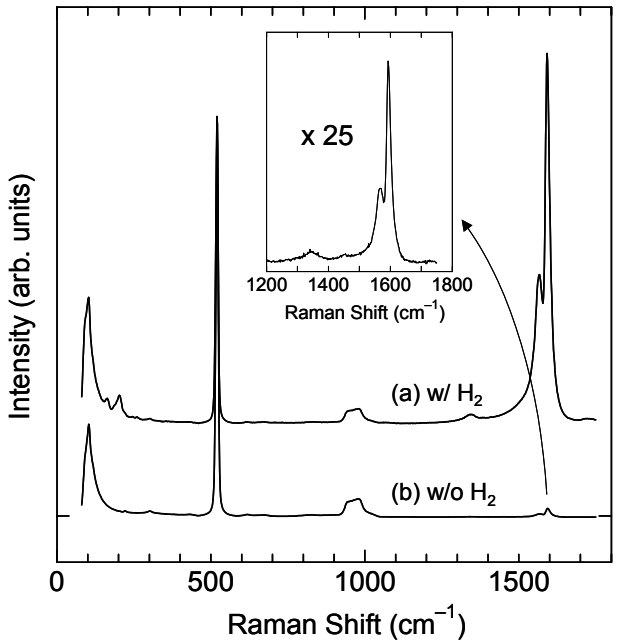


Fig. 2-25. Raman spectra taken by 488 nm of SWNTs synthesized on Si surface when (a) Ar/H_2 (3 % H_2) or (b) Ar was flowed during heat-up of the electric furnace. CVD was performed at 750ºC for (a) 10 min and (b) 30 min. Inset magnifies G-band in the case of (b). CVD times for Si and quartz are 10 min and 1 h, respectively. Spectral magnitudes are normalized by the height of Si peak at 520 cm^{-1}.

b. Effect of bimetallic catalyst

In this study, bimetallic Co-Mo catalyst is employed for the synthesis of SWNTs on flat substrates. To date, several types of bimetallic catalysts such as Fe-Co [14,62], Co-Mo [9,11], and Fe-Mo [5,10,63,64] have been used for the mass synthesis of SWNTs by impregnating them into porous support powders (e.g., silica, alumina, or MgO). Some of these studies [9,11,63,64] discussed the effect of bimetals on the growth of SWNTs.

Figure 2-26 shows Raman scattering spectra of SWNTs grown from different catalysts on quartz substrates measured with 488-nm laser light. In all the cases, CVD was performed for 1 h at 800°C. The CVD experiment and Raman scattering measurement shown in Fig. 2-26a to 2-26d were performed in the same batch to ensure comparability. Figure 2-26a shows the Raman spectrum of SWNTs grown from a standard acetic Co-Mo catalyst (0.01 wt% each), which results in the strongest Raman intensity of all the cases.

Figure 2-26b shows a spectrum of SWNTs grown from a bimetallic catalyst of molybdenum acetate and cobalt *nitrate*, $Co(NO_3)_2$-$6H_2O$. The condition of Fig. 2-26b is

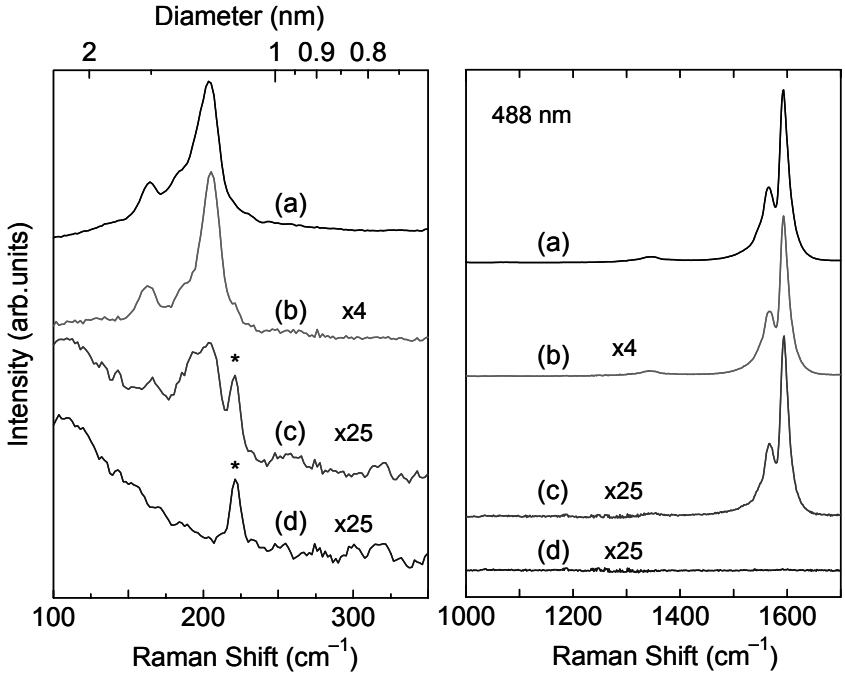


Fig. 2-26. Raman spectra (taken by 488 nm) of SWNTs generated on quartz substrates from various catalysts, (a) Co acetate and Mo acetate 0.01 wt% each, (b) Co nitrate and Mo acetate 0.01 wt% each, (c) Co acetate 0.02 wt%, and (d) Mo acetate 0.02 wt%. The weight concentration here is defined as the ratio of metallic weight in salt to total solution weight used for the dip-coating process (see experimental section). The right panel shows G-band while left panel exhibits RBM. The asterisk at 220 cm^{-1} denotes the background noise of our measurement system.

seemingly similar to the case of Fig. 2-26a; however, the amount of SWNTs in the former is appreciably lower than that in the latter. This difference may be explained by the study conducted by Sun et al. [65] who prepared cobalt catalysts by impregnating a mixture of cobalt (II) nitrate and cobalt (II) acetate salts onto silica gel powder. They tested various nitrate/acetate ratios from 1:0 (all nitrate) to 0:1 (all acetate) and demonstrated that only when acetate was solely used, the fine dispersion of Co particles of approximately 2 nm in diameter was obtained; however, when nitrate was used, the resultant Co particles became as large as 10 nm in diameter. They reported that this was caused by a strong interaction between the metal acetate and the SiO_2 support [65]. Although the structure of SiO_2 in Ref. 33 is different from that in the present study, the lower catalytic activity observed in Fig. 2-26b compared with that observed in Fig. 2-26a may be caused by the weaker interaction between Co and the SiO_2 surface.

Figure 2-26c shows a spectrum of SWNTs grown from 0.02 wt% Co catalyst, in which the observed intensity of the G-band is much lower (1/25 of Fig. 2-26a). Furthermore, when 0.02 wt% Mo catalyst was employed, no signals of SWNTs were detected, as shown in Fig. 2-26d, indicating that monometallic Mo is inactive as a catalyst for SWNTs. Our observation here agrees with the results obtained by Alvarez et al. [11] who discussed the role of Mo in the stabilization of Co. The result in Fig. 2-26 shows clearly that the combination of Co and Mo acetates provides the best result among the tested cases.

c. Merits and application of current technique

Since the production of SWNTs requires an active catalyst with a size comparable to the diameter of a SWNT (i.e., a few nanometers [4]), it is very important to mount small amounts of catalytic metals on the surface and, at the same time, to prevent them from agglomerating into large particles even under the high temperature of the CVD reaction. An obvious merit of our dip-coating technique is the ease with which extremely small amounts of bimetallic catalyst can be loaded on the surface; this is partly because the concentration of catalyst solution can accurately be adjusted merely by diluting.

Figure 2-27 presents a plan-view HR-TEM image of the quartz substrate heated to 800°C with an Ar/H_2 flow of 300 sccm without the subsequent CVD reaction. It is revealed that the Co catalyst particles (observed as black circles) are finely monodispersed over the substrate with approximate diameters of 1–2 nm without producing agglomerated metals even after heating under the Ar/H_2 reductive atmosphere [65]. This good dispersion is partially explained by the strong chemical interaction between metal acetate and the SiO_2

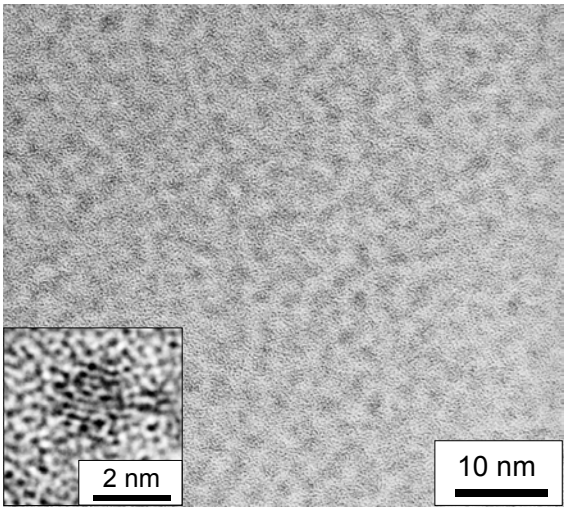


Fig. 2-27. Plan-view HR-TEM image of the quartz substrate surface after reduction by heated up to 800°C without undergoing CVD reaction. Catalyst particles are seen as black circles and are finely mono-dispersed on the surface. Inset magnifies a typical image of the catalyst particle.

base, as stated above. The mechanism of finely dispersed Co-catalyst formation and the role of Mo will be investigated and discussed in detail in Section 2.4. Such chemical interactions would not occur when the catalyst is loaded by conventional sputtering or vacuum vapor deposition method.

The lowering of CVD temperature is also an important factor because a high temperature accelerates the chemical reaction between the catalyst metal and silicon to create inactive metallic silicide [51,59] and an agglomeration of catalysts. The alcohol CCVD method is superior, as demonstrated in Fig. 2-17 as well as in previous reports [14,49,62], in producing relatively high-quality SWNTs at lower temperatures. This low-temperature process is beneficial to our direct synthesis technique because conventionally used support materials are not required in our method.

To the best of the author's knowledge, this is the first study to directly synthesize visually recognizable amounts of SWNTs on the surface of a quartz substrate. It has recently been reported [66,67] that SWNTs exhibit excellent bleached absorption properties due to their strong third-order optical nonlinearity ($\chi^{(3)}$) along with an absorption of approximately 1.55 μm light that is used in optical telecommunication. These characteristics have motivated attempts to apply SWNTs in optical switching [66,67] and mode-locked lasers.

Figure 2-28 shows an optical absorption spectrum of SWNTs directly grown on the quartz surface. As a reference, Fig. 2-28 also shows the spectrum of SWNTs synthesized by the alcohol CCVD method on zeolite support using Fe-Co catalyst (refer to Section 2.1), which was suspended in 1 wt% SDS-added D_2O after strong sonication, centrifugation, and decantation of its supernatant, based on the procedure reported in Ref. 68. In the spectrum shown in Fig. 2-28a, several broad peaks can be observed and this broadening is due to the bundling of SWNTs [69]. Sharper peaks are observed when the SWNT bundles are removed by centrifugation (Fig. 2-28b). The difference in the locations of the peaks between Figs. 2-28a and 2-28b arises due to the difference in the bandgap of the contained SWNTs (i.e., difference in chirality). Further, the spectrum of Fig. 2-28a is considered to be red-shifted due to the effect of bundling. There are a few recognizable groups of peaks in the spectra. The peaks at approximately 1450 nm in Fig. 2-28a are derived from the first-energy gaps of semiconducting tubes E^S_{11}, and the peaks at approximately 800 nm are derived from the second-energy gaps E^S_{22} [69]. These results suggest the possibility of applying our sample to the aforementioned optical applications, which will be demonstrated in detail at the end of Chapter 4.

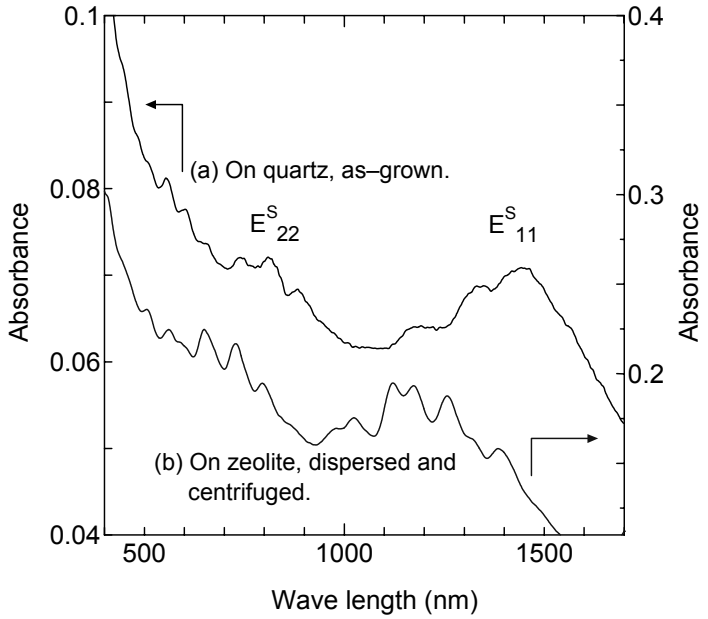


Fig. 2-28. Optical absorption spectra of (a) SWNTs synthesized directly on the surface of quartz, and (b) those synthesized on zeolite support using Fe/Co catalyst as a reference. The spectrum in the case of (b) was measured by dispersing the specimen in 1 wt% SDS-added D_2O solution followed by a strong sonication, centrifugation, and decantation of its supernatant based on the procedure in Ref. 68.

d. Applicability of current technique to Si/SiO_2 microstructures

Although the conventional vacuum vapor deposition technique has an important advantage of being a dry process in which cleanness is easier to maintain than in the wet process, the catalyst metal is mounted only on the side facing the linearly incoming metallic vapor flux. Furthermore, such a vacuum process is not only expensive but also involves a difficulty in uniformly loading the catalyst onto a large surface area due to the limited size of the available vacuum chamber. On the other hand, the proposed liquid-based dip-coat process is not subject to such a limitation; further, by this method, the catalyst can be loaded even onto the surfaces of infinitely long fibers or strips at a considerably lower cost.

An additional merit of the dip-coat method is its applicability to solid surfaces that have complex surface geometry, such as microstructures fabricated by micro-electro-mechanical-system (MEMS) processes. Due to the nature of the dip-coat method, it is possible to load the catalyst even onto a surface with complex geometry at which the metallic vapor flux does not reach, such as the inner walls of concentrically hollow optical fibers. The feasibility of the proposed technique toward MEMS structures is going to be presented here. It should be noted that such an incorporation of SWNTs into MEMS structures is an important fundamental technology that connects micro and nano regimes.

Figure 2-29 shows the FE-SEM images for several examples of direct incorporation of SWNTs on Si microstructures. Figure 2-29a shows the surface of the Si substrate on which a trigonal array of cylindrical pillars was fabricated. The diameter and height of the pillar were 2 μm and ~7 μm, respectively. The catalyst was supported on the substrate by the dip coating of 0.01 wt% Co-Mo acetate solution, as described in Section 2.3.2. The ACCVD was performed at a reaction temperature and ethanol vapor pressure of 750°C and 10 Torr, respectively. It was frequently observed (approximately 30% of the pillar intervals) that SWNTs, either bundled or isolated, were bridged between the top surfaces of neighboring pillars, as shown in Fig. 2-29a. SWNTs were also observed on the bottom surface of the substrate and the side surface of the pillar; however, they grew along the surface and therefore do not depart from it. This may be explained that only SWNTs on the top surface of the pillar had the opportunity to overcome the van der Waals attractive force from the surface at the circular edge of the pillar.

Figure 2-29b shows the FE-SEM image of the bridged SWNT between the tips of the interfacing Si cantilevers at intervals of 5 μm. The CVD conditions were identical to those in the case of Fig. 2-29a. These cantilevers were fabricated in the same Si piece, as shown

in the inset, over a penetrated hole manufactured in the substrate. Such a SWNT suspended in space should be useful for several optical investigations of SWNTs, such as a more accurate measurement of polarized Raman scattering of SWNTs under reduced environmental effects. The reproducibility of this suspension is considerably high, and thus far, the bridging has been observed in all the trials (5 out of 5 pieces).

Figure 2-29c shows the growth of SWNTs on the surface of a quartz grating. It should be noted that the SWNTs were selectively grown in the shallow grooves of the grating. This can be explained by the fact that the Co-Mo acetate solution used in the dip-coat process was selectively trapped inside the grooves due to the capillary force exerted on the liquid. On the other hand, Fig. 2-29d shows SWNTs that are grown preferentially on the top surface of the Si/SiO_2 substrate on which deep grooves were fabricated. In this case, it is possible that the high aspect ratio of the groove cross section prevented the residual air in the deep grooves from being replaced with the Co-Mo solution. The examples shown in Figs. 2-29c and 2-29d indicate the possibility that the SWNT growth can be spatially controlled by exploiting the difference in the wettability of microstructures. It should be noted that all the surfaces presented in Fig. 2-29 are sufficiently clean and devoid of agglomerated catalyst metals that could have caused roughness of the surface after CVD.

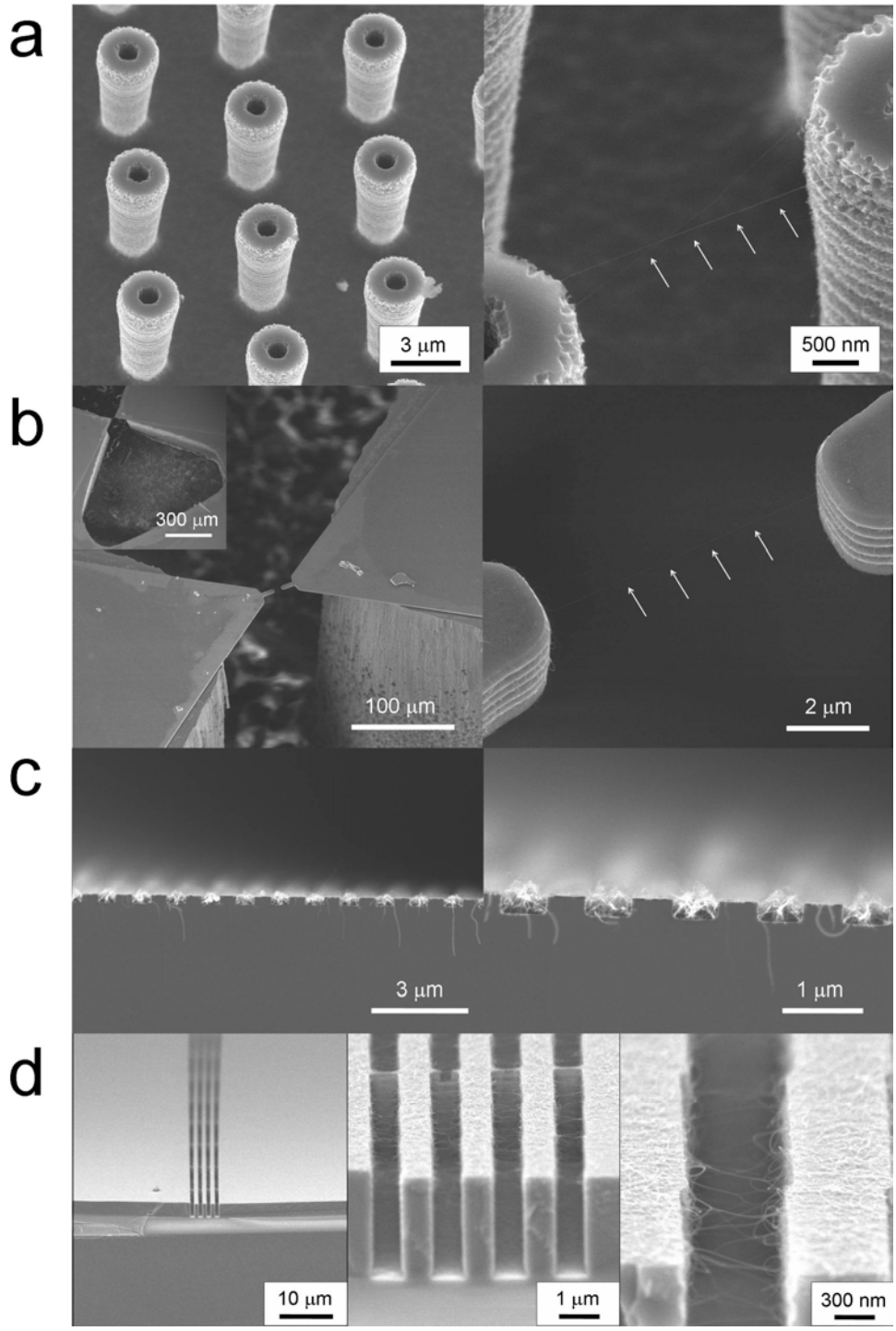


Fig. 2-29. FE-SEM images for several examples of direct growth of SWNTs in Si/SiO_2 microstructures from Co-Mo catalyst supported by the dip-coat technique. SWNTs were directly synthesized on (a) arrays of cylindrical Si pillar, (b) interfacing cantilevers fabricated over a hole penetrating the Si substrate, (c) inside nano-grooves of a quartz grating plane, and (d) top surface of Si/SiO_2 substrates on which deep grooves were fabricated. See text for details.

2.3.4 Summary of direct growth of SWNTs on flat substrates

This section presented a new method of synthesizing SWNTs with sufficient quality directly on the surface of Si and quartz substrates. It was observed that the Co-Mo catalyst supported by the proposed method combined with the alcohol CCVD method produces SWNTs with high quality and selectivity directly on the flat Si/SiO_2 surface. It was demonstrated that intermediate support materials such as oxide porous materials or Al deposition layers are unnecessary for the growth of SWNTs on the Si/SiO_2 surface, differently from conventional understandings.

The proposed dip-coat technique with Co-Mo bimetallic catalyst was observed to excel in controlling the amount of supported metals and can yield finely monodispersed Co particles with a diameter range of 1–2 nm. The SWNTs were synthesized directly on the Si surface even at a temperature of 650°C, which is much lower than previously reported temperatures of 800–1000°C. On the quartz surface, an abundant amount of SWNTs were produced to the extent that the surface was blackened with SWNTs. It was demonstrated that the proposed technique is applicable to the direct incorporation of SWNTs into Si-based MEMS structures.

The proposed dip-coating method is an easy and cost-effective approach that is suitable for mounting small amounts of catalysts on the surface. The strong interaction between metal acetate and the SiO_2 base may aid the fine dispersion of the catalyst, which is difficult to achieve by conventional sputtering and deposition techniques. Further elucidation of the Co-Mo catalyst formation process is presented in Section 2.4.

2.4 Morphology and chemical state analysis of Co-Mo catalysts supported on substrates by TEM and XPS analyses

2.4.1 Questions to be resolved for dip-coat supported Co-Mo catalysts

In Section 2.3.3, it has been presented that the catalyst supported by the dip-coating of bimetallic Co-Mo acetates on Si/SiO_2 substrates yield high quality SWNTs without generating agglomerated metals on the substrate. However, the mechanism concerning the high activity and selectivity of Co-Mo catalysts in the growth of SWNTs has not been fully clarified at that time. As clarified in Section 2.3.3, the catalytic performances in the SWNT growth have the order of {Co-Mo acetates > Co (nitrates)-Mo (acetates) >> Co acetates >> Mo acetates}. Although this result is supporting an inference that Co species are stabilized by Co-molybdate at an optimum Co/Mo ratio and that Mo carbides release active carbon to catalytic Co particles from which SWNTs selectively grow during the CVD reaction [11,70-72], the detailed correlation between the morphology and the chemical state of Co-Mo catalysts during their preparation and activation has not been verified so far. The effect of Mo in bimetallic catalysts on the growth of SWNTs should also be clarified.

In this Chapter, to resolve these questions, Co-Mo catalysts are prepared on quartz substrates from metal acetate solutions using a procedure of dip coating, followed by calcination and reduction, instead of using single crystals or porous materials as catalyst support. This allows one to quantitatively characterize the catalyst morphology using transmission electron microscopy (TEM), and the chemical state of metal species using X-ray photoelectron spectroscopy (XPS). Based on evidences discovered from a series of measurements, a model is then developed to understand why Co-Mo catalysts prepared with the above method show high selectivity and activity for the growth of high-purity SWNTs densely and vertically aligned on quartz substrates during the alcohol CCVD process.

2.4.2 Methods for catalyst characterization

2.4.2.1 TEM observation and its sample preparation

The morphology of Co-Mo catalysts after calcination and after reduction is characterized using TEM. The samples for plan-view TEM observations are sputter-coated with a 10-nm SiO_2 layer to avoid structural variation during TEM observations. For the samples for XTEM observations, two identical substrates are adhered to each other from the catalyst

side by using glue without depositing a SiO_2 layer. The samples for plan-view TEM and XTEM observations have a sandwich structure of SiO_2(quartz) / catalyst / SiO_2(10nm) and SiO_2(quartz) / catalyst / glue / catalyst / SiO_2(quartz), respectively. Then, these substrates are sliced and punched into circular discs with a diameter of 3 mm and a thickness of 2 mm.

Finally, these discs are further thinned by conventional mechanical grinding, polishing, and dimpling, followed by Ar ion milling at an acceleration voltage 4 kV at an incidence angle of 6° with a Gatan 691 Precision Ion Polishing System (PIPS). Plan-view TEM and XTEM observations are done using a JEOL JEM-4000EX at 400 kV and 2010F at 200 kV, respectively. Because there is no crystalline orientation information from the fused quartz substrates, no orientation adjustment during XTEM observations is performed to make the incident angle of electron beam parallel to the direction of quartz-glue interfaces.

2.4.2.2 Procedure for XPS measurement

The chemical states of the Co-Mo catalysts after calcination by heated at 400°C in air and after reduction by heated up to 800°C in the flow of Ar/H_2 (3% H_2), as their details described in Section 2.3, are characterized using XPS. The measurements are done using a PHI 1600 X-ray photoelectron spectrometer equipped with an Mg Kα (1253.6 eV) source operating at 300 W. To decrease the influence of oxidation and contamination for XPS samples, these substrates are sealed in a plastic box filled with Ar gas as soon as they are removed from the furnace or the CVD reactor, and then transferred to an analysis chamber (2.0×10^{-9} Torr) through a loading chamber (5.3×10^{-6} Torr) for XPS measurements. All these procedures are finished in 30 min. Binding energies (BEs) are referenced to the C 1s peak at 284.6 eV to compensate for the charging effect. The BE curves are fitted using a mixed Gaussian/Lorentzian curve after subtracting the background using the Shirley algorithm [73], in which spin-orbital-splitting intensities are fixed at their theoretical ratios. The surface atomic ratios of the calcined and the reduced quartz substrates coated with Co-Mo catalysts are estimated from peak intensities in the XPS spectra and atomic sensitivity factors.

2.4.3 Results of TEM and XPS analyses

2.4.3.1 Morphology of calcined and reduced Co-Mo catalyst

First, it is mentioned that the reduced samples for TEM observations should be considerably oxidized even if the catalysts are in metallic state right after reduction due to the following two reasons: 1) An oxide layer or a glue layer was coated on the catalysts; 2) More than two weeks was taken to prepare the TEM samples ready for observation.

Figure 2-30 shows plan-view TEM images of the calcined and the reduced Co-Mo catalysts on the quartz substrates. For both samples for after calcination and after reduction shown in Figs. 2-30a and 2-30d, respectively, well-dispersed nano-sized particles with diameters of 1 - 2 nm can be observed. Figures 2-30b and 2-30e reveal that the Co-Mo catalyst particles after reduction seemed to shrink to a smaller size, while remaining good dispersion without agglomerating into larger ones. The number density of these uniformly

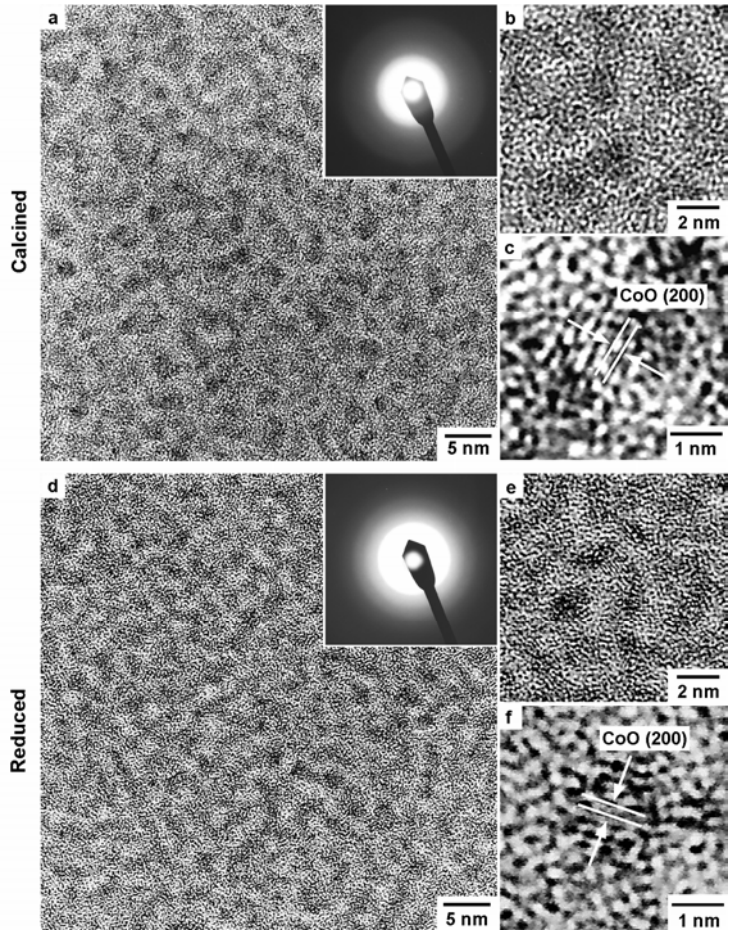


Fig. 2-30. Plan-view TEM images of (a) calcined and (d) reduced Co-Mo catalysts on quartz substrates, and HR-TEM images of (b) (c) calcined and (e) (f) reduced Co-Mo catalysts. SAED patterns are shown in the insets of (a) and (d).

distributed catalyst particles after reduction was estimated from the TEM images to be as high as ~1.3×10^{17} m^{-2}.

Selected area electron diffraction (SAED) patterns shown in the insets of Figs. 2-30a and 2-30d, and high-resolution TEM (HR-TEM) images shown in Figs. 2-30b and 2-30e revealed that most of the nano-sized catalyst particles were amorphous, and only some of them were crystalline. As indicated in Figs. 2-30c and 2-30f, these crystalline particles exhibit lattice distances of 2.13 - 2.38 Å, which are approximately consistent with CoO (200) lattice constant (2.13 Å), but significantly differ from those of Co (111) (2.05 Å), Co_3O_4 (311) (2.44 Å), MoO_2 (110, $11\bar{1}$) (3.41 Å), MoO_3 (021) (3.26 Å), and $CoMoO_4$ (002, 220) (3.36 Å) lattices. Because Co:Mo = 1.6:1 in ethanol solutions, the amount of Co species should be in excess on the substrates. Therefore, we conclude that most of those nano-sized particles, whether crystalline or amorphous, might be mainly composed of CoO. This conclusion is supported with the surface composition analysis using XPS, which is shown later in this section.

Figure 2-31 shows XTEM images of the reduced Co-Mo catalysts on the quartz substrates. Because the incident angle of electron beam deviated from the parallel direction of quartz-glue interfaces, as shown in Fig. 2-31a, catalyst particles were seemingly located within a vertical range of ~ 10 nm. High-resolution XTEM images in Fig. 2-31b exhibited that these spherical- or elliptical-like particles with diameters of 1 - 2 nm were well

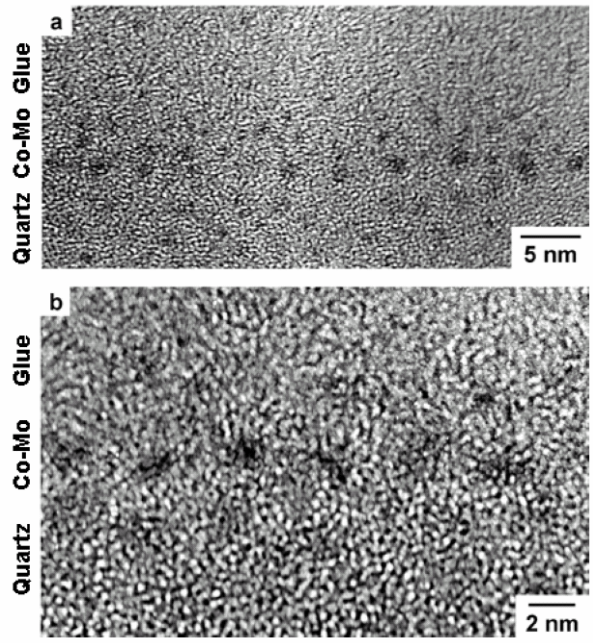


Fig. 2-31. (a) XTEM and (b) HRXTEM images of reduced Co-Mo catalysts on quartz substrates.

dispersed without aggregation, which is consistent with corresponding plan-view images. These results indicate that Co-Mo catalysts existed as well-dispersed nano-sized particles on the quartz substrates just before the CVD reaction. This morphology should be closely associated with the subsequent growth of densely and vertically aligned SWNTs, and the mechanism for this dispersion is going to be investigated by XPS in the nest subsection.

2.4.3.2 Chemical state of calcined and reduced Co-Mo catalysts analyzed by XPS

Figure 2-32 shows BEs of C 1s, Si 2p, and O 1s levels for the calcined and the reduced catalysts on the quartz substrates. As indicated in Figs. 2-32b and 2-32c, the BEs of Si 2p at 103.4 - 103.6 eV, and O 1s at 532.3 - 532.5 eV agree well with quartz references (Si:103.3 - 103.7 eV, O: 532.1 - 532.7 eV) [74,75]. This suggests that the BE shift due to the charging effect has been corrected well with the C 1s BE as a reference. The spectra of C 1s and Si 2p indicate the absence of acetate residues (288.2 - 289.3 eV) [76,77], metal carbides (282.7 - 283.1 eV) [78,79], and metal silicides (99.1 - 99.6 eV) [80-82]. Moreover, the spectra of O 1s indicate the formation of metal oxide species (530.3 - 530.4 eV) [83].

Figure 2-33a shows BEs of Mo 3d levels for the calcined and the reduced catalysts on the quartz substrates. Both spectra exhibit a pair of spin-orbit BEs at 232.4 - 232.5 and 235.4 - 235.5 eV, whereas a pair of new spin-orbit BEs appeared at 229.0 and 232.0 eV only for the reduced catalysts. The Mo $3d_{5/2}$ BE at 232.4 - 232.5 eV is attributed to Mo^{6+} in MoO_3 (232.2 - 233.0 eV) [70,84-88] and/or non-stoichiometric Co molybdates, $CoMoO_x$ (232.1.232.3 eV for stoichiometric Co molybdates where x = 4) [70,87,88]. The new Mo $3d_{5/2}$ BE at 229.1 eV is attributed to Mo^{4+} in MoO_2 (229.0 - 230.1 eV) [70,84-87]. These results indicate that the decomposition of Mo acetates resulted in the formation of Mo^{6+} in

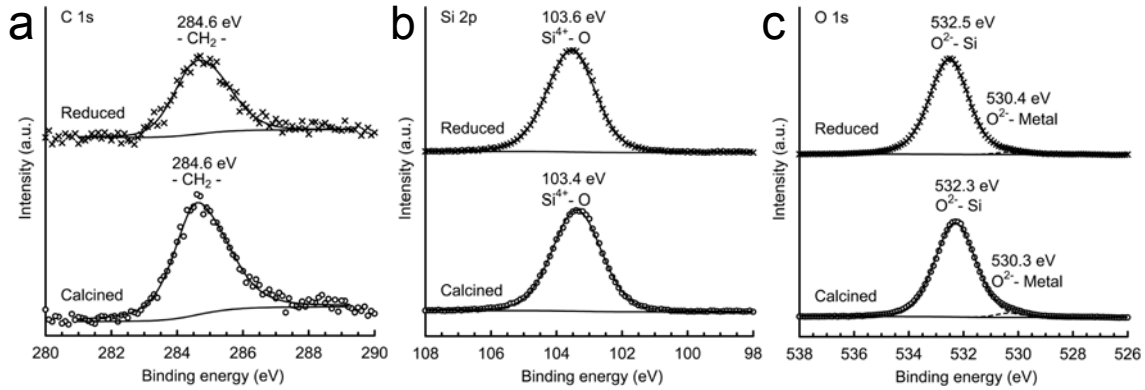


Fig. 2-32. XPS spectra of (a) C 1s, (b) Si 2p, and (c) O 1s levels for calcined and reduced Co-Mo catalysts on quartz substrates.

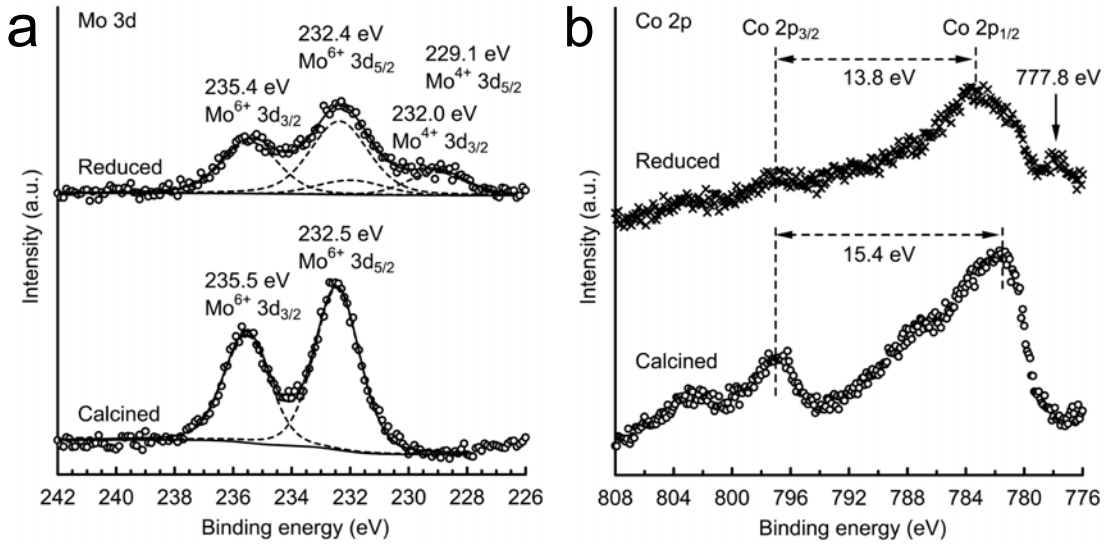


Fig. 2-33. XPS spectra of (a) Mo $3d_{5/2}$ and $3d_{3/2}$, and (b) Co $2p_{3/2}$ and $2p_{1/2}$ levels for both calcined and reduced Co-Mo catalysts supported on quartz substrates.

MoO_3 and/or $CoMoO_x$, and the reduction of calcined catalysts converted Mo oxide species to MoO_y ($y \leq 2$) or even metallic Mo that was not detected due to its oxidization during *ex situ* XPS analyses.

Figure 2-33b shows BEs of Co 2p levels for the calcined and the reduced Co-Mo catalysts on the quartz substrates. The reduced samples showed remarkable differences from calcined ones in two aspects. One is the appearance of a new BE at 777.8 eV, which is attributed to metallic Co (777.8 - 778.5 eV) [70,87,89,90]. The other is the decreased distance between the $2p_{3/2}$ and $2p_{1/2}$ spin-orbit BEs by as large as 1.6 eV, while the $2p_{1/2}$ BE remained almost unchanged. This should result from the change in chemical state of Co oxide species during reduction, rather than from the charging effect due to particle sizes [91] or layered structures [92] with different dielectric properties.

To clarify the above changes, the Co $2p_{3/2}$ BEs are decomposed and fitted as shown in Fig. 2-34. The spectra for calcined and the reduced catalysts are composed of two $2p_{3/2}$ components at 780.9 - 781.0 eV and 783.3 - 783.5 eV, and two distinct shake-up satellites at 786.9 - 787.0 eV and 790.2 - 790.6 eV. The two $2p_{3/2}$ BEs are attributed to Co^{2+} oxide species based on these intense shake-up satellites 6.0- 6.5 eV higher than the primary spin-orbit BEs [88,93]. The two $2p_{3/2}$ BEs at 780.9 - 781.0 eV and 783.3 - 783.5 eV are further assigned to Co^{2+} in CoO and Co^{2+} in $CoMoO_x$, respectively, due to their agreement with CoO (780.0 - 780.7 eV) [70,89,90,94,95] and $CoMoO_4$ (780.5 - 781.2) [87-89,96]

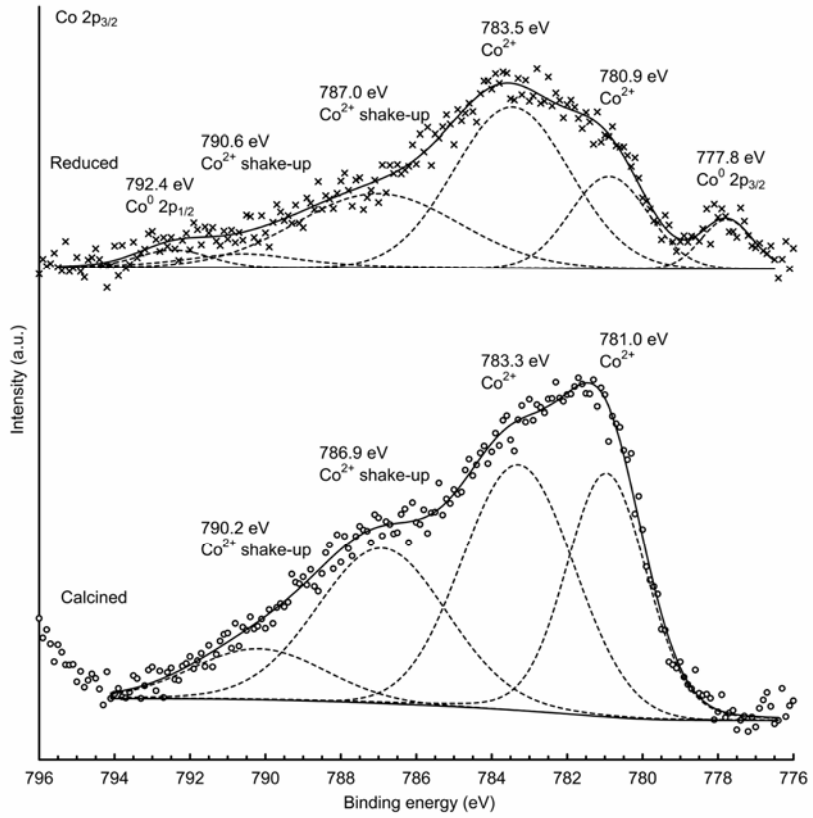


Fig. 2-34. XPS spectra of Co 2p3/2 levels for calcined and reduced Co-Mo catalysts on quartz substrates.

references. The relatively large BE deviation of Co^{2+} in $CoMoO_x$ from Co^{2+} in $CoMoO_4$ might result from the polarization effect or the non-stoichiometry when Co^{2+} ions are incorporated into highly oxidized MoO_3 matrix [89,96,97]. The BE intensity ratio of Co^{2+} in $CoMoO_x$ to that in CoO increased from 1.3 to 2.6 after reduction, indicating that more $CoMoO_x$ was formed at the expense of CoO and MoO_3. This change leads to the seemingly decreased distance between Co $2p_{3/2}$ and $2p_{1/2}$ BEs shown in Fig. 2-33b. Therefore, it is concluded that the calcination of dip-coated substrates decomposed Co acetates into Co oxide species existing as CoO and $CoMoO_x$, and the subsequent reduction resulted in the formation of metallic Co and more $CoMoO_x$.

Table 2-2 shows the surface atomic ratios of the calcined and the reduced quartz substrates coated with Co-Mo catalysts. The quantity of metals as low as less than 10% of the total composition supports the approximate estimation in the experimental section that the quartz substrates might be covered with the metallic catalyst layers. The calcined and the reduced samples had Co/Mo atomic ratios of 2.1 - 2.3, approximately consistent with

Table 2-2. Surface composition of quartz substrates dip-coated with Co-Mo catalysts after calcination and after reduction.

	Co	Mo	Si	O	C
Calcined (atomic %)	5.1	2.2	27.9	59.7	5.1
Reduced (atomic %)	3.2	1.5	29.8	61.7	3.7

the initial ratio of 1.6 in metal acetate solutions, so that only excess Co species were observed in TEM images. It is noteworthy that the atomic ratios of Co and Mo to total elements decreased by 63 % and 68 % after reduction, respectively, which could be explained from the decrease in catalyst coverage, i.e., the decrease in catalyst particle size, as confirmed in TEM images.

2.4.3.3 Mechanism and formation process of Co-Mo catalyst

Based on the above results, a model was deduced for the evolution in morphology and chemical state of Co-Mo catalysts on the quartz substrates during calcination and reduction as illustrated in Fig. 2-35. It is assumed that a layer of bimetallic acetate film (Co:Mo = 1.6:1 in atomic ratio) is formed on the quartz substrates after the dip coating from dilute metal acetate solutions. After calcination in air at 400°C, metal acetates are decomposed into CoO, $CoMoO_x$ (x = 4 for stoichiometric Co molybdates), and MoO_3, which exist as well-dispersed nano-sized particles. After reduction in Ar/H_2 up to 800°C, existing $CoMoO_x$ remains unchanged, whereas CoO and MoO_3 are reduced into Co and MoO_y ($y \leq 2$), and more $CoMoO_x$ are formed at the expense of Co and MoO_3. During this process, no distinct agglomeration occurs although catalyst particles partially de-wet into smaller sized ones. Finally, SWNTs start to grow from the metallic Co particles that have comparable diameter to that of SWNTs, at the time ethanol vapor is supplied over the catalyst.

Furthermore, it is deduced that even if Mo and Co species uniformly coexist on SiO_2 surfaces during calcination, Mo preferentially promotes the formation of metal oxides at catalyst/SiO_2 interfaces, because Mo has a stronger affinity to oxygen than Co [26]. Because of Co:Mo = 1.6:1 in atomic ratio, the excess Co easily diffuses into MoO_3 [96] and forms $CoMoO_x$ underlayers/boundaries, whereas the residue Co exists as CoO particles either located on $CoMoO_x$ underlayers or attached to $CoMoO_x$ boundaries.

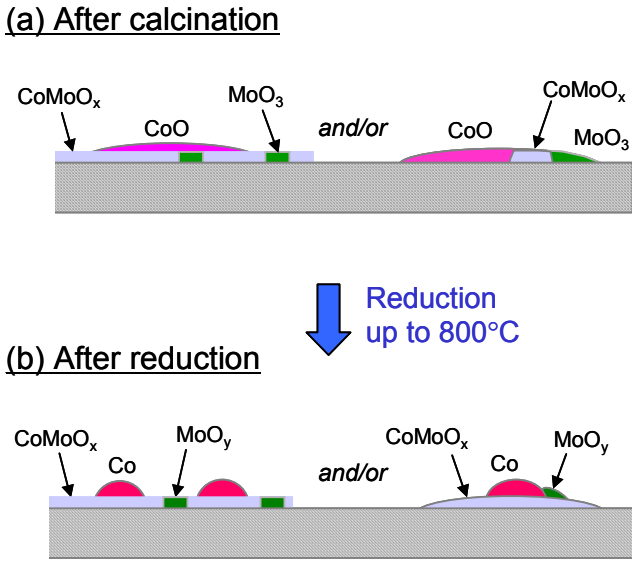


Fig. 2-35. Chemical state and morphology of Co-Mo catalysts on quartz substrates after (a) calcination and (b) reduction.

The formation of well-dispersed nano-sized catalyst particles during calcination is attributed mainly to the decomposition of metal acetates on oxide substrates. It is suggested that the strong coordination of carboxylic groups with metal ions mediates the decomposition of metal acetates to prevent the formation of large particles [65,98], as was discussed in Section 2.3. As a result, compared with metal nitrates, metal acetates form better-dispersed nano-sized particles during calcination [65,98], thereby accounting for their best performance for the growth of SWNTs.

As the temperature rises from R.T. during reduction, CoO and MoO_3 under the flow of Ar/H_2 start to be reduced into metallic Co and MoO_y, respectively, whereas $CoMoO_x$ remains unchanged due to their extreme stability against reduction [99,100]. These metallic Co was detected in XPS analyses under particular protection from exposure to oxygen, whereas only metal oxides were confirmed in TEM observations. In addition, the decreased CoO intensity and the increased $CoMoO_x$ intensity support the following deduction. The firstly reduced metallic Co reacts with MoO_3/MoO_y until Mo oxides are depleted to form $CoMoO_x$, and the residue Co remains metallic and works as a catalyst. That is, the formation of metallic Co possibly competes with that of Co molybdates, and finally becomes dominant.

The stable existence of well-dispersed nano-sized Co particles during reduction is attributed to the immobilization effect of $CoMoO_x$ underlayers. Although metallic Co particles vigorously migrate on SiO_2 surfaces [90], they should be easily trapped on $CoMoO_x$ underlayers, owing to the strong interactions between MoO_3 and metallic Co [96]. The decreased size and the spherical- or elliptical-like shape of catalyst particles after reduction, which were observed in plan-view TEM and XTEM images, suggest that metallic Co might de-wet on quartz substrates. This deduction was confirmed by the decreased metal/substrate atomic ratio after reduction indicated by XPS analyses [90]. Although these metallic Co particles de-wet partially on $CoMoO_x$, their interfacial interactions are strong enough to limit their mobility and prevent them from agglomerating into large particles. Therefore, it is concluded that the role of Mo in bimetallic Co-Mo catalysts is to stabilize well-dispersed nano-sized metallic Co particles from agglomeration. Without Mo [90,91] or $CoMoO_x$ [71,88], the catalyst selectivity for the growth of SWNTs decreases or even disappears due to the agglomeration of Co particles.

2.4.4 Summary of formation process and role of Co-Mo catalyst

High-purity SWNTs with diameters of 1.2 nm were grown densely (~1.0×10^{17} m^{-2}) and vertically on the quartz substrates where bimetallic Co-Mo catalysts with a stoichiometry of ~1.6 were dip-coated from metal acetate solutions, followed by calcination and reduction. HRTEM and XPS studies on the morphology and chemical state of the calcined and the reduced catalysts provided critical evidence for their catalytic mechanism.

The results show that calcination in air at 400°C decomposes metal acetates into metal oxide species composed of CoO, MoO_3 and $CoMoO_x$ (x = 4 for stoichiometric Co molybdates), which exist as well-dispersed nano-sized particles possibly due to the mediation of strong coordination of carboxylic groups with metal ions during the acetate decomposition. The excess CoO might be either located on or attached to $CoMoO_x$ underlayers/boundaries. After reduction in Ar/H_2 up to 800 °C, metallic Co, MoO_y ($y \approx 2$) and more $CoMoO_x$ are formed at the expense of CoO and MoO_3. The strong interactions between metallic Co and $CoMoO_x$ underlayers prevent these well-dispersed (~1.3×10^{17} m^{-2}) nano-sized (1 - 2 nm) catalyst particles against agglomerating into larger ones.

The good dispersion of nano-sized catalyst particles due to the acetate decomposition, their stability against agglomeration due to the interactions between Co and $CoMoO_x$, their high activity due to the continuous supply of H_2 throughout the CVD reaction, and the *in situ* purification of growing SWNTs due to the oxygen radicals generated from the ethanol decomposition lead to the highly selective growth of high-purity SWNTs densely and vertically aligned on the quartz substrates.

2.5 Summary of Chapter 2

This chapter presented a comprehensive discussion of several important problems with regard to the research and application of SWNTs, such as developing methods for supporting the catalyst, growing SWNTs on solid flat surfaces, and elucidating the role and formation process of the catalyst.

In Section 2.1, the yield of SWNTs grown from Fe-Co catalyst supported on USY-type zeolite was systematically investigated in order to examine the feasibility of the alcohol CCVD method toward mass production. It was determined that the yield could be enhanced by reducing the catalyst prior to the CVD reaction. Furthermore, the wettability of Fe, Co, Ni, and Mo catalysts on the SiO_2 support was investigated. The resultant diameters of the SWNTs were attributed to the magnitude of $\Delta H_f°_{sublimate}/\Delta H_f°_{oxide}$, which may provide

useful guidelines for the choice of either a monometallic or bimetallic catalyst on SiO_2 supports.

Section 2.2 reported the development of a new technique for the catalyzed growth of SWNTs utilizing MPS thin film on Si substrate. The role of mesopores for supporting the catalyst was demonstrated from the reference experiments using a silica thin film without mesopores.

Section 2.3 reported the development of the dip-coat catalyst supporting method for the direct support of a small amount of catalyst on the flat substrate. It was determined that when cobalt and molybdenum acetates were used, the monodispersed Co particles with diameters of 1–2 nm were densely supported on the SiO_2 surface without agglomeration even at 800°C.

In Section 2.4, the underlying mechanism for the successful dispersion of Co was investigated by TEM and XPS. It was elucidated that the $CoMoO_x$ ($x \leq 4$) compound was formed on the SiO_2 surface and this layer aided in stabilizing the excess Co particles and preventing their agglomeration into larger particles.

The information and methods presented in this chapter will be used in Chapters 3 and 4 for the morphologically controlled growth of SWNTs and elucidation of their anisotropic optical properties.

Acknowledgments for Section 2.1

The author expresses gratitude to Mr. H. Tsunakawa, Mr. T. Ito, and Mr. Y. Kakegawa for their kind assistance in obtaining the TEM observations shown in Fig. 2-5 and Prof. T. Okubo and Mr. T. Sugawara at The University of Tokyo for the use of FE-SEM S-900, the observations from which are shown in Fig. 2-6. A part of this section has been published in *Chemical Physics Letters*, vol. 374, pp. 53–58, 2003 by Y. Murakami, S. Chiashi, Y. Miyauchi, and S. Maruyama.

Acknowledgments for Section 2.2

The author would like to thank Prof. T. Okubo at The University of Tokyo and Mr. S. Yamakita at Sony Corp. for valuable collaboration and discussions on the investigation of catalyzed growth of SWNTs from MPS pores, presented in Section 2.2. This work has been published in *Chemical Physics Letters*, vol. 375, pp. 393–398, 2003 by Y. Murakami, S. Yamakita, T. Okubo, and S. Maruyama.

Acknowledgments for Section 2.3

The author would like to express gratitude to Prof. T. Okubo and Mr. T. Sugawara at The University of Tokyo for the use of FE-SEM S-900, the observations from which are shown in Figs. 2-19 and 2-20; Mr. S. Watanabe, Ms. M. Nakagawa, and Mr. R. Tamochi at Hitachi Science Systems, Ltd. and K. Shibata at Hitachi High-Technology Corp. for their observations by FE-SEM S-5200 shown in Fig. 2-21; Mr. H. Tsunakawa at The University of Tokyo for his assistance in obtaining the TEM observation shown in Fig. 2-22; Prof. Y. Ikuhara at The University of Tokyo for the X-TEM measurement of a SWNT-grown Si substrate shown in Fig. 2-23; Dr. M. Hu and Prof. T. Okubo at The University of Tokyo for the HR-TEM observation of the catalyst on the surface of the quartz substrate shown in Fig. 2-27; Prof. R. E. Smalley at Rice University for supplying the HiPco sample corresponding to Fig. 2-28; and Profs. K. Hoshino and S. Yamashita at The University of Tokyo for supplying MEMS-processed substrates presented in Fig. 2-29. A part of this section has been published in *Chemical Physics Letters*, vol. 377, pp. 49–54, 2003 by Y. Murakami, Y. Miyauchi, S. Chiashi, and S. Maruyama and in *Japanese Journal of Applied Physics,* vol. 43, pp. 1221–1226, 2003 by Y. Murakami, S. Chiashi, Y. Miyauchi, and S. Maruyama.

Acknowledgments for Section 2.4

All the HR-TEM and XPS measurements presented in this section were performed by Dr. M. Hu and Prof. T. Okubo in the Department of Chemical System Engineering, The University of Tokyo. The author thanks them for their valuable assistance and discussions on the morphology and chemical state of the catalyst used for SWNT growth. The contents of this chapter have been published in *Journal of Catalysis,* vol. 225, pp. 230–239, 2004 by M. Hu, Y. Murakami, M. Ogura, S. Maruyama, and T. Okubo.

References for Chapter 2

1. *Carbon Nanotubes: Synthesis, Structure, Properties and Applications,* edited by M. S. Dresselhaus, G. Dresselhaus, and Ph. Avouris, Springer-Verlag, Berlin, 2001.
2. A. Thess, R. Lee, P. Nikolaev, H. Dai, P. Petit, J. Robert, C. Xu, Y. H. Lee, S. G. Kim, A. G. Rinzler, D. T. Colbert, G. E. Scuseria, D. Tománek, J. E. Fischer, R. E. Smalley, Science **273** (1996) 483.
3. C. Journet, W. K. Maser, P. Bernier, A. Loiseau, M. L. de la Chapelle, S. Lefrant, P. Deniard, R. Lee, J. E. Fisher, Nature **388** (1997) 756.
4. H. Dai, A. G. Rinzler, P. Nikolaev, A. Thess, D. T. Colbert, R. E. Smalley, Chem. Phys. Lett. **260** (1996) 471.
5. J. H. Hafner, M. J. Bronikowski, B. R. Azamian, P. Nikolaev, A. G. Rinzler, D. T. Colbert, K. A. Smith, R. E. Smalley, Chem. Phys. Lett. **296** (1998) 195.
6. J. Kong, A. M. Cassell, H. Dai, Chem. Phys. Lett. **292** (1998) 567.
7. P. Nikolaev, M. J. Bronikowski, R. K. Bradley, F. Rohmund, D. T. Colbert, K. A. Smith, R. E. Smalley, Chem. Phys. Lett. **313** (1999) 91.
8. J.-F. Colomer, J.-M. Benoit, C. Stephan, S. Lefrant, G. Van Tendeloo, J. B. Nagy, Chem. Phys. Lett. **345** (2001) 11.
9. B. Kitiyanan, W. E. Alvarez, J. H. Harwell, D. E. Resasco, Chem. Phys. Lett. **317** (2000) 497.
10. M. Su, B. Zheng, J. Liu, Chem. Phys. Lett. **322** (2000) 321.
11. W. E. Alvarez, B. Kitiyanan, A. Borgna, D. E. Resasco, Carbon **39** (2001) 547.
12. H. Yan, Q. Li, J. Zhang, Z. Liu, Carbon **40** (2002) 2693.
13. B. Zheng, Y. Li, J. Liu, Appl. Phys. A **74** (2002) 345.
14. S. Maruyama, R. Kojima, Y. Miyauchi, S. Chiashi, M. Kohno, Chem. Phys. Lett. **360** (2002) 229.
15. K. Mukhopadhyay, A. Koshio, N. Tanaka, H. Shinohara, Jpn. J. Appl. Phys. **37** (1998) L1257.
16. K. Mukhopadhyay, A. Koshio, T. Sugai, N. Tanaka, H. Shinohara, Z. Konya, J. B. Nagy, Chem. Phys. Lett. **303** (1999) 117.
17. E. Mizoguti, F. Nihey, M. Yudasaka, S. Iijima, T. Ichihashi, K. Nakamura, Chem. Phys. Lett. **321** (2000) 297.

18. I. W. Chiang, B. E. Brinson, R. E. Smalley, J. L. Margrave, R. H. Hauge, J. Phys. Chem. B **105** (2001) 1157.

19. W. Zhou, Y. H. Ooi, R. Russo, P. Papanek, D. E. Luzzi, J. E. Fischer, M. J. Bronikowski, P. A. Willis, R. E. Smalley, Chem. Phys. Lett. **350** (2001) 6.

20. M. Chike, J. Li, B. Chen, A. Cassell, L. Delzeit, J. Han, M. Mayyappan, Chem. Phys. Lett. **365** (2002) 69.

21. M. Zhang, M. Yudasaka, A. Koshio, S. Iijima, Chem. Phys. Lett. **364** (2002) 420.

22. M. S. Dresselhaus, P. C. Eklund, Advances in Physics **49** (2000) 705.

23. R. Saito, G. Dresselhaus, M. S. Dresselhaus, Phys. Rev. B **61** (2000) 2981.

24. A. Jorio, R. Saito, J. H. Hafner, C. M. Lieber, M. Hunter, T. McClure, G. Dresselhaus, M. S. Dresselhaus, Phys. Rev. Lett. **86** (2001) 1118.

25. P.W. Atkins, *Physical Chemistry 6th Ed.*, W.H. Freeman & Co., New York, 1997.

26. M. Hu, S. Noda, H. Komiyama, Surface Sci. **513** (2002) 530.

27. *CRC Handbook of Chemistry and Physics, 72th Ed.*, Edited by D.R. Lide, CRC Press, Boca Raton, 1991-1992.

28. L. Vitos, A.V. Ruban, H.L. Skriver, J. Kollar, Surface Sci. **411** (1998) 186.

29. *Binary Ally Phase Diagrams*, Edited by T. B. Massalski, ASM International, Netherlands, 1986.

30. N.R. Franklin, Y. Li, R.J. Chen, A. Javey, H. Dai, Appl. Phys. Lett. **79** (2001) 4571.

31. J. Wan, Y.H. Luo, J.L. Liu, R.G. Li, G. Jin, S.D. Choi, K.L. Wang, J. Crystal Growth **227-228** (2001) 820.

32. O.A. Nerushev, R.E. Morjan, D.I. Ostrovskii, M. Sveningsson, M. Jonsson, F. Rohmund, E.E. B. Campbell, Physica B **323** (2002) 51.

33. Y.J. Yoon, J.C. Bae, H.K. Baik, S. Cho, S. Lee, K.M. Song, N.S. Myung, Chem. Phys. Lett. **366** (2002) 109.

34. J. Duxiao, H. Nongyue, Z. Yuanying, X. Chunxiang, Y. Chunwei, L. Zuhong, Mat. Chem. Phys. **69** (2001) 246.

35. A.M. Cassell, S. Verma, L. Delzeit, M. Meyyappan, J. Han, Langmuir **17** (2001) 260.

36. G. Zheng, H. Zhu, Q. Luo, Y. Zhou, D. Zhao, Chem. Mater. **13** (2001) 2240.

37. M. Urban, D. Mehn, Z. Konya, I. Kiricsi, Chem. Phys. Lett. **359** (2002) 95.

38. A. Okamoto, T. Kawakubo, T. Hiraoka, T. Okazaki, T. Sugai, H. Shinohara, Mol. Cryst. Liq. Cryst. **387** (2002) 317.

39. F. Zheng, L. Liang, Y. Gao, J.H. Sukamto, C.L. Aardahl, Nano Lett. **2** (2002) 729.

40. N. Petkov, S. Mintova, K. Karaghiosoff, T. Bein, Mat. Sci. Eng. C **23** (2003) 145.

41. L. Huang, S. J. Wind, S.P. O'Brien, Nano Lett. **3** (2003) 299.

42. S. Yamakita, Master Thesis, The University of Tokyo, 2003.

43. D. Zhao, P. Yang, N. Melosh, J. Feng, B.F. Chmelka, G.D. Stucky, Adv. Mater. **10** (1998) 1380.

44. Y. Sakamoto, M. Kaneda, O. Terasaki, D.Y. Zhao, J.M. Kim, G. Stucky, H.J. Shin, R. Ryoo, Nature **408** (2000) 449.

45. Y. Murakami, S. Chiashi, Y. Miyauchi, S. Maruyama, unpublished.

46. M. Kusunoki, T. Suzuki, C. Honjo, T. Hirayama, N. Shibata, Chem. Phys. Lett. **366** (2002) 458.

47. J. Kong, H.T. Soh, A.M. Cassell, C.F. Quate, H. Dai, Nature **395** (1998) 878.

48. A.M. Cassell, N.R. Franklin, T.W. Tombler, E.M. Chan, J. Han, H. Dai, J. Am. Chem. Soc. **121** (1999) 7975.

49. Y. Murakami, S. Yamakita, T. Okubo, S. Maruyama, Chem. Phys. Lett. **375** (2003) 393.

50. Y. Li, W. Kim, Y. Zhang, M. Rolandi, D. Wang, H. Dai, J. Phys. Chem. B **105** (2001) 11424.

51. Y. Homma, T. Ymashita, P. Finnie, M. Tomita, T. Ogino, Jpn. J. Appl. Phys. **41** (2002) L89.

52. L. Delzeit, B. Chen, A. Cassell, R. Stevens, C. Nguyen, M. Meyyappan, Chem. Phys. Lett. **348** (2001) 368.

53. R. Y. Zhang, L. Amlani, J. Baker, J. Tresek, R. K. Tsui, Nano Lett. **3** (2003) 731.

54. H. Hongo, M. Yudasaka, T. Ichihashi, F. Nihey, S. Iijima, Chem. Phys. Lett. **361** (2002) 349.

55. Y. J. Jung, Y. Homma, T. Ogino, Y. Kobayashi, D. Takagi, B. Wei, R. Vajtai, P. M. Ajayan, J. Phys. Chem. B **107** (2003) 6859.

56. K. Matsumoto, S. Kinoshita, Y. Gotoh, K. Kurachi, T. Kamimura, M. Maeda, K. Sakamoto, M. Kuwahara, N. Atoda, Y. Awano, Jpn. J. Appl. Phys. **42** (2003) 2415.

57. Y. Ohno, S. Iwatsuki, T. Hiraoka, T. Okazaki, S. Kishimoto, K. Maezawa, H. Shinohara, T. Mizutani, Jpn. J. Appl. Phys. **42** (2003) 4116.

58. F. Nihey, H. Hongo, M. Yudasaka, S. Iijima, Jpn. J. Appl. Phys. **41** (2002) L1049.

59. T. de los Arcos, F. Vonau, M. G. Garnier, V. Thommen, H. G. Boyen, P. Oelhafen, M. Duggelin, D. Mathis, R. Guggenheim, Appl. Phys. Lett. **80** (2002) 2383.

60. M.J. Bronikowski, P.A. Willis, D.T. Colbert, K.A. Smith, R.E. Smalley, J. Vac. Sci. Technol. A **19** (2001) 1800.

61. H. Kataura, Y. Kumazawa, Y. Maniwa, I. Umezu, S. Suzuki, Y. Ohtsuka, Y. Achiba, Synth. Met. **103** (1999) 2555.

62. Y. Murakami, Y. Miyauchi, S. Chiashi, S. Maruyama, Chem. Phys. Lett. **374** (2003) 53.

63. A. M. Cassell, J. A. Raymakers, J. Kong, H. Dai, J. Phys. Chem. B. **103** (1999) 6484.

64. A. R. Harutyunyan, B. K. Pradhan, U. J. Kim, G. G. Chen, P. C. Eklund, Nano Lett. **2** (2002) 525.

65. S. Sun, N. Tsubaki, K. Fujimoto, Appl. Catal. A **202** (2002) 121.

66. Y.C. Chen, N.R. Raravikar, L.S. Schadler, P.M. Ajayan, Y.P. Zhao, T.M. Lu, G.C. Wang, X.C. Zhang, Appl. Phys. Lett. **81** (2002) 975.

67. S. Tatsuura, M. Furuki, Y. Sato, I. Iwasa, M. Q. Tian, H. Mitsu, Adv. Mater. **15** (2003) 534.

68. S. Maruyama, Y. Miyauchi, Y. Murakami, S. Chiashi, New J. Phys. **5** (2003) 149.1.

69. M. J. O'Connell, S. M. Bachilo, C. B. Huffman, V. C. Moore, M. S. Strano, E. H. Haroz, K. L. Rialon, P. J. Boul, W. H. Noon, C. Kittrell, J. P. Ma, R. H. Hauge, R. B. Weisman, R. E. Smalley, Science **297** (2002) 5936.

70. J.E. Herrera, L. Balzano, A. Borgna, W.E. Alvarez, D.E. Resasco, J. Catal. **204** (2001) 129.

71. D.E. Resasco, W.E. Alvarez, F. Pompeo, L. Balzano, J.E. Herrera, B. Kitiyanan, A. Borgna, J. Nanopart. Res. **4** (2002) 131.

72. J.E. Herrera, D.E. Resasco, J. Catal. **221** (2004) 354.

73. D.A. Shirley, Phys. Rev. B **135** (1972) 4709.

74. C.D. Wagner, D.E. Passoja, H.F. Kinisky, H.A. Six, W.T. Jansen, J.A. Taylor, J. Vac. Sci. Technol. **21** (1982) 933.

75. Y. Duval, J.A. Mielczarski, O.S. Pokrovsky, E. Mielczarski, J.J. Ehrhardt, J. Phys. Chem. B **106** (2002) 2937.

76. U. Gelius, P.F. Heden, J. Hedman, B.J. Lindberg, R. Manne, R. Nordberg, C. Nording, K. Siegbahn, Phys. Scr. **2** (1970) 70.

77. S.B.M. Hagstrom, P.O. Heden, H. Lofgren, Solid State Commun. **8** (1970) 1245.

78. L. Ramqvist, K. Hamrin, G. Johannson, A. Fahlman, C.J. Nording, J. Phys. Chem. Solids **30** (1969) 1835.

79. H. Wang, S.P. Wong, W.Y. Cheung, N. Ke, W.F. Lau, M.F. Chiah, X.X. Zhang, Mater. Sci. Eng. C **16** (2001) 147.

80. W.A. Brainard, D.R. Wheeler, J. Vac. Sci. Technol. **15** (1978) 1801.

81. J.S. Pan, E.S. Tok, C.H.A. Huan, R.S. Liu, J.W. Chai, W.J. Ong, K.C. Toh, Surf. Sci. **532** (2003) 639.

82. I. Jarrige, P. Jonnard, P. Holliger, T.P. Nguyen, Appl. Surf. Sci. **212** (2003) 689.

83. V.I. Nefedov, D. Gati, B.F. Dzhurinskii, N.P. Sergushin, Y.V. Salyn, Zh. Neorg. Khim. **20** (1975) 2307.

84. B.R. Quincy, M. Houalla, A. Proctor, D.M. Hercules, J. Chem. Phys. **94** (1990) 1520.

85. F. Solymosi, J. Cserenyi, A. Szoke, T. Bansagi, A. Oszko, J. Catal. **165** (1997) 150.

86. G. Chen, T.E. Ford, C.R. Clayton, J. Colloid Interface Sci. **204** (1998) 237.

87. M. Probst, M. Voss, R. Denecke, L. Viscido, J.M. Heras, D. Borgmann, H.-P. Steinruck, J. Electron Spectrosc. Relat. Phenom. **114** (2001) 539.

88. V.L. Parola, G. Deganello, C.R. Tewell, A.M. Venezia, Appl. Catal. A **235** (2002) 171.

89. R. Kleyna, H. Mex, M. Vos, D. Borgmann, L. Viscido, J.M. Heras, Surf. Sci. **433** (1999) 723.

90. R. Riva, H. Miessner, R. Vitali, G.D. Piero, Appl. Catal. A **196** (2000) 111.

91. V.I. Bukhtiyarov, I.P. Prosvirin, R.I. Kvon, S.N. Goncharova, B.S. Balzhinimaev, J. Chem. Soc., Faraday Trans. **93** (1997) 2323.

92. S. Suzer, Anal. Chem. **75** (2003) 7026.

93. M. Hassel, H.-J. Freund, Surf. Sci. **325** (1995) 163.

94. W.-J. Wang, Y.-W. Chen, Appl. Catal. A **77** (1991) 223.

95. Y. Brik, M. Kacimi, M. Ziyad, F. Bozon-Verdurazy, J. Catal. **202** (2001) 118.

96. L. Viscido, M. Vob, D. Borgmann, J.M. Heras, J. Mol. Catal. A **167** (2001) 199.

97. V.A. Zazhigalov, J. Haber, J. Stoch, A. Pyatnitzkaya, G.A. Komashko, V.M. Belousov, Appl. Catal. A **96** (1993) 135.

98. T. Matsuzaki, K. Takeuchi, T. Hanaoka, H. Arakawa, Y. Sugi, Catal. Today **28** (1996) 251.

99. M. Deboer, E.P.F.M. Koch, R.J. Blaauw, E.R. Stobbe, A.N.J.M. Hoffmann, L.A. Boot, A.J. Vandillen, J.W. Geus, Solid State Ionics **63** (1993) 736.

100. A.A. Halawy, M.A. Mohamed, G.C. Bond, J. Chem. Technol. Biotechnol. **58** (1993) 237.

Chapter 3:
Growth of vertically aligned SWNT films on substrates and their formation process

3.1 Research background and motivation

The possibility of conducting experimental studies on SWNTs greatly increased after the development of selective production by the laser furnace method [1] and more scalable CVD techniques such as the HiPco method [2]. In addition to the bulk synthesis of SWNTs, controlled positioning of carbon nanotubes on a substrate is considerably important for many applications such as field emission transistor (FET) [3–5], chemical sensors [6,7], and optical devices for telecommunications [8–10]. Although the vertically aligned growth of MWNTs on flat substrates has been reported [11,12], that of SWNTs has not been reported. In the case of SWNTs, only an alignment that is parallel to the substrate plane has been achieved by the application of a strong electric or magnetic field [13–15]. To date, several innovative applications using vertically aligned MWNT films such as a field emission source [11] or a toxic gas sensor [16] have been reported. However, using SWNTs instead of MWNTs for these applications is desirable because the former have several superior electrical/mechanical properties in addition to structural perfection.

This chapter reports the achievement, for the first time, of vertically aligned growth of SWNTs on a flat substrate with the CVD process. Initially, the morphology and quality of the aligned SWNTs are investigated by FE-SEM, HR-TEM, and resonant Raman scattering (RRS) analysis. This chapter also shows that the RRS spectra of vertically aligned SWNTs exhibit a characteristic spectral shape that originates due to their aligned morphology. Finally, the growth and alignment formation processes of the vertically aligned SWNT film with respect to CVD reaction time is investigated by optical absorption and FE-SEM observations. A model for the growth process of the vertically aligned SWNT film is formulated based on the measured optical absorption characteristics, using which the growth of the aligned SWNT film will be discussed.

3.2 Experimental and analysis procedures

The catalyst preparation procedure and the CVD process are essentially the same as those presented in Section 2.3. After an as-delivered quartz substrate with both sides optically polished (Fujitok #19983, 25 × 25 × 0.5 mm) is baked for 5 min in air at 500°C, bimetallic Co-Mo catalyst is supported on the substrate by dip coating its acetate solution. Subsequently, the substrate is heated in air at 400°C to decompose these acetates into metal oxides, which are reduced in the CVD chamber during the heating of an electric furnace with an Ar/H_2 (3% H_2) flow of 300 sccm; this is done so that the catalytic activity is retrieved. When the SWNT growth temperature is attained in the electric furnace, the supply of Ar/H_2 gas can be cut off or the gas flow can be continued during the CVD reaction. The effect of the Ar/H_2 gas flow during the CVD reaction will be investigated in the next section.

All the CVD experiments in this chapter were performed at 800°C under an ethanol vapor pressure of 10 Torr for 10 min, unless specified otherwise. The Ar/H_2 gas is supplied only during the heating stage and is cut off during the CVD reaction, unless specified otherwise. The flow rate of the Ar/H_2 gas during the heating stage is 300 sccm under a pressure of 300 Torr. If Ar/H_2 is supplied during the CVD reaction, the flow rate remains at 300 sccm but the partial pressure is lowered to 7 Torr. To ensure reproducibility, the background pressure of the CVD chamber should be less than 2×10^{-2} Torr. The schematic of the CVD apparatus is presented in Fig. 2-15.

In order to obtain the microscopic characterizations of the SWNTs, an FE-SEM observation was performed with a Hitachi S-900 at 4 KV, a Hitachi S-4700 at 1 kV, or a Hitachi S-5200 at 2 kV. The HR-TEM observations were performed with a JEOL 2000EX at 120 kV.

For obtaining Raman scattering measurements, a micro-Raman setup (Seki Technotron STR-250) comprising an optical microscope (Olympus BX51), a spectrometer (Chromex 501is), and a CCD (Andor DV401-FI) was used. The measurements were conducted in the backscattering configuration with an incident laser power of 0.3–1.0 mW, a 50× objective lens, and a laser spot diameter of approximately 3–5 μm. Linearly polarized 488- (2.54 eV) and 514.5-nm (2.41 eV) laser lights were used. The scattered light was collected into the microscope, passed through a depolarizer, and finally, guided to the spectrometer.

3.3 Effect of CVD chamber vacuum on SWNT growth

First, it should be mentioned that the morphology and the growth speed of SWNTs largely depend on the cleanness of the CVD chamber just before the CVD process begins. Namely, the speed of vacuum deterioration by de-gas generation from the chamber wall, measured by a pilani gauge with the valve to the vacuum pump closed, is an important factor that controls the growth. Figure 3-1 shows the optical absorbance spectra of samples prepared at different de-gassing speeds $V_{\text{de-gas}}°$ [cm^3/sec] expressed in the equivalent speed at standard state (1 atm, 0°C). The volume of our CVD chamber is approximately 1000 cm^3. The resulting morphology (i.e., random or vertically aligned) are denoted for each spectrum and the magnitude of absorbance is a measure of the amount of SWNTs grown on the substrate. The morphology was random when the de-gas generation speed was high, as shown in Fig. 3-1(iii). On the other hand, when the de-gas generation was suppressed, SWNT growth increased and this lead to a vertical alignment of SWNTs, as shown in Fig. 3-1(i) or 3-1(ii). This result clearly reveals that de-gas generated from the CVD chamber wall poisoned the catalyst and thus lowered its activity. Hence, greater chamber cleanness

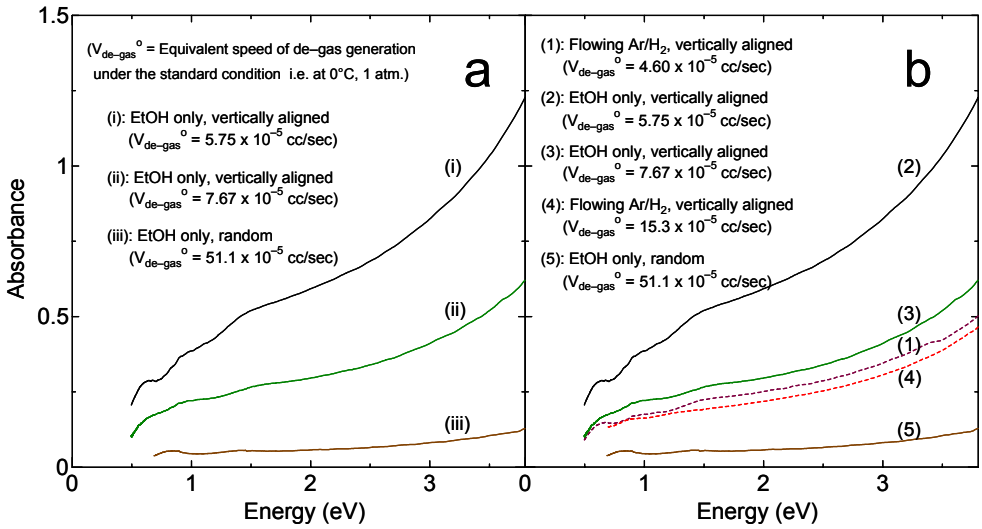


Fig. 3-1. (a) Optical absorption spectrum of SWNT films grown on quartz substrates either with (2,3,5) or without (1,4) flowing Ar/H_2 during CVD reaction. The Arabic number denotes order of cleanness of the CVD chamber. To each spectrum, the morphology of SWNT film (vertically aligned or random) and the de-gas generation speed $V_{\text{de-gas}}°$ [cm^3/sec] (see text for definition) is presented. (b) Selected presentation for the spectra measured from SWNT film grown without Ar/H_2 flow from the case of (a). To each spectrum (i-iii), the morphology of SWNT film and the vacuum deterioration speed is denoted.

is necessary for a higher degree of catalyst activity that is consequently required for the vertical alignment of SWNTs, as discussed below.

In Fig. 3-1b, the optical absorption spectra of SWNT films grown with a flow of Ar/H_2 during the CVD reaction are compared with those without a flow of Ar/H_2 (shown in Fig. 3-1a). The numbers in parentheses denote the order of chamber cleanness in these five experiments. When the cleanness is low, the flow of Ar/H_2 is thought to enhance the activity of the catalyst, presumably because H_2 acts as an anti-oxidation agent for de-gassing contaminations. However, when the chamber cleanness is high, the existence of H_2 decelerates the growth of SWNTs. This may be due to the fact that the strong adsorption of H_2 on the surface of transition metals [17] can reduce the active surface area of the catalyst.

The "vacuum deterioration" shown in Fig. 3-1 is considered to be caused by the generation of de-gases from the chamber wall and not by a leak in the chamber. This is because at this vacuum level, the deterioration speed can be lowered by evacuating the chamber with flowing several tens of sccm of Ar/H_2 for a few hours. We consistently used an oil-free pump (ULVAC DVS-321) for evacuation; this is because vertically aligned SWNT growth has not been achieved using an ordinary oil pump, presumably due to catalyst poisoning by the diffusion of oil-derived molecules into the CVD chamber.

3.4 Microscopic and optical analyses

3.4.1 Morphological investigations by FE-SEM and HR-TEM

Figure 3-2 shows cross-sectional images of the vertically aligned SWNT film grown on a quartz substrate acquired by a Hitachi FE-SEM S-900 at 4 kV at a tilted (upper row) and horizontal direction (lower row). The vertical alignment of SWNTs with an approximate height of 6 μm is observed along with their spatial uniformity. Typically, the film is optically uniform over the entire area of the substrate both in terms of appearance and the results of reflectance interferometry (data not shown). This alignment is believed to arise from the significantly high density of the SWNTs, as discussed below.

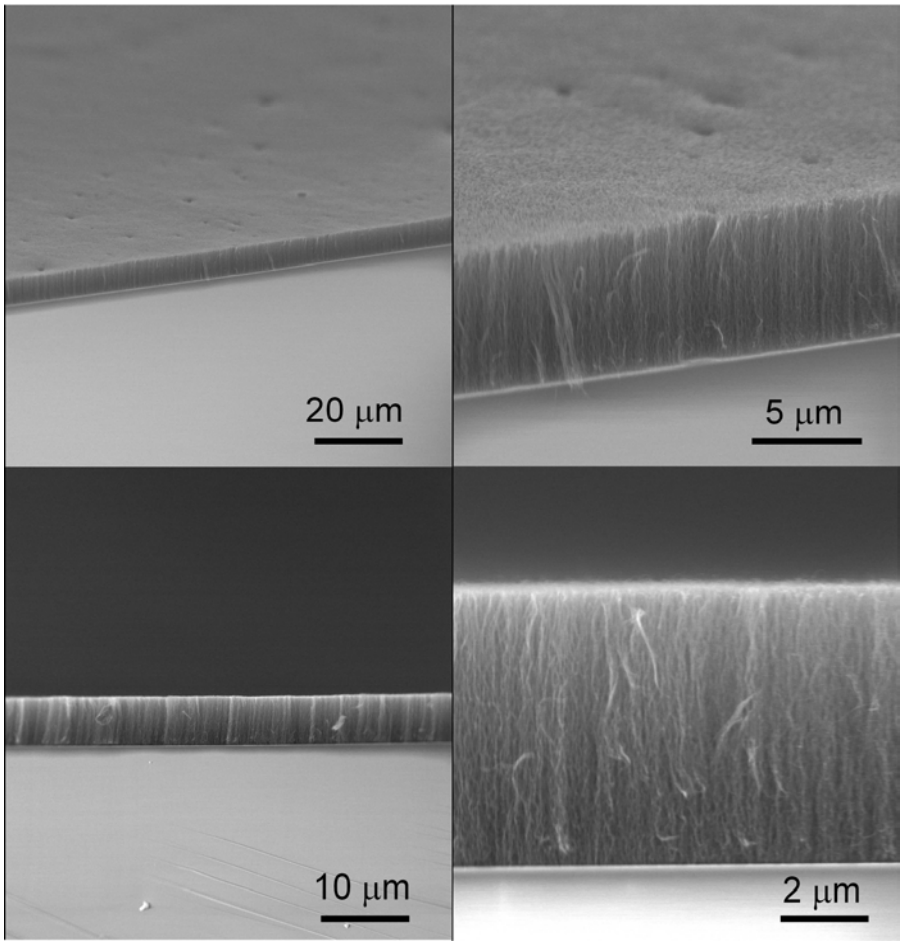


Fig. 3-2. Cross-sectional image of vertically aligned SWNT film with approximate thickness of 5 μm grown on a quartz substrate. The images were taken at fractured edge of the substrate by Hitachi FE-SEM S-900 at 4 kV, from tilted (upper row) and horizontal direction for the substrate (lower row).

Figure 3-3 shows higher magnification images of the vertically aligned film with an approximate thickness of 2 μm acquired by a Hitachi FE-SEM S-5200 at 2 kV for (a) the entire cross section, (b) the upper part of the film, (c) the mid cross section, and (d) the lower part of the film. Images (a), (b), and (d) are acquired at a 30° tilted angle from the horizon, and (c) is acquired from the horizontal direction. In the magnified image shown in Fig. 3-3c, most of the SWNTs are bundled and their typical diameter is ~15 nm. The degree of alignment as well as optical anisotropy in the film will be investigated and discussed in Section 4.1.

Figure 3-3d shows the morphology of the bottom of the SWNT film and clearly reveals that thinner bundles, with diameters of ~4 nm just above the substrate surface, coalesce into thicker bundles as the SWNTs grow away from the substrate. Furthermore, as shown in Fig. 3-3(d), it appears as though the roots of the SWNTs are pulled upward, presumably by an

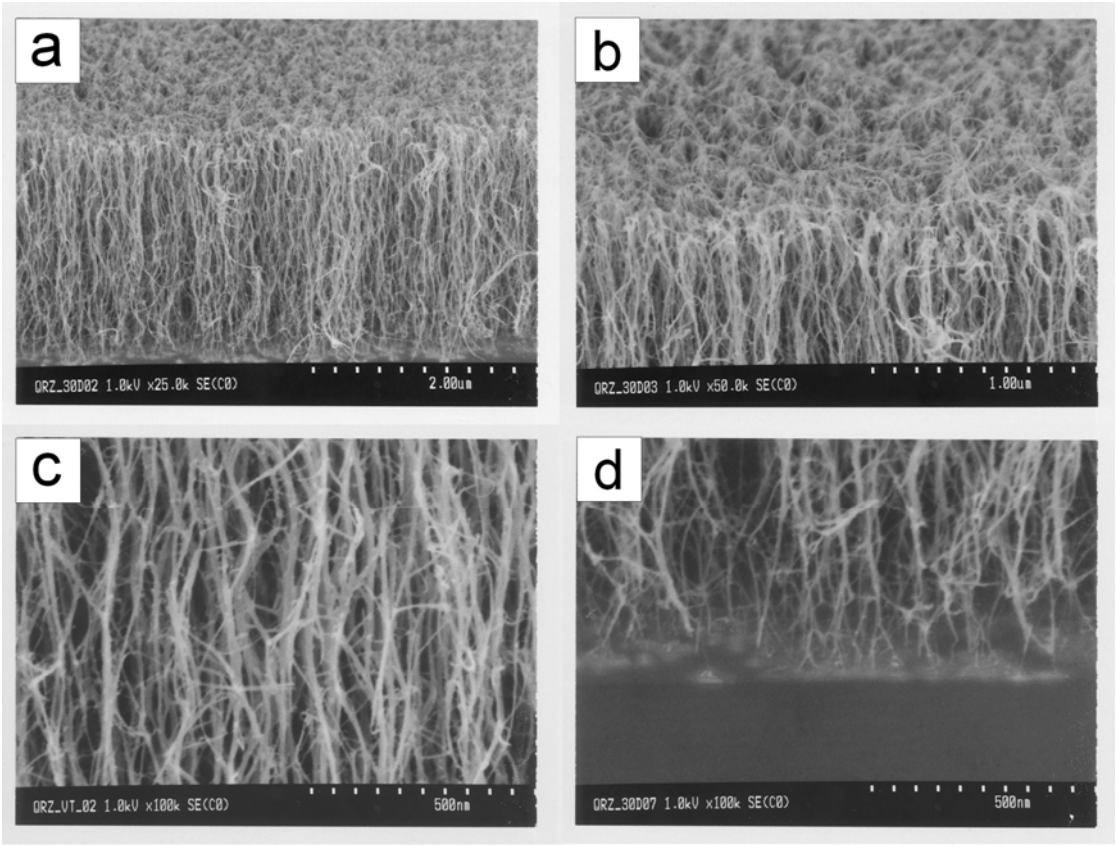


Fig. 3-3. High-magnification images of vertically aligned SWNT film with approximate thickness of 2 μm grown on a quartz substrate, for (a) whole cross-section, (b) upper part of the film, (c) mid cross-section, and (d) lower part of the film. The images were taken at fractured edge of the substrate by Hitachi FE-SEM S-5200 at 2 kV. Images (a, b, d) are taken from 30° from the substrate plane and (c) is taken from horizontal direction to the substrate.

internal frictional force among the SWNT bundles. This internal force is considered to originate from the difference in the catalyst activity at a later stage of the growth where the activity begins to deteriorate (refer to Section 3.6 for details). This is because a difference in catalyst activity can cause a difference in the extending speed depending on the SWNT bundle. Further, it should be noted that on the surface of the quartz substrate, aggregated metal particles that would be observed if the diameter exceeded 2–3 nm by FE-SEM S-5200 were not observed. This result is consistent with the HR-TEM image of the substrate surface shown in Section 2.4.

Figure 3-4 shows the HR-TEM image of the vertically aligned SWNT film. The film was weakly sonicated in methanol for 5–10 s and dropped onto a TEM microgrid. Observations were performed on the film fragments that retained their alignment to a large extent. Two types of film edges were observed. One is shown in Fig. 3-4a in which the degree of alignment is relatively high and almost no metallic particles were found among the SWNTs.

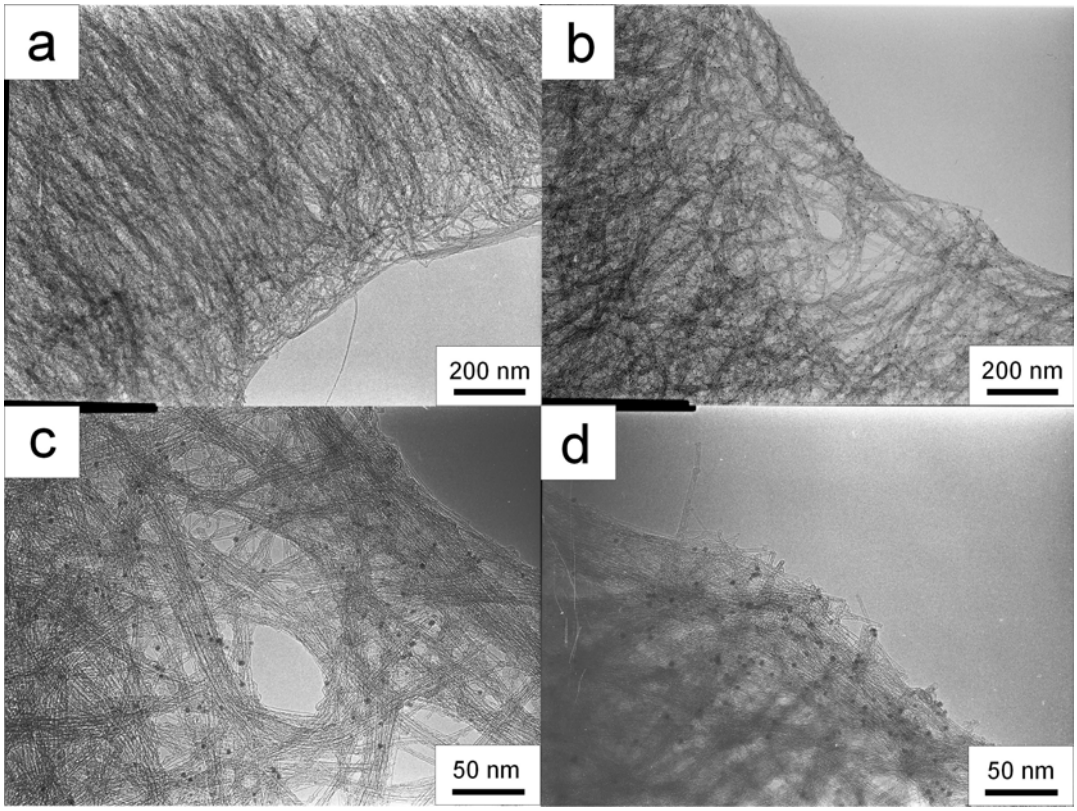


Fig. 3-4. HR-TEM images of a fragment of a vertically aligned SWNT film deposited on a TEM grid after a weak sonication in methanol for 5 - 10 s, taken by JEOL 2000EX at 120 kV. Images are those presumably correspond to (a) the upper side of the film and (b-d) lower side of the film, as observed by FE-SEM in Fig. 3-3. Panels (c, d) are the magnification from the edge observed in the panel (b).

The other type is shown in Fig. 3-4b, in which abundant particles were found among the SWNTs and the degree of alignment is less than that shown in Fig. 3-4a. Figure 3-4c and d are magnifications of the film fragment edge shown in Fig. 3-4b. These images revealed metallic particles with diameters of 2–3 nm, and they are considered to be cobalt carbide (Co_2C). However, a determination of the elemental composition of the particle using an experimental investigation technique such as EELS analysis is necessary for further discussion.

Figure 3-5 shows another HR-TEM image of the vertically aligned SWNT film. In this case, however, the film was directly rubbed onto a TEM microgrid (i.e., the film had not undergone dispersion in solvent) in order to precisely investigate the morphology and quality of the SWNTs. This observation was conducted in a manner similar for the case shown in Fig. 3-4 but at a higher magnification; the film fragment that retained alignment was found and investigated. Figure 3-5a shows the upper edge of the observed film

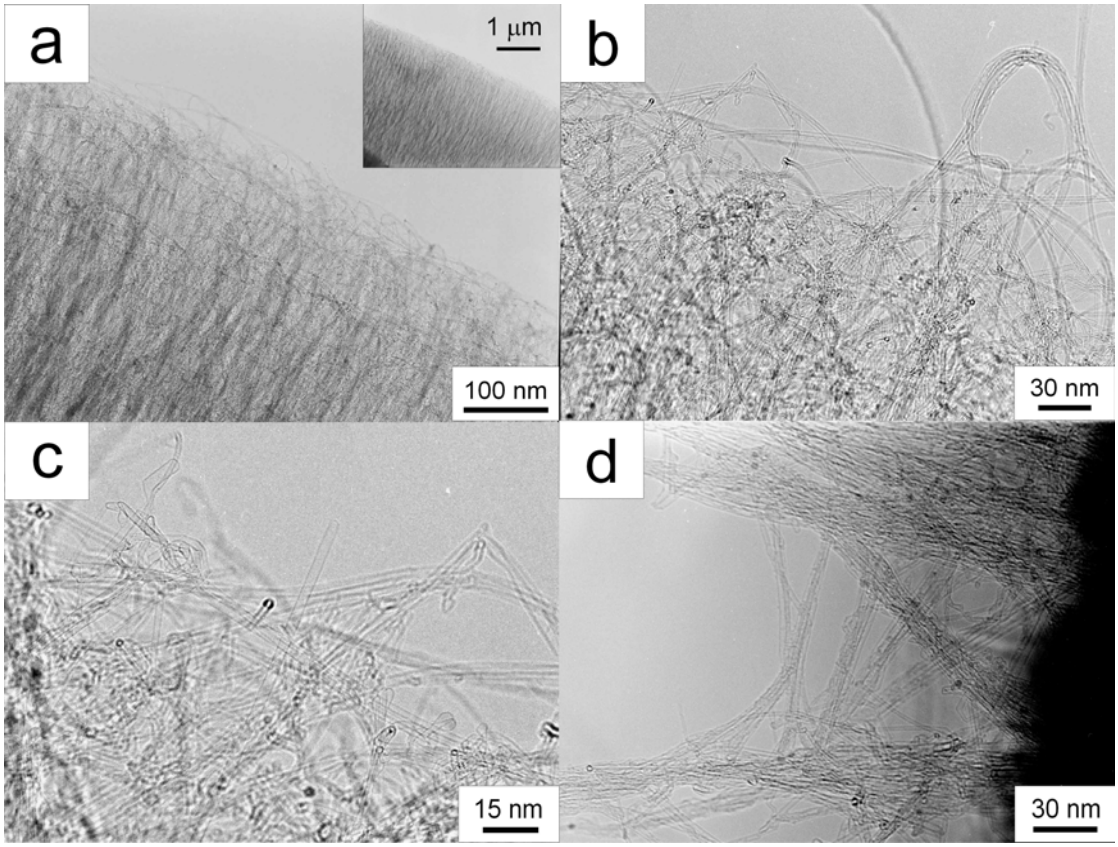


Fig. 3-5. HR-TEM images of a fragment of the vertically aligned SWNT film directly rubbed against a TEM grid, taken by JEOL 2000EX at 120 kV. Images are (a-c) Images are those presumably corresponds to (a-c) the top side of the film taken at various magnification, and (d) lower side of the film in which metal particles are observed among SWNTs.

fragment at a lower magnification, and the entire image of the film fragment is indicated in the inset. The morphology observed in Fig. 3-5a coincides with that of the upper side of the film observed by FE-SEM shown in Fig. 3-3b. Figure 3-5b is a magnification of the upper edge of Fig. 3-5a, where closed and empty SWNT ends are occasionally observed; these are further magnified in Fig. 3-5c. Similar to the case of Fig. 3-4, two types of edges in the film fragments were confirmed in the observation shown in Fig. 3-5, and one of these is shown in Fig. 3-5a, b, and c. The other type of edge is shown in Fig. 3-5d and is considered to be a peeled interface between the film and the substrate where the darkened area toward the right is the film, which is oriented perpendicular to the page. Particles with diameters of 2–3 nm are observed among the entangled SWNTs, as shown in Figs. 3-4c and 3-4d; these are considered to be Co_2C.

From the HR-TEM observations shown in Figs. 3-4 and 3-5, the growth of the SWNT film in the present study is ascribed to the base growth from the catalyst particles that remain on the substrate. These images, especially those observed for the film that did not undergo dispersion in the solvent, as shown in Fig. 3-5, indicate that each SWNT is sufficiently clean, i.e., virtually free from amorphous carbon and other impurities on the SWNT wall. No MWNTs were observed in repeated TEM observations whereas several double-walled carbon nanotubes (DWNTs) were found; however, their population is negligible compared with that of SWNTs. By measuring the diameter of more than 50 SWNTs, the diameter of the specimen was determined to be in the range of 0.8–3.0 nm with an average diameter d_{av} of ~1.9 nm and a standard deviation σ of ~0.4 nm. This diameter is larger when compared with that of typical CVD-grown SWNTs; in addition, the diameter distribution is broader.

3.4.2 Resonant Raman scattering analysis

In order to spectroscopically investigate the quality of the sample, Raman scattering measurement was performed on the vertically aligned (Fig. 3-6a, c) and the randomly oriented SWNT films (Fig. 3-6b, d) using 488- and 514.5-nm laser lights. The tangential modes of the 488-nm laser light including the D-band (~1350 cm^{-1}) and the G-band (~1593 cm^{-1}) are shown in the right panel. In all the measurements, the laser is incident perpendicular to the substrate, i.e., from the top of the film. The ratio of G- to D-bands is sufficiently high (25–35); therefore, the quality of the current sample is confirmed to be sufficiently high even in the pristine state.

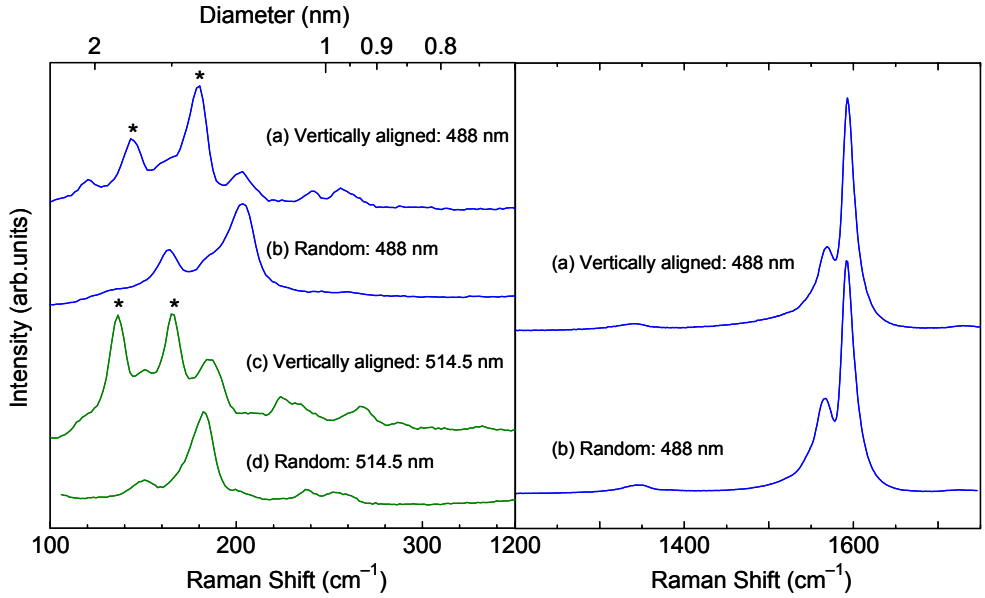


Fig. 3-6. Raman scattrering spectrum of (a, c) vertically aligned and (b, d) random SWNT film grown on quartz substrates measured with normal laser incidence to the substrate. The low frequency RBM is shown for both 488 and 514.5 nm in the left panel and higher frequency tangential modes are shown for 488 nm in the right panel. Asterisk denotes the RBM peak observed only when veritcally aligned SWNT is measured with perpendicularly polarized light to SWNT axis.

The difference in the spectra of "aligned" and "random" cases is partially due to the difference in the diameter distributions (d_{av} of the latter is ~1.3 nm, thinner than the former). However, it should be noted that the RBM peaks marked with "*" in the left panel are characteristically observed in vertically aligned SWNT films when the polarization direction of the incident light is perpendicular to the direction of SWNT alignment [18], which is investigated in detail in Section 4.2. These characteristic RBM peaks are suppressed when the alignment is mechanically disturbed, for example, by a tip of tweezers. Section 4.2 will discuss that these characteristic peaks can be explained by the resonance of $\Delta\mu = \pm 1$ excitation (μ denotes the cutting line index of the 2D Brillouin zone of graphite [19]) caused by the absorption of cross-polarized light [20,21]. Since the RBM peaks in 488 and 514.5 nm are highly sensitive to morphology, vertical alignment can be recognized by Raman scattering measurement without resorting to cross-sectional FE-SEM observation as was done for the case shown in Fig. 3-2. However, since the RBM spectral shape of SWNTs is highly affected by their physical and chemical environment in addition to the incident laser power [18], as shown in Section 4.2, a more stable and reproducible method for evaluating the morphology is required. Further, in Section 4.1, it will be shown that

optical absorption spectroscopy, which is generally simpler than Raman scattering measurement, is a strong tool for distinguishing or even quantitatively evaluating the morphology of SWNTs.

3.5 Discussion of vertical alignment formation in SWNTs

The differences in the growth amount and diameter distribution between the vertically aligned SWNT films and the randomly oriented films provide important insights into the reason that SWNTs could grow vertically from the substrate. An exceedingly higher amount of grown SWNTs in the case of vertical alignment was clarified by both FE-SEM observations (Figs. 3-2 and 3-3) and the difference in the magnitude of optical absorbance (Fig. 3-1). The increased average diameter and broader diameter distribution in the vertically grown SWNT film was demonstrated by both HR-TEM observation (Figs. 3-4 and 3-5) and Raman scattering analysis (Fig. 3-6).

The vertical alignment is considered to arise from the higher growth density of SWNTs, due to which the SWNTs grow into thicker and hence more mechanically rigid bundles by coalescing with each other as the growth proceeds, as shown in Fig. 3-3d. Consequently, those bundles are only able to grow away from the substrate because of physical interferences with the neighboring bundles.

Based on the foregoing investigations, it is deduced that the high amount of growth required for the vertical alignment of SWNTs is caused by the simultaneous achievement of 1) dense monodispersion of 1–2 nm Co catalyst particles supported by the dip-coat process and 2) high degree of activation of the catalyst as a result of improving the cleanness of the CVD chamber, which leads to the dense growth of SWNTs. The fine dispersion of the catalyst arises from the use of bimetallic Co-Mo acetate solution and the resulting catalyst stabilization by the $CoMoO_x$ layer, as discussed in Section 2.4. Hence, it is concluded that the augmentation and maintenance of catalyst activity by enhancing the chamber cleanness is essential for the alignment to enhance the catalyst activity. The increase in the diameter distribution observed in the unaligned case presented in Section 2.3 supports this conclusion.

Finally, in this section, the area densities of the catalyst particles and SWNTs are estimated and compared in order to evaluate the efficiency in the use of the catalyst. The catalyst density is directly obtained from the TEM image (Fig. 2-30), and it is

approximately 1.3×10^{17} [m^{-2}]. The approximate mass density of the film was estimated to be ~3.5×10^{-2} [g/cm^3] by comparing the weight of the substrate measured by a precision electric microbalance before and after removing the film from the substrate. Then the number density of SWNTs is calculated, assuming the SWNTs are (n, m) = (14, 14) tubes with diameter of 1.93 nm, to be ~0.85×10^{16} [m^{-2}]. This is approximately one-order lower density compared to that of the catalyst particles.

3.6 Transient investigations and modeling of growth process of vertically aligned SWNT films

3.6.1 Growth and formation process of vertically aligned SWNT film

A series of CVD experiments was performed for different CVD reaction times of 15, 30, 60, 180, 600, 1800, and 6000 s in order to investigate the growth process of the vertically aligned SWNTs. All the CVD conditions except the CVD reaction time were set to be the same in order to ensure inter-comparability. The speed of vacuum deterioration shown in Fig. 3-1 is also set to be the same: "2 $\rightarrow$ 5 Pa = 8 $\pm$ 1 min." In this series of experiments, the reaction temperature and ethanol pressure were selected as 800°C and 10 Torr, respectively, which are the standard CVD conditions used in this study. Figure 3-7 shows a cross-sectional FE-SEM image of the SWNT film from 15 to 600 s. The SWNT film is a mixture of random in the upper portion and weakly aligned in the lower portion at the time of 15 s, from which the alignment is gradually established as the reaction time proceeds. It should be noted that SWNTs are grown on the both sides of the substrate, and hence, the FE-SEM images in Fig 3-7 only show a half of the total thickness.

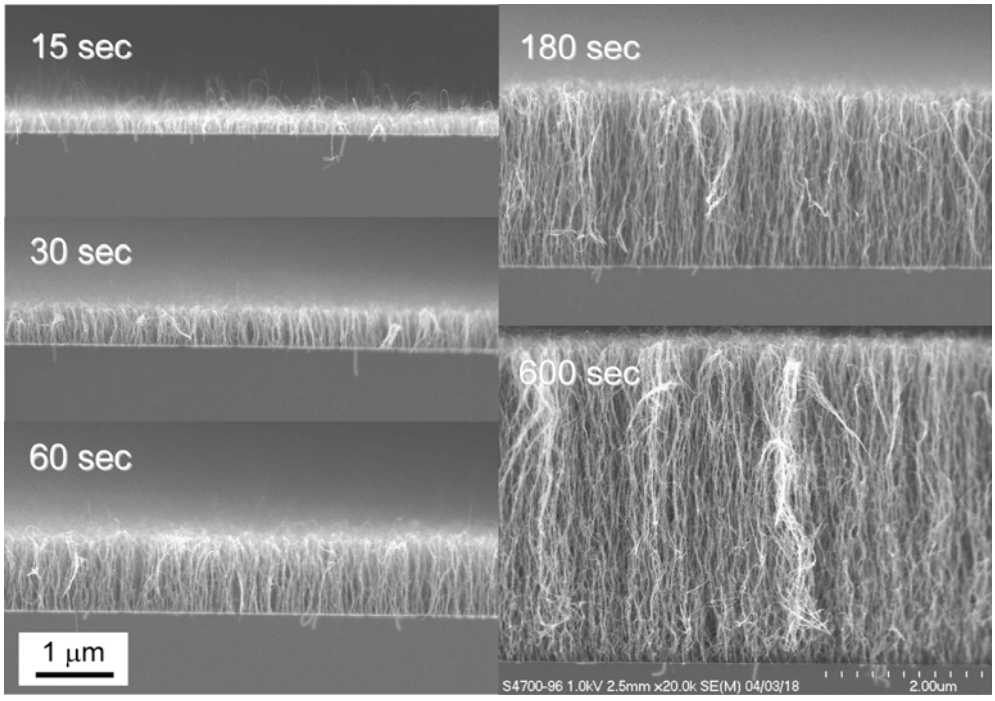


Fig. 3-7. Time-progressive growth observation of the vertically aligned SWNT film on quartz substrates by Hitachi FE-SEM S-4700 at 1 kV. The SWNT flim was grown on quartz substrates at various CVD reaction times, 15, 30, 60, 180, and 600 s. CVD reaction temperature and ethanol pressure were 800°C and 10 Torr, respectively.

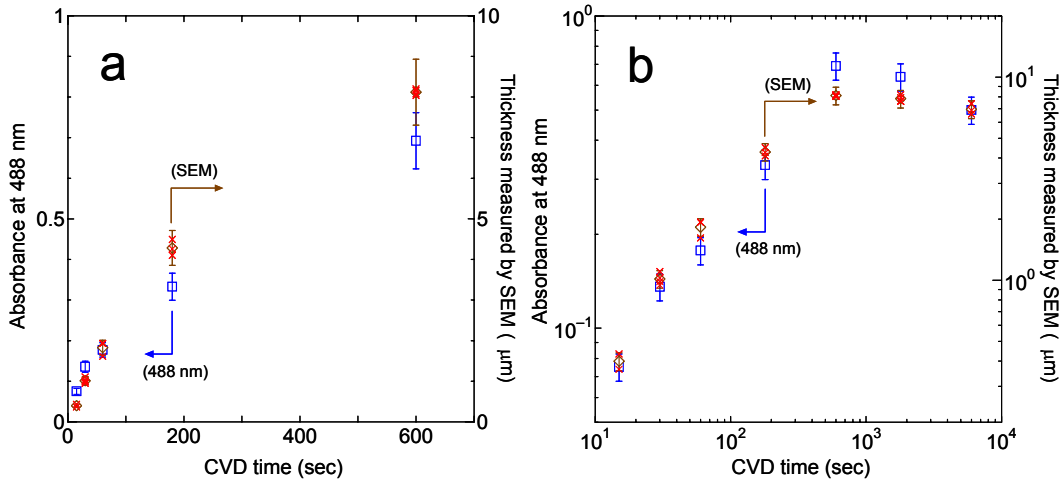


Fig. 3-8. Changes of optical absorbance at 488 nm (left ordinate) along with total film thickness measured by FE-SEM (right ordinate) plotted against CVD time taken in abscissa, represented by (a) linear scale for 15 - 600 s, or (b) logarithmic scale for 15 - 6000 s. The absorbance was measured with perpendicularly incident light to the substrate represented as square (□). Film thickness was measured by FE-SEM at several locations as each denoted by crosses (×), and the diamond (◊) denotes their averaged value.

Figure 3-8 shows the changes of the optical absorbance at 488 nm (left ordinate) and the total film thickness measured by FE-SEM (right ordinate) plotted against the CVD time in the abscissa. The absorbance was measured with a 488-nm light incident perpendicular to the substrate, which is represented as a square (□) in the figure. The measurements of the film thickness by FE-SEM were performed in multiple locations on the same sample, which are denoted by crosses (×); the diamond (◊) denotes their averaged value. While Fig. 3-8a shows the linear plots for 15–600 s corresponding to Fig. 3-7, Fig. 3-8b shows all the plots for 15–6000 s on a logarithmic scale. It should be noted that after 600 s, the growth eventually ceases; moreover, a slight decrease in the thickness is observed after 1800 s. This growth cessation is attributed to the loss of catalytic activity due to the imperfect vacuum in the chamber; this is because the final thickness of the film is directly dependent on the degree of vacuum, as confirmed in Fig. 3-1. The process for this growth cessation is quantitatively formulated and discussed in the following subsection. Since the current SWNT films are grown directly on quartz substrates, the morphology of these films can be conveniently probed by optical absorption measurements.

Figure 3-9 shows the ratio between the absorbance at 488 nm and the film thickness measured by FE-SEM (i.e., absorbance of the film per unit thickness), plotted against the CVD reaction time in the abscissa. This figure indicates a monotonous decrease of the

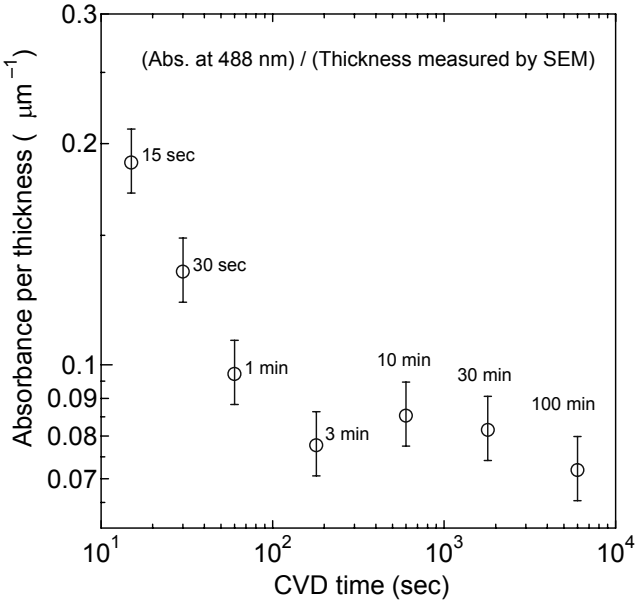


Fig. 3-9. Relationship between optical absorbance at 488 nm per unit film thickness an CVD reaction time, which is calculated from the result shown in Fig. 3-8b.

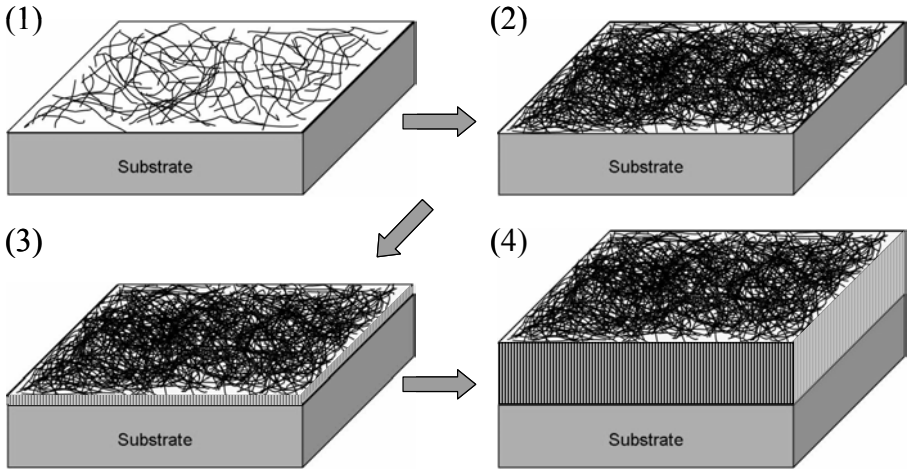


Fig. 3-10. Schematic for the growth and alignment formation process of the SWNTs directly grown on quartz substrates.

absorbance per unit film thickness with CVD reaction time. As investigated in detail in Section 4.1, the optical absorption cross section of SWNTs parallel to the axis is several factors of magnitude greater than that perpendicular to the axis. Therefore, the result shown in Fig. 3-9 clearly indicates that the degree of alignment is largely improved within the first 3 min of the CVD reaction. At ~3 min, the alignment is almost established after which the

optical nature of the film shows little variance, indicating the attainment of morphologically steady growth.

The FE-SEM observation confirmed that the morphology at a very early stage of the growth is quasi-2D along the substrate surface (shown in Fig. 3-18), as schematized in Fig. 3-10(1). The result shown in Fig 3-9 supports the following explanation of the growth process: As discussed previously in Section 3.5, the progression of the growth leads to the coalescence of SWNTs into bundles, as shown in Fig. 3-10(2). The entanglement and friction due to the bundle formation gradually immobilize each SWNT; however, while in this state, the carbon source reaches the catalyst located in the root of the SWNT. The high density of SWNTs, as well as the immobilization of an initial random layer, allows the SWNTs to only grow away from the substrate, which eventually configurates the vertical alignment of bundled SWNTs.

3.6.2 *In situ* measurement of growth process of vertically aligned SWNT film

In order to conduct an in-depth investigation of the growth process, *in situ* monitoring of the growth of the SWNT film was performed. As schematically described in Fig. 3-11, a 488-nm Ar^+ laser light is guided into the CVD chamber through an aperture (ϕ = 5 mm) created in the wall of the annular electric furnace, so that the laser light passes perpendicularly through the quartz substrate placed in the center of the chamber. The laser light leaves the chamber through an aperture on the opposite side of the wall, and its

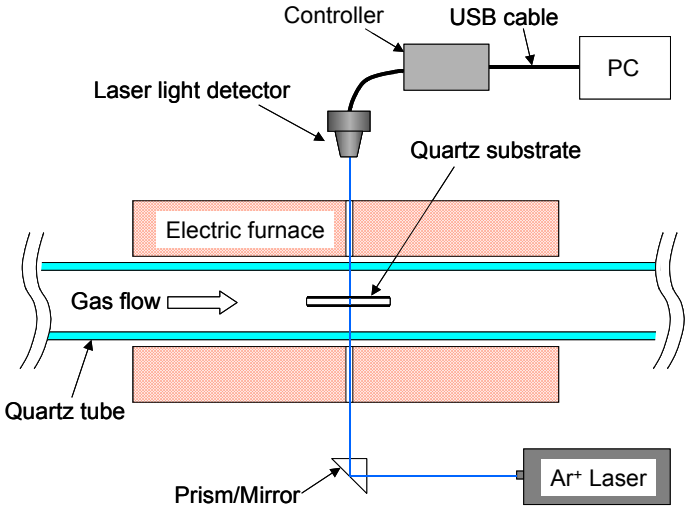


Fig. 3-11. Schematic description of in situ growth monitoring system by a real-time measurement on optical absorption of 488 nm laser light which is introduced into the CVD chamber.

intensity is measured by a laser light detector (Coherent, LM-2 VIS #33-0936-000) combined with a computer-based data-logging system (Coherent, LaserPAD #1008557). The attenuation in the laser intensity is used to calculate the absorbance of the sample for every time instant of the CVD reaction.

Figure 3-12 shows the changes of the light absorbance at 488 nm measured with respect to the CVD time for two different experiments, referred to as "A" and "B" in this section. The fundamental difference between these experiments lies in the catalyst activity before the CVD reaction, i.e., the chamber cleanness in "A" is higher than that in "B," as their detailed CVD conditions described in the figures. As recognized in Fig. 3-12, experiment "B" resulted in a higher yield of SWNTs than "A", and this is reflective of the difference in the catalyst activity. In order to quantitatively explain the shapes of the transitional curves shown in Fig. 3-12 (hereafter referred to as "growth curves"), several growth-limiting models were initially tested, such as 1) diffusion limit imposed on the carbon-source molecules that try to reach the catalyst as the film grows and 2) constant-speed deterioration of catalyst activity due to the background pressure of impurity-gas species. However, it appears that these models cannot quantitatively explain the shape of the growth curve shown in Fig. 3-12. Another reasonable possibility is a growth limitation imposed by the deterioration of catalyst activity caused by the decomposition of the carbon source molecules themselves. This possibility will be investigated in the next subsection.

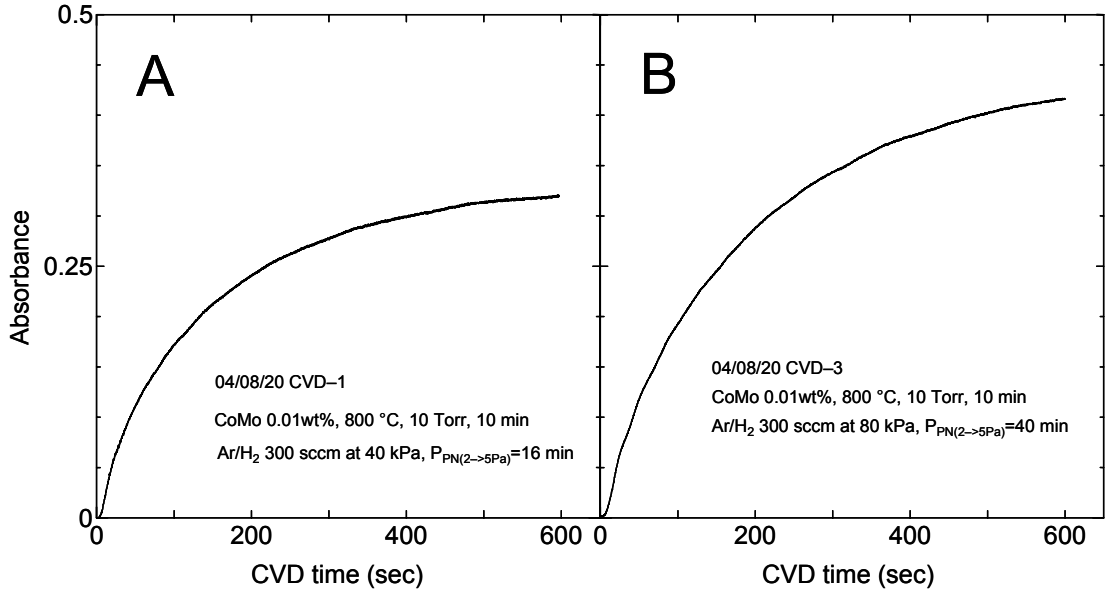


Fig. 3-12. *In situ* measurements of optical absorbance of 488 nm laser light by catalyst supporting quartz substrates for 10 min CVD processes. Two experiments 'A' and 'B' were performed at different chamber cleanness, whose details are described in the figures.

3.6.3 Formulation for growth process of vertically aligned SWNT film

Catalyst activity $\eta(t)$ [mol/m^{2}s] is defined as the ability of catalyst within 1 m^2 on the substrate to separate C atoms during unit time at time t. The initial catalyst activity is denoted as $\eta(0) = \eta_0$. The molar number of the C atoms that were separated as SWNTs at time t per 1 m^2 is denoted as $M(t)$ [mol/m^2]. That is,

$$\frac{dM}{dt} = \eta \tag{1}$$

Here, it is postulated that the deterioration of η per unit time is proportional to the molar number of the separated C atoms within the unit time, and the proportionality constant linking them is denoted as κ [s^{-1}], which represents the time constant for catalyst deactivation, or

$$-\frac{d\eta}{dt} = \kappa\frac{dM}{dt} = \kappa\eta \tag{2}$$

Hence, $M(t)$ is written as

$$M = \frac{\eta_0}{\kappa}\left(1 - \mathrm{e}^{-\kappa t}\right) \tag{3}$$

Further, *active period* τ [s] is defined as

$$\tau = \kappa^{-1} \tag{4}$$

Under this postulation, the total molar number of the separated C atoms during the CVD process is equal to $\eta_0\tau$, regardless of the CVD process.

The optical absorbance A is defined by the molar optical absorption cross section ε [m^2/mol], the molar concentration of optical absorbent specie, [J] [mol/m^3], and the thickness of the sample, l [m], as

$$A = \varepsilon \cdot [J] \cdot l \tag{5}$$

Since [J] is assumed to be constant along the thickness of the film, [J]·l [mol/m^2] is equal to $M(t)$ [mol/m^2]. Further, since ε is considered to be a function of t until vertical alignment is established (See Fig. 3-9), Eq. 5 can be rewritten as

$$A(t) = \varepsilon(t) \cdot M(t) \tag{6}$$

The product ε[J] represents the absorbance per unit thickness of the film. If it is denoted as $s(t)$, Eq. 5 can also be written as

$$A(t) = s(t) \cdot l(t) \tag{7}$$

The experimentally measurable values are $A(t)$ and $s(t)$; therefore, $\varepsilon(t)$, $l(t)$, and $M(t)$ should be treated as unknowns

The molar concentration of the C atom per unit area per unit film thickness *after* the establishment of the alignment, $[J]_\infty$, is estimated to be ~3.0×10^3 [mol/m^3] (~3.5×10^{-2} [g/cm^3]). This value is obtained by comparing the weight of the substrate measured by our precision electric microbalance before and after removing the film from the substrate. Using this value, the final thickness of the film, l_∞ [m], at $t \to \infty$ can be expressed as

$$l_\infty \approx 3.3\times10^{-4}\frac{\eta_0}{\kappa} = 3.3\times10^{-4}\eta_0\tau \qquad (8)$$

Figure 3-13a, which is a partial presentation of Fig. 3-9 corresponding to below 10 min, indicates the absorbance at 488 nm per unit thickness of the film, $s(t)$, vs. the CVD time t measured from a series of experiments performed under almost the same vacuum deterioration speed of "2 $\rightarrow$ 5 Pa = 8 ± 1 min." However, in general, the catalyst activity and the growth speed are largely affected by the vacuum deterioration speed, as discussed in Section 3.3. Therefore, Fig. 3-13a does not represent a universal process for the alignment formation. A universal process for the formation, in order to be independent of both η_0 and κ, is obtained by expressing it as shown in Fig. 3-13b in which the absorbance at 488 nm is indicated in the abscissa. This figure represents the absorbance per unit film thickness at a specific absorbance, which would be universal if the SWNT film finally achieves the morphologically steady state (i.e., the state in which the vertical alignment is established; refer to Fig. 3-9). From Fig. 3-13b, it can be recognized that the absorption per

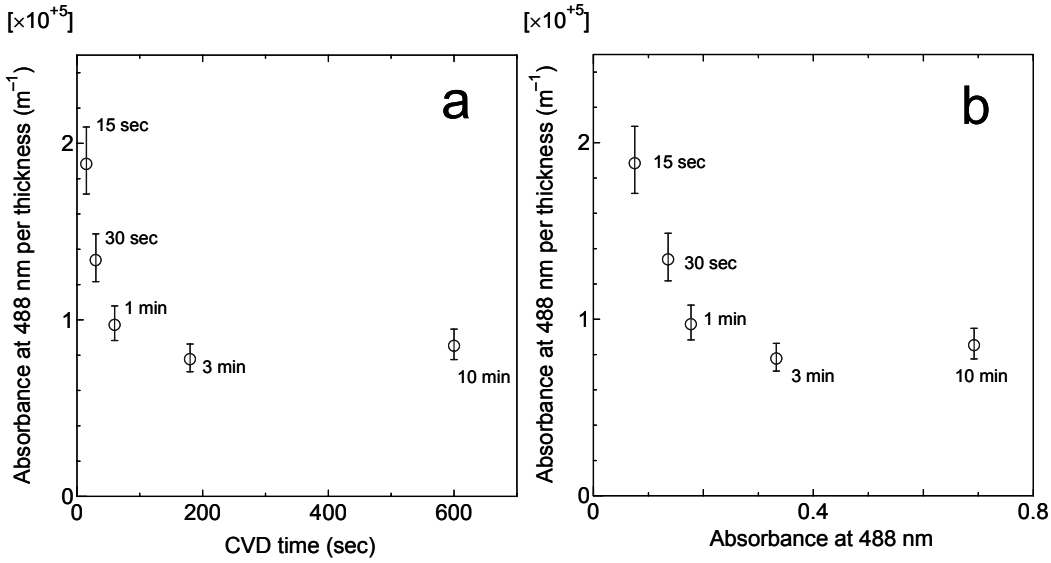


Fig. 3-13. (a) Partial presentation of Fig. 3-9 for below 10 min and (b) that re-plotted for the relationship between optical absorbance per thickness of the film and the absorbance at 488 nm.

unit film thickness $s(A)$ decreases monotonically until A is ~0.3, and subsequently, a steady state $s(A)_{A\to\infty} \equiv s_\infty \approx 8.4 \times 10^4$ [m^{-1}] is attained.

The plots in Figure 3-14 are identical to those in Fig. 3-13b but with the addition of two functional lines described as follows. The morphology at $t = 0$ is considered to be random, and there exists a constant initial value $s(0) = \varepsilon_{\text{random}} \cdot [J]_{\text{random}}$ corresponding to the initial state. Two test cases, denoted as "Case 1" and "Case 2," are introduced and indicated with a solid line and broken line, respectively, in Fig. 3-14. These lines represent two extreme cases that are expected from the experimentally measured plots. and are chosen so that $s(0)$ and $s(\infty)$ are exponentially related as

$$s(A) = s_\infty \left[1 + \frac{X}{\exp\{Y(A - Z)\} + 1} \right] \tag{9}$$

Here X, Y, and Z are constants: $X = 1.45$, $Y = 37.1$, and $Z = 0.123$ for "Case 1" and $X = 3.03$, $Y = 22.0$, and $Z = 0.065$ for "Case 2". It is obvious that the functional form of Eq. 9 does not have any physical meaning, except that it is a reasonable expression connecting two states $s(0)$ and $s(\infty)$. However, the choice of such functional expression would be irrelevant if the current model were to explain the measured phenomena regardless of the difference between "Case 1" and "Case 2."

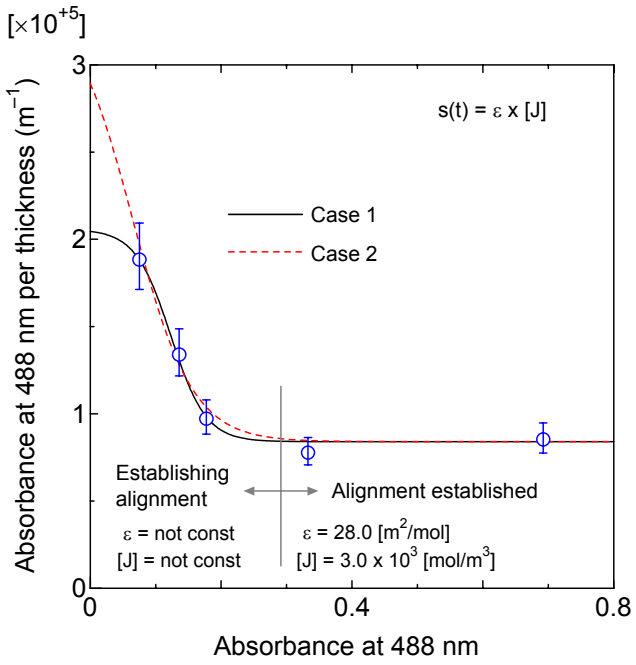


Fig. 3-14. Re-presentation of Fig. 5-12b with two functional lines, 'Case 1' (solid line) and 'Case 2' (dotted line), which are described by Eq. 9.

Prior to calculating $M(t)$ from Eq. 6, $\varepsilon(t)$ should be determined. In this study, it is reasonable to consider that although an optical absorption by van Hove singularities is suggested by the eDOS intensity of SWNTs, the optical absorption at 488 nm (2.54 eV) is primarily due to the baseline extended from higher energy (~5 eV) absorption features whose intensity is dependent on the molar number of the contained C atom. This will be described in detail in Section 4.1.

Since s is a product of ε and $[J]$, it is not possible to extract only ε from Fig. 3-14. Although $\varepsilon_{t\to\infty} = 28.0$ [m^2/mol] is calculated from the measurement, $\varepsilon_{t\to 0}$ (= $\varepsilon_{A\to 0}$) has to be calculated by some method. In the following paragraphs, a method of calculating $\varepsilon(A)$ that describes the initial growth stage of the SWNT film will be briefly presented.

First, Λ_0 denotes the optical absorbance of linearly polarized light whose polarization is parallel to the SWNT axis by collinear transition dipole moments of ideally aligned (i.e., no physical disturbance) SWNTs. Although transition dipoles exist *perpendicular* to the SWNT axis as presented in Section 4.1, they are not considered here because of their weaker strength. Further, the measured absorbance by normally ($\theta = 0$) and tangentially ($\theta = 90°$) incident p-polarized lights on the substrate are denoted as $\Lambda'_{\perp}$ and $\Lambda'_{\parallel}$, respectively, as schematized in Fig. 3-15.

Figure 3-16 presents the optical absorbance at 488, 633, and 1000 nm measured from the sample shown in Figs. 3-7 to 3-9 as "3 min" by changing the incident angle θ to the substrate. The absorbance in the ordinate is normalized by the $\cos^{-1}\theta$ increment of the

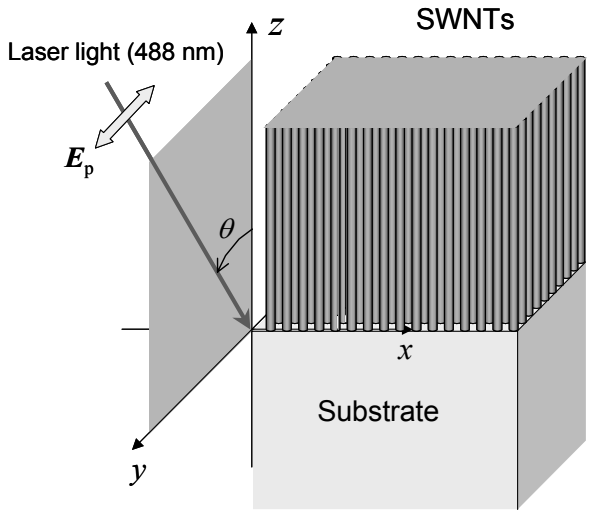


Fig. 3-15. Schematic drawing of p-polarized light incidence onto the vertically aligned SWNT film on a quartz substrate at an angle of θ. $\boldsymbol{E}_p$ denotes electronic vector of the p-polarized light to the substrate.

light-path length, and each series of measured points fit well with the $\sin^2\theta$ curves. $\Lambda'_{\perp}$ corresponds to the absorbance at $\theta = 0$ and $\Lambda'_{\parallel}$ corresponds to the extrapolated absorbance at $\theta = 90°$, using which the total absorbance Λ_0 is expressed as

$$\Lambda_0 = \Lambda'_{\parallel} + 2\Lambda'_{\perp} \tag{10}$$

The 3D-wise (Fig. 3-17a) and 2D-wise (Fig. 3-17b) initial morphologies are envisaged as two extreme cases. In reality, the initial state lies somewhere in between these two cases. In the following expressions, the parameters at the initial, 3 min, and steady state are denoted by the subscripts "$t\to 0$," "t = 3min," and "$t\to\infty$," respectively. From Fig. 3-16, $\Lambda'_{\perp,t=3\text{min}}$ and $\Lambda'_{\parallel,t=3\text{min}}$ are observed to be 0.39 and 1.00, respectively; the hypothetical absorbance of the film in 3D-wise and 2D-wise random morphology, $\Lambda_{\text{random,3D},t=3\text{min}}$ and $\Lambda_{\text{random,2D},t=3\text{min}}$, respectively, at 3 min are expressed as

$$\Lambda_{\text{random,3D},t=3\,\text{min}} = \frac{1}{3}\Lambda_{0,t=3\,\text{min}} = \frac{1}{3}\left\{\Lambda'_{\parallel,t=3\,\text{min}} + 2\Lambda'_{\perp,t=3\,\text{min}}\right\} = 0.593 \tag{11}$$

$$\Lambda_{\text{random,2D},t=3\,\text{min}} = \frac{1}{2}\Lambda_{0,t=3\,\text{min}} = \frac{1}{2}\left\{\Lambda'_{\parallel,t=3\,\text{min}} + \Lambda'_{\perp,t=3\,\text{min}}\right\} = 0.89 \tag{12}$$

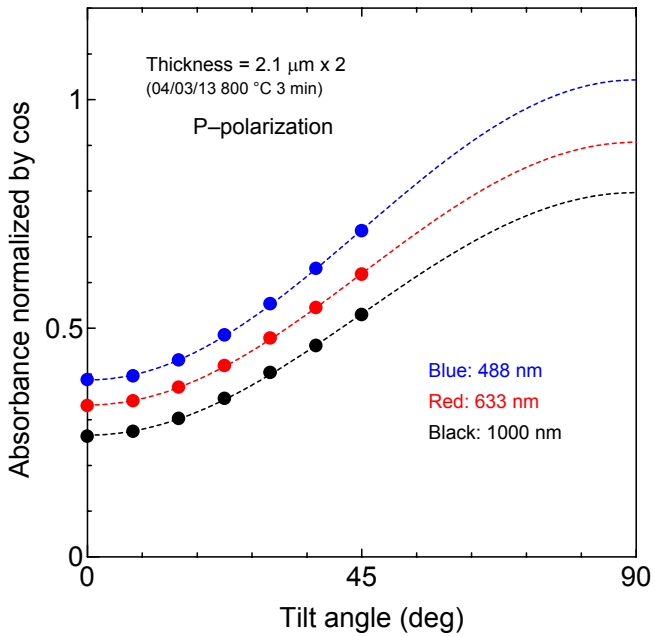


Fig. 3-16. Dependence of optical absorbance at 488, 633 and 1000 nm measured for the sample shown in . Figs. 3-7 - 3-9 as "3 min", on incident angle of the light θ to the substrate. Absorbance in ordinate is normalized by $\cos^{-1}\theta$ increment of the light path length and each series of measured points are fitted with $\sin^2\theta$ curves.

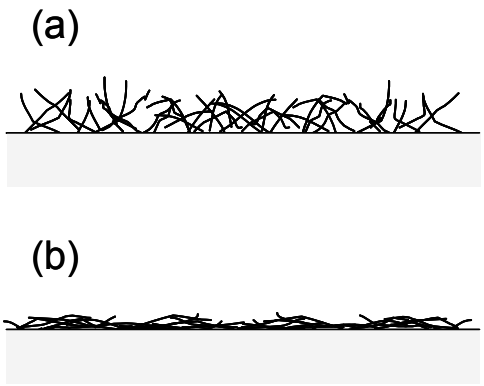


Fig. 3-17. Schematic descriptions of (a) 3D-wise and (b) 2D-wise random morphology of the SWNT films grown on quartz substrates.

Since the morphology reaches its steady state at 3 min, the relationship

$$\Lambda_{\text{random,3D},t=3\,\text{min}} \frac{M_{t\to 0}}{M_{t=3\,\text{min}}} < \Lambda'_{\perp,t\to 0} < \Lambda_{\text{random,2D},t=3\,\text{min}} \frac{M_{t\to 0}}{M_{t=3\,\text{min}}} \tag{13}$$

is obtained. If this is divided by $\Lambda'_{\perp,t=3\text{min}}$,

$$\frac{\Lambda_{\text{random,3D},t=3\,\text{min}}}{\Lambda'_{\perp,t=3\,\text{min}}} < \frac{\Lambda'_{\perp,t\to 0} \dfrac{M_{t=3\,\text{min}}}{M_{t\to 0}}}{\Lambda'_{\perp,t=3\,\text{min}}} < \frac{\Lambda_{\text{random,2D},t=3\,\text{min}}}{\Lambda'_{\perp,t=3\,\text{min}}} \tag{14}$$

$$\Leftrightarrow \frac{\Lambda_{\text{random,3D},t=3\,\text{min}}}{\Lambda'_{\perp,t=3\,\text{min}}} < \frac{\varepsilon_{\perp,t\to 0}[J]_{t\to 0} l_{t\to 0} \dfrac{M_{t=3\,\text{min}}}{M_{t\to 0}}}{\varepsilon_{\perp,t=3\,\text{min}}[J]_{t=3\,\text{min}} l_{t=3\,\text{min}}} < \frac{\Lambda_{\text{random,2D},t=3\,\text{min}}}{\Lambda'_{\perp,t=3\,\text{min}}} \tag{15}$$

Using the relationships $\varepsilon_{\perp,t=3\text{min}} = \varepsilon_{\perp,t\to\infty}$ and $M = \varepsilon \cdot [J]$, Eq. 15 is rewritten as

$$1.52 < \frac{\varepsilon_{\perp,t\to 0}}{\varepsilon_{\perp,t\to\infty}} < 2.28 \tag{16}$$

which represents the possible range of the ratios between $\varepsilon_{\perp,t\to 0}$ and $\varepsilon_{\perp,t\to\infty}$.

ε and $[J]$ could not explicitly be distinguished in Fig. 3-14; however, if both parameters are assumed to vary in a manner so as to maintain the ratio $\varepsilon \cdot [J]$ almost constant, Eqs. 9 and 16 give

$$\varepsilon(A) = \varepsilon_{\perp,t\to\infty}\left[1 + \frac{X'}{\exp\{Y(A-Z)\}+1}\right] \tag{17}$$

It should be noted that $\varepsilon_{\perp,t\to\infty}$ is an experimentally measured constant (= 28.0 [m^2/mol]) and X' is a constant determined solely from the experimentally obtained relation Eq. 16 as

$$\text{Case}\,1 : 0.525 < X' < 1.29, \quad \text{Case}\,2 : 0.644 < X' < 1.59 \tag{18}$$

It should be repeated that the parameters Y and Z were provided in the context of Eq. 9 to represent "Case 1" and "Case 2," shown in Fig. 3-14. By substituting Eq. 17 into Eq. 6 and using Eq. 3, the following expression is obtained.

$$A = \varepsilon_{\infty}\left[1+\frac{X'}{\exp\{Y(A-Z)\}+1}\right]\cdot\frac{\eta_0}{\kappa}\left(1-\mathrm{e}^{-\kappa t}\right) \tag{19}$$

Here, $\varepsilon_{\perp,t\to\infty}$ was rewritten as ε_{∞}. This equation is implicit for A but explicit for t; this can be solved for t as

$$t = -\frac{1}{\kappa}\ln\left\{1-\frac{A}{\frac{\eta_0\varepsilon_{\infty}}{\kappa}\left\{1+\frac{X'}{\exp\{Y(A-Z)\}+1}\right\}}\right\} \tag{20}$$

It should be reiterated that the parameters X', Y, Z, and ε_{∞} are experimentally determined parameters from either Fig. 3-14 or Fig. 3-16, not fitting parameters. Only η_0 and κ, which are physically evident as introduced in Eqs. 1 and 2, are used as the fitting variables to explain the observed phenomena.

Figure 3-18 shows the growth curves calculated from Eq. 20 for "Case 1," in which η_0 and κ were selected so that the calculated growth curve (dotted line) is the best match for the measured curve (solid line) presented in Fig. 3-12 for both experiments "A" and "B." $\{\eta_0 = 7.58 \times 10^{-5}$ [mol/m^{2}s], $\kappa = 6.49 \times 10^{-3}$ [s^{-1}] ($\Leftrightarrow$ $\tau = 154$ [s])$\}$ and $\{\eta_0 = 8.67 \times 10^{-5}$ [mol/m^{2}s], $\kappa = 5.64 \times 10^{-3}$ [s^{-1}] ($\Leftrightarrow$ $\tau = 177$ [s])$\}$ were obtained for experiments "A" and "B," respectively, that best fit the measured growth curves. The upper row (lower row) of Fig. 3-18 corresponds to the assumption of 3D-wise (2D wise) morphology at the initial growth stage, as schematized in Fig. 3-17. Importantly, when a 2D-wise initial morphology is assumed, the current model overestimates the optical absorbance at the initial growth stage, while under the assumption of 3D-wise initial growth, the calculated growth curve displays an excellent agreement with the measured curve.

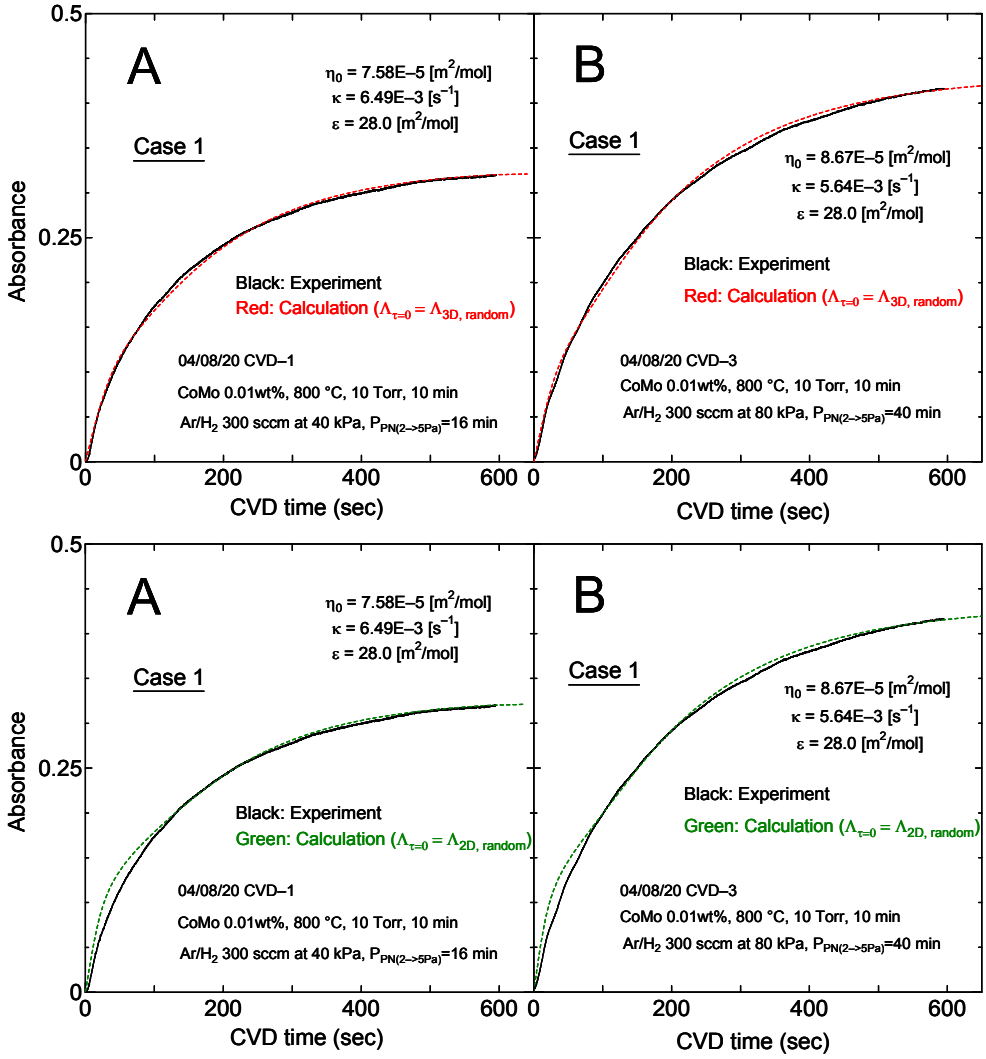


Fig. 3-18. Growth curves calculated from Eq. 20 for the experiments 'A' and 'B' in case of 'Case 1' (dotted lines), along with the experimentally measured curves shown in Fig. 3-12 (solid lines). η_0 and κ were chosen to be $\eta_0 = 7.58 \times 10^{-5}$ [mol/ m^2 s], $\kappa = 6.49 \times 10^{-3}$ [s^{-1}] for experiment 'A', and $\eta_0 = 8.67 \times 10^{-5}$ [mol/ m^2 s], $\kappa = 5.64 \times 10^{-3}$ [s^{-1}] for experiment 'B'. The upper row written in red (The lower low written in green) corresponds to the assumption of 3D-wise (2D-wise) random morphology at initial stage of the growth.

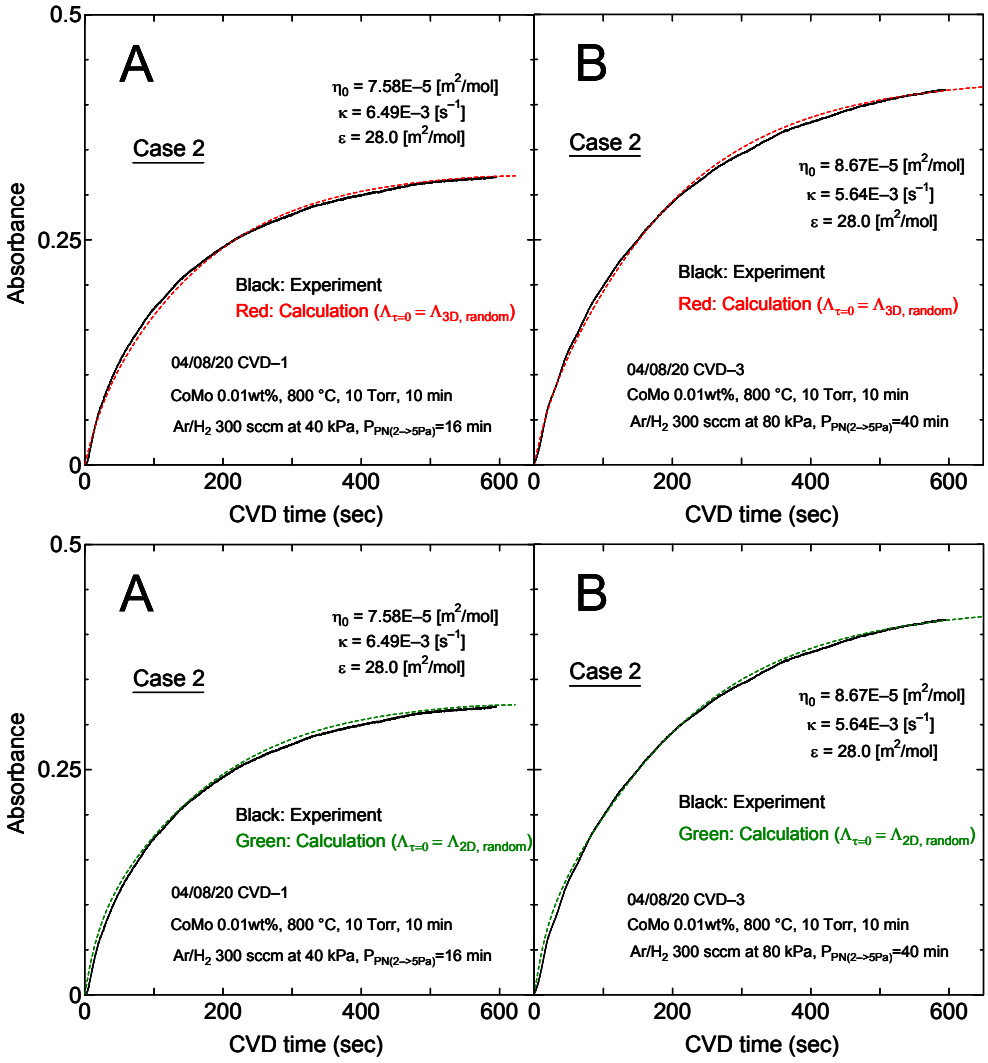


Fig. 3-19. Growth curves calculated from Eq. 20 for the experiments 'A' and 'B' in case of 'Case 2' (dotted lines), along with the experimentally measured curves shown in Fig. 3-12 (solid lines). η_0 and κ are the same as those employed in the case of Fig. 3-18. Upper row, written in red (lower low written in green) corresponds to the assumption of 3D-wise (2D wise) random morphology at initial stage of the growth, similarly to the case of Fig. 3-18.

Figure 3-19 shows the growth curves calculated from Eq. 20 for experiments "A" and "B" for "Case 2." In the calculation, η_0 and κ were the same as those used in Fig. 3-18. Further, in this case, the calculated curve (dotted line) and the measured curve (solid line) agree excellently in the case of 3D-wise initial morphology, while the calculated absorbance exceeds the measured value at an earlier growth stage in the case of 2D initial

morphology. Two important conclusions are derived from the results shown in Figs. 3-18 and 3-19. First, the current model agrees well with the measured growth curve *regardless of* the two extreme assumptions "Case 1" and "Case 2" shown in Fig. 3-14. This implies that this model has only two physically-clear variables η_0 (initial catalyst activity) and κ (deactivation constant for catalyst) as the control parameters. Second, the initial morphology is deduced to be rather close to 3D-wise randomness because this agrees well with the behavior of the measured absorbance at the initial growth stage.

This discussion on the initial morphology of the SWNT film is supported by the FE-SEM observations shown in Fig. 3-20, which shows the morphology at a very early stage of the growth. This figure reveals that even when the thickness is ~30 nm, SWNTs and their bundles start to stand up and grow away from the substrate, although the measured absorbance A at this point is merely ~0.002. Even in the slightly developed case when the film thickness is ~150 nm, the morphology is clearly close to that of 3D wise and the measured absorbance was only 0.07. Therefore, these FE-SEM observations support the idea that with the exception of the very early stage of the growth in which the optical absorbance is virtually negligible, the initial morphology in the context of this study can be regarded as 3D-wise random, as indicated by Fig. 3-17a or 3-20. This indicates that the upper rows of Figs. 3-18 and 3-19 should be considered, in which the growth curves are well explained by only the two physically clear parameters η_0 and κ introduced in the present model.

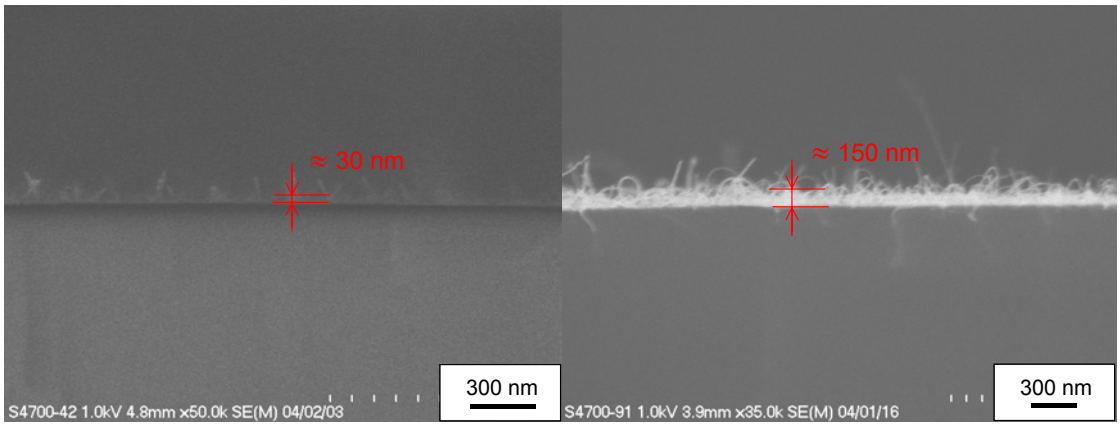


Fig. 3-20. Initial morphology of the SWNT films observed by Hitachi FE-SEM S-4700 at 1 kV. Film thickness in the right and left panels are ~ 30 and ~ 150 nm whose optical absorbance at 488 nm are ~ 0.002 and 0.07, respectively.

Using the current model, the final achievable absorbance A_∞ and thickness l_∞ that are finally achieved are calculated from the expressions,

$$A_\infty = \varepsilon_\infty \frac{\eta_0}{\kappa}, \quad l_\infty = \varepsilon_\infty \frac{\eta_0}{\kappa} \cdot \frac{1}{s(\infty)} \qquad (21)$$

from Eq. 20. A_∞ and l_∞ for experiments "A" and "B" are then predicted from Eq. 21 to be

$$A_\infty = 0.33, \quad l_\infty = 3.85\,[\mu\mathrm{m}] \quad (\text{experiment 'A'})$$
$$A_\infty = 0.43, \quad l_\infty = 5.07\,[\mu\mathrm{m}] \quad (\text{experiment 'B'})$$

Since l_∞ denotes the sum of the film thickness on both sides of the substrate, the thickness *per side* would be 1.93 and 2.53 μm for experiments "A" and "B," respectively.

3.7 Summary of Chapter 3

This chapter demonstrated the possibility of growing vertically aligned SWNTs on flat substrates under the optimized CVD condition by the alcohol CCVD method and the highly monodispersed Co catalyst described in Chapter 2. It was observed that the cleanness of the CVD chamber, which highly affects the speed of catalyst deactivation, is an important factor that controls the resultant morphology and the amount of SWNT growth. The morphology and quality of the aligned SWNT film were investigated by FE-SEM, HR-TEM, and Raman scattering analyses, from which the high selectivity and quality of the synthesized SWNTs were confirmed. The mechanism of vertical growth was discussed in terms of both microscopic and optical absorption measurements. The SWNT film developed in this study can be used in various applications and augments the possibility of SWNT-based devices that have thus far been proposed using randomly oriented SWNTs deposited on a substrate. This method is also suitable to obtain SWNTs with nearly constant lengths defined by the thickness of the aligned SWNT film.

In order to further investigate the growth process of the aligned SWNT film, *in situ* growth measurement was performed by monitoring the optical absorbance of the substrate with a laser detection system incorporated into the CVD apparatus. Growth models were proposed and it was suggested that the growth curve was explained by two controlling factors, initial catalyst activity η_0 and deactivation constant for catalyst κ. This model predicts that the total amount of SWNTs grown is determined by a single index η_0/κ (= $\eta_0 \cdot \tau$) independent of the CVD process if the reaction temperature is the same, which should be verified by further investigations. It was explained that the degree of the chamber

cleanness and that of catalyst reduction are strongly correlated to the resultant η_0 and κ values; however, their physical/chemical origins have not been elucidated in this chapter. Investigations on the dependences of η_0 and κ values on the reaction temperature and pressure would assist in elucidating these origins. In essence, "η_0/κ" should be enhanced with avoiding catalyst deactivation in order to achieve further thicker growth of the vertically aligned SWNT films.

Acknowledgements for Chapter 3

The author would like to thank Prof. T. Okubo and Mr. T. Sugawara at The Univ. Tokyo for the use of FE-SEM Hitachi S-900 in Fig. 3-2, Mr. S. Watanabe, Ms. M. Nakagawa, Mr. R. Tamochi at Hitachi Science Systems Ltd. and K. Shibata at Hitachi High-Technology Corp. for the observation by FE-SEM Hitachi S-5200 in Fig. 3-3, Mr. H. Tsunakawa at The Univ. Tokyo for his assistances in TEM observation in Figs. 3-4 and 3-5, Mr. T. Nishii at J-Power Co. Ltd. for the use of FE-SEM Hitachi S-4700 in Figs. 3-7 and 3-20. Part of this Chapter has been published in *Chemical Physics Letters*, vol. 385, pp. 298-303, 2004 by Y. Murakami, S. Chiashi, Y. Miyauchi, M. Hu, M. Ogura, T. Okubo, and S. Maruyama.

References for Chapter 3

1. A. Thess, R. Lee, P. Nikolaev, H. Dai, P. Petit, J. Robert, C. Xu, Y.H. Lee, S.G. Kim, A.G. Rinzler, D.T. Colbert, G.E. Scuseria, D. Tománek, J.E. Fischer, R.E. Smalley, Science **273** (1996) 483.
2. M.J. Bronikowski, P.A. Willis, D.T. Colbert, K.A. Smith, R.E. Smalley, J. Vac. Sci. Technol. A **19** (2001) 1800.
3. P. Avouris, Chem. Phys. **281** (2002) 429.
4. J.A. Misewich, R. Martel, P. Avouris, J.C. Tsang, S. Heinze, J. Tersoff, Science **300** (2003) 783.
5. M. Freitag, Y. Martin, J.A. Misewich, R. Martel, P. Avouris, Nano Lett. **3** (2003) 1067.
6. T. Someya, J. Small, P. Kim, C. Nuckolls, J.T. Yardley, Nano Lett. **3** (2003) 877.

7. J. Li, Y. Lu, Q. Ye, M. Cinke, J. Han, M. Meyyappan, Nano Lett. **3** (2003) 929.

8. Y.C. Chen, N.R. Raravikar, L.S. Schadler, P.M. Ajayan, Y.P. Zhao, T.M. Lu, G.C. Wang, X.C. Zhang, Appl. Phys. Lett. **81** (2002) 975.

9. Y. Sakakibara, S. Tatsuura, H. Kataura, M. Tokumoto, Y. Achiba, Jpn. J. Appl. Phys. **42** (2003) L494.

10. S. Yamashita, Y. Inoue, S. Maruyama, Y. Murakami, H. Yamaguchi, M. Jablonski, S.Y. Set, Opt Lett. **29** (2004) 1581.

11. S. Fan, M.G. Chapline, N.R. Franklin, T.W. Tombler, A.M. Cassell, H. Dai, Science **283** (1999) 512.

12. B.Q. Wei, R. Vajtai, Y. Jung, J. Ward, R. Zhang, G. Ramanath, P.M. Ajayan, Nature **416** (2002) 495.

13. Y. Zhang, A. Chang, J. Cao, Q. Wang, W. Kim, Y. Li, N. Morris, E. Yenilmez, J. Kong, H. Dai, Appl. Phys. Lett. **79** (2001) 3155.

14. E. Joselevich, C.M. Lieber, Nano Lett. **2** (2002) 1137.

15. J.E. Fischer, W. Zhou, J. Vavro, M.C. Llaguno, C. Guthy, R. Haggenmueller, M.J. Casavant, D.E. Walters, R.E. Smalley, J. Appl. Phys. **93** (2003) 2157.

16. A. Modi, N. Koratkar, E. Lass, B. Wei, P.M. Ajayan, Nature **424** (2003) 171.

17. P.W. Atkins, *Physical Chemistry 6th Ed.*, W.H. Freeman & Co., New York, 1997.

18. Y. Murakami, S. Chiashi, E. Einarsson, S. Maruyama, Phys. Rev. B in press.

19. R. Saito, G. Dresselhaus, M.S. Dresselhaus, *Physical Properties of Carbon Nanotubes*, Imperial College Press, London, 1998.

20. H. Ajiki and T. Ando, Physica B **201** (1994) 349.

21. A. Grüneis, R. Saito, G.G. Samsonidze, T. Kimura, M.A. Pimenta, A. Jorio, A.G. Souza Filho, G. Dresselhaus, M.S. Dresselhaus, Phys. Rev. B **67** (2003) 165402.

Chapter 4:
Anisotropic optical properties of SWNTs and their optical applications

4.1 Determination of optical anisotropy of the vertically aligned SWNT film and optical absorption cross-section of SWNTs

4.1.1 Research background for polarized optical properties of SWNTs

Single-walled carbon nanotubes (SWNTs) are a new group of carbon material possessing one-dimensional cylindrical geometry formed by rolling-up an sp^2-bonded graphene sheet [1]. Their 1D structure and nanoscale diameter give rise to quantization of wave vectors in the circumferential direction, and strong divergences in the electronic density of states (eDOS) known as van Hove singularities (See Chapter 1), which formulate discrete energy levels or "subbands" in the eDOS of SWNTs [2]. The energies of these subbands are solely determined by the chirality of the SWNT, resulting in unique properties that make SWNTs an important candidate for various electronic and optical applications [3-9]. In particular, since the inter-subband gap energies correspond to infrared to visible light, and are roughly tunable by the diameter, several innovative optical applications such as saturable absorbers for all-optic telecommunication devices [5-7], ultra-small infrared photo-emitters [8] and photo-detectors [9] have been recently proposed. The 1D shape of a SWNT would be more advantageous in polarization-sensitive optical devices, provided a sound understanding of its anisotropic optical properties.

Despite the significant potential of SWNTs, there have been quite few experimental studies on the fundamental optical absorption properties of SWNTs which can provide confirmation of earlier theoretical works in the inter-subband [10] and higher energy regions [11,12]. So far, measurements of the optical anisotropy of aligned SWNTs embedded within a polymer matrix have been reported, [13,14] in addition to a recent investigation of the anisotropic optical absorption cross-section by Islam et al. using magnetically aligned SWNTs in gel [15]. However, all of these studies were limited to less than 3.5 eV mainly because of UV absorption of the employed polymers, hence no report has presented polarized optical absorption properties of SWNTs for higher energy. The elucidation of absorption properties in this region containing the π-plasmon around 5 eV, is urgent because they form the baselines in the inter-subband region that are of interest in many optical measurements and applications.

In this Section, anisotropic optical absorption properties of SWNTs for the energy range 0.5 - 6 eV were investigated by polarized optical absorption measurements of the vertically aligned SWNT film grown on an optically polished quartz substrate [16] shown in Chapter 3. In addition to inter-subband absorption below 3 eV, this study presents for the first time

the remarkable polarization dependence of absorption peaks at 4.5 eV and 5.25 eV. Furthermore, the important relevance of these absorption peaks of SWNTs to the optical properties of graphite, which have not yet been fully elucidated, is revealed. In the end, a method for determining a nematic order parameter for an aligned SWNT film by separating the collinear absorption peak at 4.5 eV from other transition dipoles is introduced, followed by determination the optical absorption cross-section of the SWNTs.

4.1.2 Experimental and optical measurement setup

A vertically aligned SWNT film is synthesized on both sides of a 25 × 25 × 0.5 mm optically polished quartz substrate from dip-coat supported Co catalyst [16] using the alcohol CCVD method [17], as presented in previous Chapter 3. The film consists only of SWNTs that are sufficiently clean, i.e. contain virtually no amorphous carbon and no multi-walled carbon nanotubes, as confirmed by resonant Raman scattering (G/D ratio > 25) [16] and high-resolution transmission electron microscopy (HR-TEM) [18]. From measurements of diameters of more than 50 SWNTs by HR-TEM, it was confirmed that the diameter ranges between 0.8 and 3.0 nm with an average of ~ 2.0 nm and a standard deviation of ~ 0.4 nm [18], which is a relatively broad diameter distribution. According to further FE-SEM observations, most SWNTs in the film form bundles with a typical diameter of ~15 nm.

For optical absorption measurements, a UV-vis-NIR spectrophotometer (Shimadzu UV-3150) with a rotating substrate holder (Shimadzu 206-22620-91) set behind a UV-vis-NIR polarizer in the sample light path was used. The reference light path remained blank. After baseline acquisition with both light paths blank, we scanned from 200 - 2500 nm at a specified incident angle (θ) and polarization toward the substrate (s or p). $\theta = 0$ is defined for normal incidence to the substrate. By convention, incident light is s-polarized (p-polarized) when its electric field vector is perpendicular (parallel) to the plane of incidence. It was confirmed that the reflectance baseline of the bare quartz substrate for $0° < \theta < 45°$ is quite exiguous, contributing to a measured absorbance of less than 0.03 for p- and 0.06 for s-polarizations, although corrections for this contribution have been made in the following results.

4.1.3 Dependence of optical absorption spectrum on SWNT morphology

In Section 4.2, the morphological dependence of the RRS spectrum from SWNTs will be presented, using which the morphological difference between random and aligned films can be discerned. However, as shown in Section 4.2.3, since the shape of the RBM spectra is remarkably affected by the physical and chemical environment of SWNTs and the power of incident laser, a more reproducible method for morphological evaluation is required. The following subsections will show that optical absorption spectroscopy, which is generally simpler than Raman scattering measurement, is a strong tool for distinguishing or even quantitatively evaluating the morphology of SWNTs.

Figure 4-1 shows the optical absorption spectra of the sample corresponding to Fig. 3-1 for 0.5–6 eV with an arbitrary ordinate. It should be noted that the difference in the absorption at approximately 5 eV shows a strong dependence on the morphology of the sample. The results indicate that when the SWNTs are randomly grown on the substrate, the peak at ~4.5 eV is dominant, and when they are vertically aligned, the peak at ~5.25 eV becomes dominant. The spectrum (iv) in Fig. 4b was measured from the sample with considerable non-uniformity in which both random and aligned domains coexist, and both two distinct peaks at ~4.5 and 5.25 eV are observed. This implies that the morphology of SWNTs is indicated by the optical absorption spectrum at ~5 eV; this is investigated in greater detail in the following subsections.

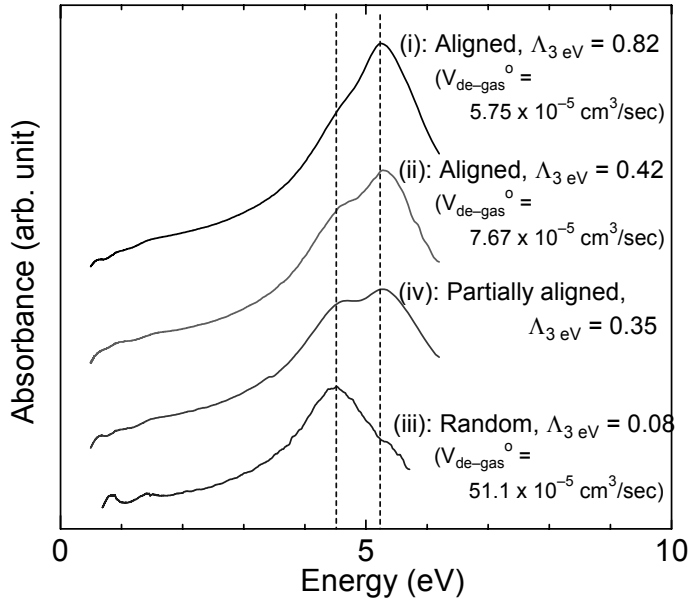


Fig. 4-1. Absorption spectra for different SWNT film morphology in which the film is (i, ii) vertically aligned, (iii) random, and (iv) partially aligned with spatial non-uniformity. $\Lambda_{3\,eV}$ denotes absorbance at 3 eV. In parenthesis denotes the de-gassing speed $V_{de\text{-}gas}°$ that was defined in Section 3.3.

4.1.4 Polarized optical absorption of vertically aligned SWNT film

Figure 4-2 shows polarized absorption spectra from the aligned SWNT film for s- and p-polarized light normalized by the $\cos^{-1}\theta$ increment of the light path length. The angle θ was changed from 0° to 45° in increments of 7.5°. The SWNT film used for measurements has a thickness of 2.1 μm per side, hence a total thickness of 4.2 μm. The examined specimen is identical to that presented in the Fig. 5-7 as "180 sec", and employed Figs. 3-7 - 3-9. In the case of s-polarization, dominant absorption by non-collinear dipoles perpendicular to the SWNT axis, and weaker collinear dipole absorption arising from disorder in the alignment, result in an absorption spectrum that is independent of θ. The case of p-polarization, on the other hand, shows a clear anisotropy, reflecting a dominance of absorption by collinear dipoles parallel to the SWNT axis. In the lower energy region (< 3 eV), structure from resonant inter-subband absorption for $\Delta\mu = 0$ transitions (where μ denotes the cutting-line index in the 2D Brillouin zone of graphite [2]) is observed as absorption maxima. These peaks are the first (~0.64 eV) and second (~0.93 eV) subband gaps in a semiconducting SWNT and the first gap (~1.45 eV) in a metallic SWNT, the energies of which correspond to SWNTs with a diameter of ~ 1.9 nm [19].

Most noticeable is the polarization dependence of the peaks at 4.5 and 5.25 eV. These absorption peaks have been observed in several studies of randomly oriented SWNT films

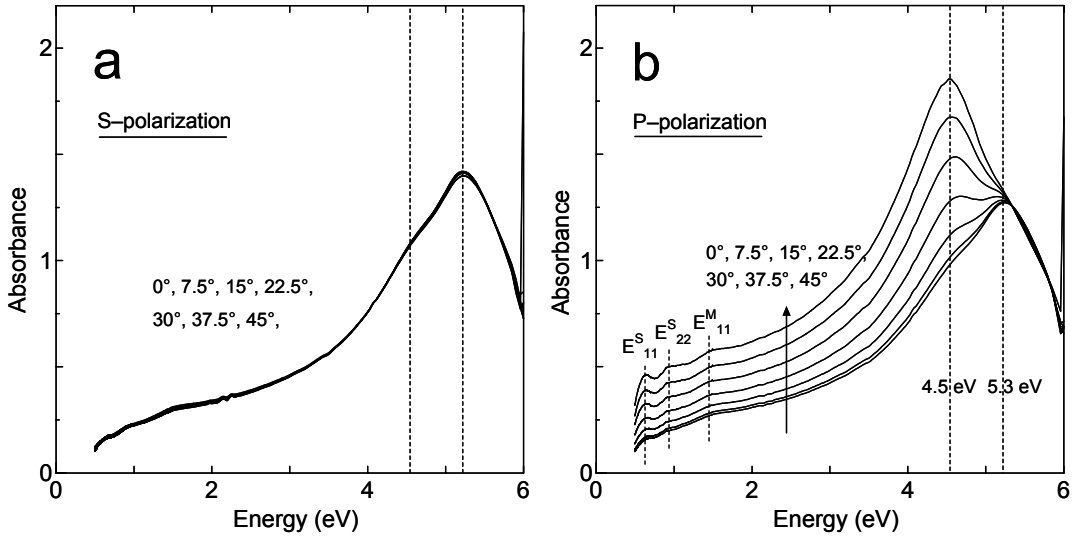


Fig. 4-2. Absorption spectra of 4.2 μm-thick (2.1 μm on one side) vertically aligned SWNT film measured with (a) s- and (b) p-polarization toward the substrate. Incident angle of the light is varied from the normal incidence θ = 0° to 45° at a step of 7.5° corresponding to the spectrum from bottom to top. All spectra are normalized by $\cos^{-1}\theta$ increment of the light path length. Perpendicular dotted lines indicate locations of inter-subband absorption of E^S_{11}, E^S_{22}, E^M_{11}, and of absorptions at 4.5 eV and 5.25 eV, from left to right.

[20-23] but considerable disagreements are found among the discussions. Kataura et al. [20] attributed the peak at 4.5 eV to π-plasmon absorption observed in a purified SWNT film while the 5.2 eV peak was only seen in the pristine sample containing amorphous carbon. Pichler et al. [21] stated from their EELS measurements on purified SWNTs that the 5.2 eV peak observed at low electron momentum transfer was due to a π-plasmon along the SWNT axis. Reed and Sarikaya, however, performed EELS on purified SWNTs in a TEM [22], and showed that a peak at 4.2-4.5 eV was measured for 'aloof' incidence of the electron beam, while the peak at ~5.2 eV was observed when the beam penetrated the center of an isolated SWNT. They explained these peaks as surface (4.2-4.5 eV) and bulk (~5.2 eV) π-plasmon excitations.

4.1.5 Anisotropic optical properties of graphite

Apart from SWNTs, it is known that absorption at ~4.5 eV is commonly observed in graphitic materials [24-26]. It is known that the imaginary part of the dielectric function for graphite in the direction perpendicular to the *c*-axis Im$\{\varepsilon_{\perp}\}$ has a maximum at 4.5 eV [27,28], whereas the maximum of the EELS function in the same direction Im$\{-\varepsilon_{\perp}^{-1}\}$ is found at ~ 7 eV as shown in Fig. 4-3 that is constructed based on the reflectivity data taken by Venghaus [30] from EELS measurement on stripped pyrolytic graphite. In the direction parallel to the *c*-axis, however, the optical properties of graphite have not yet been fully elucidated because of difficulties in preparing good optical surfaces parallel to the *c*-axis [27,29]. Nonetheless, according to EELS data by Venghaus [30] measured from 2 - 18 eV shown in Fig. 6-3, the maximum in Im$\{-\varepsilon_{\parallel}^{-1}\}$ appears at ~5.2 eV, and a broad maximum in Im$\{\varepsilon_{\parallel}\}$ at ~ 4.0 eV [27,28].

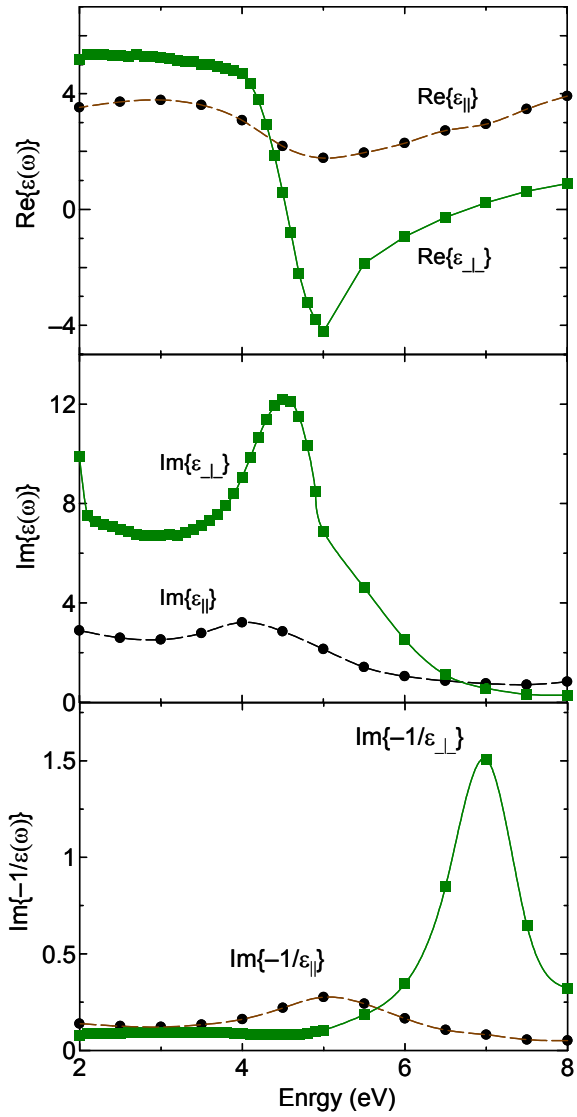


Fig. 4-3. Real (Re$\{\varepsilon\}$) and imaginary part of dielectric functions (Im$\{\varepsilon\}$), and EELS function (Im$\{-\varepsilon^{-1}\}$) of graphite for the direction both parallel (||) and perpendicular ($\perp$) to the *c*-axis. This figure was constructed based on the refractivity data presented in *Handbooks of Optical Constants of Solids II* [27] whose original data were taken by H. Venghaus by EELS measurement on stripped pyrolytic graphite at 60 keV [30].

From the fact that these two peaks are observed at almost the same positions regardless of the diameter and SWNT preparation method [18,20-23], it is reasonably deduced that the observed peaks at 4.5 and 5.25 eV in Fig. 4-2 originate from the optical properties of graphite, and that they correspond to the maxima in Im$\{\varepsilon_{\perp}\}$ (parallel to SWNT axis) and Im$\{-\varepsilon_{\|}^{-1}\}$(perpendicular to SWNT axis), respectively. We found that similar polarization behavior of the absorption peaks at 4.5 and 5.25 eV in the present study are seen in Ref. 31,

in which a purified HiPco SWNT thin-film aligned on a glass plate was measured. Although no explanation was given by the authors, their results are consistent with the above discussion.

In a practical sense, the magnitude of these peaks at 4.5 and 5.25 eV can provide a quantitative and convenient index for evaluating the degree of SWNT alignment. However, more importantly, this optical relevance between SWNTs and graphite above the inter-subband region indicates the possibility of studying the optical properties of graphite by studying SWNTs as arrays of *graphene* cylinders.

4.1.6 Modeling and formulation of multi-dipole optical absorption of SWNTs

4.1.6.1 Transition probability

This subsection describes the formulation of anisotropic optical absorption by multiple transition dipoles of SWNTs. The time-dependent Schrödinger equation for Hamiltonian H is expressed as

$$i\hbar\frac{\partial\Psi(t)}{\partial t} = H\Psi(t) \tag{1}$$

According to the time-dependent perturbation theory, the perturbed Hamiltonian H is expressed as a summation of the unperturbed Hamiltonian H_0 and the perturbation H' as

$$H = H_0 + H' \tag{2}$$

In case there is no perturbation, the eigenvalue E_n and the eigenfunction Φ_n for H_0 that are related by

$$H_0\Phi_n = E_n\Phi_n \tag{3}$$

are assumed to be known. Then, the unperturbed Schrödinger equation

$$i\hbar\frac{\partial\Psi_0(t)}{\partial t} = H_0\Psi_0(t) \tag{4}$$

has its general solution as

$$\Psi_0(t) = \sum_{n=0} c_n \exp\left(-i\frac{E_n}{\hbar}t\right)\Phi_n \tag{5}$$

where c_n denotes an arbitrary constant, and the exponential term is derived from the time-evolution operator of the wave function. Since Φ_n forms a complete orthogonal basis, $\Psi(t)$ can be expanded in terms of Φ_n as

$$\Psi(t) = \sum_{n=0} c_n(t) \exp\left(-i\frac{E_n}{\hbar}t\right)\Phi_n \tag{6}$$

Therefore, $\Psi(t)$ is determined by calculating the time-dependent coefficient $c_n(t)$. Substituting Eq. (6) into Eq. (1) and taking the inner product with Φ_f lead to

$$i\hbar\exp\left(-\frac{iE_f t}{\hbar}\right)\frac{dc_f}{dt} = \sum_{n=0}\exp\left(-i\frac{E_n}{\hbar}t\right)c_n(t)\left\langle\Phi_f\left|H'\right|\Phi_n\right\rangle \tag{7}$$

If the initial state of the system lies in one of the bases, $\Psi(0) = \Phi_i$, that is,

$$c_i(0) = 1, \quad c_n(0) = 0 \quad (n \neq i) \tag{8}$$

Further, it is assumed that the state does not significantly deviate from the initial state within the range of consideration, that is,

$$c_i(t) \approx 1, \quad c_n(t) \approx 0 \quad (n \neq i) \tag{9}$$

Then Eq. 7 for $c_f(t)$ can be rewritten as

$$i\hbar \frac{dc_f}{dt} = \exp\left(\frac{i(E_f - E_i)t}{\hbar} \right) \left\langle \Phi_f \left| H' \right| \Phi_n \right\rangle \tag{10}$$

and this can be solved as

$$c_f(t) = \left\langle \Phi_f \left| H' \right| \Phi_n \right\rangle \frac{1 - \exp(i\varpi_{fi} t)}{\hbar \varpi_{fi}}, \quad \left(\varpi_{fi} \equiv \frac{E_f - E_i}{\hbar} \right) \tag{11}$$

Since $c_n(t)$ is an expansion coefficient for the wave function $\Psi(t)$, as expressed in Eq. 6, their squared values represent the possibility of obtaining the eigenvalue corresponding to the basis Φ_n as indicated by an instance for H_0,

$$\begin{aligned} \left\langle \Psi \left| H_0 \right| \Psi \right\rangle &= \sum_n \sum_m c_n^*(t) \exp\left(-i \frac{E_n}{\hbar} t \right) c_m(t) \exp\left(-i \frac{E_m}{\hbar} t \right) \left\langle \Phi_n \left| H_0 \right| \Phi_m \right\rangle \\ &= \sum_n \sum_m c_n^*(t) c_m(t) \exp\left(-i \frac{E_n - E_m}{\hbar} t \right) E_m \delta_{nm} \\ &= \sum_n \left| c_n(t) \right|^2 E_n \end{aligned} \tag{12}$$

Therefore, the probability of the transition $\Phi_i \rightarrow \Phi_f$ equals to $|c_f(t)|^2$ and this is obtained by squaring Eq. (11) as

$$\left| c_f(t) \right|^2 = \left| \left\langle \Phi_f \left| H' \right| \Phi_n \right\rangle \right|^2 \left(\frac{2 \sin \frac{\varpi_{fi} t}{2}}{\hbar \varpi_{fi}} \right)^2 \tag{13}$$

This relation is valid for the condition mentioned in Eq. 9.

4.1.6.2 Optical absorption by dipole transition moment

The perturbed Hamiltonian for the one-photon process $H^{(1)}$ (refer to Appendix) is written as

$$H^{(1)} = \frac{e}{m} \sqrt{\frac{\hbar}{2\varepsilon_0 V}} \sum_j \sum_{\boldsymbol{k},\gamma} \frac{1}{\sqrt{\varpi_{\boldsymbol{k}}}} \left\{ \mathrm{e}^{i\boldsymbol{k}\cdot\boldsymbol{r}_j} (\boldsymbol{e}_{\boldsymbol{k},\gamma} \cdot \boldsymbol{p}_j) a_{\boldsymbol{k},\gamma} + \mathrm{e}^{-i\boldsymbol{k}\cdot\boldsymbol{r}_j} (\boldsymbol{e}_{\boldsymbol{k},\gamma} \cdot \boldsymbol{p}_j) a_{\boldsymbol{k},\gamma}^* \right\} \tag{14}$$

where e, m, V, and ε_0 denote the electric charge, mass of electron, volume of space, and dielectric function of vacuum, respectively. Vectors $\boldsymbol{e}$, $\boldsymbol{p}$, $\boldsymbol{k}$, and $\boldsymbol{r}$ denote the unit vector for the oscillatory direction of *vector potential* (which is parallel to the electronic potential

vector $\boldsymbol{E}$), momentum vector of electron, wave vector of electromagnetic wave, and position vector in real space, respectively. Furthermore, γ (= 1 or 2), j ($1 \le j \le N$), $a_{\boldsymbol{k},\gamma}$, and $a_{\boldsymbol{k},\gamma}^{*}$ denote the coordinate label perpendicular to $\boldsymbol{k}$, index number of electron, annihilation operator of photon, and creation operator of photon, respectively.

We define the initial and final state of the system as

$$\Phi_i = \left|a\right\rangle\left|n_1, n_2, \cdots, n_{\boldsymbol{k},\gamma}, \cdots\right\rangle, \quad \Phi_f = \left|b\right\rangle\left|n_1, n_2, \cdots, n_{\boldsymbol{k},\gamma} \pm 1, \cdots\right\rangle \tag{15}$$

where $|a\rangle$ and $|b\rangle$ denote the initial and final electronic state, respectively. Therefore, the matrix element for absorption of a photon by an electron in coordinate $\boldsymbol{k}$, γ, is written as

$$\begin{aligned}\left\langle \Phi_f \left| H^{(1)} \right| \Phi_i \right\rangle &= \frac{e}{m}\sqrt{\frac{\hbar}{2\varepsilon_0 V \varpi_{\boldsymbol{k}}}}\left\langle b\left|\sum_j \mathrm{e}^{i\boldsymbol{k}\cdot\boldsymbol{r}_j}(\boldsymbol{e}_{\boldsymbol{k},\gamma}\cdot\boldsymbol{p}_j)\right|a\right\rangle\left\langle n_{\boldsymbol{k},\gamma}-1\left|a_{\boldsymbol{k},\gamma}\right|n_{\boldsymbol{k},\gamma}\right\rangle \\ &= \frac{e}{m}\sqrt{\frac{n_{\boldsymbol{k},\gamma}\hbar}{2\varepsilon_0 V \varpi_{\boldsymbol{k}}}}\left\langle b\left|\sum_j \mathrm{e}^{i\boldsymbol{k}\cdot\boldsymbol{r}_j}(\boldsymbol{e}_{\boldsymbol{k},\gamma}\cdot\boldsymbol{p}_j)\right|a\right\rangle\end{aligned} \tag{16}$$

Here, using the formula

$$\int_{-\infty}^{\infty}\left(\frac{\sin x}{x}\right)^2 dx = \pi \tag{17}$$

Equation 13 is rewritten with the assumption that $|\langle\Phi_f|H'|\Phi_i\rangle|^2$ is constant, as

$$\left|c_f(t)\right|^2 = \left|\left\langle \Phi_f \left| H' \right| \Phi_n \right\rangle\right|^2 \frac{2\pi}{\hbar^2} t\delta(\varpi_{\boldsymbol{k}} - \varpi_{ab}) \tag{18}$$

which is known as Fermi's golden rule. By substituting Eq. 15 into Eq. 18 with $H' = H^{(1)}$,

$$\begin{aligned}\left|c_f(t)\right|^2 &= \left|\frac{e}{m}\sqrt{\frac{n_{\boldsymbol{k},\gamma}\hbar}{2\varepsilon_0 V \varpi_{\boldsymbol{k}}}}\left\langle b\left|\sum_j \mathrm{e}^{i\boldsymbol{k}\cdot\boldsymbol{r}_j}(\boldsymbol{e}_{\boldsymbol{k},\gamma}\cdot\boldsymbol{p}_j)\right|a\right\rangle\right|^2 \frac{2\pi}{\hbar^2} t\delta(\varpi_{\boldsymbol{k}} - \varpi_{ab}) \\ &\Leftrightarrow \left|c_f(t)\right|^2 \propto \left|\left\langle b\left|\frac{e}{m}\sum_j \mathrm{e}^{i\boldsymbol{k}\cdot\boldsymbol{r}_j}(\boldsymbol{e}_{\boldsymbol{k},\gamma}\cdot\boldsymbol{p}_j)\right|a\right\rangle\right|^2\end{aligned} \tag{19}$$

By taking the first term of the expansion (i.e., only dipole transition),

$$\exp\left(i\boldsymbol{k}\cdot\boldsymbol{r}_j\right) = 1 + i\boldsymbol{k}\cdot\boldsymbol{r}_j - \frac{1}{2}(\boldsymbol{k}\cdot\boldsymbol{r}_j)^2 + \cdots \tag{20}$$

and the relationship in an electronic system,

$$\left\langle b\left|\boldsymbol{p}_j\right|a\right\rangle = \frac{im}{\hbar}(E_b - E_a)\left\langle b\left|\boldsymbol{r}_j\right|a\right\rangle \tag{21}$$

the electronic dipole absorption is expressed from Eq. 19 as

$$\left|c_f(t)\right|^2 \propto (E_b - E_a)^2 \left|\left\langle b\left|e\sum_j (\boldsymbol{e}_{\boldsymbol{k},\gamma}\cdot\boldsymbol{r}_j)\right|a\right\rangle\right|^2 \tag{22}$$

Electronic dipole $\boldsymbol{\mu}$ is introduced here as

$$\boldsymbol{\mu} = -e\sum_j \boldsymbol{r}_j \tag{23}$$

with which the transition probability for $\Phi_i \rightarrow \Phi_f$ is expressed as

$$\left|c_f(t)\right|^2 \propto (E_b - E_a)^2 \left|\left\langle b\left|\sum_j (\boldsymbol{e}_{\boldsymbol{k},\gamma}\cdot\boldsymbol{\mu})\right|a\right\rangle\right|^2 \propto \left|\boldsymbol{\mu}\cdot\boldsymbol{E}\right|^2 \tag{24}$$

This equation indicates that the absorption probability is proportional to the square of $\boldsymbol{\mu}\cdot\boldsymbol{E}$.

4.1.6.3 Formulation for multiple dipole absorption by vertically aligned SWNTs

First, an *x*-*y*-*z* orthogonal coordinate is defined in which the *z*-axis is normal to the substrate and the light propagation vector ***k*** is within the *y*-*z* plane, as described in Fig. 4-4. The angle between the ***k*** and the *z*-axis is denoted as θ ($0 \le \theta \le \pi/2$). The orientation of the SWNT axis vector ***l*** is described by φ ($0 \le \varphi \le \pi/2$) as the deviation angle of ***l*** from the

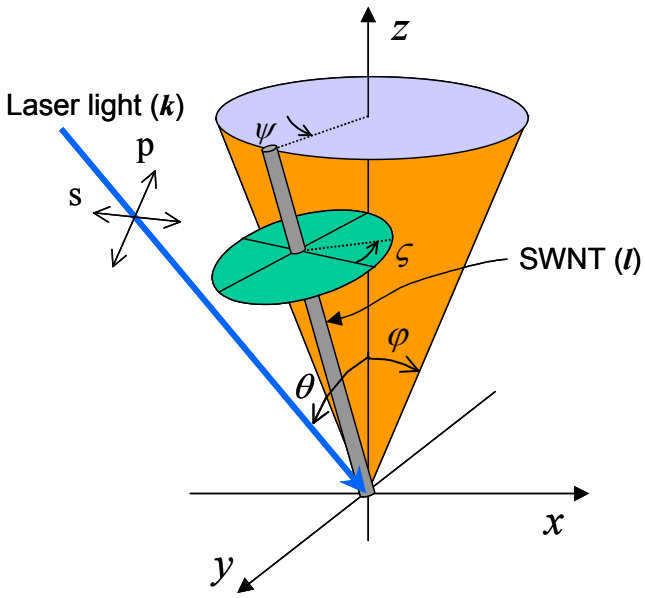


Fig. 4-4. Schematical representation of corrdinates (*x*, *y*, *z*) and angles (θ, φ, ψ, ζ) used in the formulation of *multi-dipole* optical absorption of polarized light propergaging in ***k*** by a SWNT with axial vactor ***l***.

z-axis, and $\psi\,(0 \le \psi \le 2\pi)$ is the rotational angle of a plane constructed by $\boldsymbol{l}$ and *z*-axes from the *z*-*x* plane. SWNT has assumed to have collinear dipole moment $\boldsymbol{\mu}_{\parallel}$ parallel to $\boldsymbol{l}$, and the non-collinear dipole moment $\boldsymbol{\mu}_{\perp}$ perpendicular to $\boldsymbol{l}$. The direction of $\boldsymbol{\mu}_{\perp}$ is either radial or tangential to the SWNT circumference depending on the type of dipole considered. Since $\boldsymbol{\mu}_{\perp}$ has all component around $\zeta\,(0 \le \zeta \le 2\pi)$, the dipole located at the circumferential angle ζ is expressed as

$$\boldsymbol{\mu}_{\perp} = \boldsymbol{\mu}_{\perp(\zeta=0)} \cos\zeta + \boldsymbol{\mu}_{\perp(\zeta=\pi/2)} \sin\zeta \tag{25}$$

Here, $\boldsymbol{\mu}_{\parallel}$, $\boldsymbol{\mu}_{\perp(\zeta=0)}$ and $\boldsymbol{\mu}_{\perp(\zeta=\pi/2)}$ are written as

$$\boldsymbol{\mu}_{\parallel} = \mu_{\parallel}\begin{pmatrix} -\sin\varphi\cos\psi \\ \sin\varphi\sin\psi \\ \cos\varphi \end{pmatrix},\quad \boldsymbol{\mu}_{\perp(\zeta=0)} = \mu_{\perp}\begin{pmatrix} \sin\psi \\ \cos\psi \\ 0 \end{pmatrix},\quad \boldsymbol{\mu}_{\perp(\zeta=\pi/2)} = \mu_{\perp}\begin{pmatrix} \cos\varphi\cos\psi \\ -\cos\varphi\sin\psi \\ \sin\varphi \end{pmatrix} \tag{26}$$

and the electronic vectors for s- and p-polarization are given as $\boldsymbol{E}_{\mathrm{s}} = E(1\ 0\ 0)^{\mathrm{T}}$ and $\boldsymbol{E}_{\mathrm{p}} = E(0\ \cos\theta\ \sin\theta)^{\mathrm{T}}$, respectively.

The absorption of s-polarized light by the transition dipole perpendicular to the SWNT axis is represented as

$$\begin{aligned}\Lambda^{S}{}_{\perp}(\varphi,\psi,\zeta) = \left|\boldsymbol{\mu}_{\perp}\cdot\boldsymbol{E}_{s}\right|^{2} = \mu_{\perp}{}^{2}E^{2}(&\sin^{2}\psi\cos^{2}\zeta + 2\cos\varphi\cos\psi\sin\psi\cos\zeta\sin\zeta \\ &+ \cos^{2}\varphi\cos^{2}\psi\sin^{2}\zeta)\end{aligned} \tag{27}$$

Using the following relationships

$$\Lambda^{\mathrm{S}}{}_{\perp}(\varphi,\psi) = \frac{\int_{-\pi}^{\pi}\Lambda^{\mathrm{S}}{}_{\perp}(\varphi,\psi,\zeta)d\zeta}{\int_{-\pi}^{\pi}d\zeta},\quad \Lambda^{\mathrm{S}}{}_{\perp}(\varphi) = \frac{\int_{-\pi}^{\pi}\Lambda^{\mathrm{S}}{}_{\perp}(\varphi,\psi)d\psi}{\int_{-\pi}^{\pi}d\psi} \tag{28}$$

$\Lambda^{\mathrm{S}}{}_{\perp}$ is reduced to

$$\Lambda^{\mathrm{S}}{}_{\perp} = \frac{1}{4}\mu_{\perp}{}^{2}E^{2}(1+\cos^{2}\varphi) \tag{29}$$

In actual conditions, however, φ has a some distribution described by an unknown function $f(\varphi)$; then, the experimentally observed $\Lambda^{\mathrm{S}}{}_{\perp}$' is written as

$$\Lambda^{\mathrm{S}}{}_{\perp}' = \frac{\int_{0}^{\frac{\pi}{2}} f(\varphi)\cdot\Lambda^{\mathrm{S}}{}_{\perp}(\varphi)d\varphi}{\int_{0}^{\frac{\pi}{2}} f(\varphi)d\varphi} = \frac{1}{4}\mu_{\perp}{}^{2}E^{2}(1+<\cos^{2}\varphi>) \tag{30}$$

On the other hand, absorption of s-polarized light by the transition dipole parallel to the SWNT axis is represented as

$$\Lambda^{S}{}_{\|}(\varphi,\psi) = \left|\boldsymbol{\mu}_{\|} \cdot \boldsymbol{E}_{s}\right|^{2} = \mu_{\|}{}^{2} E^{2} (\sin^{2}\varphi \cos^{2}\psi) \tag{31}$$

Similarly, using the relationships,

$$\Lambda^{S}{}_{\|}(\varphi) = \frac{\int_{-\pi}^{\pi} \Lambda^{S}{}_{\|}(\varphi,\psi) d\psi}{\int_{-\pi}^{\pi} d\psi} \tag{32}$$

and then $\Lambda^{S}{}_{\|}(\varphi)$ is reduced to

$$\Lambda^{S}{}_{\|}(\varphi) = \left|\boldsymbol{\mu}_{\|} \cdot \boldsymbol{E}_{S}\right|^{2} = \frac{1}{2} \mu_{\|}{}^{2} E^{2} \sin^{2}\varphi \tag{33}$$

The experimentally observed $\Lambda^{S}{}_{\perp}$' is written as

$$\Lambda^{S}{}_{\|}' = \frac{\int_{0}^{\frac{\pi}{2}} f(\varphi) \cdot \Lambda^{S}{}_{\|}(\varphi) d\varphi}{\int_{0}^{\frac{\pi}{2}} f(\varphi) d\varphi} = \frac{1}{2} \mu_{\|}{}^{2} E^{2} < \sin^{2}\varphi > \tag{34}$$

Therefore, the absorbance of s-polarized light by *whole dipoles* measured by the experiment Λ^{S}' is

$$\Lambda^{S}{}' = \frac{1}{2} \Lambda_{0,\|} < \sin^{2}\varphi > + \frac{1}{2} \Lambda_{0,\perp} (1 + < \cos^{2}\varphi >) \tag{35}$$

where $\mu_{\|}{}^{2} E^{2} \equiv \Lambda_{0,\|}$ and $\mu_{\perp}{}^{2} E^{2} \equiv 2 \times \Lambda_{0,\perp}$ were defined. Since Λ^{S}' is function of only φ, it provides a constant baseline regardless of θ.

The absorbance of p-polarized light by the transition dipole perpendicular to the SWNT axis Λ^{P} is written as

$$\begin{aligned}\Lambda^{P}{}_{\perp}(\theta,\varphi,\psi,\zeta) = \left|\boldsymbol{\mu}_{\perp} \cdot \boldsymbol{E}_{p}\right|^{2} = \mu_{\perp}{}^{2} E^{2} (&\cos\theta \cos\psi \cos\zeta - \cos\theta \cos\varphi \sin\psi \sin\zeta \\ &+ \sin\theta \sin\varphi \sin\zeta)^{2}\end{aligned} \tag{36}$$

Similarly to the case of s-polarization (Eq. 28), the experimentally measured $\Lambda^{P}{}_{\perp}$' is expressed as

$$\Lambda^{P}{}_{\perp}'(\theta) = \frac{1}{4} \mu_{\perp}{}^{2} E^{2} \left\{\cos^{2}\theta (1 + < \cos^{2}\varphi >) + 2 \sin^{2}\theta < \sin^{2}\varphi >\right\} \tag{37}$$

Further, the absorbance of p-polarized light by the transition dipole parallel to the SWNT axis Λ^{P} is written as

$$\Lambda^{P}{}_{\|}'(\theta) = \frac{1}{4}\mu_{\|}{}^{2}E^{2}(\cos^{2}\theta < \sin^{2}\varphi > +2\sin^{2}\theta < \cos^{2}\varphi >) \tag{38}$$

Therefore, the absorbance of p-polarized light by *whole dipoles* measured by experiment Λ^{P}' is

$$\begin{aligned}\Lambda^{P}{}'(\theta) = \frac{1}{2}\Lambda_{0,\|}(\cos^{2}\theta < \sin^{2}\varphi > +2\sin^{2}\theta < \cos^{2}\varphi >) \\ + \frac{1}{2}\Lambda_{0,\perp}\left\{\cos^{2}\theta(1+ < \cos^{2}\varphi >) + 2\sin^{2}\theta < \sin^{2}\varphi >\right\}\end{aligned} \tag{39}$$

In all, the experimentally measured values $\Lambda'_{(\theta=0)}$ and $\Lambda'_{(\theta=\pi/2)}$ are introduced using Eqs. 35 and 39 as

$$\Lambda'_{(\theta=0)} \equiv \Lambda^{P}{}'(0) = \Lambda^{S}{}' = \frac{1}{2}\Lambda_{0,\|} < \sin^{2}\varphi > + \frac{1}{2}\Lambda_{0,\perp}(1+ < \cos^{2}\varphi >) \tag{40}$$

$$\Lambda'_{(\theta=\pi/2)} \equiv \Lambda^{P}{}'(\pi/2) = \Lambda_{0,\|} < \cos^{2}\varphi > + \Lambda_{0,\perp} < \sin^{2}\varphi > \tag{41}$$

These Eqs. 40 and 41, of course, satisfy the requirement of *total absorbance* Λ_0 as

$$\begin{aligned}\Lambda_{0} &\equiv 2\times\Lambda'_{(\theta=0)} + \Lambda'_{(\theta=\pi/2)} \\ &= \Lambda_{0,\perp}(1+ < \cos^{2}\varphi >) + \Lambda_{0,\perp} < \sin^{2}\varphi > + \Lambda_{0,\|} < \cos^{2}\varphi > + \Lambda_{0,\|} < \sin^{2}\varphi > \\ &= 2\times\Lambda_{0,\perp} + \Lambda_{0,\|}\end{aligned} \tag{42}$$

Therefore, the anisotropy α in the case of multiple dipole absorption is introduced in terms of $\Lambda'_{(\theta=0)}$ and $\Lambda'_{(\theta=\pi/2)}$ as

$$\alpha = \frac{\Lambda'_{(\theta=\pi/2)} - \Lambda'_{(\theta=0)}}{\Lambda'_{(\theta=\pi/2)} + 2\Lambda'_{(\theta=0)}} = \frac{\Lambda_{0,\|} - \Lambda_{0,\perp}}{\Lambda_{0,\|} + 2\Lambda_{0,\perp}} \cdot \frac{1}{2}\left(3 < \cos^{2}\varphi > -1\right) \tag{43}$$

4.1.7 Determination of optical anisotropy and bare optical absorption cross-section of SWNTs

Figure 4-5a presents a portion of Fig. 4-2b as solid lines magnified for 0.5–3 eV. Since at each energy point the absorbance increases well according to $\sin^{2}\theta$, these spectra are extrapolated into the absorbance at $\theta = 90°$ ($\Lambda'_{(\theta=\pi/2)}$), denoted by a dotted line. Figure 4-5b shows α for 0.5–3 eV calculated using Eq. 43. In a lower energy region (< 2 eV), α increases as the collinear absorption by the $\Delta\mu = 0$ inter-subband transition (E^{S}_{11}, E^{S}_{22}, and E^{M}_{11}) becomes dominant. In contrast, a lower value of α at a higher energy region is due to

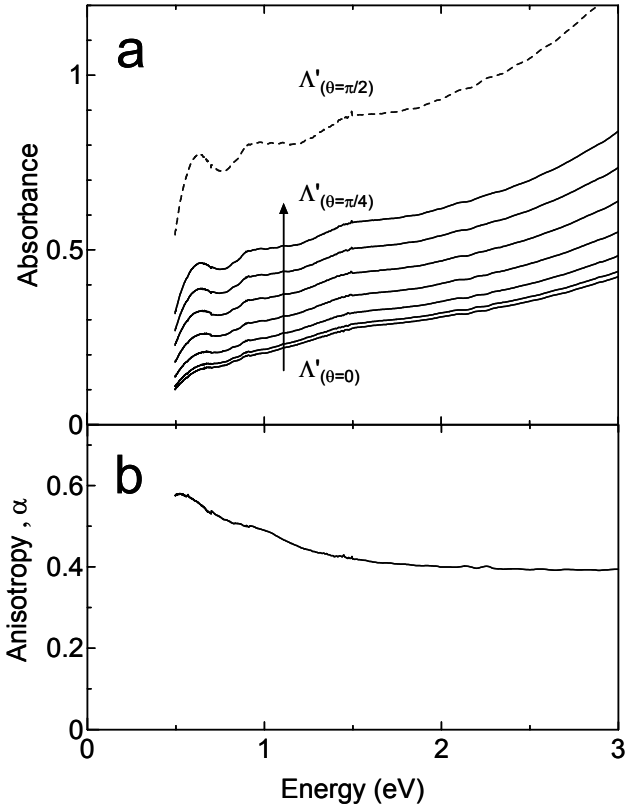


Fig. 4-5. (a) Part of measured absorption spectra presentned in Fig. 4-2b for 0.3 - 3 eV by p-polarization from θ = 0° to 45° at a step of 7.5° (solid lines) and its extrapolation to the case of θ = 90° (dashed line). (b) Calculated anisotropy α from Eq. 43.

the magnification of non-collinear dipoles that are perpendicular to the SWNT axis, which is investigated in detail below, as well as due to the weakening of the $\Delta\mu = 0$ inter-subband transition.

In order to determine the bare optical absorption cross section of SWNTs for both parallel ($\sigma_{\parallel}$) and perpendicular ($\sigma_{\perp}$) polarizations, one has to determine a *nematic order parameter S* that is defined by

$$S = \frac{1}{2}\left(3 < \cos^2 \varphi > -1\right) \tag{44}$$

In the present case, α cannot be substituted for S because α is rewritten as

$$\alpha = \frac{\sigma_{\parallel} - \sigma_{\perp}}{\sigma_{\parallel} + 2\sigma_{\perp}} \cdot S \quad < S \tag{45}$$

from Eq. 42 and using the Beer-Lambert law.

In order to determine *S*, it is necessary to separate the dependence of the collinear dipole on polarization from the entire spectra. As observed in Fig. 4-2b, the collinear absorption peak at ~4.5 eV exhibits the clearest dependence on polarization. Hence, based on the observed absorption maxima of either Im$\{\varepsilon\}$ or Im$\{-\varepsilon^{-1}\}$ at ~2.8, 4.0, 4.4, and 5.2 eV from the reflectance measurement of a SWNT film by Lee et al. [32], Lorentzian curve fitting was performed for 2.5–6.0 eV, as described below.

Figure 4-6 shows the decomposed spectra obtained by setting four peaks at 2.8, 4.0, 4.5, and 5.3 ± 0.1 eV. Their widths were practically fixed at 4.0, 1.3, 0.98, and 1.72 ± 0.02 eV, respectively. It was confirmed that the same peak positions and widths also decompose the absorption spectra of other SWNTs with different diameters. Figure 4-6b is the Lorentzian fitting for the absorption spectra of a randomly oriented SWNT film shown in Fig. 4-1(i)

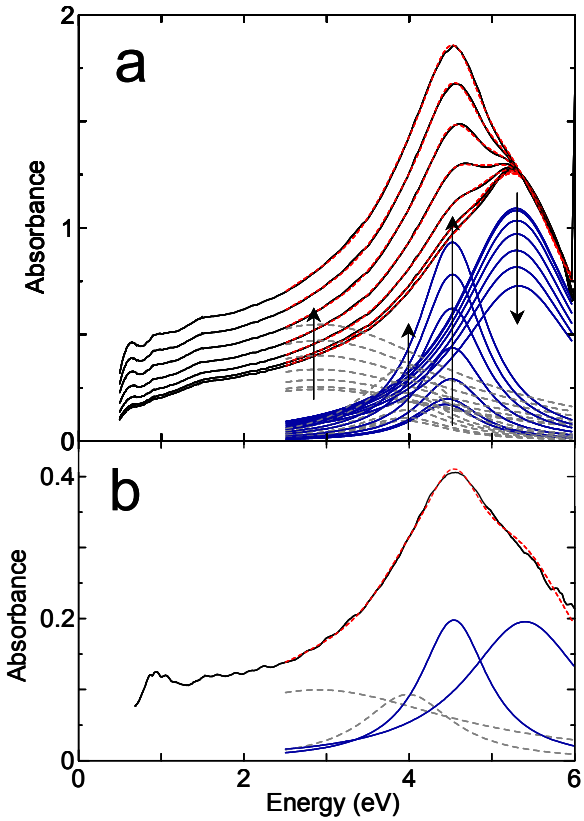


Fig. 4-6. (a) Measured absorption spectra presetned in Fig. 4-2b from θ = 0° to 45° at a step of 7.5° by p-polarization and their Lorentzian fitting with four curves. See text for peak locations and widths. Arrows indicate the direction of change of each Lorentizan component from θ = 0° to 45°. Dotted lines overlapping the measured spectrum repreesnts sum of these Lorentzian curves. (b) Lorentzian curve fitting performed to randomely oriented SWNT film corresponds to the spectrum (i) in Fig. 4-1 using the same peak position and widths.

that has a smaller diameter than the case of Fig. 4-6a. The spectra of Fig. 4-6b can also be fitted well according to this scheme.

Figure 4-7a plots the change in each Lorentzian amplitude. The baseline of the non-collinear peak at 5.25 eV may have some ambiguity because it is located at the border of the measured range and could be affected by the collinear dipoles at a higher energy. The plot for the peak at 4.5 eV is fitted with $\sin^2\theta$, and $S \approx 0.75$ and $\langle\varphi\rangle \approx 24°$ are calculated from Eqs. 11 and 13.

The molar absorption cross sections of this SWNT film sample, parallel to ($\eta_{\parallel}$) and perpendicular to ($\eta_{\perp}$) the z-axis, are directly determined from Fig. 4-5a using the density of C atoms in the current vertically aligned SWNT film, which is ~3.0×10^3 mol/m^3 (3.5×10^{-2} g/cm^3) as estimated by SEM and TEM measurements. The molar cross section η was defined in this study based on the definition of absorbance $\Lambda = -\log_{10}T = \eta \cdot n \cdot l$, where T, n, and l are the optical transmission, molar concentration of C, and film thickness, respectively. Therefore, the bare optical absorption cross section of the SWNTs parallel to

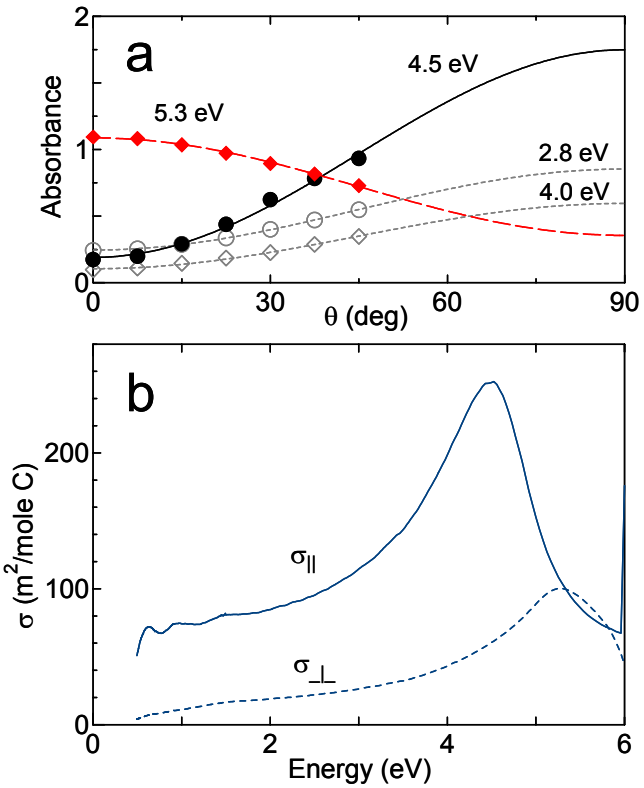


Fig. 4-7. (a) Dependence of each Lorentzian amplitude on the incident angle θ. Curves fitted by either $\sin^2\theta$ or $\cos^2\theta$ are also shown. (b) Bare optical cross-sections parallel to ($\sigma_{\parallel}$) and perpendicular to ($\sigma_{\perp}$) the SWNT axis for 0.5 - 6 eV calculated using Eqs. 3, 4.

($\sigma_{\|}$) and perpendicular to ($\sigma_{\perp}$) the SWNT axis can be calculated by the relationships derived from Eqs. 9, 10, and 13 as

$$\sigma_{\|} = \frac{1}{3}\left\{2\eta_{\perp} + \eta_{\|} + \frac{2\left(\eta_{\|} - \eta_{\perp}\right)}{S}\right\} \tag{46}$$

$$\sigma_{\perp} = \frac{1}{3}\left(2\eta_{\perp} + \eta_{\|} - \frac{\eta_{\|} - \eta_{\perp}}{S}\right) \tag{47}$$

Figure 4-7b shows $\sigma_{\|}$ and $\sigma_{\perp}$ for 0.5–6 eV. The $\Delta\mu = 0$ inter-subband absorption is seen clearly in $\sigma_{\|}$ as observed in Ref. 10. In the higher energy region (above 3 eV), $\sigma_{\|}$ attains a maximum (~30 m^2/mole C) at 4.5 eV and $\sigma_{\perp}$ attains its maximum (~10 m^2/mole C) at 5.25 eV. It should be noted that even in the low energy region (<3 eV), there exists a small but non-zero $\sigma_{\perp}$, which is partly due to the extension of the Im$\{-\varepsilon_{\|}^{-1}\}$ π-plasmon at 5.25 eV into the lower energy region. In addition, depolarization effects in a SWNT for cross-polarized light, as shown by Ajiki and Ando [10], can be imperfect when SWNTs are bundled, leading to inter-subband absorption transitions where $\Delta\mu = \pm 1$ [33], as discussed in detail later in Section 4.2. Therefore, the existence of multiple absorption dipoles, both parallel and perpendicular to the SWNTs axis, should be taken into account in optical measurements, even for the inter-subband energy region.

4.1.8 Summary of anisotropy optical properties of SWNTs

In summary, the anisotropic optical absorption properties of SWNTs for 0.5–6 eV were elucidated based on the polarized optical absorption measurements of a vertically aligned SWNT film. This is the first study investigating the absorption features of SWNTs at 4.5 and 5.25 eV and their polarization dependence. In contrast to earlier theoretical studies [11,12], the positions of the absorption peaks near 5 eV including the π-plasmon did not disperse depending on the incident polarization, diameter, and chirality of SWNTs. The method of determining an order parameter for an aligned SWNT film was presented by extracting the collinear absorption element at 4.5 eV; then, the bare optical absorption cross sections for both parallel and perpendicular polarizations were determined up to 6 eV. It was found that the tail of the non-collinear absorption peak at 5.25 eV appreciably contribute to the $\sigma_{\perp}$ in the inter-subband transition region (< 3 eV).

For practical purposes, the peaks at 4.5 and 5.25 eV provide convenient quantitative indexes to evaluate the degree of alignment of SWNTs. Due to the fact that these peaks were observed at almost the same positions regardless of the diameter and the sample preparation method, they are attributed to the maxima in $\mathrm{Im}\{\varepsilon_{\perp}\}$ (~4.5 eV) and $\mathrm{Im}\{-\varepsilon_{\parallel}^{-1}\}$ (~5.25 eV) reflecting the optical properties of graphite. These results suggest an important possibility of investigating the unresolved optical properties of graphite in the direction parallel to the *c*-axis by simple measurements of the optical absorption of aligned SWNT films, as an array of *graphene* cylinders.

4.2 Polarization dependence of Raman scattering characteristics from vertically aligned SWNT film

4.2.1 Introduction – Role of Raman scattering in SWNT analysis

Resonant Raman scattering (RRS) spectroscopy has been an important tool to obtain structural information including quality and diameter, as well as distinguishing between metallic and semiconducting single-walled carbon nanotubes (SWNTs) [2,34]. In the radial breathing mode (RBM) that appears in lower frequency region, the resonant nature of electronic transitions between van Hove singularities in the valence and conduction bands has been utilized to experimentally probe for chiral distribution of SWNTs [19,35-37]. It was demonstrated experimentally by Jorio and co-workers [38] that, from their RRS measurements on G-band modes of isolated SWNTs, the possibility of $\Delta\mu = \pm 1$ transitions should be taken into account in addition to the usual $\Delta\mu = 0$ transition (μ denotes the cutting-line index [2,38]). Understanding the significance of the $\Delta\mu = \pm 1$ transition is important because it crucially affects the interpretation of RBM spectra needed for the assignment of chirality as well as the distinction between metallic and semiconducting SWNTs based on the Kataura plot [20]. Theoretical work by Grüneis and co-workers [33] indicated that the $\Delta\mu = \pm 1$ transition is induced by absorption of light polarized across the SWNT axis, and hence polarized Raman analysis should be effective to study this subject.

So far several studies employing polarized RRS on SWNTs, either bundled or isolated, have been reported [13,38-42]. While some of them focused solely on the G-band's intensity and structure by changing the polarization direction [38,39,41], a small number of papers investigated the dependence of the RBM by the change of polarization. Hwang et al. [13] and Duesberg et al. [40] performed polarized RRS experiments on nearly isolated SWNTs on a glass plate and presumably bundled SWNTs aligned in a melt-spun PMMA fiber, respectively, and showed that the scattering intensities of both RBM and G peaks are maximized when the polarization of the light is parallel to the SWNT axis and are suppressed when perpendicular. In both reports the change of only one isolated RBM peak was presented at a fixed laser wavelength. Grüneis et al. [42] recently reported, from their Raman measurement on randomly-oriented SWNT bundles, unexpected RBM peaks between E^S_{22} and E^M_{11} (subscript number denotes serial number of van Hove singularities) that apparently deviated from their tight-binding-based Kataura plot as well as from the data based on photo-luminescence [43]. They reported that the unexpected RBM peaks were an observation of $\Delta\mu = \pm 1$ excitations caused by the absorption by SWNTs of

perpendicularly polarized light, because the dipole selection rules give different absorption energies for light with parallel and perpendicular polarization [33,42]. They discussed that, in contrast to isolated SWNTs, bundled SWNTs could absorb the cross-polarized light due to an imperfection of the "depolarization effect" that was predicted by Ajiki and Ando [10]. Since all the RBM peaks measured from their randomly aligned and bundled SWNTs were plotted [42] the peaks had not been unambiguously classified especially in the higher energy region above E^{M}_{11} on the Kataura plot, where the E_{ii} plots start to broaden and overlap each other [20].

In Chapter 3, a method to synthesize vertically aligned SWNT films directly on the surface of quartz substrates [16] using the alcohol chemical vapor deposition (ACCVD) method [17,44] has been developed. Since this SWNT film has a macroscopic thickness (approximately 5 μm) and is uniform over the substrate (25 × 25 mm^2) [16,45], it is ideal for optical measurements including Raman scattering analysis. In this Section, it is demonstrated that the spectral shape of the RBM from this aligned SWNT film exhibits a remarkable dependence on the relationship between the light polarization vector (***e***) and the SWNT axis direction (***l***). The obtained spectra was analyzed quantitatively and it is concluded that each specified peak falls clearly into one of two groups, where the peaks in one group dominate for the case of $\boldsymbol{e} \perp \boldsymbol{l}$ and the others dominate for $\boldsymbol{e} \,//\, \boldsymbol{l}$. The grouping of RBM peaks is also observed by the difference in behavior toward an adsorption of molecules and a change in the incident laser power. These results evidence the $\boldsymbol{e} \,//\, \boldsymbol{l}$ and $\boldsymbol{e} \perp \boldsymbol{l}$ peaks are $\Delta\mu = 0$ and $\Delta\mu = \pm 1$ resonance, respectively. From the experimental investigations performed in this report, both types of RBM peaks in a higher energy range (1.96 - 2.54 eV) that are often used in RRS analysis of SWNTs are unambiguously distinguished, over wide range of tube diameter (0.8 - 1.8 nm).

4.2.2 Raman scattering measurement

When performing Raman scattering measurements a micro-Raman setup (Seki Technotron, STR-250) composed of an optical microscope (Olympus, BX51), a spectrometer (Chromex, 501is) and a CCD (Andor, DV401-FI) was used. Laser wavelengths of 488 (2.54), 514.5 (2.41) and 633 nm (1.96 eV) were used. The measurements were done in back-scattering configuration with an incident laser power of 0.2 - 0.5 mW with a spot size ≥ 5 μm at the sample surface and a 50× objective lens, unless otherwise stated. The energy density used in this study (≤ 2.5 × 10^3 W/cm^2) is

chosen to be sufficiently low compared with that typically used in micro Raman measurement on SWNTs (e.g. 1×10^6 W/cm^{-2} in Ref. 21), in order to avoid any unexpected effects on Raman spectra caused by laser heating [47,48]. Specifically, we monitored the location of the G^+ band (at approximately 1593 cm^{-1} at room temperature [48,49]) to make sure it did not descend below 1592 cm^{-1} (or above 100°C [48,49]) during the measurements. The laser light incident on the sample was linearly polarized by a polarizer put in the path of the laser light. Scattered light was collected back into the microscope, passing a half mirror and then a depolarizer before entering the spectrometer. In some experiments (in Fig. 4) we placed a polarizer just before the depolarizer in order to check the spectral dependence on the polarization of scattered light. Before every series of measurements the spectrometer was calibrated with sulfur (153.8, 219.1 and 473.2 cm^{-1}) and naphthalene (1382.2 and 1576.6 cm^{-1}) characteristic peaks. All the Raman spectra shown in this Section is an arithmetic average of more than 5 measurements within the same sample.

4.2.3 Experimental results and analyses

4.2.3.1 Raman spectrum dependence on laser polarization

Figure 4-8 shows an FE-SEM micrograph of the vertically aligned SWNTs taken from the side at the fractured edge of the substrate. The film thickness is around 5 μm and

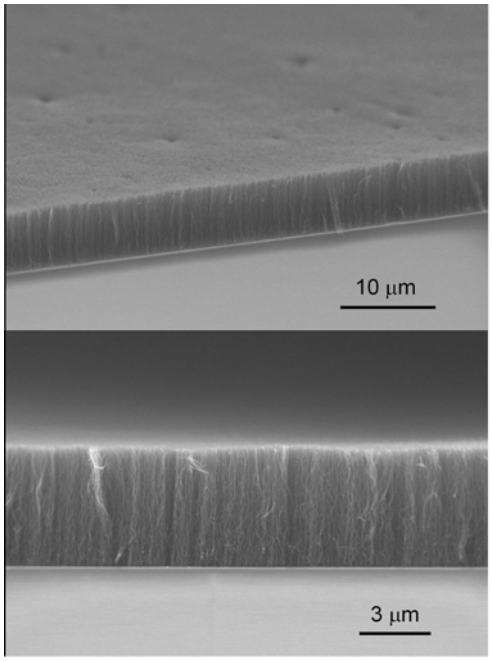


Fig. 4-8. A cross-sectional FE-SEM image of a vertically aligned SWNT film at a fractured edge of the quartz substrate taken from tilted angle (top) and horizon (bottom)

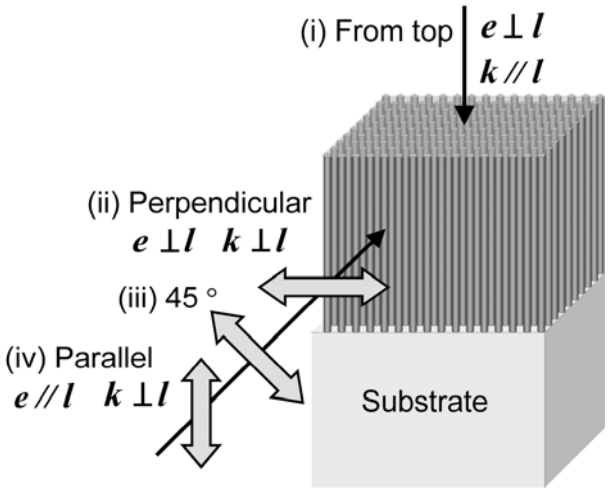


Fig. 4-9. Schematical description of relationships between the laser propagation direction (***k***), the laser polarization direction (***e***), and the SWNT axis direction (***l***) in the measurement.

aligned bundles of SWNTs are visible, which typically have diameter of approximately 15 nm as shown in Fig. 3-3. The overall density of SWNTs has been estimated to be ≈ 1.0 × 10^{17} m^{-2} [16]. From TEM observations, it has been confirmed that no MWNTs are present, and almost all SWNTs are clean i.e. free of amorphous carbon [18]. According to TEM measurements this specimen has a diameter distribution ranging from d = 0.8 ~ 3.0 nm, with an average diameter d_{av} ≈ 1.9 nm and a standard deviation σ = 0.4 ~ 0.5 nm [18]. This distribution is exceptionally broad compared to typical arc-discharge and laser-furnace (within ± 0.2 nm) [20], HiPco SWNTs (d_{av} = 0.98 nm, σ = 0.2 nm) [50], and ACCVD SWNTs grown on zeolite powder at 650°C [51], and therefore it is suitable for probing a wide range of chiralities at the same time.

In the following, 4 different configurations of the laser propagation direction (***k***), the laser polarization direction (***e***), and the SWNT axis direction (***l***) are employed as schematized in Fig. 4-9. The "From top" configuration is $\boldsymbol{k} \,//\, \boldsymbol{l}$ and $\boldsymbol{e} \perp \boldsymbol{l}$, where laser is incident perpendicular to the substrate (or the SWNT film). In the "perpendicular" and "parallel" configurations, the relationships are $\{\boldsymbol{k} \perp \boldsymbol{l}$ and $\boldsymbol{e} \perp \boldsymbol{l}\}$ and $\{\boldsymbol{k} \perp \boldsymbol{l}$ and $\boldsymbol{e} \,//\, \boldsymbol{l}\}$, respectively, and in the "45°" configuration the angle between ***e*** and ***l*** is 45° while maintaining $\boldsymbol{k} \perp \boldsymbol{l}$. In the latter 3 cases, the quartz substrate supporting the SWNT film was broken and stood on its edge using adhesive tape in order to measure on the cross-section of the film.

Figure 4-10 shows RBM spectra taken in (i) from top, (ii) perpendicular, (iii) 45° and (iv) parallel configurations for 488, 514.5, and 633 nm laser wavelengths. On the top of each panel, corresponding diameter scale calculated by the formula 'd (nm) = 248 / ν (cm^{-1})

[36]' is presented. In the 488 nm case, the high frequency spectra including D and G bands are also shown. All the RBM peaks were normalized by the height of G^+ band at 1593 cm^{-1}. The G^+ band was used for the normalization of the spectra assuming it represents resonance, although it is known that the G^+ peak as well as G^- peak are composed of A_1 and E_1 modes located very close (~ 2 cm^{-1}) to each other [38]. At each wavelength, the spectra of cases (i) and (ii) (where $\boldsymbol{e} \perp \boldsymbol{l}$) show the same shape while that of case (iv) (where $\boldsymbol{e}$ // $\boldsymbol{l}$) exhibits a remarkably different spectral shape. The spectra in case (iii) lie in the intermediate between (i) and (iv). It is obvious that some peaks are observed with certain intensities only in the

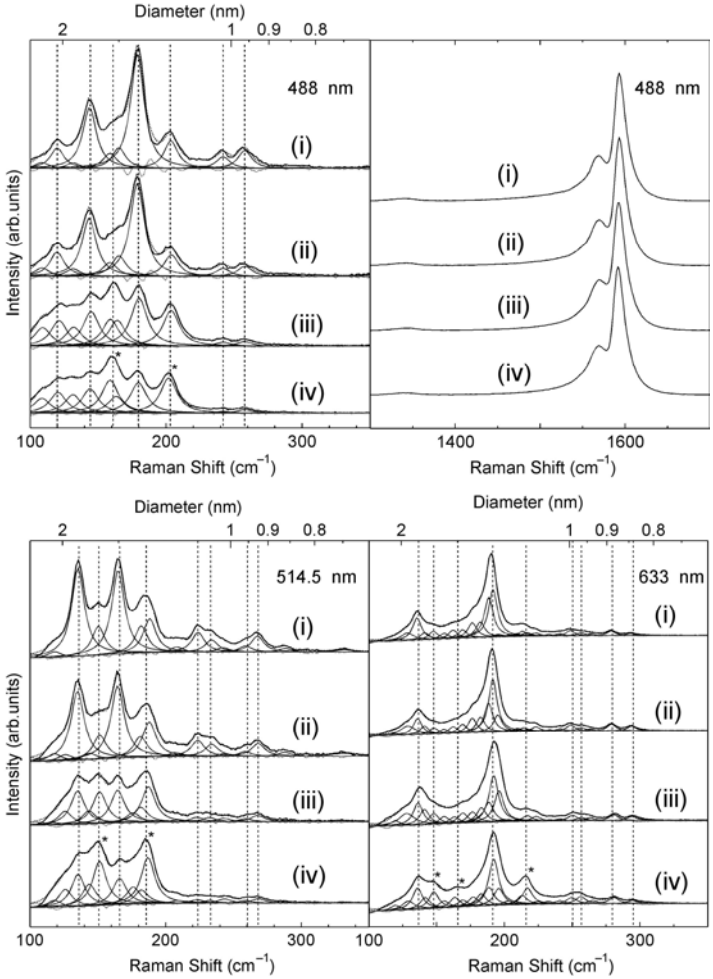


Fig. 4-10. RBM spectra measured by 488, 514.5, and 633 nm lasers for different incident configurations (i - iv, see Fig. 4-9). G band spectra taken at 488 nm are also shown. The RBM spectra were normalized by the corresponding G^+ height and decomposed into Lorentzian curves by maintaining the FWHM values within a spectrum. Asterisks denote the peaks dominantly observed in parallel polarization condition. The oscillatory line on the baseline denotes differential between experimental spectrum and sum of Lorentzian curves.

$\boldsymbol{e} \perp \boldsymbol{l}$ case and diminish in the $\boldsymbol{e} \,//\, \boldsymbol{l}$ configuration, while the other group behaves oppositely. This is especially remarkable for the 488 and 514.5 nm cases.

These spectra are decomposed into Lorentzian curves, keeping the full-width half-maximum (FWHM) of the peaks within each spectra the same. For 633 nm we employed the location of E^S_{22} and E^M_{11} peaks in 180 - 300 cm^{-1} presented by Strano [52] from the photoluminescence experiments: For the range below 180 cm^{-1}, due to the absence of data, we set peak locations so that the sum of the Lorentzian peaks consistently fits all cases. As for 488 and 514.5 nm, since no consistent set of data has been reported in the higher energy region for E^S_{33} and E^S_{44}, we performed decomposition using the least number of peaks necessary for consistent fitting. We allowed ± 1 cm^{-1} freedom to each peak's location based on the resolution of our Raman measurement system.

A slight downshift of G^+ peak from 1593 to 1592 cm^{-1} is seen in the "parallel" configuration due primarily to heating of the SWNTs by the laser, which is more significant when $\boldsymbol{e} \,//\, \boldsymbol{l}$ because light absorption is much enhanced [18]. It is noted that even when the incident laser intensity is further lowered (laser power of 0.1 mW with a spot size of ≈ 7 μm, corresponding to ≈ 250 W/cm^{-2}), the measured spectral shapes for (i) ~ (iv) are essentially the same as those shown in Fig. 4-10, with only a lowered signal-to-noise (S/N) ratio in these cases. Therefore, the spectral changes depending on the measurement condition in Fig. 4-10 are not those induced by the laser heating.

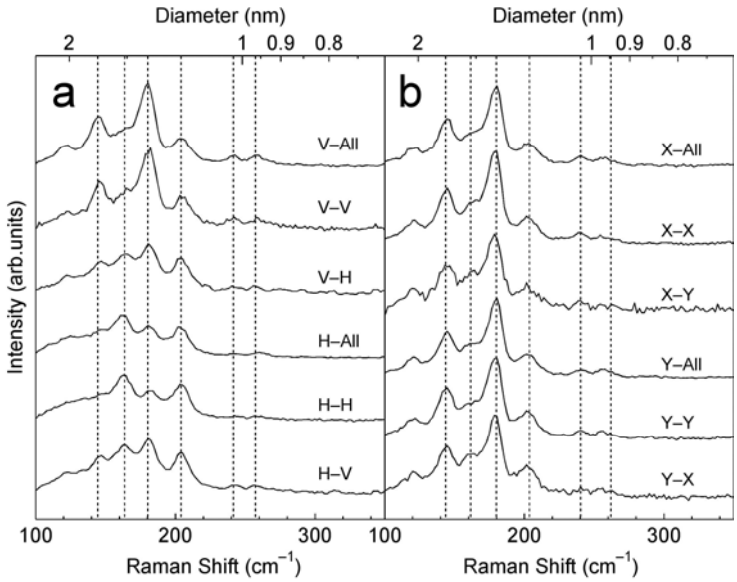


Fig. 4-11. RBM spectra taken at 488 nm with laser light incident (a) from side and (b) from top of the film. A polarizer was inserted in a scattering light path except the case denoted "-All". The "X-Y" description represents the polarization directions of incident and scattered light.

Figure 4-11 shows RBM spectra measured by polarized 488 nm light. To represent the polarization of both incident and scattered light we employ the "X-Y" description often used in polarized Raman studies [39-41]. A polarizer was inserted in the scattering light path, as stated above, except the "-All" cases. In Fig. 4-11a "V" and "H" denote polarization perpendicular and parallel to the SWNT axis, respectively. The intensity ratio of {V-V : V-H : H-H : H-V ≈ 40 : 15 : 100 : 15} at the G^+ band indicates the cross-term "V-H" and "H-V" (either intrinsically or due to disorder in the SWNT alignment) is so weak that the spectra of "V-all" and "H-all" are essentially the same as "V-V" and "H-H". Figure 4-11b shows the same measurement but the light is incident perpendicularly to the substrate in the "from top" configuration, which confirms that in the case of $\boldsymbol{k} \parallel \boldsymbol{l}$ the scattering spectra are independent of "X-Y" relation, as expected.

Figures 4-12a and 4-12b show the change of the height of selected Lorentzian peaks shown in Fig. 4-10 divided by the G^+ intensity among the "from top" - "45°" - "parallel" conditions for 488 and 514.5 nm. The ordinate for each peak is normalized by the value in the case of "from top", to show the grouping behavior of the RBM peaks toward the polarization. The collective peak at 185 cm^{-1} for 514.5 nm is decomposed into two adjacent peaks of at 183 and 188 cm^{-1}. Although some ambiguity remains in the quantitative decomposition, the 188 cm^{-1} peak is recognized to be $\boldsymbol{e} \,//\, \boldsymbol{l}$ peak based on Fig. 4-10. The

peaks apparently associated with the ***e*** // ***l*** configuration for 488 nm and 514.5 nm are {160 and 203 cm^{-1}} and {152 and 188 cm^{-1}}, respectively. As for the 633 nm case, since nearly 20 E^{S}_{22} and E^{M}_{11} peaks are plotted by Strano [52] within 1.96 ± 0.1 eV in the 180 - 300 cm^{-1} range, it was difficult to unambiguously classify each peak into the either of the two groups according to our decomposition method: however, at least the peaks observed at 148, 164, and 217 cm^{-1} should be the ***e*** // ***l*** peaks as identified in Fig. 4-10.

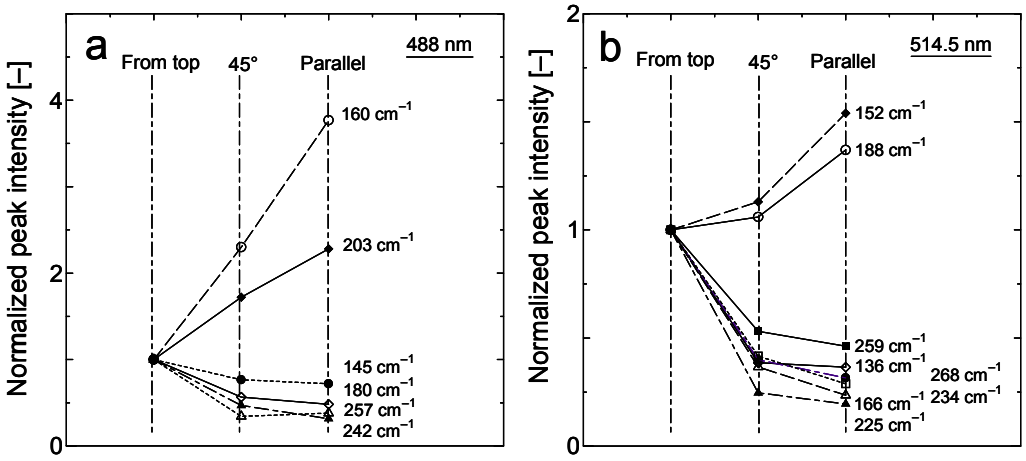


Fig. 4-12. The change in intensities of selected RBM peaks divided by the G^{+} band among "from top" - "45°" - "parallel" conditions for (a) 488 and (b) 514.5 nm. The ordinate was normalized by the values of the "from top" condition.

4.2.3.2 RBM peak behavior by molecular adsorption

It should be noted that in the "from top" measurement, the $\boldsymbol{e} \perp \boldsymbol{l}$ peaks can be suppressed by adsorbing a certain kind of molecules onto the SWNTs. The CVD chamber used for SWNT growth (refer to Fig. 2-15) is evacuated by an oil-free pump (ULVAC, DVS-321). However, if the specimen is placed in a chamber evacuated by ordinary oil pumps (e.g., ULVAC GVD-050, ALCATEL 2015I) in our laboratory, the spectrum shows the same change as that observed in Fig. 4-10 from (i) to (iv). Figure 4-13 shows this change measured in the "from top" condition with 488-nm light. The spectrum of an as-synthesized sample (Fig. 4-13a) changes into that shown in Fig. 4-13b after evacuation for 1 h by the oil pump. This spectral change is reversible; this is because the spectrum of a different molecule-adsorbed sample (Fig. 4-13c) prepared by the same method is readily recovered by heating it at 200°C for 1 h in the CVD chamber evacuated by the oil-free pump (Fig. 4-13d). Although have not yet determined the adsorption molecule species and the microscopic adsorption details, because of its relatively prompt recovery at low temperature (200°C), this easily reproducible result implies that this is a physisorption of some oil-derived molecules diffused from the oil pumps. A slight blue shift of the RBM frequency (~3 cm^{-1}) observed in Fig. 4-13b and c, which is thought to occur due to a hardening of the radial breathing motion of SWNTs by adhered molecules, agrees with the current discussion.

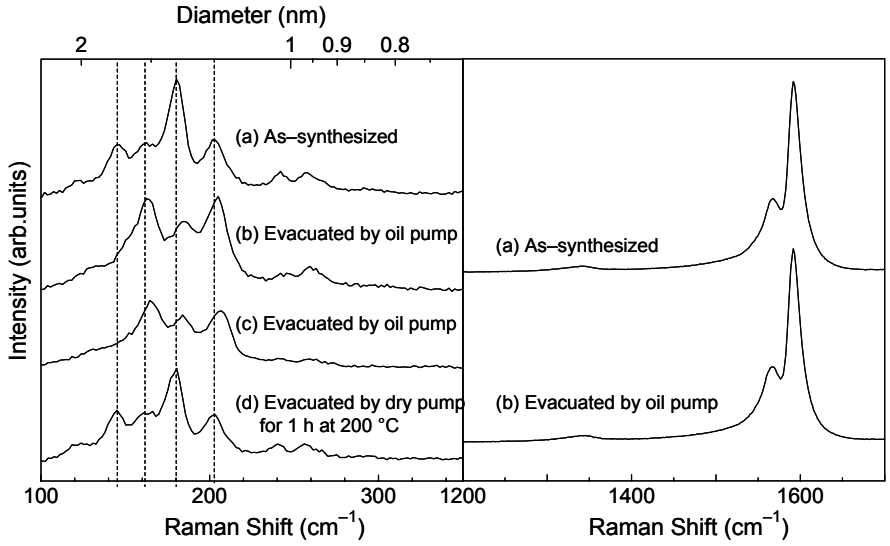


Fig. 4-13. The change in RBM spectra measured in the "from top" condition by 488 nm light. Spectra are (a) the as-synthesized sample and (b) after evacuation by an oil-pump for 1h at 200°C. The original spectrum of a different molecule-adsorbed sample (c) is recovered after heating it at 200°C for 1 h in a CVD chamber evacuated by an oil-free pump (d). The spectra are normalized by the height of the G^+ peak. The right panel shows corresponding tangential mode spectra of (a) and (b).

The right panel of Fig. 4-13 shows a higher frequency region of the left panel and no essential change between the tangential modes of Fig. 4-13a and b. However, since the intensity of the BWF peak [53] is weak before adsorption (Fig. 4-13a), we cannot perfectly negate the possibility of chemisorption by judging the decrease of BWF, as observed by Strano et al. [54]. Furthermore, it was confirmed that a mere wetting of the as-synthesized random SWNT ropes grown on catalyst-supporting zeolite powder by methanol decreases the peak at 180 cm^{-1} as measured by 488-nm light (results not shown), similarly to the observation in Fig. 4-13. Therefore, it is certain that the adsorption of a particular molecule (presumably organic) diminishes the RBM peaks that were preferentially observed for $\boldsymbol{e} \perp \boldsymbol{l}$, while the peaks that are dominant in the $\boldsymbol{e} \,//\, \boldsymbol{l}$ configuration are almost unaffected.

Further, a series of experiments were performed using optical absorption measurements in order to support the above experimental results. First, the vertically aligned SWNT film on a quartz substrate (whose Raman spectra are shown in Fig. 4-14a) was adsorbed by the molecules and its optical absorption spectrum was measured (Fig. 4-14b). The identical specimen was then returned to its original state by the method stated above, and the optical absorption spectrum was measured again (Fig. 4-14c). The effect of adsorption on optical

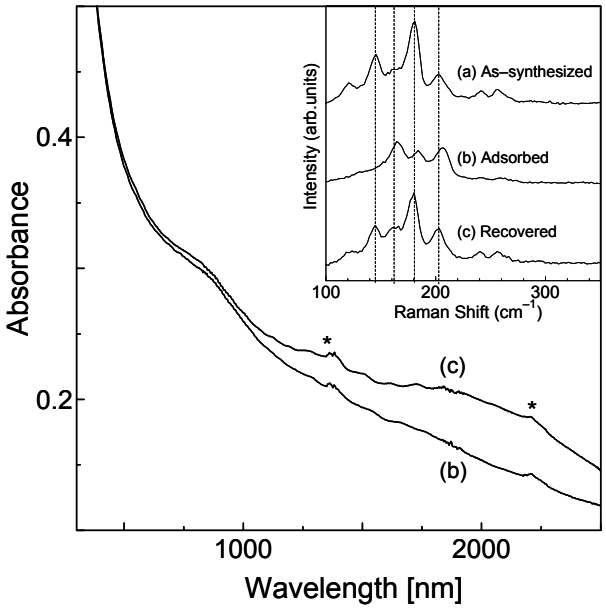


Fig. 4-14. Optical absorption spectra of (b) an adsorbed sample and (c) the same sample after recovery by heating in vacuum at 200°C for 1 h. In the inset are corresponding Raman spectra taken at 488 nm in the "from top" configuration, along with (a) the original spectra before adsorption, to which all spectra are normalized by the height of the G^+ band. Asterisks indicate the switching noise of the spectrophotometer.

absorption is more significant in the low energy region, closer to Fermi level (E_F), as reported in Ref. 55. This observation is interpreted and discussed in a later subsection.

4.2.3.3 RBM peak dependence on laser intensity

The grouping behaviors in RBM peaks are observed in several experimental situations. The most notable of these behaviors is the dependence of the RBM spectral shape on the input laser power. Figure 4-15a shows the change in the RBM spectrum measured for the "from top" configuration with a 488-nm laser at an incident laser intensity ranging from 0.75 to 2.42 mW, whose spectral change is reversible to the laser intensity. This change exhibits an apparent similarity to that observed in Fig. 4-13 for molecular adsorption. Figure 4-15b plots the height of each Lorentzian-decomposed peak normalized by the peak at 0.75 mW (ordinate) against the input laser power (abscissa). While the intensities of the 160 and 203 cm^{-1} peaks for $\boldsymbol{e}$ // $\boldsymbol{l}$ absorption increase linearly with the laser power, the $\boldsymbol{e}\perp\boldsymbol{l}$ peaks seem insensitive to the laser power, as though they were photosaturated. Although the mechanism of this insensitiveness is yet to be determined, this result indicates the certainty of a recognizable difference in the electronic characteristics between the two types of RBM peaks.

Figure 4-15a shows that some of the peaks red-shifteds due to the heating by the laser. Figure 4-15c plots the relative shift of each RBM peak against that of the G^+ band, both from the case of 0.75 mW. While the $\boldsymbol{e}$ // $\boldsymbol{l}$ peaks exhibit a linear red shift of frequency as

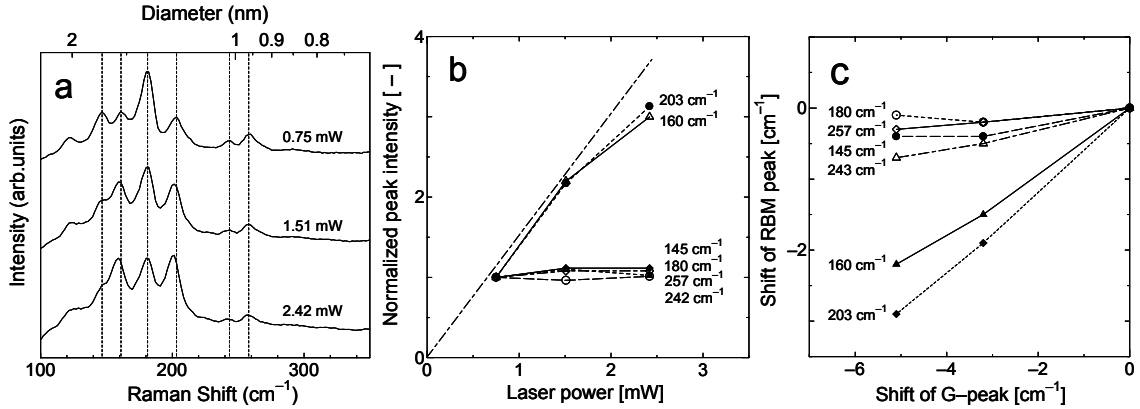


Fig. 4-15. (a) Spectral change of RBM peaks by changing the laser power intensity from 0.75 to 2.42 mW, using 488 nm light in the "from top" configuration. The spectra were normalized by the G^+ band. (b) The intensity variance of each Lorentzian-decomposed RBM peak over the incident laser power. Ordinate values were normalized by those in the case of 0.75 mW. (c) The relationship between the frequency downshift of RBM peak and that of the G^+ peak by heating of SWNTs, both from the case of 0.75 mW.

the temperature rises, the $\boldsymbol{e} \perp \boldsymbol{l}$ peaks do not exhibit a noticeable shift. This is considered to be caused by the difference in the manner of heating by the light incident on the $\boldsymbol{e} \,//\, \boldsymbol{l}$ and $\boldsymbol{e} \perp \boldsymbol{l}$ cases, because the light absorption of the former is several factors higher than the latter [18]. The observations in Fig. 4-15 are further explained in the following subsections.

4.2.4 Discussion and interpretation of obtained data

4.2.4.1 Interpretation of data based on $\Delta\mu = \pm 1$ transition by cross-polarized light

The reason of why only one group of RBM peaks survives in the course of molecular adsorption in Figs. 4-13 and 4-14 can be interpreted as follows. The peaks observed in the $\boldsymbol{e} \,//\, \boldsymbol{l}$ configuration (corresponding to the E^S_{33} and E^S_{44} peaks with energies of 2.41 and 2.54 eV) survive, because they were well lower than E_F (i.e., approximately 1.21 and 1.27 eV below E_F, respectively) and hence almost uninfluenced by the charge-transfer effect [54] caused by molecular adsorption. On the other hand, the peaks observed in the $\boldsymbol{e} \perp \boldsymbol{l}$ configuration diminish when adsorbed because they were close to E_F and hence likely to be subjected to the charge transfer. This proves that the $\boldsymbol{e} \perp \boldsymbol{l}$ peaks obtained thus far have their origin in $\Delta\mu = \pm 1$ resonance (such as E^M_{12}, E^S_{12}, E^S_{24}, etc.), which was predicted by Grüneis et al. [33] who also observed a few peaks in the lower energy region between E^S_{22} and E^M_{11} from a measurement of randomly oriented SWNT ropes [42]. The reason for the difference in the excitation selection rule for optical absorption by SWNTs between parallel- and cross-polarized lights is briefly explained as follows. The transition probability is represented here as

$$W(\boldsymbol{k}) \propto \left| \boldsymbol{p} \cdot \left\langle \Psi^c(\boldsymbol{k}) \middle| \nabla \middle| \Psi^v(\boldsymbol{k}) \right\rangle \right|^2 \tag{48}$$

This is obtained by replacing $\boldsymbol{p}$ and $\boldsymbol{e}_{k,\gamma}$ with ∇ and $\boldsymbol{P}$, respectively, in Eq. 19 in Section 4.1 as

$$\boldsymbol{p} = i\hbar\nabla, \quad \boldsymbol{P} = \mathrm{e}^{i\boldsymbol{k}\cdot\boldsymbol{r}_j} \cdot \boldsymbol{e}_{\boldsymbol{k},\gamma} \tag{49}$$

The absorption matrix element for $\boldsymbol{k} \rightarrow \boldsymbol{k}$' transition was given by Grüneis et al. [33] as

$$\left\langle \Psi^c(\boldsymbol{k}) \middle| \nabla \middle| \Psi^v(\boldsymbol{k}') \right\rangle \propto \left\{ \sum_{j=1}^{N} e^{i(\boldsymbol{k}-\boldsymbol{k}')\cdot\boldsymbol{R}_j^B} U_z\left(2\pi\frac{j}{N}\right)\boldsymbol{v}_g - \sum_{j=1}^{N} e^{i(\boldsymbol{k}-\boldsymbol{k}')\cdot\boldsymbol{R}_j^A} U_z\left(2\pi\frac{j}{N}\right)\boldsymbol{v}_g{}^* \right\} \tag{50}$$

Here, U_z (φ) denotes the rotational matrix around the z-axis by the degree of φ, and $\boldsymbol{v}_g$ denotes the transition dipole moment vector given by [33]

$$\boldsymbol{v}_g \propto U_y(-\pi/6+\theta)\sum_{i=1}^{3} e^{i\boldsymbol{k}'\cdot\boldsymbol{b}_i}\boldsymbol{b}_i \qquad (51)$$

in which θ ($0 \le \theta \le 30°$) denotes the chiral angle of the SWNT under consideration. The atomic coordinate vectors (or *symmetry vectors*) $\boldsymbol{R}^A{}_j$ and $\boldsymbol{R}^B{}_j$ are defined as the position of the j^{th} atom with respect to the unit cell origin by translational vectors $\boldsymbol{R}^A$ and $\boldsymbol{R}^B$, as described in Fig. 4-16a for the case of (4, 2) SWNT. The red and blue circles in the figure denote non-equivalent atoms in the unit cell of graphite. It is noted that $\boldsymbol{R}^A{}_j$ and $\boldsymbol{R}^B{}_j$ in Eq. 50 are periodic of N atoms, which are equal to the number of hexagons in the unit cell of the SWNT. $\boldsymbol{b}_i$ is a vector connecting an atom to its neighboring non-equivalent atom, as schematized in Fig. 4-16b. Therefore, $\boldsymbol{v}_g$ is constant when chirality is given.

a. When $\boldsymbol{k} - \boldsymbol{k}' = \boldsymbol{K}$ ($\Delta\boldsymbol{k} = \boldsymbol{K}$)

Equation 50 can be rewritten as

$$\left\langle \Psi^c(\boldsymbol{k})\middle|\nabla\middle|\Psi^v(\boldsymbol{k}')\right\rangle \propto \left\{\sum_{j=1}^{N} e^{i\boldsymbol{K}\cdot\boldsymbol{R}_j^B} U_z(2\pi\frac{j}{N})\boldsymbol{v}_g - \sum_{j=1}^{N} e^{i\boldsymbol{K}\cdot\boldsymbol{R}_j^A} U_z(2\pi\frac{j}{N})\boldsymbol{v}_g{}^*\right\} \qquad (52)$$

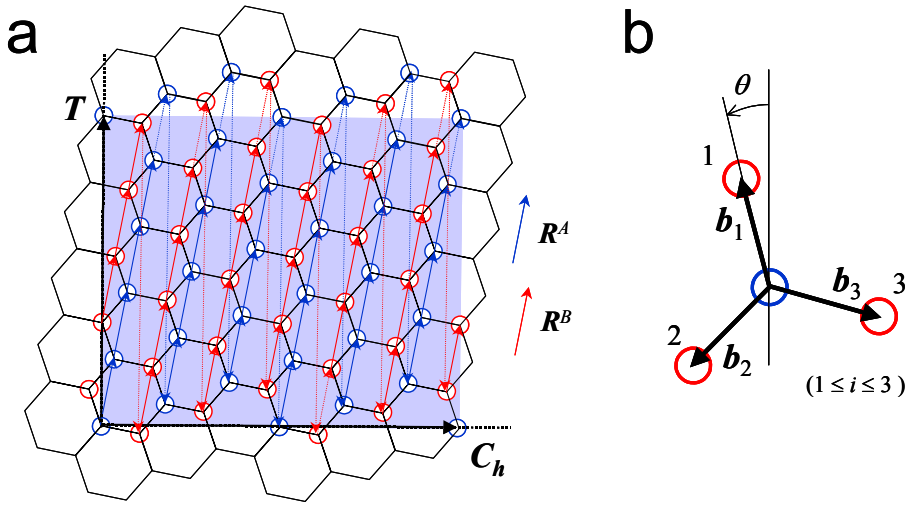


Fig. 4-16. (a) Schematic description of atomic coordinates represented by $\boldsymbol{R}^A{}_j$ and $\boldsymbol{R}^B{}_j$ ($1 \le j \le N$). Red and Blue circles denote non-equivalent atoms in the unit cell of graphite. $\boldsymbol{T}$ and $\boldsymbol{C}_h$ denote translational and chiral vector of (4, 2) SWNT and the shadowed area denotes its unit cell. (b) Schematic for the vectors bi that connects neighboring non-equivalent atoms. θ ($0 \le \theta \le 30°$) is chiral angle of the SWNT.

Using the following relations,

$$\boldsymbol{R} = p\boldsymbol{a}_1 + q\boldsymbol{a}_2, \qquad \boldsymbol{K} = \frac{1}{N}(-t_2\boldsymbol{b}_1 + t_1\boldsymbol{b}_2) \tag{53}$$

$$\boldsymbol{a}_1 = \left(\frac{\sqrt{3}}{2}, \frac{1}{2}\right)a, \quad \boldsymbol{a}_2 = \left(\frac{\sqrt{3}}{2}, -\frac{1}{2}\right)a \tag{54}$$

$$\boldsymbol{b}_1 = \left(\frac{1}{\sqrt{3}}, 1\right)\frac{2\pi}{a}, \quad \boldsymbol{b}_2 = \left(\frac{1}{\sqrt{3}}, -1\right)\frac{2\pi}{a} \tag{55}$$

$\boldsymbol{R}$ and $\boldsymbol{K}$ can be expressed as

$$\boldsymbol{R} = \frac{a}{2}\begin{pmatrix}\sqrt{3}p + \sqrt{3}q \\ p - q\end{pmatrix}, \quad \boldsymbol{K} = \frac{2\pi}{aN}\begin{pmatrix}-\frac{1}{\sqrt{3}}t_2 + \frac{1}{\sqrt{3}}t_1 \\ -t_2 - t_1\end{pmatrix} \tag{56}$$

Therefore,

$$\boldsymbol{K}\cdot\boldsymbol{R} = \frac{2\pi}{N}(t_1 q - t_2 p) = \frac{2\pi}{N} \qquad (\because t_1 q - t_2 p = 1) \tag{57}$$

Since $\boldsymbol{R}_j = j\boldsymbol{R}$ $(1 \le j \le N)$,

$$\boldsymbol{K}\cdot\boldsymbol{R}_j = 2\pi\frac{j}{N} \equiv \varphi_j \qquad (1 \le j \le N, \;\; 0 \le \varphi_j \le 2\pi) \tag{58}$$

Equation 52 can be written using this relationship as

$$\left\langle \Psi^c(\boldsymbol{k})\middle|\nabla\middle|\Psi^v(\boldsymbol{k}')\right\rangle \propto \left\{\sum_{j=1}^{N} e^{i\varphi_j^B} U_z(\varphi_j^B)\boldsymbol{v}_g - \sum_{j=1}^{N} e^{i\varphi_j^A} U_z(\varphi_j^A)\boldsymbol{v}_g{}^*\right\} \tag{59}$$

When the first term of Eq. 12 and its real part are considered, this can be written as

$$\sum_{j=1}^{N} e^{i\varphi_j} U_z(\varphi_j)\boldsymbol{v}_g = \sum_{j=1}^{N}\cos\varphi_j \cdot \begin{bmatrix}\cos\varphi & -\sin\varphi & 0 \\ \sin\varphi & \cos\varphi & 0 \\ 0 & 0 & 1\end{bmatrix}\begin{bmatrix}v_x \\ v_y \\ v_z\end{bmatrix} = \sum_{j=1}^{N}\begin{bmatrix}v_x\cos^2\varphi \\ v_y\cos^2\varphi \\ 0\end{bmatrix} \tag{60}$$

Here, the relationships

$$\int_0^{2\pi}\cos\varphi d\varphi = \int_0^{2\pi}\sin\varphi d\varphi = 0, \qquad \int_0^{2\pi}\cos^2\varphi d\varphi = \int_0^{2\pi}\sin^2\varphi d\varphi = \pi \neq 0 \tag{61}$$

were used. The second term of Eq. 12 is also calculated in a similar manner.

Equation 60 indicates that the $\Delta\boldsymbol{k} = \boldsymbol{K}$ transition is induced solely by the cross-polarized light on the SWNT axis, and not by the light polarized parallel to the axis.

b. When $\boldsymbol{k} - \boldsymbol{k}' = 0$ ($\Delta\boldsymbol{k} = 0$)

Similarly to the above case, Eq. 50 in this case can be rewritten as

$$\left\langle \Psi^c(\boldsymbol{k})\middle|\nabla\middle|\Psi^v(\boldsymbol{k}')\right\rangle \propto \left\{\sum_{j=1}^{N} U_z(2\pi\frac{j}{N})\boldsymbol{v}_g - \sum_{j=1}^{N} U_z(2\pi\frac{j}{N})\boldsymbol{v}_g{}^*\right\}$$
$$= \sum_{j=1}^{N}\begin{bmatrix}\cos\varphi & -\sin\varphi & 0\\ \sin\varphi & \cos\varphi & 0\\ 0 & 0 & 1\end{bmatrix}\begin{bmatrix}v_x\\ v_y\\ v_z\end{bmatrix} = \sum_{j=1}^{N}\begin{bmatrix}v_x\cos\varphi - v_y\sin\varphi\\ v_x\sin\varphi + v_y\cos\varphi\\ v_z\end{bmatrix} = \begin{bmatrix}0\\ 0\\ Nv_z\end{bmatrix} \quad (62)$$

which means that $\Delta\boldsymbol{k} = 0$ transition is induced solely by the light polarized parallel to the SWNT axis and not by the cross-polarized light on the axis.

c. When $\boldsymbol{k} - \boldsymbol{k}' = \boldsymbol{K}_0$ ($\boldsymbol{K}_0 \neq 0$, $\boldsymbol{K}_0 \neq \boldsymbol{K}$)

Using Eq. 56,

$$\boldsymbol{K}_0 \cdot \boldsymbol{R}_j = \frac{a}{2}\left\{\sqrt{3}(p+q)k_{0x} + (p-q)k_{0y}\right\} \equiv \lambda \quad (63)$$

Therefore,

$$\left\langle \Psi^c(\boldsymbol{k})\middle|\nabla\middle|\Psi^v(\boldsymbol{k}')\right\rangle \propto \sum_{j=1}^{N} e^{i\lambda} U_z(2\pi\frac{j}{N})\boldsymbol{v}_g$$
$$= \cdots = \sum_{j=1}^{N}\begin{bmatrix}v_x\cos\varphi\cos\lambda - v_y\sin\varphi\cos\lambda\\ v_x\sin\varphi\cos\lambda + v_y\cos\varphi\cos\lambda\\ v_z\cos\lambda\end{bmatrix} = \begin{bmatrix}0\\ 0\\ 0\end{bmatrix} \quad (64)$$

Here, the relationships

$$\int_0^{2\pi}\cos\varphi\cos\lambda d\varphi = \int_0^{2\pi}\sin\varphi\cos\lambda d\varphi = 0 \qquad (\lambda \neq \varphi) \quad (65)$$

were used. Equation 64 indicates that no transition occurs if $\Delta\boldsymbol{k} = \boldsymbol{K}_0$ ($\boldsymbol{K}_0 \neq 0$, $\boldsymbol{K}_0 \neq \boldsymbol{K}$). The above results indicate that the selection rule for transition varies depending on the polarization of the incident light. If the polarization is parallel to the axis, a $\Delta\boldsymbol{k} = 0$ (i.e., $\Delta\mu = 0$) transition occurs; however, if it is perpendicular to the axis, a quasi-nonvertical $\Delta\boldsymbol{k} = \boldsymbol{K}$ (i.e., $\Delta\mu = \pm 1$) transition occurs. The resonant energy is different in both cases, as schematically shown in Fig. 4-17 for (8,7) and (10,10) SWNTs.

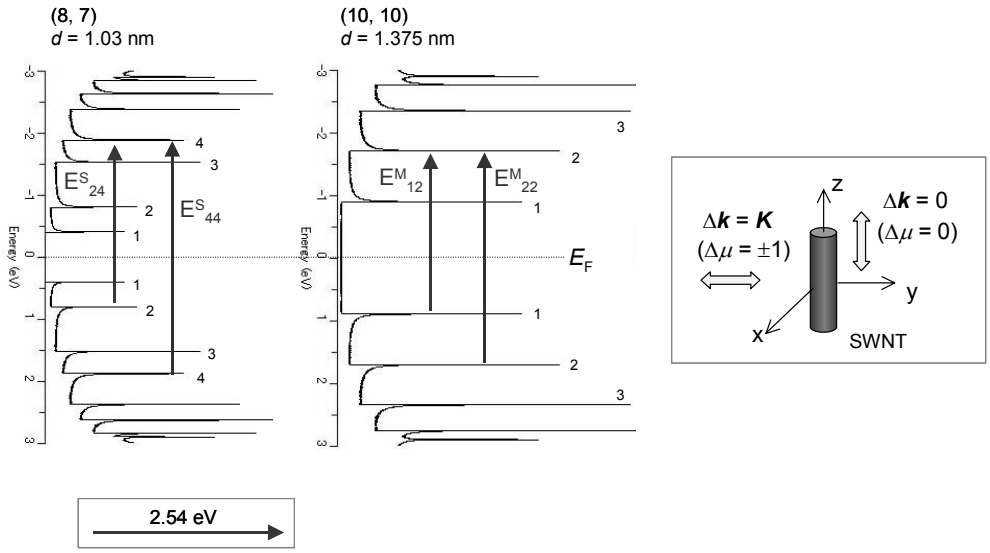


Fig. 4-17. Schematic for $\Delta\mu = 0$ and $\Delta\mu = \pm 1$ transitions for the case of $\Delta E = 2.54$ eV for (8,7) and (10,10) SWNTs. The DOS presented here were calculated by tight-binding method with parameters $\gamma_0 = 2.9$ eV, $a_{c\text{-}c} = 0.144$ nm, and $s = 0.129$.

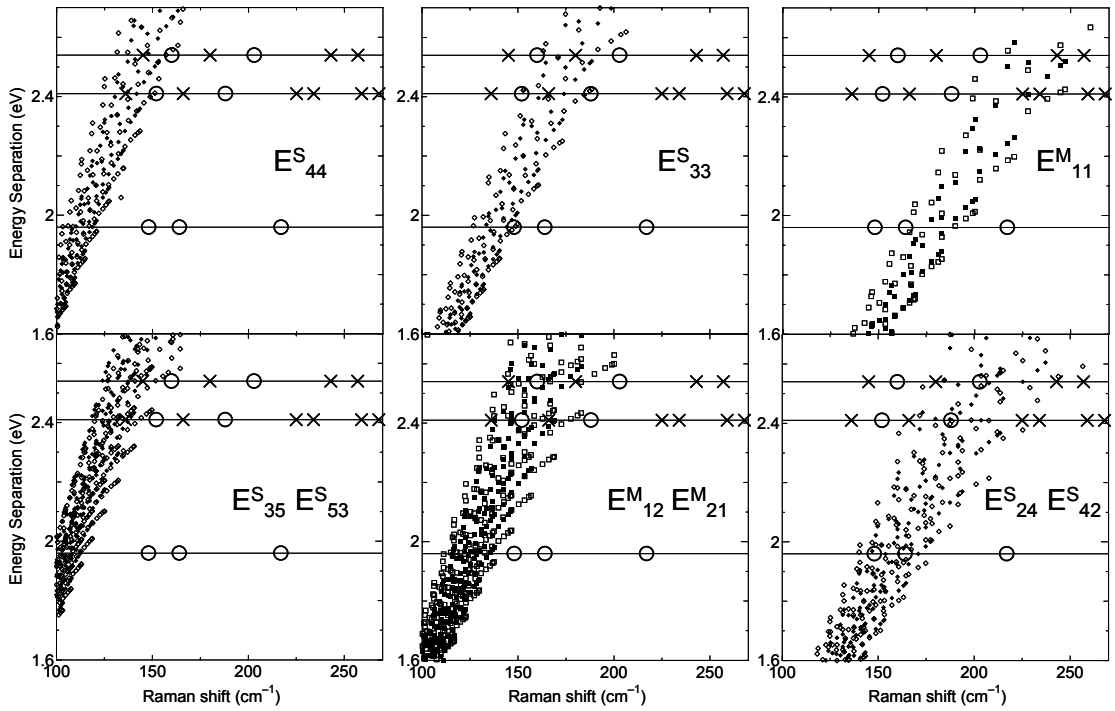


Fig. 4-18. The locations of several unambiguous $\boldsymbol{e} \,//\, \boldsymbol{l}$ ($\Delta\mu = 0$) peaks marked with circles and $\boldsymbol{e} \perp \boldsymbol{l}$ ($\Delta\mu = \pm 1$) with crosses on a Kataura plot calculated from tight-binding (solid symbols) and GW-method (open symbols). Panels in the upper row represent the plots for the $\Delta\mu = 0$ transition while panels in the lower row correspond $\Delta\mu = \pm 1$.

In Figure 4-18, several unambiguous $\boldsymbol{e} \,//\, \boldsymbol{l}$ (i.e., $\Delta\mu = 0$) peaks are indicated in Fig. 4-18 by circles and $\boldsymbol{e} \perp \boldsymbol{l}$ (i.e., $\Delta\mu = \pm 1$) peaks are indicated by crosses on a Kataura plot calculated using the tight-binding (solid symbols) and GW methods [56] (open symbols). The tight-binding DOS was calculated with $\gamma_0 = 2.9$ eV, $a_{c\text{-}c} = 0.144$ nm, and $s = 0.129$ [57]. It should be noted that these Kataura plots differ (especially for semiconducting SWNTs) from the plot based on fluorescence measurements [43]; however, it is still quantitatively effective to discuss the transition energies of metallic as well as semiconducting SWNTs for the higher energy regions (E^S_{33} and E^S_{44}) where the availability of the data obtained by fluorescence measurements are fairly limited. The upper row of Fig. 4-18 shows the plots for the $\Delta\mu = 0$ transition, while the lower row shows those for the $\Delta\mu = \pm 1$ transition. The figure indicates that in both the $\Delta\mu = 0$ and $\Delta\mu = \pm 1$ transitions, the plotted points are present on the edge of the band distribution, i.e., near-zig-zag type SWNTs. This is consistent with the experimental results obtained by Doorn et al. [37] who measured Raman scattering from micelle-dispersed HiPco SWNTs and observed that the near-zig-zag type tubes have a stronger scattering intensity than the near-armchair type tubes. They also showed that the scattering intensity from mod(n – m, 3) = 2 tubes in the E^S_{22} transition is one order higher than that from mod(n – m) = 1 tubes in the same transition; this result is in agreement with the theoretical prediction by Grüneis et al. [33]—the optical absorption matrix element is higher along the K-M line than the K-Γ line. Therefore, strong scattering would arise from the near-zig-zag type SWNTs in transitions E^S_{11} and E^S_{35} for mod(n – m, 3) = 1 tubes and E^S_{22} and E^S_{24} for mod(n - m, 3) = 2 tubes. Based on the tight-binding and GW-based Kataura plots in Fig. 4-18, intense $\Delta\mu = \pm 1$ peaks observed at 145 cm^{-1} for 2.54 eV and 136 cm^{-1} for 2.41 eV belong to either "E^M_{12} (E^M_{21})" or "E^S_{35} (E^S_{53})," and the peaks at 180 cm^{-1} for 2.54 eV and 166 cm^{-1} for 2.41 eV belong to "E^M_{12} (E^M_{21})."

4.2.4.2 Another possibility of interpreting the data

The results from Figs. 4-10 to 4-15 have been completely explained by the difference in the selection rule between the cases of parallel- and cross-polarized light absorptions, i.e., the former results in $\Delta\mu = 0$ and the latter in $\Delta\mu = \pm 1$ photoexcitation of electrons, as discussed in the previous subsection. Nevertheless, this subsection describes another possibility of interpreting those data along with a series of experimental results presented as follows. It is noted here that both the interpretations—the one in the current subsection and

another that was discussed in Section 4.2.4.1—are self-consistent, and further investigations are required to resolve them.

Figure 4-19 shows the Raman spectra obtained with a 488-nm laser light and from the side of the film so that the polarization of the incident light is perpendicular (red) and parallel (blue) to the SWNT axis, in addition to from the top (black), as schematically shown in Fig. 4-9. This is similar to the measurement shown in Fig. 4-10; however, using finer diffraction grating in the measurement, the spectral resolution in Fig. 4-19 was twice that shown in Fig. 4-10. Further, the ordinate is expressed in terms of the absolute CCD count. Although these three spectra were measured consecutively under the same conditions (e.g., laser power, laser spot size, CCD exposure, and other optical settings), the relativity in the ordinate is considered to be imperfect due to the nature of the micro-Raman method.

Figure 4-19 shows that the prominent peak at 180 cm^{-1} in Fig. 4-10 is actually composed of at least an isolated satellite peak at 174 cm^{-1} (FWHM of ~3 cm^{-1}), a shoulder at 178 cm^{-1}, and the primary peak at 181 cm^{-1}. In the result shown in Fig. 4-10, the Lorentzian-fitted peaks at 145, 160, 180, and 203 cm^{-1} have a FWHM of ~11 cm^{-1}. can be

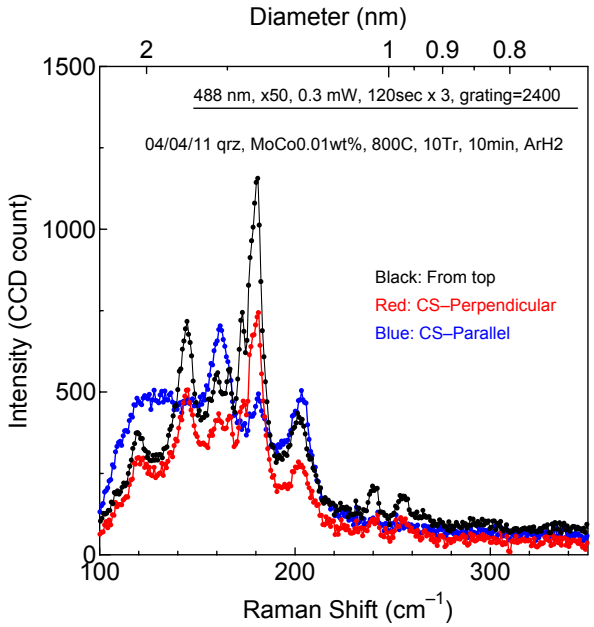


Fig. 4-19. Raman spectra taken with 488 nm laser light from top of the film (black), and from side so that polarization of incident light is perpendicular (red) and parallel (blue) to the SWNT axis as schematized in Fig. 4-9. This is similar to the measurement shown in Fig. 4-10, however, spectral resolution here was doubled from the case of Fig. 4-10 using finer diffraction grating in the measurement. The ordinate is expressed in absolute CCD count and detailed measurement conditions are written in the figure.

interpreted as collective peaks of the "$2n + m$ = const" *family* [58] that are located close to each other in the Kataura plot. Furthermore, the peak at ~160 cm^{-1} is observed to split into 160 and 167 cm^{-1} spikes with a FWHM of ~3 cm^{-1}, as shown in Fig. 4-19, when cross-polarized light is incident on the film (i.e., "from top" and "perpendicular"), while the split is not observed in the case of parallel-polarized light. Regarding the other peaks at 145 and 203 cm^{-1}, the difference in splitting is not observed and they have larger FWHMs of ~9 cm^{-1}.

The reason for the presence of two types of FWHMs (i.e., ~3 cm^{-1} and ~9 cm^{-1}) in a spectrum can be interpreted by either of the following factors: the first is the difference between the physical environment of bundled and isolated SWNTs. Isolated SWNTs are considered to have small FWHMs—as low as 1.5 cm^{-1}—as shown by Kataura et al. [59], while the bundled SWNTs have higher FWHMs due to augmented phonon scattering by neighboring SWNTs. The other factor is the increase in the inter-subband E_{ii} slope in the lower Raman shift region in the "Raman shift" (abscissa) vs. "Energy" (ordinate) Kataura plot. That is, in the lower Raman shift region, the augmented density of RBM peaks along the "Raman shift" axis may cause a coagulation of the peaks, thus leading to an apparent increase in FWHMs.

Furthermore, it is known that bundling cause a slight red shift in resonant energy when compared with the case of isolated SWNTs, as reported by O'Connell et al. [60]. Therefore, the result shown in Fig. 4-10 along with that in Fig. 4-13 leads to another possible interpretation: the group of dominant RBM peaks in the $\boldsymbol{e}\perp\boldsymbol{l}$ configuration correspond to the scattering from the isolated SWNTs, and those in the $\boldsymbol{e}$ // $\boldsymbol{l}$ configuration correspond to the scattering from the bundled SWNTs. The slight difference in the resonant energies between the isolated and bundled SWNTs can be reflected in the RBM spectra due to the following morphological reasons: in the $\boldsymbol{e}\perp\boldsymbol{l}$ configuration (refer to Fig. 4-9), the incident laser light penetrates a greater depth in the SWNT film because it is relatively free from strong collinear absorption (i.e., $\Delta\mu = \pm 1$) by the SWNT bundles (refer to Section 4.1). Therefore, the light is scattered mainly by more isolated SWNTs that presumably reside randomly among the aligned SWNT bundles. In the $\boldsymbol{e}$ // $\boldsymbol{l}$ configuration, on the other hand, the incident laser light could be dominantly absorbed and scattered by SWNT bundles within a shallower penetration depth, in which a smaller amount of light is scattered by the isolated SWNTs.

This interpretation does not contradict the experimental observations presented in Figs. 4-13 to 4-15. In Fig. 4-13, the decrease of the $\boldsymbol{e}\perp\boldsymbol{l}$ peaks caused by the molecule adsorption

is interpreted as the effect of adsorption being more significant for isolated SWNTs than bundled SWNTs, due to the higher degree of surface exposure in the former. Accordingly, the decrease in the optical absorbance in the lower energy region shown in Fig. 4-13 would be caused mainly by the charge transfer from randomly residing isolated SWNTs due to the adsorption. The observation in Fig. 4-15c can be explained as follows: It is more difficult to heat isolated SWNTs due to their higher thermal conductivity—as confirmed by their small FWHM value—compared with bundled SWNTs, in which phonon scattering is more significant. In essence, the result shown in Fig. 4-15c indicates an important possibility of calculating the thermal conductivity of SWNTs, which strongly depends on whether they are isolated or bundled, by measuring the FWHM of the RBM spectrum. The result shown in Fig. 4-15b is not straightforward; however, it can be explained that isolated SWNTs are more likely to be photo saturated than bundled SWNTs because the relaxation time of the former (especially when they are semiconducting) is expected to be longer than the latter.

In order to further examine this interpretation, Raman scattering measurements were performed on the non-aligned SWNTs grown from Co-Mo catalyst supported on zeolite powder (refer to Section 2.1) using 488-nm laser light. Figure 4-20 shows the RBM spectra measured from SWNTs that underwent 3 s (black) and 10 min (red) CVD reactions. In the

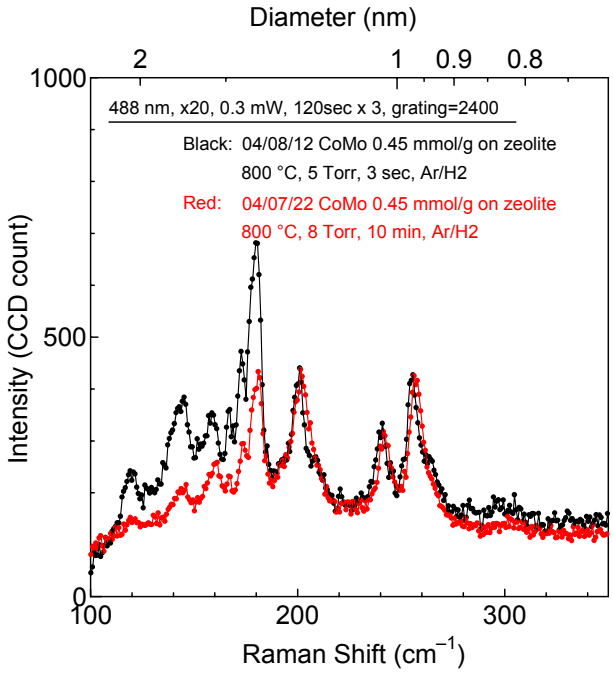


Fig. 4-20. RBM spectra taken with 488 nm laser light from randomly grown SWNTs on zeolite support powder. CVD reaction times are 3 sec (Black) and 10 min (Red). Detailed measurement and CVD conditions are written in the figure.

case of the 3 s CVD, the most prominent peak is observed at ~180 cm^{-1}, and the spectrum is similar to that measured from the vertically aligned SWNT film with the $\boldsymbol{e} \perp \boldsymbol{l}$ configuration (refer to Figs. 4-10 and 4-11). In the case of the 10-min CVD, however, several RBM peaks—especially those below 180 cm^{-1}—are reduced when compared with the 3-s case, and the thickening of SWNT bundles is considered to be responsible for this spectral change. Therefore, if the thickening of bundles is responsible, it is considered that the peaks at 180 and 145 cm^{-1} originate from isolated SWNTs and they decrease when SWNTs are bundled because of a slight red shift in the resonant condition.

Finally, Fig. 4-21 presents the RBM spectra measured from the "3 s" SWNTs grown on zeolite powder that underwent different treatments: as-synthesized state (black), molecular-adsorbed state by evacuation with an oil-pump (red), and wetted with a few drops of methanol and then dried at room temperature for several hours (blue). The figure shows that despite the samples being identical, the RBM peaks in the lower frequency region—especially those below 180 cm^{-1}—exhibit remarkable reduction in both treatments. In the case of adsorption with oil-derived molecules (red), the charge transfer due to the

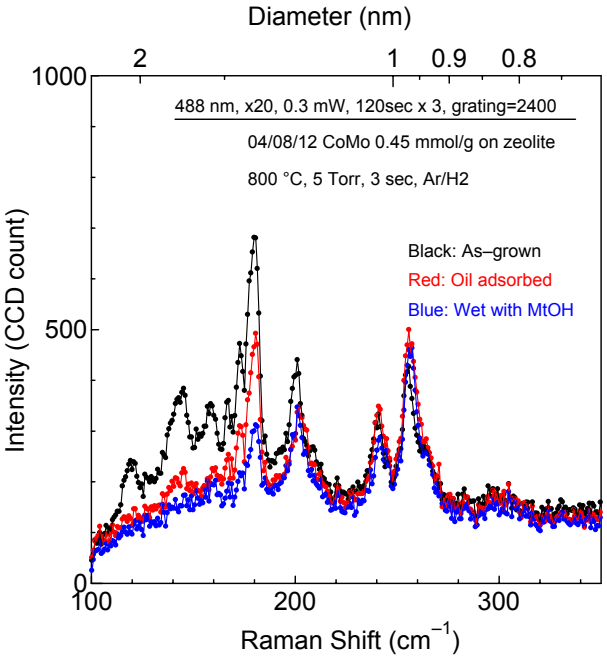


Fig. 4-21. RBM spectra measured with 488 nm laser light from the "3 sec" SWNTs grown on zeolite powder that underwent different treatment, as-synthesized state (Black), molecular-adsorbed state by evacuated with an oil-pump as Fig. 4-13 (Red), and wetted with a few drops of methanol and then dried in room temperature for several hours (Blue). Detailed measurement conditions are written in the Figure.

adsorption is considered to be solely responsible for the spectral change, as observed in Fig. 4-13. The only difference between Figs. 4-21 and 4-13 is that the oil-adsorbed spectrum in the former shows a reduction of the peak at 160 cm^{-1}. This is unresolved and requires further investigation; however, it may be explained that, in addition to isolated SWNTs, SWNTs with larger diameter are considered to be more easily subject to the charge transfer because of their weaker eDOS.

Further, when the treatment involves wetting with methanol (blue), the spectral change is considered to originate from both the charge transfer due to adsorption of methanol molecules and a change in morphology (e.g., thickening of bundles) caused by surface tension effect in the drying process. Complete elucidation of the mechanism responsible for this RBM spectral change has not been attained yet, however at least, it is clear that the shape of the RBM spectrum should be regarded as being fairly sensitive to both the physical and morphological environments of the considered SWNTs. Therefore, the conventional knowledge that the shape of the RBM spectrum represents the intrinsic character (i.e., diameter distribution or metal/semiconducting ratio) of the SWNTs should be altered for the characterization of SWNTs; this is because the spectrum is by and large reflecting their extrinsic conditions, as proved by the results shown in this section.

4.2.5 Summary of polarization dependence of Raman scattering

Resonant Raman scattering from the vertically aligned SWNT films was investigated by changing the polarization of the incident laser light with respect to the direction of alignment. The shape of the RBM spectrum was observed to exhibit strong dependence on the incident polarization. The RBM peaks were grouped into two types according to their behavior: In one type, the peak intensity was strong when the light polarization was perpendicular to the SWNT axis ($\boldsymbol{e} \perp \boldsymbol{l}$), while in the other type, the peak intensity was strong when the light polarization was parallel to the SWNT axis ($\boldsymbol{e} \,//\, \boldsymbol{l}$). The molecular adsorption experiment demonstrated that charge transfer between SWNTs and adsorbed molecules was responsible for the subsequent change in the RBM spectrum.

In view of the changes observed in the RBM spectrum, two self-consistent interpretations are proposed: In the first, the former group ($\boldsymbol{e} \perp \boldsymbol{l}$) originates from the $\Delta\mu = \pm 1$ transition while the latter ($\boldsymbol{e} \,//\, \boldsymbol{l}$) corresponds to the $\Delta\mu = 0$ transition, which is consistent with earlier theoretical predictions [10,33]. The considerable reduction of $\Delta\mu = \pm 1$ RBM peaks during molecular adsorption is supported by a charge transfer near the Fermi level, as elucidated by optical absorption measurement. Some of the observed $\Delta\mu = \pm 1$ peaks at energies

commonly used in RRS (2.41 and 2.54 eV) are unambiguously attributed to specific $E_{i,i\pm1}$ energy bands in the Kataura plot.

In the second interpretation, based on the fact that the resonant energy of bundled SWNTs slightly differs (i.e., red shifted) from that of isolated SWNTs, the $\boldsymbol{e} \perp \boldsymbol{l}$ RBM peaks originate from isolated SWNTs whereas the $\boldsymbol{e} \,//\, \boldsymbol{l}$ peaks originate from bundled SWNTs. The coexistence of scatterings from isolated and bundled SWNTs in one RBM spectrum is supported by the coexistence of two different FWHM values (i.e., ~3 cm^{-1} and ~9 cm^{-1}). The reason for the dependence of the dominant source of scattering (either isolated or bundled SWNTs) on the incident light polarization was explained in terms of the morphology of the vertically aligned film. This interpretation was also consistent with observations in Figs. 4-13 to 4-15. Furthermore, the observation in Fig. 4-20 that the peaks at ~145 and 180 cm^{-1} are prominently noticed from random SWNTs grown on zeolite support powder for 3 s is also consistent with the proposed interpretation. However, in order to decide the appropriate interpretation, further measurements with a higher wavenumber resolution (<2 cm^{-1}) are essential.

In this section, it was presented that the RBM spectra are not representing the intrinsic character of the examined SWNTs (e.g., diameter distribution or metal/semiconducting ratio) even with the use of several *fixed* laser excitation energies. Since the RBM spectra are drastically affected by the extrinsic conditions of SWNTs, such as the morphology, degree of bundling, and/or existence of molecular adsorption, considerable caution must be paid when attempting to demonstrate the selective enrichment or removal of either the semiconducting or metallic SWNTs based on RRS analysis. The apparent change of the RBM spectral shape should be compensated by the use of *continuous*-energy laser light in order to correctly distinguish whether the observed reduction in the RBM intensity is due to the selective removal of specific type of SWNTs or this is due to the mere shift of resonant energy caused by the change in the SWNT environment. Furthermore, a wavenumber resolution of at least less than 2 cm^{-1} should be used in order to identify the physical state of SWNTs, i.e., isolated or bundled.

In any interpretation, the RBM spectra can be varied even from a measurement from the identical sample depending on the incident polarization and physical environment of the SWNTs. Information on the nature of each RBM peak revealed in this section will aid in providing a sounder characterization of SWNTs by RRS analysis.

4.3 Optical applications of SWNT film directly synthesized on solid surfaces

4.3.1 Motivation and research background

Optical pulsed lasers are of great interest in many industrial and scientific fields. Passively mode-locked fiber lasers are one of the best pulse sources currently available because of their simplicity and ability to generate transform-limited optical pulses in the picosecond and sub-picosecond regimes [61]. Since there is no necessity for expensive modulators that are required in actively mode-locked lasers, passively mode-locked lasers are cheaper as well as structurally simpler. Instead of the modulators, however, a passively mode-locked laser requires a mode locker; this is a device whose response depends on the incident light intensity. The mode locker is usually a fast saturable absorber, such as a semiconductor-based [62] or fiber-based saturable absorber [63,64].

The semiconductor-based saturable absorbers, however, require complex and expensive clean-room-based fabrication systems and processes. Furthermore, since the semiconductor-based saturable absorber is a reflective device, its use is limited to certain types of linear cavity topology. The fiber-based saturable absorber is simple but requires long nonlinear fibers, typically longer than tens of meters, which makes the laser unstable and lowers the repetition rate of the output light.

It was recently discovered that SWNTs exhibit excellent characteristics as saturable absorbers due to their strong third-order non-linearity in electric susceptibility ($\chi^{(3)}$) and their ultrafast relaxation of excited electrons [35,36]. Moreover, the E^{S}_{11} absorption maxima of SWNTs is near the 1.55 μm wavelength band, as shown in Fig. 2-27, which is considerably advantageous for their application in optical telecommunication. Furthermore, Set et al. recently proposed and demonstrated a saturable absorber incorporating a carbon nanotube (SAINT) [67–70], which possesses several important properties, such as ultrafast recovery time, polarization insensitivity, a theoretically high optical damage threshold, mechanical and environmental robustness, chemical stability, and the ability to operate in transmission, reflection, and bidirectional modes.

SAINTs were previously fabricated by the following process: SWNTs produced by the laser-ablation method [71] were purified and dispersed in ethanol, which was then sprayed onto the surface of a quartz substrate to form a thin film of SWNTs. However, such a process is laborious and the optical uniformity of the obtained film is low, in which light scattering is not negligible due to the microscopic roughness of the film. In this section, it is

demonstrated that the SWNT film grown directly on quartz substrates developed in Section 2.3 can be employed as a new SAINT material. The mode-lock properties exhibited with the proposed SAINT are investigated and described.

4.3.2 Experimental setup

A schematic of the mode-locked fiber ring laser is shown in Fig. 4-22. A very short (40 cm) fluoride-based Er-doped fiber (EDF), backward pumped by a 980-nm laser diode (LD), is used as the laser gain medium. The use of fluoride-based EDF is advantageous because of its high gain coefficient [72]. Two optical isolators are inserted to prevent back reflection in the cavity and to ensure unidirectional operation. The output light from the EDF is launched through a fiber collimator and focused through an aspherical lens onto the SAINT, which is directly synthesized on a quartz substrate. The spot size on the SAINT is ~10 μm. The output light from the SAINT is collected and launched back into the fiber cavity via another set of matching spherical lens and collimator. A 1-m-long dispersion-shifter fiber (DSF) was attached to each collimator, resulting in a total cavity length of 4.1 m. The output of the laser is tapped through the 30% port of a fiber coupler, whereas the 70% port is used to feed the output back into the cavity.

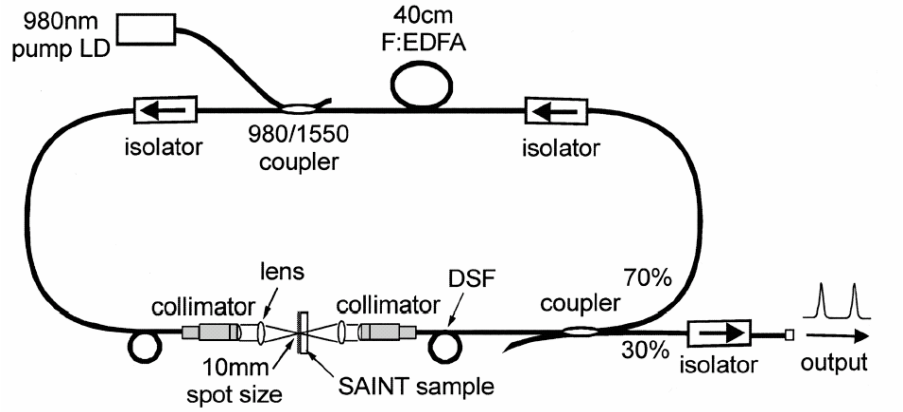


Fig. 4-22. Schematic description of mode-locked fiber laser with a SWNT film directly grown a quartz substrate used as a SAINT device. This figure is cited from Ref. 73.

4.3.3 Principles of mode-locked ring fiber laser

Pulsed light can be generated by a mode-locking method. The frequency in the resonant mode differs by integral multiples of $c/2L$, where c and L denote the speed of light and the length of the resonator used, respectively. However, the phase of these "modes" from which continuous wave (CW) light is produced is generally random. When the phase of all modes is locked, a series of intense pulses is obtained by constructive interferences between light packets. The formulation for the n^{th}-mode wave with amplitude ε_0 and frequency ω propagating in a resonator of length L can be expressed as

$$\varepsilon_n(t) = \varepsilon_0 e^{i\omega t} \tag{66}$$

Using the relationship

$$\omega = \frac{2\pi c}{\lambda} = 2\pi c \frac{n}{2L} = 2\pi\left(\frac{nc}{2L}\right) \quad \left(\because \lambda = \frac{2L}{n}\right) \tag{67}$$

Equation 66 is rewritten as

$$\varepsilon_n(t) = \varepsilon_0 \exp\left\{i\left(\omega_0 + \frac{\pi nc}{L}\right)t\right\} \tag{68}$$

where ω_0 denotes the angular frequency for the lowest mode. The superimposed wave made up by summing N modes ($n = 0, 1, \cdots, N-1$) of the mode-locked waves is written as

$$\varepsilon(t) = \sum_n \varepsilon_n(t) = \varepsilon_0 e^{i\omega_0 t} \sum_{n=0}^{N-1} e^{\frac{i\pi nct}{L}} \tag{69}$$

Further, using the relationship

$$\begin{aligned} \sum_{n=0}^{N-1} e^{\frac{i\pi nct}{L}} &= 1 + e^{\frac{i\pi ct}{L}} + e^{\frac{2i\pi ct}{L}} + \cdots \\ &= \frac{\sin(N\pi ct/2L)}{\sin(\pi ct/2L)} \cdot e^{\frac{(N-1)i\pi ct}{2L}} \end{aligned} \tag{70}$$

Substituting Eq. 69 into Eq. 70,

$$\varepsilon(t) = \sum_n \varepsilon_n(t) = \varepsilon_0 \exp\left[i\left\{\omega_0 + \frac{(N-1)\pi c}{2L}\right\}t\right] \cdot \frac{\sin(N\pi ct/2L)}{\sin(\pi ct/2L)} \tag{71}$$

is obtained. Since the intensity of the output light, referred to as I, is proportional to the square of the magnitude of the wave, it is expressed as

$$I(t) \propto e^* e = {\varepsilon_0}^2 \frac{\sin^2(N\pi ct/2L)}{\sin^2(\pi ct/2L)} \tag{72}$$

The functional shape is schematically expressed in Fig. 4-23. Equation 72 means that the pulse width shown in Fig. 4-23 decreases with an increase in the number of superposed

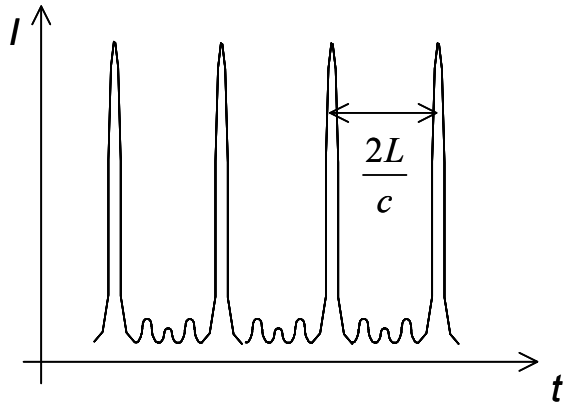


Fig. 4-23. Schematic of intensity of mode-locked light I as a function of time t given by Eq. 72.

waves N, and the pulse frequency is given by $2L/c$. The physical meaning of this observation can be described by Heisenberg's uncertainty principle:

$$\Delta E \cdot \Delta t \approx h \quad \text{or} \quad \Delta\omega \cdot \Delta t \approx 2\pi \tag{73}$$

4.3.4 Results and summary

At a pump power of approximately 17 mW, the laser self-starts to mode lock and produces single pulses in a round-trip time, as shown in Fig. 4-24a. Due to the use of very short fluoride-based EDF, the fundamental repetition rate is 50.4 MHz, eight times higher than that of the previous SAINT-based mode-locked fiber lasers [68–70]. The average output optical power is ~–7 dBm (200 μW). The output spectrum in Fig. 4-24b shows that the 3-dB spectral width is ~3.0 nm. The second-harmonic generation autocorrelation trace was measured with a two-photon absorption autocorrelator (Alnair APM-1000) and an estimated FWHM of 0.9 ps. The resulting time-bandwidth product of 0.34 indicates that the pulses are transform limited. This fundamental mode-locked operation was reproducible and stable for several hours in the laboratory. It was also observed that the laser could produce multiple pulses in a round-trip time (multiple-pulse mode) by adjustment of intracavity dispersion and polarization with the addition of several meters of SMFs and a polarization controller. When the SAINT is removed from the laser cavity, it is not possible to mode lock the laser even with a high pump power. Direct synthesis of SWNTs was performed on the fiber ends, as shown in the FE-SEM image and Raman scattering spectrum in Figs. 4-25 and 4-26, respectively. However, the mode-locking operation with this device was not stable, probably because of the terminal reflection at the fiber ends.

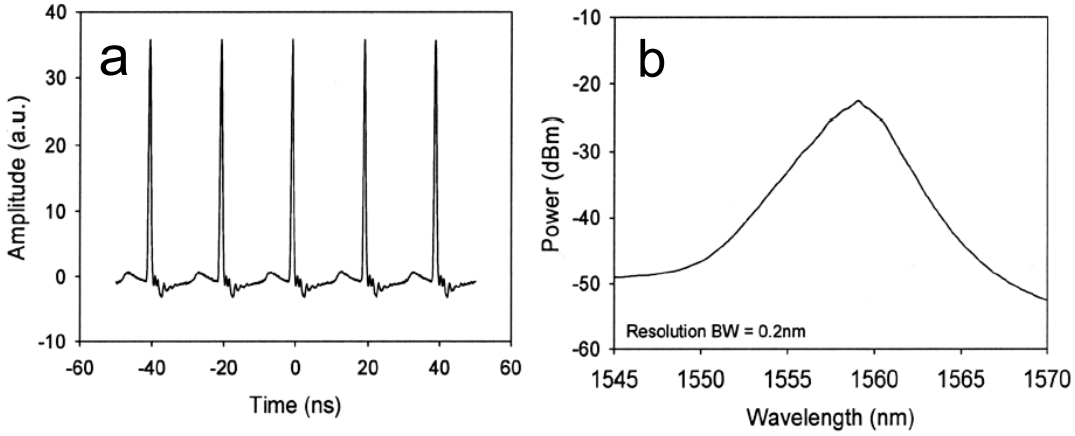


Fig. 4-24. (a) Pulse waveform and (b) spectrum of the output laser light. These figures were cited from Ref. 73.

In summary, the SWNT film grown directly on the surface of the quartz substrate developed in the previous section was demonstrated to serve as a new SAINT device for optical applications. It was successfully applied to passively mode lock a fiber laser to produce sub-picosecond pulses at a 50-MHz repetition rate.

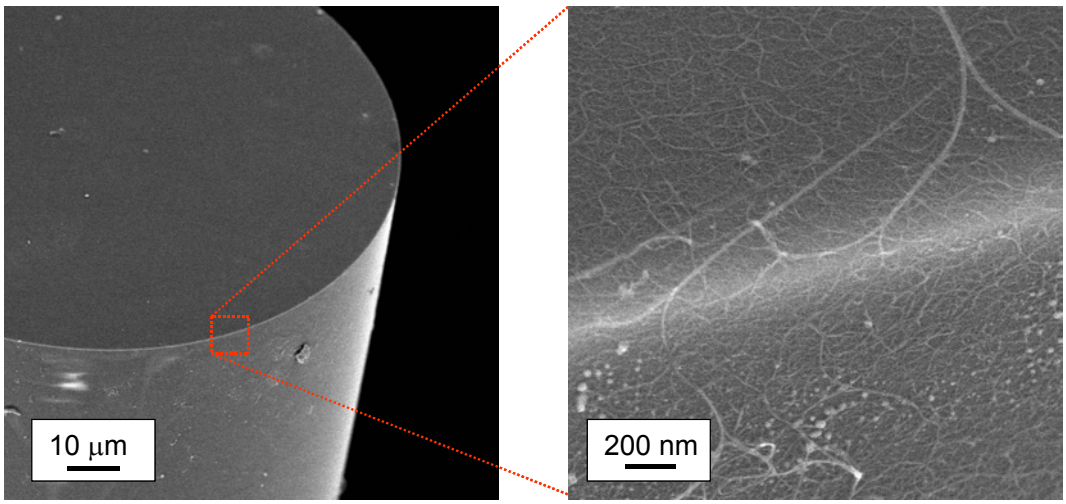


Fig. 4-25. FE-SEM image of SWNTs directly grown on the tip surface of an optical fiber whose diameter is 0.1 mm. Right panel is partial magnification of the left.

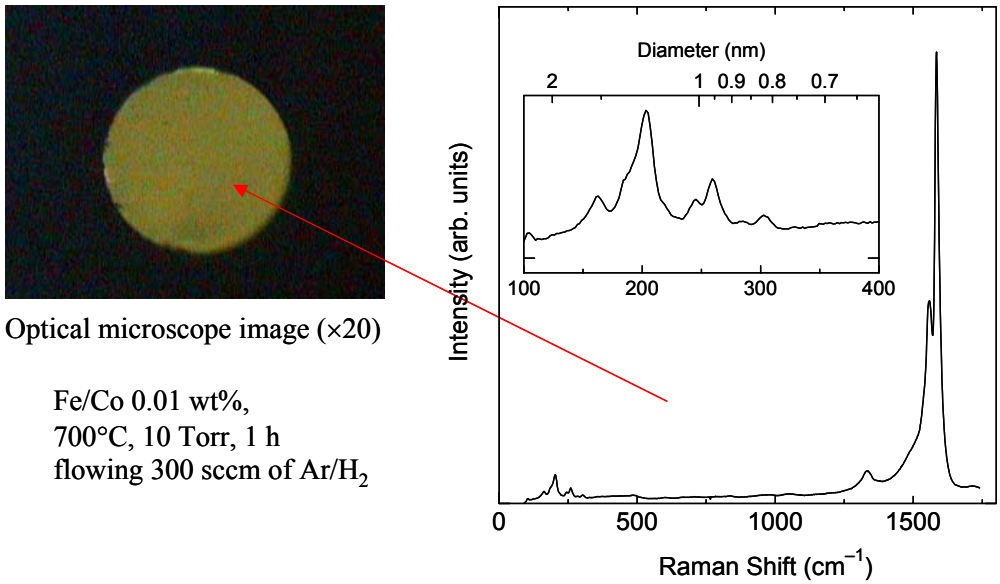


Fig. 4-26. Raman scattering spectra taken by 488 nm laser light from the SWNT film directly grown on the end of an optical fiber (diameter = 0.1 mm). The sample is the same as that presented in Fig. 4-25. The picture in the left is an optical microscope image (×20) of the top end of the optical fiber after CVD.

4.4 Summary of Chapter 4

In this chapter, the fundamental optical properties and practical applications of SWNTs were investigated and described using the SWNT films directly grown on quartz substrates.

In Section 4.1, the anisotropic optical absorption properties of SWNTs were elucidated for a wide energy range of 0.5–6.0 eV. The optical absorption cross sections for both parallel and perpendicular to the SWNT axis were determined. The peaks at 4.5 and 5.25 eV were discovered to correspond to the maximum of $\mathrm{Im}\{\varepsilon_{\perp}\}$ (parallel to the SWNT axis) and that of $\mathrm{Im}\{-\varepsilon_{\parallel}^{-1}\}$ (perpendicular to the SWNT axis), respectively, originating from the optical properties of graphite.

In Section 4.2, it was demonstrated that the shape of the RBM exhibited a strong dependence on the polarization. The RBM peaks were grouped into two types according to their behavior: In one type, the peak intensity was strong only for perpendicular polarization ($e \perp l$), while in the other, the peak intensity was strong only for parallel polarization ($e \,//\, l$). The RBM spectra can be varied even from a measurement from the identical sample depending on the incident polarization and physical environment of SWNTs. The knowledge on the nature of each RBM peak shown in this section will help provide a sounder characterization of SWNT specimens by RRS analysis.

In Section 4.3, the randomly oriented SWNT film grown on the quartz substrate was demonstrated to serve as a SAINT device for optical applications at a 1.55-μm wavelength. A passively mode-locked fiber laser was successfully fabricated to produce sub-picosecond pulses at a 50-MHz repetition rate.

Acknowledgement for Chapter 4

The author cordially thanks Prof. S. Yamashita and Mr. Y. Inoue at The University of Tokyo and Dr. S. Y. Set at Alnair Labs for their valuable collaboration and discussions on the mode-locked fiber laser development presented in Section 4.3. The contents of Section 4.3 have been published in *Optics Letters*, vol. 29, pp. 1581–1583, 2004 by S. Yamashita, Y. Inoue, S. Maruyama, Y. Murakami, H. Yamaguchi, M. Jablonski, and S.Y. Set. Thanks are also due to Dr. H. Kataura at the National Institute of Advanced Industrial Science and Technology (AIST) for the discussion and Mr. M. Oba for his assistance in constructing the Kataura plot shown in Fig. 4-18.

References for Chapter 4

1. S. Iijima and T. Ichihashi, Nature **363** (1993) 60.
2. R. Saito, G. Dresselhaus, and M.S. Dresselhaus, *Physical Properties of Carbon Nanotubes*, Imperial College Press, London, 1998.
3. *Carbon Nanotubes: Synthesis, Structure, Properties and Applications,* edited by M. S. Dresselhaus, G. Dresselhaus, and Ph. Avouris, Springer-Verlag, Berlin, 2001.
4. R. Martel, T. Schmidt, H. R. Shea, T. Hertel, P. Avouris, Appl. Phys. Lett. **73** (1998) 2447.
5. Y.C. Chen, N.R. Raravikar, L.S. Schadler, P.M. Ajayan, Y.P. Zhao, T.M. Lu, G.C. Wang, X.C. Zhang, Appl. Phys. Lett. **81** (2002) 975.
6. Y. Sakakibara, S. Tatsuura, H. Kataura, M. Tokumoto, Y. Achiba, Jpn. J. Appl. Phys. **42** (2003) L494.
7. S. Yamashita, Y. Inoue, S. Maruyama, Y. Murakami, H. Yamaguchi, M. Jablonski, S.Y. Set, Opt Lett. **29** (2004) 1581.
8. J.A. Misewich, R. Martel, P. Avouris, J.C. Tsang, S. Heinze, J. Tersoff, Science **300** (2003) 783.
9. M. Freitag, Y. Martin, J.A. Misewich, R. Martel, P. Avouris, Nano Lett. **3** (2003) 1067.
10. H. Ajiki and T. Ando, Physica B **201** (1994) 349.
11. M. F. Lin and D. S. Chuu, Phys. Rev. B **57** (1998)10183.
12. F. L. Shyu and M. F. Lin, Phys. Rev. B **60** (1999) 14434.
13. J. Hwang, H. H. Gommans, A. Ugawa, H. Tashiro, R. Haggenmueller, K. I. Winey, J. E. Fischer, D. B. Tanner, A. G. Rinzler, Phys. Rev. B **62** (2000) 13310.
14. M. Ichida, S. Mizuno, H. Kataura, Y. Achiba, A. Nakamura, Appl. Phys. A **78** (2004) 1117.
15. M. F. Islam, D. E. Milkie, C. L. Kane, A. G. Yodh, J. M. Kikkawa, Phys. Rev. Lett. **93** (2004) 037404.
16. Y. Murakami, S. Chiashi, Y. Miyauchi, M. Hu, M. Ogura, T. Okubo, S. Maruyama, Chem. Phys. Lett. **385** (2004) 298.
17. S. Maruyama, R. Kojima, Y. Miyauchi, S. Chiashi, M. Kohno, Chem. Phys. Lett. **360** (2002) 229.

18. Y. Murakami, E. Einarsson, T. Edamura, S. Maruyama, Carbon, To be submitted.

19. M. S. Strano, S. K. Doorn, E. H. Haroz, C. Kittrell, R. H. Hauge, R. E. Smalley, Nano Lett. **3** (2003) 1091.

20. H. Kataura, Y. Kumazawa, Y. Maniwa, I. Umezu, S. Suzuki, Y. Ohtsuka, Y. Achiba, Synth. Met. **103** (1999) 2555.

21. T. Pichler, M. Knupfer, M. S. Golden, J. Fink, A. Rinzler, R. E. Smalley, Phys. Rev. Lett. **80** (1998) 4729.

22. B. W. Reed and M. Sarikaya, Phys. Rev. B **64** (2001) 195404.

23. R. C. Haddon, J. Sippel, A. G. Rinzler, F. Papadimitrakopoulos, MRS Bullet. **29** (2004) 252.

24. E. A. Taft and H. R. Philipp, Phys. Rev. **138** (1965) A197.

25. M. K. Kelly, P. Etchegoin, D. Fuchs, W. Kratschmer, K. Fostiropoulos, Phys. Rev. B **46** (1992) 4963.

26. A. G. Marinopoulos, L. Reining, V. Olevano, A. Rubio, T. Pichler, X. Liu, M. Knupfer, J. Fink, Phys. Rev. Lett. **89** (2002) 076402.

27. A. Borgheshi and G. Guizzetti, in Handbook of Optical Constants of Solids II, edited by E. D. Palik (Academic Press Inc., San Diego, 1991).

28. F. J. Garcia-Vidal and J. M. Pitarke, Eur. Phys. J. B **22** (2001) 257.

29. A. B. Djurisic and E. H. Li, J. Appl. Phys. **85** (1999) 7404.

30. H. Venghaus, Phys. Stat. Solidi B **71** (1975) 609.

31. Y. Kim, N. Minami, W. Zhu, S. Kazaoui, R. Azumi, M. Matsumoto, Jpn. J. Appl. Phys. **42** (2003) 7629.

32. H. Lee H, T. D. Kang, K. H. An, D. J. Bae, Y. H. Lee, Jpn. J. Appl. Phys. **42** (2003) 5880.

33. A. Grüneis, R. Saito, G.G. Samsonidze, T. Kimura, M.A. Pimenta, A. Jorio, A.G. Souza Filho, G. Dresselhaus, M.S. Dresselhaus, Phys. Rev. B **67** (2003) 165402.

34. M. S. Dresselhaus and P. C. Eklund, Adv. Phys. **49** (2000) 705.

35. H. Kuzmany, W. Plank, M. Hulman, Ch. Kramberger, A. Grüneis, Th. Pichler, H. Peterlik, H. Kataura, Y. Achiba, Eur. Phys. J. B **22** (2001) 307.

36. A. Jorio, R. Saito, J. H. Hafner, C. M. Lieber, M. Hunter, T. McClure, G. Dresselhaus, M. S. Dresselhaus, Phys. Rev. Lett. **86** (2001) 1118.

37. S. K. Doorn, D. A. Heller, P. W. Barone, M. L. Usrey, M. S. Strano, Appl. Phys. A **78** (2004) 1147.

38. A. Jorio, M. A. Pimenta, A. G. Souza Filho, Ge. G. Samsonidze, A. K. Swan, M. S. Ünlü, B. B. Goldberg, R. Saito, G. Dresselhaus, M. S. Dresselhaus, Phys. Rev. Lett. **90** (2003) 107403.

39. A. Jorio, G. Dresselhaus, M. S. Dresselhaus, M. Souza, M. S. S. Dantas, M. A. Pimenta, A. M. Rao, R. Saito, C. Liu, H. M. Cheng, Phys. Rev. B **85** (2000) 2617.

40. G. S. Duesberg, I. Loa, M. Burghard, K. Syassen, S. Roth, Phys. Rev. Lett. **85** (2000) 5436.

41. A. Jorio, A. G. Souza Filho, V. W. Brar, A. K. Swan, M. S. Ünlü, B. B. Goldberg, A. Righi, J. H. Hafner, C. M. Lieber, R. Saito, G. Dresselhaus, M. S. Dresselhaus, Phys. Rev. B **65** (2002) 121402.

42. A. Grüneis, R. Saito, J. Jiang, Ge. G. Samsonidze, M. A. Pimenta, A. Jorio, A. G. Souza Filho, G. Dresselhaus, M. S. Dresselhaus, Chem. Phys. Lett. **387** (2004) 301.

43. R. B. Weisman and S. M. Bachilo, Nano Lett. **3** (2003) 1235.

44. Y. Murakami, Y. Miyauchi, S. Chiashi, S. Maruyama, Chem. Phys. Lett. **374** (2003) 53.

45. S. Maruyama, E. Einarsson, Y. Murakami, T. Edamura, Chem. Phys. Lett., To be submitted.

46. A. Jorio, M. A. Pimenta, A. G. Souza Filho, R. Saito, G. Dresselhaus, M. S. Dresselhaus, New J. Phys. **5** (2003) 139.

47. H. D. Li, K. T. Yue, Z. L. Lian, Y. Zhan, L. X. Zhou, S. L. Zhang, Z. J. Shi, Z. N. Gu, B. B. Liu, R. S. Yang, H. B. Yang, G. T. Zou, Y. Zhang, S. Iijima, Appl. Phys. Lett. **76** (2000) 2053.

48. N. R. Raravikar, P. Keblinski, A. M. Rao, M. S. Dresselhaus, L. S. Schadler, P. M. Ajayan, Phys. Rev. B **66** (2002) 235424.

49. S. Chiashi, Y. Murakami, Y. Miyauchi, S. Maruyama, Chem. Phys. Lett. **386** (2004) 89.

50. A. Kukovecz, Ch. Kramberger, V. Georgakilas, M. Prato, H. Kuzmany, Euro. Phys. J. B **28** (2002) 223.

51. Y. Miyauchi, S. Chiashi, Y. Murakami, Y. Hayashida, S. Maruyama, Chem. Phys. Lett. **387** (2004) 198.

52. M. S. Strano, J. Am. Chem. Soc. **125** (2003) 16148.

53. S. D. M. Brown, A. Jorio, P. Corio, M. S. Dresselhaus, G. Dresselhaus, R. Saito, K. Kneipp, Phys. Rev. B **63** (2001) 155414.

54. M. S. Strano, C. A. Dyke, M. L. Usrey, P. W. Barone, M. J. Allen, H. Shan, C. Kittrell, R. H. Hauge, J. M. Tour, R. E. Smalley, Science **301** (2003) 1519.

55. M. S. Strano, C. B. Huffman, V. C. Moore, M. J. O'Connell, E. H. Haroz, J. Hubbard, M. Miller, K. Rialon, C. Kittrell, S. Ramesh, R. H. Hauge, R. E. Smalley, J. Phys. Chem. B **107** (2003) 6979.

56. S. Maruyama, T. Miyake, S. Okada, S. Ogawa, K. Oba, Chem. Phys. Lett., To be submitted.

57. R. Saito, G. Dresselhaus, M. S. Dresselhaus, Phys. Rev. B **61**, (2000) 2981.

58. C. Fantini, A. Jorio, M. Souza, L. O. Ladeira, A. G. Souza Filho, R. Saito, Ge. G. Samsonidze, G. Dresselhaus, M. S. Dresselhaus, M. A. Pimenta, Phys. Rev. B **93** (2004) 087401.

59. H. Kataura, T. Ueno, Y. Miyata, S. Okubo, S. Suzuki, Y. Achiba, in presentation at *International Conference on the Science and Application of Nanotubes,* San Luis Potosi, Mexico, July 19-24, 2004.

60. M. J. O'Connell, S. M. Bachilo, C. B. Huffman, V. C. Moore, M. S. Strano, E. H. Haroz, K. L. Rialon, P. J. Boul, W. H. Noon, C. Kittrell, J. Ma, R. H. Hauge, R. B. Weisman, R. E. Smalley, Science **297** (2002) 593.

61. M. E. Fermann, J. Appl. Phys. B **58** (1994) 197.

62. U. Keller, D. Miller, G. Boyd, T. Chiu, J. Ferguson, M. Asorn, Opt. Lett. **17** (1992) 505.

63. V. J. Matsas, T. P. Newson, D. J. Richardson, D. J. Payne, Electron. Lett. **28** (1992) 1391.

64. N. J. Doran, D. Wood, Opt. Lett. **14** (1988) 56.

65. Y.C. Chen, N.R. Raravikar, L.S. Schadler, P.M. Ajayan, Y.P. Zhao, T.M. Lu, G.C. Wang, X.C. Zhang, Appl. Phys. Lett. **81** (2002) 975.

66. S. Tatsuura, M. Furuki, Y. Sato, I. Iwasa, M. Q. Tian, H. Mitsu, Adv. Mater. **15** (2003) 534.

67. S. Y. Set, H. Yaguchi, M. Jablonski, Y. Tanaka, Y. Sakakibara, A. Rozhin, M. Tokumoto, H. Kataura, Y. Achiba, K. Kikuchi, in Optical Fiber Communication Conference (OFC), Vol. 86 of OSA Trends in Optics and Photonics Series (Optical Society of America, Washington, D.C., 2003), paper FL2.

68. S. Y. Set, H. Yaguchi, Y. Tanaka, M. Jablonski, Y. Sakakibara, A. Rozhin, M. Tokumoto, H. Kataura, Y. Achiba, K. Kikuchi, in Optical Fiber Communication Conference (OFC), Vol. 86 of OSA Trends in Optics and Photonics Series (Optical Society of America, Washington, D.C., 2003), paper PD44.

69. S. Y. Set, H. Yaguchi, Y. Tanaka, M. Jablonski, Y. Sakakibara, M. Tokumoto, H. Kataura, Y. Achiba, S. Yamashita, K. Kikuchi, in Optical Fiber Communication Conference (OFC), Vol. 86 of OSA Trends in Optics and Photonics Series (Optical Society of America, Washington, D.C., 2003), paper CThPDA9.

70. S. Y. Set, H. Yaguchi, Y. Tanaka, M. Jablonski, J. Lightwave Technol. **22** (2004) 51.

71. A. Thess, R. Lee, P. Nikolaev, H. Dai, P. Petit, J. Robert, C. H. Xu, Y. H. Lee, S. G. Kim, A. G. Rinzler, D. T. Colbert, G. E. Scuseria, D. Tomanek, J. E. Fischer, R. E. Smalley, Science **273** (1996) 483.

72. Y. Kubota, T. Teshima, N. Nishimura, S. Kanto, S. Sakaguchi, Z. Meng, Y. Nakata, T. Okada, IEEE Photon. Technol. Lett. **15** (2003) 525.

73. S. Yamashita, Y. Inoue, S. Maruyama, Y. Murakami, H. Yamaguchi, M. Jablonski, S.Y. Set, Opt Lett. **29** (2004) 1581.

Chapter 5:
Summary

Starting with the development and characterization of the growth of SWNTs, the underlying mechanism and the direction for the choice of catalyst were investigated in Chapter 2. The findings and conclusions obtained in Chapter 2 are as follows:

1) The yield of SWNTs was defined on the basis of TGA with a confirmedatory support by TEM observations. The yield could be enhanced by the reduction of the catalyst prior to the CVD reaction.

2) The observed difference in the wettability of Fe, Co, Ni, and Mo on SiO_2 support and the resultant diameter of the SWNTs were explained by the magnitude of the ratio $\Delta H_f^\circ{}_{sublimate}/\Delta H_f^\circ{}_{oxide}$. This provides a useful guidance for the choice of the catalyst on SiO_2 support.

3) A dip-coat catalyst supporting method was developed for the direct support of a small amount of catalyst on the flat substrate. It was found that when cobalt and molybdenum acetates were used, the monodispersed Co particles with a diameter of 1–2 nm were densely supported on the SiO_2 surface without agglomeration even at 800°C.

4) The underlying mechanism for the successful dispersion of Co was investigated by TEM and XPS. It was elucidated that the $CoMoO_x$ ($x \leq 4$) compound was formed on the SiO_2 surface, and this layer was observed to stabilize the excess Co particles by preventing them from agglomerating into larger particles.

The findings obtained in Chapter 3 are summarized below:

1) Vertically aligned growth of SWNTs on flat substrates was demonstrated for the first time to be possible under an optimum CVD condition. The cleanness of the chamber is an important factor that controls the speed of catalyst deactivation during CVD. Based on the HR-TEM analyses, it was confirmed that the growth is considered to be the “root growth” and that the produced SWNTs possess high purity without containing MWNT or amorphous carbons.

2) Growth and alignment formation processes were investigated in terms of FE-SEM observations and optical absorption measurements using light incident normal to the substrate. Experimentally measured growth curves were explained by a proposed model in which the initial catalyst activity η_0 and the deactivation constant κ describe the entire growth process. The deterioration in the growth speed is considered to be an accumulated loss of initial catalyst activity related to the decomposition of ethanol molecules.

Chapter 4 presented several original findings that were obtained from optical measurements of the vertically aligned SWNT film These are as follows:

1) Anisotropic optical absorption properties of SWNTs were elucidated for a wide energy range of 0.5–6.0 eV. The optical absorption cross sections for both parallel and perpendicular to the SWNT axis were determined. The absorption peaks at 4.5 and 5.25 eV were discovered to exhibit strong dependences on the light polarization.

2) The peaks at 4.5 and 5.25 eV correspond to the maximum of $\mathrm{Im}\{\varepsilon_{\perp}\}$ parallel to the SWNT axis and that of $\mathrm{Im}\{-\varepsilon_{\parallel}^{-1}\}$ perpendicular to the axis, respectively, originating from the optical properties of graphite. This optical relevance between SWNTs and graphite implies the possibility of investigating unresolved optical properties of graphite in the direction parallel to the *c*-axis by measurements of the optical absorption of the aligned SWNT films.

3) The shape of the RBM spectrum was observed to exhibit a strong dependence on the incident light polarization. The RBM peaks were grouped into two types according to their behavior: In one type, the peak intensity was strong only for perpendicular polarization ($\boldsymbol{e} \perp \boldsymbol{l}$), while in the other type, the peak intensity was strong only for parallel polarization ($\boldsymbol{e} \,//\, \boldsymbol{l}$).

4) The RBM spectra can be varied even from a measurement from the identical sample depending on the incident polarization and physical environment of SWNTs. The knowledge on the nature of each RBM peak revealed in this section will aid in providing a sounder characterization of SWNTs by RRS analysis.

5) The SWNT film grown directly on the surface of the quartz substrate, which was developed in Section 2.3, was demonstrated to serve as a new SAINT device for optical applications. It was successfully applied to passively mode lock a fiber laser to produce sub-picosecond pulses at a 50-MHz repetition rate.

The author hopes that the findings presented in this thesis will contribute to the further development of fundamental studies and applications of SWNTs.

Appendix:

Perturbated Hamiltonian for one-photon process

A.1 Description of electromagnetic wave by vector potential

Maxwell's equation for electromagnetic waves propagating in vacuum is given by

$$\begin{aligned} &\text{rot}\,\boldsymbol{E} + \frac{\partial \boldsymbol{B}}{\partial t} = 0, \quad \text{div}\,\boldsymbol{B} = 0 \\ &\text{rot}\,\boldsymbol{H} - \frac{\partial \boldsymbol{D}}{\partial t} = 0, \quad \text{div}\,\boldsymbol{D} = 0 \end{aligned} \tag{1}$$

With the relations $\boldsymbol{D} = \varepsilon_0 \boldsymbol{E}$ and $\boldsymbol{B} = \mu_0 \boldsymbol{H}$, Eq. 1 is rewritten as

$$\begin{aligned} &\text{rot}\,\boldsymbol{E} + \frac{\partial \boldsymbol{B}}{\partial t} = 0, \quad \text{rot}\,\boldsymbol{B} - \varepsilon_0 \mu_0 \frac{\partial \boldsymbol{E}}{\partial t} = 0 \\ &\text{div}\,\boldsymbol{B} = 0, \quad \text{div}\,\boldsymbol{E} = 0 \end{aligned} \tag{2}$$

The *vector potential* $\boldsymbol{A}$ is introduced with the definition

$$\boldsymbol{B} = \text{rot}\,\boldsymbol{A} \tag{3}$$

that satisfies div $\boldsymbol{B} = 0$. From Eqs. 2 and 3, $\boldsymbol{E}$ is expressed in terms of $\boldsymbol{A}$ as

$$\boldsymbol{E} = -\frac{\partial \boldsymbol{A}}{\partial t} \tag{4}$$

The differential equation for $\boldsymbol{A}$ is then obtained by substituting Eqs 3 and 4 into Eq. 2 as

$$\nabla^2 \boldsymbol{A} - \frac{1}{c^2}\frac{\partial^2 \boldsymbol{A}}{\partial^2 t} = 0, \quad \left[c = \sqrt{\frac{1}{\varepsilon_0 \mu_0}} = 3 \times 10^8 \ \text{m} \cdot \text{s}^{-1} \right] \tag{5}$$

Since $\boldsymbol{A}$ has a freedom in the magnitude of its baseline by the gradient of some scalar field $\nabla\psi$ due to the relation $\nabla \times (\nabla\psi) = 0$, this freedom is conventionally eliminated by employing so-called *Coulomb gauge* in which $\nabla^2\psi$ is adjusted in order to set div $\boldsymbol{A} = 0$.

The plane waves confined in a cube with edge length L (i.e. with volume $V = L^3$) are considered. The wave numbers for x, y, and z direction k_x, k_y, and k_z, respectively, are represented using integers n_x, n_y, and n_z as

$$k_x = \frac{2\pi}{L} n_x, \quad k_y = \frac{2\pi}{L} n_y, \quad k_z = \frac{2\pi}{L} n_z \tag{6}$$

in order to conform with the periodic boundary condition. Then, the plane-wave solution for $\boldsymbol{A}$ is obtained in terms of wave number vector $\boldsymbol{k}$ (= $[k_x\ k_y\ k_z]^{\mathrm{T}}$) and position vector $\boldsymbol{r}$ as

$$\boldsymbol{A}(r,t) = \boldsymbol{A}_0 \mathrm{e}^{i(\boldsymbol{k}\cdot\boldsymbol{r} - \varpi t)} \tag{7}$$

Furthermore, since the following relationship holds,

$$\text{div}\,\boldsymbol{A}(r,t) = \nabla \cdot \boldsymbol{A} = i\boldsymbol{k} \cdot \boldsymbol{A}_0 \mathrm{e}^{i(\boldsymbol{k}\cdot\boldsymbol{r} - \varpi t)} = 0 \quad \Leftrightarrow \quad \boldsymbol{k} \cdot \boldsymbol{A} = 0 \tag{8}$$

$\boldsymbol{A}$ is perpendicular to $\boldsymbol{k}$. Using a unit vector $\boldsymbol{e}$ in the direction of $\boldsymbol{A}$, Eq. 7 can be rewritten as

$$\boldsymbol{A}(r,t) = \boldsymbol{A}_0 \mathrm{e}^{i(\boldsymbol{k}\cdot\boldsymbol{r}-\varpi t)} = \boldsymbol{e}A_0 \mathrm{e}^{i(\boldsymbol{k}\cdot\boldsymbol{r}-\varpi t)} \tag{9}$$

In order for $\boldsymbol{A}$ to be real number, Eq. 9 and its complex conjugate are added together as

$$\boldsymbol{A}(r,t) = \sqrt{\frac{1}{V}}\boldsymbol{e}_{\boldsymbol{k},\gamma}\left\{q_{\boldsymbol{k}}(t)\mathrm{e}^{i\boldsymbol{k}\cdot\boldsymbol{r}} + q_{\boldsymbol{k}}{}^{*}(t)\mathrm{e}^{-i\boldsymbol{k}\cdot\boldsymbol{r}}\right\} \tag{10}$$

where $V^{-1/2}$ is a normalization constant. $q_{\boldsymbol{k}}(t)$ is given as

$$q_{\boldsymbol{k}}(t) = |q_{\boldsymbol{k}}|\exp\{-i(\varpi_{\boldsymbol{k}}t + \delta_{\boldsymbol{k}})\}, \quad \varpi_{\boldsymbol{k}} = c|\boldsymbol{k}| \tag{11}$$

Both $|q_{\boldsymbol{k}}|$ and δ are the parameters to be determined for the description of considered field.

Direction of $\boldsymbol{e}$ is projected on the orthogonal coordinates $\gamma = 1$ and $\gamma = 2$ that are perpendicular to the direction of propagation, as schematized in Fig. A-1. The general solution for $\boldsymbol{A}$ is expressed as a summation of all possible $\boldsymbol{k}$ and γ, as

$$\boldsymbol{A}(r,t) = \sqrt{\frac{1}{V}}\sum_{\boldsymbol{k}}\sum_{\gamma=1}^{2}\boldsymbol{e}_{\boldsymbol{k},\gamma}\left\{q_{\boldsymbol{k},\gamma}(t)\mathrm{e}^{i\boldsymbol{k}\cdot\boldsymbol{r}} + q_{\boldsymbol{k},\gamma}{}^{*}(t)\mathrm{e}^{-i\boldsymbol{k}\cdot\boldsymbol{r}}\right\} \tag{12}$$

Similarly, $\boldsymbol{E}$ and $\boldsymbol{B}$ can be expressed using Eqs, 3, 4, and 12, as

$$\boldsymbol{E}(r,t) = \sqrt{\frac{1}{V}}\sum_{\boldsymbol{k}}\sum_{\gamma=1}^{2}\boldsymbol{e}_{\boldsymbol{k},\gamma}i\varpi_{\boldsymbol{k}}\left\{q_{\boldsymbol{k},\gamma}(t)\mathrm{e}^{i\boldsymbol{k}\cdot\boldsymbol{r}} - q_{\boldsymbol{k},\gamma}{}^{*}(t)\mathrm{e}^{-i\boldsymbol{k}\cdot\boldsymbol{r}}\right\} \tag{13}$$

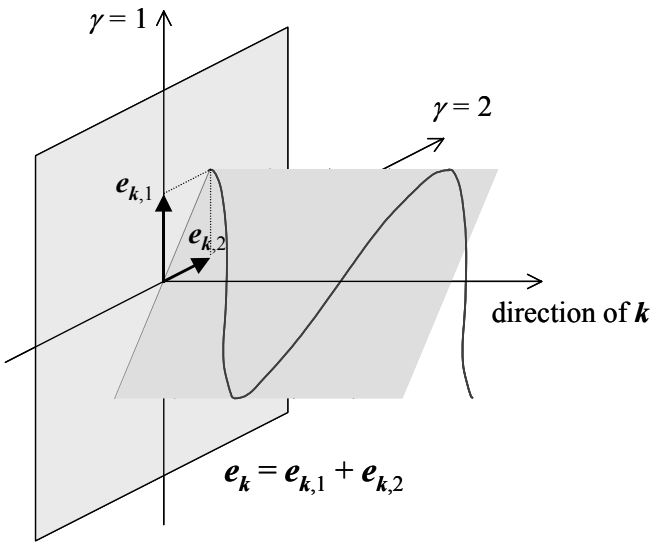


Fig. A-1. Schematic for light propagation described by $\boldsymbol{e}$ and $\boldsymbol{k}$. The coordinate $\gamma = 1$ and $\gamma = 2$ is perpendicular to the direction of wave propagation.

$$\boldsymbol{B}(r,t)=\sqrt{\frac{1}{V}}\sum_{\boldsymbol{k}}\sum_{\gamma=1}^{2}i\left[\boldsymbol{k}\times\boldsymbol{e}_{\boldsymbol{k},\gamma}\right]\left\{q_{\boldsymbol{k},\gamma}(t)\mathrm{e}^{i\boldsymbol{k}\cdot\boldsymbol{r}}-q_{\boldsymbol{k},\gamma}{}^{*}(t)\mathrm{e}^{-i\boldsymbol{k}\cdot\boldsymbol{r}}\right\} \tag{14}$$

The behavior of $\boldsymbol{A}$ at the origin $\boldsymbol{r}=0$ is described as

$$\boldsymbol{A}(0,t)=\sqrt{\frac{1}{V}}\sum_{\boldsymbol{k}}\sum_{\gamma=1}^{2}\boldsymbol{e}_{\boldsymbol{k},\gamma}\left\{q_{\boldsymbol{k},\gamma}(t)+q_{\boldsymbol{k},\gamma}{}^{*}(t)\right\}=\sqrt{\frac{1}{V}}\sum_{\boldsymbol{k}}\sum_{\gamma=1}^{2}\boldsymbol{e}_{\boldsymbol{k},\gamma}Q_{\boldsymbol{k},\gamma}(t) \tag{15}$$

Here, $Q_{\boldsymbol{k},\gamma}(t)$ denotes amplitude of the ($\boldsymbol{k}$, γ) component of $\boldsymbol{A}$ at the origin, given by

$$Q_{\boldsymbol{k},\gamma}(t)\equiv\left\{q_{\boldsymbol{k},\gamma}(t)+q_{\boldsymbol{k},\gamma}{}^{*}(t)\right\}=2\left|q_{\boldsymbol{k},\gamma}\right|\cos(\varpi_{\boldsymbol{k}}t+\delta_{\boldsymbol{k}}) \tag{16}$$

and its time derivative $\dot{Q}_{\boldsymbol{k},\gamma}(t)$ is expressed as

$$\dot{Q}_{\boldsymbol{k},\gamma}(t)=-i\varpi_{\boldsymbol{k}}\left\{q_{\boldsymbol{k},\gamma}(t)-q_{\boldsymbol{k},\gamma}{}^{*}(t)\right\} \tag{17}$$

Therefore, using Eqs. 13 and 14, $q_{\boldsymbol{k},\gamma}$ and $q_{\boldsymbol{k},\gamma}$* are expressed as

$$\dot{q}_{\boldsymbol{k},\gamma}(t)=\frac{1}{2}\left\{Q_{\boldsymbol{k},\gamma}(t)+\frac{i}{\varpi_{\boldsymbol{k}}}\dot{Q}_{\boldsymbol{k},\gamma}(t)\right\} \tag{18}$$

$$\dot{q}_{\boldsymbol{k},\gamma}{}^{*}(t)=\frac{1}{2}\left\{Q_{\boldsymbol{k},\gamma}(t)-\frac{i}{\varpi_{\boldsymbol{k}}}\dot{Q}_{\boldsymbol{k},\gamma}(t)\right\} \tag{19}$$

A.2 Description of photons

According to the electromagnetic theory, the energy density U of electromagnetic wave is given by

$$U(r,t)=\frac{1}{2}(\boldsymbol{D}\cdot\boldsymbol{E}+\boldsymbol{B}\cdot\boldsymbol{H})=\frac{1}{2}(\varepsilon_0\boldsymbol{E}\cdot\boldsymbol{E}+\frac{1}{\mu_0}\boldsymbol{B}\cdot\boldsymbol{B}) \tag{20}$$

By substituting Eqs. 13 and 14 into Eq. 21, total energy of the electromagnetic wave H inside the volume V (= L^3) is expressed as

$$\begin{aligned}H=\iiint U d\boldsymbol{r}=\cdots&=\frac{\varepsilon_0}{2}\sum_{\boldsymbol{k}}\sum_{\gamma=1}^{2}(\varpi_k+c^2k^2)\left\{q_{\boldsymbol{k},\gamma}q_{\boldsymbol{k},\gamma}{}^{*}+q_{\boldsymbol{k},\gamma}{}^{*}q_{\boldsymbol{k},\gamma}\right\}\\&=2\varepsilon_0\sum_{\boldsymbol{k}}\sum_{\gamma=1}^{2}\varpi_k{}^{2}q_{\boldsymbol{k},\gamma}q_{\boldsymbol{k},\gamma}{}^{*}\end{aligned} \tag{21}$$

d

Then, substituting Eqs. 18 and 19 into Eq. 21,

$$H = \frac{\varepsilon_0}{2}\sum_{\boldsymbol{k}}\sum_{\gamma=1}^{2}(\dot{Q}_{\boldsymbol{k},\gamma}{}^2 + \varpi_k{}^2 Q_{\boldsymbol{k},\gamma}{}^2) \tag{22}$$

Comparing the equation for energy of 1-D harmonic oscillator

$$(\text{Energy of 1-D harmonic oscillator}) = \frac{m}{2}(\dot{x}^2 + \varpi^2 x^2) \tag{23}$$

and Eq. 22, it is derived that $Q_{\boldsymbol{k},\gamma}(t)$ represents a generalized coordinate and $P_{\boldsymbol{k},\gamma}(t)$ given by

$$P_{\boldsymbol{k},\gamma} = \varepsilon_0 \dot{Q}_{\boldsymbol{k},\gamma} \tag{24}$$

represents a generalized momentum. Then, the Hamiltonian H can be represented in terms of generalized coordinate and generalized momentum is written as

$$H = \sum_{\boldsymbol{k}}\sum_{\gamma=1}^{2}(\frac{1}{2\varepsilon_0}P_{\boldsymbol{k},\gamma}{}^2 + \frac{1}{2}\varepsilon_0 \varpi_k{}^2 Q_{\boldsymbol{k},\gamma}{}^2) \tag{25}$$

The momentum P has to be written as an operator in order to transform H into the quantum-mechanical form,

$$H = \sum_{\boldsymbol{k}}\sum_{\gamma=1}^{2}(-\frac{\hbar^2}{2\varepsilon_0}\frac{\partial^2}{\partial Q_{\boldsymbol{k},\gamma}{}^2}P_{\boldsymbol{k},\gamma}{}^2 + \frac{1}{2}\varepsilon_0 \varpi_k{}^2 Q_{\boldsymbol{k},\gamma}{}^2) \tag{26}$$

Now the problem is reduced to the basic quantum mechanics for case of 1-D harmonic oscillator. Therefore, an eigenvalue for H in Eq. 26, which correspond to intrinsic energy E is given by

$$E = \sum_{\boldsymbol{k}}\sum_{\gamma=1}^{2}(n_{\boldsymbol{k},\gamma} + \frac{1}{2})\hbar\varpi_k\,, \quad (n_{\boldsymbol{k},\gamma} = 0, 1, 2, \cdots) \tag{27}$$

The number of oscillator $n_{\boldsymbol{k},\gamma}$ is the number of photon whose energy is $\hbar\varpi_{\boldsymbol{k}}$. Furthermore, the annihilation and creation operators $a_{\boldsymbol{k},\gamma}$ and $a_{\boldsymbol{k},\gamma}$* are given from the analogy to the case of 1-D harmonic oscillator as

$$a_{\boldsymbol{k},\gamma}{}^* = \sqrt{\frac{2\varepsilon_0\varpi_k}{\hbar}}\left(Q_{\boldsymbol{k},\gamma} - \frac{i}{\varepsilon_0\varpi_k}P_{\boldsymbol{k},\gamma}\right) = \sqrt{\frac{2\varepsilon_0\varpi_k}{\hbar}}q_{\boldsymbol{k},\gamma}{}^* \tag{28}$$

$$a_{\boldsymbol{k},\gamma} = \sqrt{\frac{2\varepsilon_0\varpi_k}{\hbar}}\left(Q_{\boldsymbol{k},\gamma} + \frac{i}{\varepsilon_0\varpi_k}P_{\boldsymbol{k},\gamma}\right) = \sqrt{\frac{2\varepsilon_0\varpi_k}{\hbar}}q_{\boldsymbol{k},\gamma} \tag{29}$$

Using Eqs. 28 and 29, Eq. 25 can be rewritten as

$$H = \frac{1}{2}\sum_{\boldsymbol{k}}\sum_{\gamma=1}^{2}\hbar\varpi_k\left(a_{\boldsymbol{k},\gamma}{}^{*}a_{\boldsymbol{k},\gamma} + a_{\boldsymbol{k},\gamma}a_{\boldsymbol{k},\gamma}{}^{*}\right) \tag{30}$$

Further, Using Eqs. 28 and 29, Eqs. 12, 13, and 14 are rewritten as

$$\boldsymbol{A}(r) = \sqrt{\frac{\hbar}{2\varepsilon_0 V}}\sum_{\boldsymbol{k}}\sum_{\gamma=1}^{2}\frac{\boldsymbol{e}_{\boldsymbol{k},\gamma}}{\sqrt{\varpi_k}}\left\{\mathrm{e}^{i\boldsymbol{k}\cdot\boldsymbol{r}}a_{\boldsymbol{k},\gamma} + \mathrm{e}^{-i\boldsymbol{k}\cdot\boldsymbol{r}}a_{\boldsymbol{k},\gamma}{}^{*}\right\} \tag{31}$$

$$\boldsymbol{E}(r) = \sqrt{\frac{\hbar}{2\varepsilon_0 V}}\sum_{\boldsymbol{k}}\sum_{\gamma=1}^{2}\boldsymbol{e}_{\boldsymbol{k},\gamma}i\sqrt{\varpi_k}\left\{\mathrm{e}^{i\boldsymbol{k}\cdot\boldsymbol{r}}a_{\boldsymbol{k},\gamma} - \mathrm{e}^{-i\boldsymbol{k}\cdot\boldsymbol{r}}a_{\boldsymbol{k},\gamma}{}^{*}\right\} \tag{32}$$

$$\boldsymbol{B}(r) = \sqrt{\frac{\hbar}{2\varepsilon_0 V}}\sum_{\boldsymbol{k}}\sum_{\gamma=1}^{2}\left[\boldsymbol{k}\times\boldsymbol{e}_{\boldsymbol{k},\gamma}\right]\frac{i}{\sqrt{\varpi_k}}\left\{\mathrm{e}^{i\boldsymbol{k}\cdot\boldsymbol{r}}a_{\boldsymbol{k},\gamma} - \mathrm{e}^{-i\boldsymbol{k}\cdot\boldsymbol{r}}a_{\boldsymbol{k},\gamma}{}^{*}\right\} \tag{33}$$

in terms of annihilation and creation operators $a_{\boldsymbol{k},\gamma}$ and $a_{\boldsymbol{k},\gamma}{}^{*}$. It is noted that time-dependent term $\exp(-i\varepsilon t/\hbar)$ is embedded in the wave function to which above operators couple, if based on the Schrödinger's representation.

A.3 Interaction between electron and electromagnetic wave

The force $\boldsymbol{F}$ exerted on a particle with charge q moving in electromagnetic field $\boldsymbol{E}$ and $\boldsymbol{B}$ with the speed $\boldsymbol{v}$ is given by

$$\boldsymbol{F} = e\left\{\boldsymbol{E} + (\boldsymbol{v}\times\boldsymbol{B})\right\} \tag{34}$$

which is called Lorentz force. Corresponding Newton's equation of motion is written as

$$\begin{aligned} m\ddot{x} &= eE_x + e(\dot{y}B_z - \dot{z}B_y) \\ m\ddot{y} &= eE_y + e(\dot{z}B_x - \dot{x}B_z) \\ m\ddot{z} &= eE_z + e(\dot{x}B_y - \dot{y}B_x) \end{aligned} \tag{35}$$

$\boldsymbol{E}$ and $\boldsymbol{B}$ are given in terms of vector potential $\boldsymbol{A}$ in Eqs. 3 and 4, respectively, and using these relations Eq. 35 is rewritten as

f

$$
\begin{aligned}
m\ddot{x} &= -e\frac{\partial A_x}{\partial t} + e\left\{\dot{y}\left(\frac{\partial A_y}{\partial x} - \frac{\partial A_x}{\partial y}\right) - \dot{z}\left(\frac{\partial A_x}{\partial z} - \frac{\partial A_z}{\partial x}\right)\right\} \\
m\ddot{y} &= -e\frac{\partial A_y}{\partial t} + e\left\{\dot{z}\left(\frac{\partial A_z}{\partial y} - \frac{\partial A_y}{\partial z}\right) - \dot{x}\left(\frac{\partial A_y}{\partial x} - \frac{\partial A_x}{\partial y}\right)\right\} \\
m\ddot{z} &= -e\frac{\partial A_z}{\partial t} + e\left\{\dot{x}\left(\frac{\partial A_x}{\partial z} - \frac{\partial A_z}{\partial x}\right) - \dot{y}\left(\frac{\partial A_z}{\partial y} - \frac{\partial A_y}{\partial z}\right)\right\}
\end{aligned}
\tag{36}
$$

In current case, Lagrangean has to be calculated firstly in order to determine Hamiltonian of the system. This is mainly because the force is dependent on the speed of the particle in the case of Lorentz force in Eq. 34. Namely, momentum of the charged particle in electromagnetic field is not simply given by [mass × velocity].

The Lagrangean L that satisfy the Lagrange's equation of motion

$$
\frac{d}{dt}\left(\frac{\partial L}{\partial \dot{x}}\right) - \frac{\partial L}{\partial x} = 0 \tag{37}
$$

and, at the same time, Eq. 36 is found to be

$$
L = \frac{m}{2}(\dot{x}^2 + \dot{y}^2 + \dot{z}^2) + e(\dot{x}A_x + \dot{y}A_y + \dot{z}A_z) \tag{38}
$$

Subsequently, the momentum of the particle in field $\boldsymbol{A}$ is obtained as

$$
\begin{aligned}
p_x &= \frac{\partial L}{\partial \dot{x}} = m\dot{x} + eA_x \\
p_y &= \frac{\partial L}{\partial \dot{y}} = m\dot{y} + eA_y \\
p_z &= \frac{\partial L}{\partial \dot{z}} = m\dot{z} + eA_z
\end{aligned}
\tag{39}
$$

Namely, an existence of an electromagnetic field $\boldsymbol{A}$ changes kinetic energy of the moving particle as

$$
\frac{1}{2m}\boldsymbol{p}_j^{\,2} \quad \rightarrow \quad \frac{1}{2m}\left(\boldsymbol{p}_j + e\boldsymbol{A}\right)^2 \tag{40}
$$

Here, the subscript j denotes index number for the electron in the system. Therefore, the change of Hamiltonian ΔH due to the existence of $\boldsymbol{A}$ is expressed as

$$
\begin{aligned}
\Delta H &= \sum_j \left\{\frac{1}{2m}\left(\boldsymbol{p}_j + e\boldsymbol{A}(\boldsymbol{r}_j)\right)^2\right\} - \sum_j \frac{1}{2m}\boldsymbol{p}_j^{\,2} \\
&= \frac{e}{2m}\sum_j \left\{\boldsymbol{p}_j \cdot \boldsymbol{A}(\boldsymbol{r}_j) + \boldsymbol{A}(\boldsymbol{r}_j)\cdot \boldsymbol{p}_j\right\} + \frac{e^2}{2m}\sum_j \boldsymbol{A}^2(\boldsymbol{r}_j)
\end{aligned}
\tag{41}
$$

Since $\boldsymbol{p}_j = -i\hbar\nabla_j$ in the quantum-mechanical expression,

$$\boldsymbol{p}_j \cdot \boldsymbol{A}(\boldsymbol{r}_j) = -i\hbar\left\{\nabla_j \boldsymbol{A}(\boldsymbol{r}_j) + \boldsymbol{A}(\boldsymbol{r}_j)\cdot\nabla_j\right\} = -i\hbar\boldsymbol{A}(\boldsymbol{r}_j)\cdot\nabla_j \tag{42}$$

in which the relation div $\boldsymbol{A} = 0$ was used, and hence, ΔH is expressed as

$$\Delta H = \frac{e}{m}\sum_j \boldsymbol{A}(\boldsymbol{r}_j)\cdot\boldsymbol{p}_j + \frac{e^2}{2m}\sum_j \boldsymbol{A}^2(\boldsymbol{r}_j) \tag{43}$$

Let the first and second terms to be $H^{(1)}$ and $H^{(2)}$, respectively. The $H^{(1)}$ is expressed as

$$H^{(1)} = \frac{e}{m}\sqrt{\frac{\hbar}{2\varepsilon_0 V}}\sum_j\sum_{\boldsymbol{k},\gamma}\frac{1}{\sqrt{\varpi_{\boldsymbol{k}}}}\left\{\mathrm{e}^{i\boldsymbol{k}\cdot\boldsymbol{r}_j}(\boldsymbol{e}_{\boldsymbol{k},\gamma}\cdot\boldsymbol{p}_j)a_{\boldsymbol{k},\gamma} + \mathrm{e}^{-i\boldsymbol{k}\cdot\boldsymbol{r}_j}(\boldsymbol{e}_{\boldsymbol{k},\gamma}\cdot\boldsymbol{p}_j)a_{\boldsymbol{k},\gamma}{}^*\right\} \tag{44}$$

This is a linear equation of $\boldsymbol{a}_{\boldsymbol{k},\gamma}$ and $\boldsymbol{a}_{\boldsymbol{k},\gamma}{}^*$, which means that the $H^{(1)}$ either increase or decrease the number of photon by one through the *one-photon process*. On the other hand, the $H^{(2)}$ is a quadric equation of $\boldsymbol{a}_{\boldsymbol{k},\gamma}$ and $\boldsymbol{a}_{\boldsymbol{k},\gamma}{}^*$ indicating that this Hamiltonian describes the *two-photon process*.

h

Acknowledgements

During the course of this thesis, I have been privileged to receive the advice and assistance of many people. I would like to thank them all, but mentioning only a few is allowed here. First and foremost, I would like to express my sincere gratitude to my supervisor, Prof. Shigeo Maruyama, for his continued advice and invaluable guidance throughout the course of my research. I would also like to thank Prof. Tatsuya Okubo and Dr. Minghui Hu for their many helps and discussions in the fulfillment of this thesis. Without them, many important experimental facts and discussions regarding the role of the catalyst would not appear in this thesis. I would also like to acknowledge Prof. Shinji Yamashita for the precious collaboration on the application of single-walled carbon nanotubes to optical devices from which I fortunately could learn many things, Prof. Yuichi Ikuhara for his brilliant cross-sectional TEM observation on the nanotube-grown substrates, and Prof. Kazunori Hoshino for his providing elaborated Si-based microstructures. For precious advices and discussions on the thesis, I would like to express my gratitude to Prof. Yoichiro Matsumoto and Prof. Atsumu Tezaki. Thanks are also gratefully extended to Dr. Hideo Tsunakawa for his kind and repeated assistances in my TEM operations. Special thanks are owed to Mr. Mitsuru Inoue and Mr. Makoto Watanabe who kindly supported me performing many affairs in the laboratory. I am grateful to all my current and former lab-mates, with whom I have fortunately been enjoying my research life here. Finally, I want to express my hearty gratitude to my wife, Asuka, for her kind support, encouragement, and patience throughout my fulfillment of the thesis research.

List of publications

First Author Publications:

1. Y. Murakami and B. B. Mikić, “Parametric Optimization of Multichanneled Heat Sinks for VLSI Chip Cooling,” *IEEE Transactions on Components and Packaging Technologies*, vol. 24, pp. 2-9, 2001.

2. Y. Murakami and B. B. Mikić, “Parametric Investigation of Viscous Dissipation Effects on Optimized Air Cooling Microchanneled Heat Sinks,” *Heat Transfer Engineering*, vol. 24, pp. 53-62, 2003.

3. Y. Murakami, Y. Miyauchi, S. Chiashi, and S. Maruyama, “Characterization of Single-Walled Carbon Nanotubes Catalytically Synthesized from Alcohol,” *Chemical Physics Letters*, vol. 374, pp. 53-58, 2003.

4. Y. Murakami, S. Yamakita, T. Okubo, and S. Maruyama, “Single-Walled Carbon Nanotubes Catalytically Grown from Mesoporous Silica Thin Film,” *Chemical Physics Letters*, vol. 375, pp. 393-398, 2003.

5. Y. Murakami, Y. Miyauchi, S. Chiashi, and S. Maruyama, “Direct Synthesis of High-Quality Single-Walled Carbon Nanotubes on Silicon and Quartz substrates,” *Chemical Physics Letters*, vol. 377, pp. 49-54, 2003.

6. Y. Murakami, S. Chiashi, Y. Miyauchi, and S. Maruyama, “Direct Synthesis of Single-Walled Carbon Nanotubes on Silicon and Quartz-Based Systems,” *Japanese Journal of Applied Physics*, vol. 43, pp. 1221-1226, 2004.

7. Y. Murakami, S. Chiashi, Y. Miyauchi, M. Hu, M. Ogura, T. Okubo, and S. Maruyama, “Growth of Vertically Aligned Single-Walled Carbon Nanotube films on Quartz Substrates and their Optical Anisotropy,” *Chemical Physics Letters*, vol. 385, pp. 298-303, 2004.

8. Y. Murakami, S. Chiashi, E. Einarsson, and S. Maruyama, “Polarization Dependence of Resonant Raman Scattering from Vertically Aligned Single-Walled Carbon Nanotube Films,” *Physical Review B*, vol. 71, pp. 085403-1-085403-8, 2005.

9. Y. Murakami, E. Einarsson, T. Edamura, and S. Maruyama, “Polarization Dependence of the Optical Absorption of Single-Walled Carbon Nanotubes," *Physical Review Letters*, ~~in press.~~ vol. 94, pp. 087402-1-087402-4, 2005.

Co-Author Publications:

1. S. Maruyama, Y. Miyauchi, T. Edamura, Y. Igarashi, S. Chiashi, and Y. Murakami, "Synthesis of Single-Walled Carbon Nanotubes with Narrow Diameter-Distribution from Fullerene," *Chemical Physics Letters*, vol. 375, pp. 553-559, 2003.

2. S. Maruyama, Y. Miyauchi, Y. Murakami, and S. Chiashi, "Optical Characterization of Single-Walled Carbon Nanotubes Synthesized by Catalytic Decomposition of Alcohol," *New Journal of Physics*, vol. 5, pp. 149.1-149.12, 2003.

3. S. Chiashi, Y. Murakami, Y. Miyauchi, and S. Maruyama, "Cold Wall CVD Generation of Single-Walled Carbon Nanotubes and in situ Raman Scattering Measurement of the Growth Stage,", *Chemical Physics Letters*, vol. 386, pp. 89-94, 2004.

4. Y. Miyauchi, S. Chiashi, Y. Murakami, Y. Hayashida, and S. Maruyama, "Fluorescence Spectroscopy of Single-Walled Carbon Nanotubes Synthesized from Alcohol," *Chemical Physics Letters*, vol. 387, pp. 198-203, 2004.

5. S. Maruyama, Y. Murakami, Y. Miyauchi, and S. Chiashi, "Generation of Single-Walled Carbon Nanotubes from Alcohol and Generation Mechanism by Molecular Dynamics Simulations," *Journal of Nanoscience and Nanotechnology*, vol. 4, pp. 360-367, 2004.

6. M. Hu, Y. Murakami, M. Ogura, S. Maruyama, and T. Okubo, "Morphology and Chemical State of Co-Mo Catalysts for Growth of Single-Walled Carbon Nanotubes Vertically Aligned on Quartz Substrates," *Journal of Catalysis*, vol. 225, pp. 230-239, 2004.

7. S. Yamashita, S. Maruyama, Y. Murakami, Y. Inoue, H. Yaguchi, M. Jablonski, and S. Y. Set, "Saturable Absorbers Incorporating Carbon Nanotubes Directly Synthesized onto Substrates/Fibers and their Applications to Mode-Locked Fiber Lasers," *Optics Letters*, vol. 29, pp. 1581-1583, 2004.

8. H. Igarashi, H. Murakami, Y. Murakami, S. Maruyama, and N. Nakashima, "Purification and Characterization of Zeolite-Supported Single-Walled Carbon Nanotubes Catalytically Synthesized from Ethanol," *Chemical Physics Letters*, vol. 392, pp. 529-532, 2004.

9. M. Kohno, T. Orii, M. Hirasawa, T. Seto, Y. Murakami, S. Chiashi, Y. Miyauchi, and S. Maruyama, "Growth of Single-Walled Carbon Nanotubes from Size-Selected Catalytic Metal Particles," *Applied Physics A*, vol. 79, pp. 787-790, 2004.

10. Y. Ohno, Y. Kurokawa, T. Shimada, Y. Murakami, A. Sakai, T. Okazaki, S. Kishimoto, K. Hiraga, S. Maruyama, H. Shinohara, and T. Mizutani, "Synthesis of Carbon Nanotube Peapods Directly on Si Substrates," *Applied Physics Letters*, vol. 86, pp. 023109-023111, 2005.

11. S. Maruyama, E. Einarsson, Y. Murakami, and T. Edamura, “Growth Process of Vertically Aligned Single-Walled Carbon Nanotubes,” *Chemical Physics Letters*, vol. 403, pp. 320-323, 2005.

International Conferences

1. Y. Murakami, Y. Miyauchi, S. Chiashi, and S. Maruyama, “Direct synthesis of high-purity single-walled carbon nanotube mat on silicon and quartz substrates and their applications,” *International Conference on the Science and Application of Nanotubes 2003 (NT03)*, Seoul, Korea, 2003.

2. Y. Murakami, S. Chiashi, Y. Miyauchi, and S. Maruyama, “Direct Synthesis of Single-Walled Carbon Nanotubes on Silicon and Quartz Based Sytems,” *International Symposium on Micro-Mechanical Engineering 2003 (ISMME 2003)*, Tsukuba, Japan, 2003.

3. Y. Murakami, S. Chiashi, Y. Miyauchi, M. Hu, M. Ogura, T. Okubo, and S. Maruyama, “Vertically Aligned Growth of SWNTs "Mat" on a Quartz Surface,” *227th American Chemical Society National Meeting*, Anaheim CA, USA, 2004.

4. Y. Murakami, T. Edamura, E. Einarsson, S. Chiashi, Y. Miyauchi, and S. Maruyama, “Thermal CVD Growth of Vertically Aligned Single-Walled Carbon Nanotube Films on Substrates and their Optical/Microscopical Characterizations,” *International Forum on Heat Transfer 2004 (IFHT 2004)*, Kyoto, Japan, 2004.

5. Y. Murakami, E. Einarsson, T. Edamura, and S. Maruyama, “Anisotropic Optical Absorption Properties of Single-Walled Carbon Nanotubes,” *International Symposium on Nanometer-scale Quantum Physics (nanoPHYS’05)*, Tokyo, Japan, 2005.